2014

Nonlinear Burn Condition and Kinetic Profile Control in Tokamak Fusion Reactors

Mark Daniel Boyer
Lehigh University

Nonlinear Burn Condition and Kinetic Profile Control in Tokamak Fusion Reactors

by

Mark D. Boyer II

Presented to the Graduate and Research Committee

of Lehigh University

in Candidacy for the Degree of

Doctor of Philosophy

in

Mechanical Engineering

Lehigh University

January 2014

Final Dissertation Signature Sheet

Approved and recommended for acceptance as a dissertation in partial fulfillment of the requirements for the degree of Doctor of Philosophy.

_____

Date

_____

Professor Eugenio Schuster

Dissertation Advisor

_____

Accepted Date

Committee Members:

_____

Professor Donald Rockwell

_____

Professor Herman Nied

_____

Professor Mayuresh Kothare

_____

Professor Arnold Kritz

Acknowledgements

First of all, I would like to express sincere gratitude to my advisor, Professor Eugenio Schuster, for his guidance and support, and for introducing me to the exciting and challenging problems that I have worked on throughout my time at Lehigh University.

I would like to thank the Plasma Control and Operations Group of the DIII-D National Fusion Facility at General Atomics, especially Dr. Mike Walker and Dr. Dave Humphreys for their support during experimental campaigns and during my stay at General Atomics. In addition, I would like to express appreciation to Dr. Sylvain Bremond and Dr. Remy Nouailletas for hosting my visiting research at CEA Cadarache. The contributions of these collaborators were crucial to the completion of my dissertation work.

Furthermore, I would like to thank the members and alumni of the Laboratory for Control of Complex Physical Systems at Lehigh University, especially Justin Barton, Wenyu Shi, and William Wehner, for their assistance, fruitful collaborations, and friendship throughout my time in the group.

Finally, and most of all, I am grateful to my wife, Amber, for her endless patience, love, and encouragement, and to my family for supporting me throughout my studies.

Contents

List of Tables

List of Figures

Abstract

One of the most promising devices for realizing power production through nuclear fusion is the tokamak. In order to maximize performance, it is preferable that tokamaks achieve operating scenarios characterized by good plasma confinement, improved magnetohydrodynamic stability, and a largely non-inductively driven plasma current. Such scenarios could enable steady-state reactor operation with high fusion gain, the ratio of fusion power produced to the external heating power needed to sustain reactions. There are many experimental tokamaks around the world, each exploring different facets of plasma physics and fusion technology. These experiments have reached the point where the power released from fusion is nearly equal to the power input required to heat the plasma. The next experimental step is ITER, which aims to reach a fusion gain exceeding ten for short pulses, and to sustain a gain of five for longer pulses (of lengths of $\approx$1000s). In order for ITER to be a success, several challenging control engineering problems must be addressed.

Among these challenges is to precisely regulate the plasma density and temperature, or burn condition. Due to the nonlinear and coupled dynamics of the system, modulation of the burn condition (either during ramp-up/shut-down or in response to changing power demands) without a well designed control scheme could result in undesirable transient performance. Feedback control will also be necessary for responding to unexpected changes in plasma confinement, impurity content, or other parameters, which could significantly alter the burn condition during operation. Furthermore, although stable operating points exist for most confinement scalings, certain conditions can lead to thermal instabilities. Such instabilities can either lead to quenching or a thermal excursion in which the system moves to a higher temperature equilibrium

point. In any of these situations, disruptive plasma instabilities could be triggered, stopping operation and potentially causing damage to the confinement vessel.

In this work, the problem of burn condition control is addressed through the design of a nonlinear control law guaranteeing stability of desired equilibria. Multiple actuation methods, including auxiliary heating, isotopic fueling, and impurity injection, are used to ensure the burn condition is regulated even when actuators saturate. An adaptive control scheme is used to handle model uncertainty, and an online optimization scheme is proposed to ensure that the plasma is driven to an operating point that minimizes an arbitrary cost function. Due to the possible limited availability of diagnostic systems in ITER and future reactors, an output feedback control scheme is also proposed that combines the nonlinear controller with an observer that estimates the states of the burning plasma system based on available measurements. Finally, the control scheme is tested using the integrated modeling code METIS.

The control of spatial profiles of parameters, including current, density, and temperature, is also an important challenge in fusion research, due to their effect on MHD stability, non-inductive current drive, and fusion power. In this work, the problem of kinetic profile control in burning plasmas is addressed through a nonlinear boundary feedback control law designed using a technique called backstepping. A novel implementation of the backstepping technique is used that enables the use of both boundary and interior actuation. The backstepping technique is then applied to the problem of current profile control in both low-confinement and high-confinement mode discharges in the DIII-D tokamak based on a first-principles-driven model of the current profile evolution. Both designs are demonstrated in simulations and experimental tests.

Chapter 1

Introduction

1.1 Nuclear Fusion and the Tokamak

As the world's population increases and more countries become highly industrialized, the demand for energy rapidly rises. The increasing energy usage exacerbates the major drawbacks of burning fossil fuels, which accounts for most of the world's energy production. The burning of fossil fuels results in the generation of vast amounts of greenhouse gases, contributing to the problem of global warming, and creates additional pollutants with harmful effects on the environment. Furthermore, although the supply of fossil fuels is not likely to be totally depleted for a few hundred years, extraction is becoming more difficult and an energy shortfall is predicted to occur in the next few decades [1, 2]. While solar, wind, and hydroelectric power are attractive alternatives to fossil fuels, they lack the energy density needed to satisfy growing energy demands. Nuclear fission, the production of energy through splitting heavy atomic nuclei, has a much higher energy density, and is a mature technology that already accounts for a significant portion of the world's energy production. However, fission results in the production of long lasting and highly radioactive nuclear waste

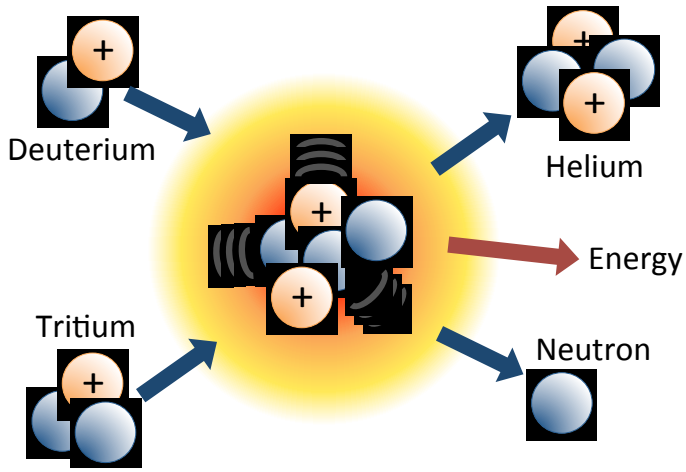

Figure 1.1: The D-T fusion reaction.

and can result in dangerous nuclear accidents. Nuclear fusion, on the other hand, generates only short term, low-level radioactive waste and poses no risk of nuclear meltdowns, while still possessing the desirable characteristics of high energy density, abundant fuel supply, and no air pollution production. For these reasons, nuclear fusion has been the focus of extensive research over the last several decades.

In nuclear fusion reactions, two light atomic nuclei combine to form a heavier nucleus and, in the process, a significant amount of energy is released. Most present day efforts consider the reaction depicted in Figure 1.1,

$$ {}_1^2D + {}_1^3T \rightarrow {}_2^4He + {}_0^1n + 17.6 \text{ MeV}, \tag{1.1} $$

in which deuterium (D) and tritium (T), two isotopes of hydrogen, fuse into a helium (He) nucleus, releasing an energetic neutron and 17.6 MeV of energy. The fuel is plentiful: deuterium can be obtained from seawater, and tritium can be bred from lithium (a metal found in large quantities in the Earth's crust) through bombardment

with a source of neutrons, i.e., through the reactions

$$^{7}_{3}Li +^{1}_{0} n \rightarrow^{4}_{2} He +^{3}_{1} T +^{1}_{0} n + 2.5 \text{ MeV} \tag{1.2}$$

$$^{6}_{3}Li +^{1}_{0} n \rightarrow^{4}_{2} He +^{3}_{1} T +^{1}_{0} n + 4.8 \text{ MeV}. \tag{1.3}$$

Indeed, tritium breeding could potentially be done within a fusion reactor by coating the walls with liquid lithium.

Due to the strong Coulombic repulsion force experienced by the positively charged D and T nuclei, the fuel must be heated to extremely high temperatures, on the order of 100 million degrees, in order for a significant number of fusion events to occur within a reactor. The major challenge to fusion energy has been to create a device capable of achieving these high temperatures and subsequently confining the fuel long enough for more energy to be released than is required by the heating process. Three approaches to this are known: gravitational confinement - the method used by stars, inertial confinement - the process of using inertia to implode the hydrogen gases long enough for fusion reactions to occur, and magnetic confinement - the use of magnetic fields to confine ionized fuel atoms. Currently, magnetic confinement is the most promising approach, and magnetic confinement devices are the likely technology for future fusion power plants.

At the temperatures required for fusion, the fuel becomes an ionized gas, called a plasma. In an applied magnetic field, the individual charged particles of the plasma travel along magnetic field lines in a helical path due to the Lorentz force. This effect, illustrated in Figure 1.2 , restricts particle motion perpendicular to the applied field, but does not confine particles in the parallel direction. Building on this concept, the tokamak [3], one of the most promising magnetic confinement devices, uses a system of magnetic coils and currents to close and twist the applied magnetic field lines into

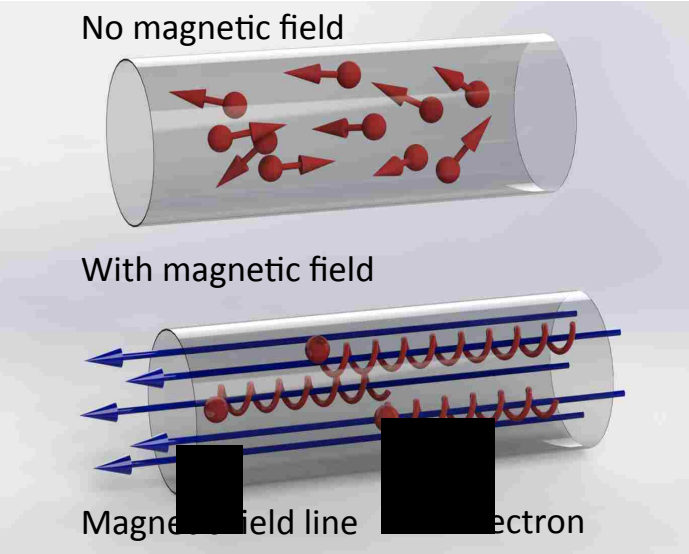

Figure 1.2: Magnetic confinement of charged particles.

a helical structure to trap the plasma inside a toroidal vessel and create a magnetic equilibrium.

A schematic of the coils and magnetic fields in a tokamak is shown in Figure 1.3. The D-shaped toroidal field (TF) coils are in blue, while the poloidal field (PF) coils are shown in gray. The current flowing in these coils as well as the plasma itself produces the helical magnetic field needed to confine the fusion plasma. The plasma current, which contributes to heating the plasma and generates the poloidal magnetic field needed for confinement, is primarily sustained inductively by the ohmic heating coil. Additional non-inductive current and plasma heating are obtained through the injection of high energy neutral particles (uncharged fuel atoms) and electromagnetic waves. Because present day tokamaks rely heavily on transformer action to generate the critical plasma current, they cannot be operated in steady state. They are instead operated in short pulses, usually referred to as discharges or shots. In present day tokamaks, typical discharge lengths are on the order of seconds or minutes. During discharges, the plasma is refueled through gas puffing valves at the plasma boundary,

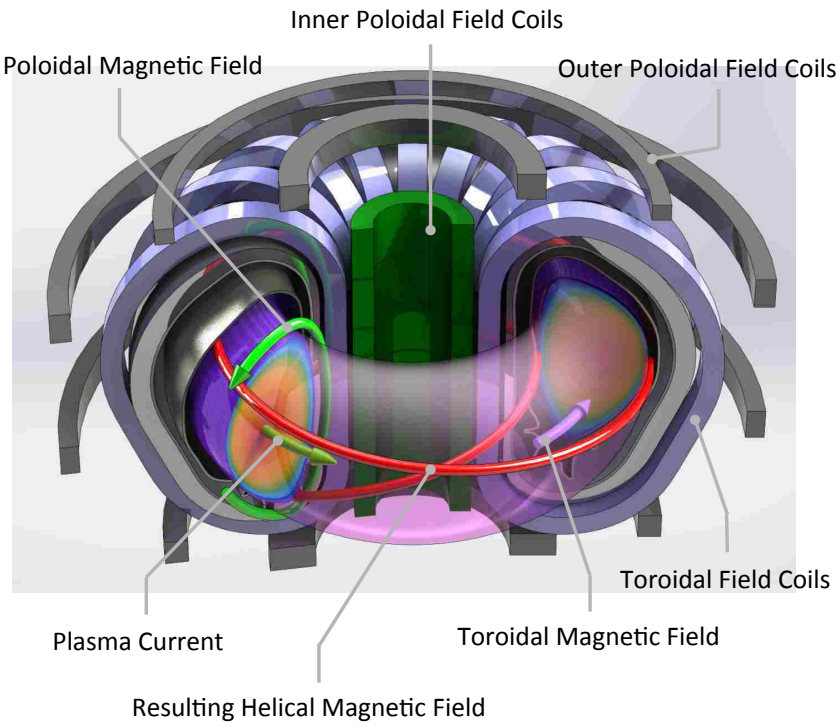

Figure 1.3: Cutaway view of a tokamak.

as well as frozen pellets of deuterium and tritium that can penetrate deep into the plasma core before ablating. Operation of a successful tokamak machine requires careful control over the fueling and heating, as well as the magnetic fields used for confinement. A schematic of the heating and fueling actuators is given in Figure 1.4.

The 17.6 MeV of energy released by the D-T fusion reaction is distributed to both products of the reaction. The neutron, which is not charged and therefore not confined within the magnetic field of the tokamak, carries 80% (14.1 MeV) of the fusion energy to the vessel wall. In an operational reactor, the wall would capture the neutrons and convert their kinetic energy into the heat needed to drive electrical generators. The other 20% (3.5 MeV) of the fusion energy is associated with the other product of the reaction, a helium ion or alpha particle. These particles are charged and are confined by the magnetic field. Through collisions with other particles, the

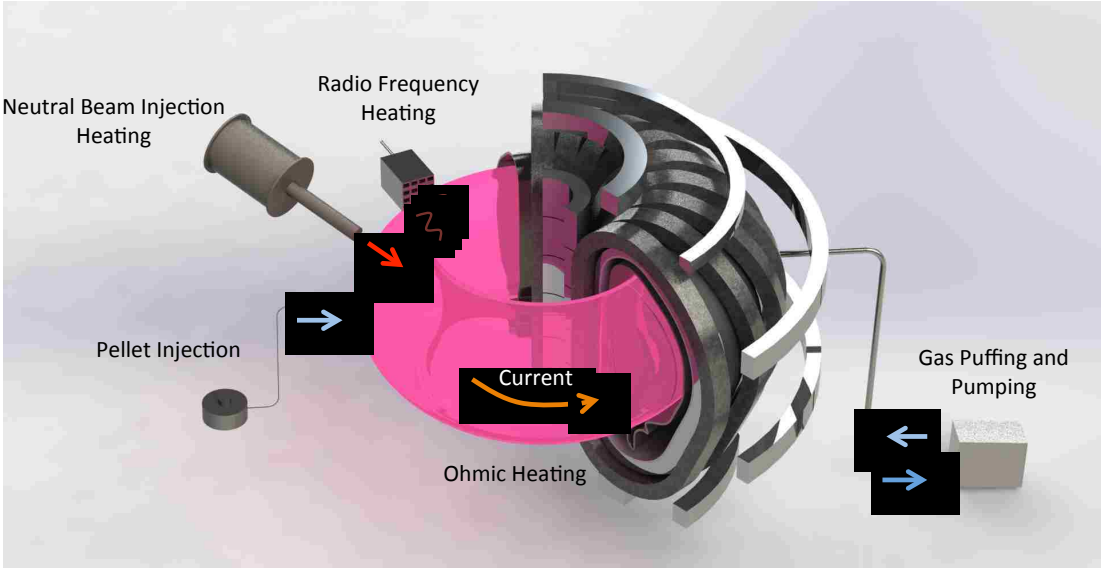

Figure 1.4: Actuators used to control kinetic variables in tokamaks.

energy of the alpha particles self-heats the plasma. Given the right conditions, the plasma can produce enough fusion power to completely heat itself. This situation, in which no external energy is required, is termed an ignited plasma. While this would be the ultimate goal of fusion research, a more modest goal is to create a plasma in which a majority of the plasma heating comes from the alpha particle heating. This is termed a burning plasma.

There are many experimental tokamaks around the world, each exploring different facets of plasma physics and fusion technology. Devices like JET in the UK, Tore-Supra in France, and DIII-D in the United States, have made significant progress towards realizing the goal of fusion energy. Experiments have reached the point where the power released from fusion is nearly equal to the power input needed to heat the plasma (the so-called break-even condition). The next experimental step is ITER, an international collaboration that is designed specifically to reach the burning plasma state. A cut-away view of the ITER tokamak is shown in Figure 1.5. The fusion gain, defined as the ratio of fusion power to heating power and denoted as Q,

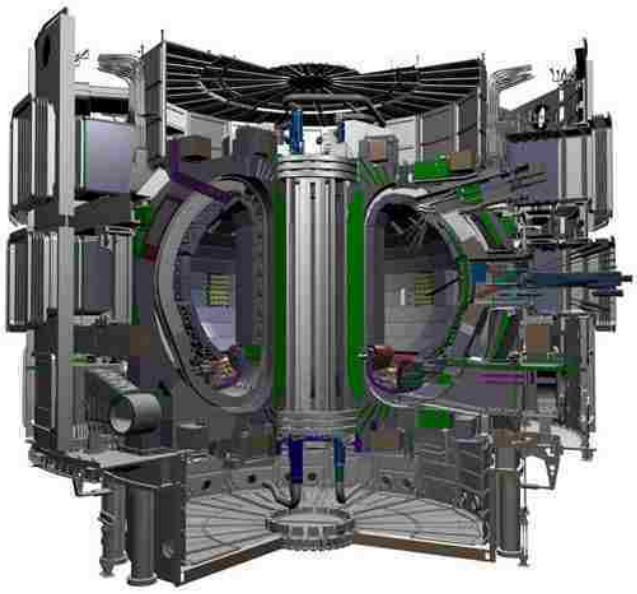

Figure 1.5: Cut-away of the ITER tokamak (source: ITER.org).

is expected to exceed ten in certain ITER operating scenarios, and to be sustained at $Q = 5$ for ≈1000s. The ITER tokamak will be used to explore so-called advanced tokamak (AT) scenarios. These operating modes are characterized by high plasma confinement and pressure as well as largely non-inductively driven plasma current. These characteristics are necessary for achieving steady-state operation.

1.2 Control Engineering Challenges for ITER

Advanced tokamak modes rely heavily on active control to reach high levels of performance and to regulate the plasma density, temperature, and confinement in order to maintain the fusion reaction. Mathematical modeling and control of tokamak plasmas is extremely challenging because tokamak plasmas are high order, highly coupled, distributed parameter, nonlinear systems. Tokamak plasmas also have many instabilities and a limited number of actuators and sensors. The control challenges are generally separated into two groups: electromagnetic control and kinetic control. Electromag-

netic control refers to controlling the magnetic and electric fields to regulate the position and shape of the plasma, as well as the total plasma current. Kinetic control refers to controlling fueling rates and auxiliary heating to modify the plasma density, temperature, and pressure. The density and temperature are critical reactor parameters, as they influence fusion power, heat loads to plasma facing components, and plasma stability. Furthermore, since the tokamak plasma is a spatially distributed system, it is important to not only control the volume averaged values of these physical quantities, but also their spatial profiles. Energy confinement, plasma stability, and the fraction of non-inductive plasma current, can all be improved through control of pressure and current profiles. This dissertation focuses on developing and studying strategies for addressing the important problems of burn condition control, kinetic profile control in burning plasmas, and current profile control.

1.3 Burn Condition Control

For nuclear fusion to become an economical alternative energy source, tokamak reactors must be capable of operating for extended periods of time in a burning plasma mode characterized by a large value of Q, the ratio of fusion power to auxiliary power. Achieving and maintaining such conditions will require precise control over the plasma density and temperature. Due to the nonlinear and coupled dynamics of the system, modulation of the burn condition (either during ramp-up/shut-down or in response to changing power demands) without a well designed control scheme could result in undesirable transient performance. Feedback control will also be necessary for responding to unexpected changes in plasma confinement, impurity content, or other parameters, which could significantly alter the burn condition during operation. Furthermore, although stable operating points exist for most confinement scalings,

certain conditions can lead to thermal instabilities. Such instabilities can either lead to quenching or a thermal excursion in which the system moves to a higher temperature equilibrium point. In any of these situations, disruptive plasma instabilities could be triggered, stopping operation and potentially causing damage to the confinement vessel. Thus, it will be important to implement an active feedback control system that can ensure good transient performance as well as stability of the desired operating points.

1.3.1 Prior Work

In past work on the problem of burn condition control, the physical and technological feasibility of various potential actuators has been studied. Prior work, including [4, 5, 6], considered modulation of the auxiliary power, modulation of the fueling rate, and controlled injection of impurities as possible actuators. While these methods can be effective approaches for burn control, each have unique drawbacks that must be considered when developing a comprehensive burn control strategy.

Controllers based solely on auxiliary power modulation [7, 8, 9] are best suited for sub-ignition operating points where the auxiliary power is nonzero. The ability of these schemes to reject thermal excursions is restricted since the maximum heating reduction is a complete shutoff of the auxiliary power and the ability to reject negative perturbations is limited by the maximum installed auxiliary heating power. For devices operating with very high fusion gain Q, the amount of auxiliary heating will be quite small compared to the total plasma heating, such that modulation of auxiliary power may have a limited effect on the plasma temperature. In hybrid and steady-state scenarios, the control authority may be further restricted by the need to use some auxiliary power sources to drive plasma current. This essentially forces the burn control system to respect a nonzero minimum auxiliary heating power constraint.

Operating points characterized by an auxiliary heating power requirement very close to the minimum required for current drive will be difficult to stabilize and control with auxiliary power modulation alone. Similarly, auxiliary power modulation alone will not be appropriate for future devices exploring ignited operation.

Controller designs based on the modulation of the deuterium-tritium fueling rate, including [10, 11, 12, 13, 14], can enable ignited operation (or operation near the minimum auxiliary power required for current drive) by increasing or decreasing the fusion power through changing the plasma density. Due to disruptive density limits, the plasma density cannot be increased arbitrarily high. The approach is also limited by the decay rate of the density, which can be quite slow when particle recycling rates are high. Additionally, the plasma density is nonlinearly coupled to many plasma parameters, such that changes in plasma density could lead to undesirable changes in the reactor operating scenario. The nonlinear coupling is important to consider in control design since, for certain conditions, increasing density results in a net increase in heating while for others, heating is decreased. For example, in [15], where a PID (proportional-integral-derivative) control law was used to regulate fusion power using the deuterium-tritium fueling rate, the sign of the controller gains had to be flipped when switching between thermally stable points and thermally unstable ones.

Controlled impurity injection can be used to cool the plasma and prevent thermal excursions. Injecting impurities increases radiative power losses and contaminates the plasma, decreasing fusion heating. Both effects lead to a reduction of the net plasma heating, causing a reduction in temperature. For large perturbations in initial temperature, this method can require large amounts of impurities to be injected. After the excursion, additional heating power, with a consequent reduction in the fusion gain Q, is needed to compensate the excess radiation losses until the impurities are completely removed from the reactor.

Most existing burn control efforts make use of only one of the available actuators (single-input control) and study the range of perturbations that can be rejected by the actuator. Prior work combining actuation concepts include [16, 17, 18, 19, 15, 20] for zero-dimensional (volume-averaged) models. Studies of kinetic control and thermal stability for 1-D (radial profile) models can be found in [21, 22, 23]. In [24], a diagonal multi-input, multi-output linear control scheme for burning plasma kinetics was developed by observing actuator influences during numerical simulations of plasma physics codes. The approximation of the nonlinear burning plasma model by a linearized one for controller design is a common denominator in previous model-based controller designs. The model is linearized, a controller is synthesized using linear techniques, and the resulting design is tested on the original nonlinear model. When tested in nonlinear simulations, these controllers succeed in stabilizing the system against a limited set of perturbations and disturbances.

In [25], a zero-dimensional nonlinear model involving approximate conservation equations for the energy and particles densities was used to synthesize a nonlinear feedback controller for burn conditions stabilization. The controller makes use of all of the previously considered actuators simultaneously, using auxiliary power modulation to prevent quenching, impurity injection to increase radiation losses and stop thermal excursions, and fueling modulation to regulate the density to the target value associated with the chosen operating point. The use of nonlinear control techniques removes the limits imposed by linearization in other works and the resulting controller can accommodate very large perturbations. The controller works for suppressing both thermal excursions and quenches, can operate at sub-ignition and ignition points (or points near the minimum power required for current drive), and can drive the system from one point to another during operation. Only those works that use non-model based control techniques, like neural networks [26, 27], have also

followed these guidelines. A zero-dimensional (volume-averaged) simulation study was performed to show the capabilities of the model-based controller and compare it with previous linear controllers.

Despite the advantages of the nonlinear controller designed in [25], a few drawbacks remain. The control scheme relies on the use of impurity injection to reject increases in temperature. This type of actuation could lead to undesirable accumulation of impurity ions within the plasma core, which could reduce the efficiency of the reactor long after the thermal excursion is rejected. Ideally, the injection of impurities would be used only when the other available methods fail to prevent a thermal excursion. Also, the model used for design and simulation assumed an optimal 50:50 mix of deuterium and tritium within the plasma at all times and did not consider the effects of particle recycling. Because experiments indicate that deuterium and tritium may have different transport properties [28], fueling efficiencies, and deposition profiles, and because the isotopic mix in the core effects the amount of fusion heating, the deuterium and tritium systems should be modeled and actuated separately. Additionally, since particle recycling will effect the response of the plasma density and isotopic mix to the available actuators, recycling effects should be included in the model used for design and simulation in some way.

1.3.2 Isotopic Fuel Tailoring

The isotopic fuel mix is a critical reactor parameter as it has a major influence on the fusion power produced. The α-particle heating power, P_α, from a burning DT plasma is given as

$$P_\alpha = Q_\alpha \gamma (1-\gamma) n_{DT}^2 \langle \sigma \nu \rangle, \tag{1.4}$$

where Q_α is the energy of the α-particles produced by the reaction (3.52 MeV),

$$n_{DT} = n_D + n_T, \tag{1.5}$$

is the deuterium-tritium density, $\langle \sigma\nu \rangle$ is the reactivity, and

$$\gamma = n_T / n_{DT}, \tag{1.6}$$

is the tritium ratio, a measure of the isotopic mix. We note that for a constant density and temperature, the fusion heating depends quadratically on the tritium ratio, with the maximum fusion power at $\gamma = 0.5$. Even with 50:50 DT injection, the possible differences in deuterium and tritium transport or fueling deposition and efficiency may lead to non-optimal fuel mix in the core, which would reduce reactor efficiency. Additionally, depending on the operating scenario, it may be desirable or even necessary to operate at a lower tritium fraction or modulate the tritium fraction during operation.

To control the tritium ratio it is possible to use a method of fueling referred to as isotopic tailoring, in which the relative mix of deuterium and tritium injected by the fueling system is modulated in real-time [29]. While it is not possible to adjust the tritium ratio within pellets on a fast enough time scale for control, the pellet injection system for ITER will include two separate injectors - one with pellets made of primarily deuterium and the other with pellets made primarily of tritium. A gas injection system will be used to supply deuterium at the edge of the plasma. Together, these systems will allow for fuel mix modulation. Diagnostics for measuring the tritium ratio in both the edge and core plasma should be available and adequate for the purposes of real-time control [30, 31, 32]. Therefore, feedback control of the tritium ratio in ITER plasmas through isotopic fuel tailoring should be feasible.

1.3.3 Results of This Work

In this work, a zero-dimensional (volume averaged) model of the evolution of the burn condition in a tokamak plasma is presented and used to design a nonlinear burn control strategy that uses all of the available actuators simultaneously to stabilize desired equilibria. The model includes a simplified model of particle recycling (refueling of the plasma from the walls of the machine), which is used to study the potential use of isotopic fueling as a means to reduce fusion heating during thermal excursions for a range of model parameters. Impurity injection is considered as a back-up means of rejecting excursions. The ability of the combined control scheme to move the system between operating points, even when one or more actuators are saturated, is demonstrated in both zero- and one-dimensional simulations. An adaptive control scheme is then added to handle model uncertainty, and an online optimization scheme is proposed to ensure that the plasma is driven to an operating point that minimizes a given cost function. Due to the possible limited availability of diagnostic systems in ITER and future reactors, an output feedback control scheme is also proposed that combines the nonlinear controller with an observer that estimates the states of the burning plasma system based on available measurements. Finally, the control scheme is tested using the integrated modeling code called METIS.

1.4 Kinetic Profile Control

Most approaches to the control of kinetic variables in tokamaks begin by considering 0-D (zero-dimensional) models of transport within the fusion plasma in which the governing equations of the system are averaged over the volume of the plasma. This allows the problem to be approached with lumped-parameter control design techniques. However, these 0-D control efforts do not take into account the 1-D (one-

dimensional) effect of modulating the bulk heating, fueling, and impurity injection on the shape of the spatial profiles. In a reactor, the heating, fueling, and impurity injection rates are indeed distributed throughout the plasma and can be used to affect the shape of the kinetic variable profiles. The shape of the temperature and density profiles not only directly affect the burn condition and particle/energy transport, but also play a significant role in determining the evolution of the current profile through the temperature dependent resistivity and pressure gradient dependent bootstrap current. It has been demonstrated that setting up a suitable spatial distribution of the toroidal plasma current can, in turn, enable certain advanced operating scenarios characterized by high fusion gain and non-inductive sustainment of plasma current that could lead to steady-state operation (see [33]).

The importance of controlling the spatial profiles of density and temperature in burning plasmas has been recognized in previous work, including [21], [22], [23], [34], and [35]. In these pieces of work, a 1-D plasma model is represented by a set of partial differential equations (PDEs) and various methods are utilized to reduce the distributed parameter model to a lumped-parameter one. The resulting set of ODEs are then linearized and conventional linear control techniques are used for controller design. In contrast, the control methods presented in [36, 37] for non-burning plasmas avoided linearization through the use of a backstepping boundary feedback technique to stabilize and regulate density and temperature profiles.

1.4.1 Results of This Work

In this work, the backstepping boundary control technique is extended to enable combined boundary+interior feedback control and the combined approach is used to develop a nonlinear control strategy for density and temperature profiles in a burning plasma. With the addition of adaptive disturbance estimation, asymptotic tracking of

an unstable set of equilibrium profiles is demonstrated in a simulation study, despite the presence of input disturbances. Because burning plasma experiments are still several years away, it is not currently possible to experimentally test the burn condition control or burning plasma kinetic profile control approaches proposed in this work. However, the backstepping boundary control technique can also be applied to the important problem of current profile control, which is an active area of research in present-day tokamaks. In this work, a backstepping current profile control algorithm is designed based on first-principles-driven models of the current profile evolution in the DIII-D tokamak for both L-mode (low confinement) and H-mode (high confinement) discharges. The effectiveness of these approaches is demonstrated in both simulations and experimental testing on DIII-D.

1.5 Dissertation Outline

This dissertation is organized as follows.

Chapter 2

In this chapter, the use of nonlinear, multi-input-multi-output control design techniques for stabilization of the burn condition of tokamak fusion reactors is studied. A simplified burning plasma model is presented, and a control scheme is designed that can overcome limitations due to actuator saturation by incorporating several available actuation techniques (auxiliary heating, isotopic fueling, and impurity injection).

Chapter 3

The model-based control scheme designed in Chapter 2 relies on knowledge of several model parameters that are, in practice, uncertain. This uncertainty could lead to

poor controller performance if unaccounted for. In this chapter, a nonlinear adaptive control strategy is used to couple the multi-input-multi-output control design with a set of parameter update laws. The design ensures asymptotic tracking of desired references. An online optimization scheme is also proposed to update the controller references in real-time to minimize a given cost function.

Chapter 4

The nonlinear adaptive control scheme proposed in Chapter 3 relies on knowledge of the states of the burning plasma system. However, in practice, only a limited number of output measurements may be available. In this chapter, the nonlinear control scheme is augmented with an observer that reconstructs the states of the system based on the available real-time measurements.

Chapter 5

In this chapter, the nonlinear burn control schemes presented in the previous chapters are tested more rigorously through closed loop simulations using METIS, an integrated tokamak modeling code.

Chapter 6

In this chapter, a backstepping boundary control technique that includes interior control and online disturbance estimation is developed and the approach is used to design a nonlinear control law for the density (deuterium, tritium, and alpha-particles) and energy profiles in burning tokamak plasmas. The ability of the controller to stabilize an unstable equilibrium is demonstrated in a simulation study.

Chapter 7

In this chapter, the problem of current profile control in L-mode discharges in DIII-D is addressed through the design of a nonlinear backstepping boundary feedback control law based on a first-principles-driven model of the current profile evolution. The controller, designed using the backstepping technique, is demonstrated in both simulations and experimental tests on DIII-D.

Chapter 8

In this chapter, the backstepping boundary+interior feedback technique is used to design a nonlinear controller for H-mode discharges in DIII-D. The performance of the design is demonstrated in both simulations and experiments.

Chapter 9

In this final chapter, the contributions of this dissertation are summarized and potential future research work is discussed.

Chapter 2

Zero-dimensional Nonlinear Burn Condition Control

2.1 Introduction

In this chapter, we consider the simultaneous use of auxiliary power, fueling modulation, isotopic fuel tailoring, and impurity injection for stabilizing and controlling a burning plasma. The isotopic fueling technique planned for ITER is used to control the tritium ratio within the plasma. In addition, we exploit the effect of the tritium ratio on the fusion heating power to modulate plasma heating and control the temperature. Doing so allows the proposed scheme to, under certain conditions, maintain control of the plasma temperature when the auxiliary power is saturated without resorting to impurity injection. We note that a non-model based PID (proportional-integral-derivative) algorithm for controlling the isotopic mix was presented in [19], however, the modulation of the isotopic mix as a means of controlling the plasma heating was not considered. For scenarios in which the modulation of auxiliary power and isotopic mix cannot achieve stability and performance requirements, we propose

the use of impurity injection as a back-up actuator to augment the isotopic mix based control. The combined control scheme simultaneously regulates the energy, density, and tritium fraction (and consequently the fusion power), and can, through the use of all of the available actuators, maintain stable control of the system despite saturation of even several of the actuators. The controller synthesis is based on the full nonlinear model, allowing the controller to deal with a larger set of perturbations in initial conditions than linear model based controllers. The controller handles both thermal excursions and quenches and depends parametrically on the equilibrium point, allowing it to be used to drive the system from one equilibrium point to another. A zero-dimensional simulation study compares the performance of the actively controlled system to the open loop system when switching between operating points, showing a significant improvement in performance. A series of simulations is performed to study the effect of different particle recycling model parameters on the performance of the controller. A one-dimensional simulation study is also done which shows that the control design based on a zero-dimensional model is potentially robust to spatially varying parameters.

This chapter is organized as follows. The burning plasma model is given in Section 2.2. The control objective is described in Section 2.3. In Section 2.4, the controller algorithm is presented. Sections 2.5 and 2.6 contain the results of zero-dimensional and one-dimensional simulation studies, respectively. Finally, the conclusions are discussed in Section 2.7.

2.2 Burning Plasma Model

In this work, we use a zero-dimensional model for a burning plasma that employs approximate energy and particle balance equations. The model considers the deuterium

and tritium ion densities separately, allowing for the possibility of different confinement characteristics and fueling rates for the individual species. It also includes an approximate global model of particle recycling for the purposes of studying the effect of recycling parameters on controller performance.

2.2.1 Particle Recycling

The particle balance describing the dynamics of the plasma density and isotopic mix is affected (and under certain conditions dominated) by the recycling of particles from plasma facing components of the confinement vessel walls. An important effect of particle recycling is an increase in the effective confinement time of particles. While a controller can quickly increase the density through increased fueling, the density can be decreased no faster than the effective decay rate, which can be dominated by the recycling effect. Recycling not only poses a problem for actively reducing the total plasma density but may also lead to accumulation of helium ash in the core, which could dilute the fusion fuel. In addition, since the recycled fuel will have a particular isotopic mix, recycling reduces the dependence of the core isotopic mix on the controlled pellet and gas injection fueling composition, an effect that was observed in [38]. This could limit the effectiveness of isotopic ratio control schemes.

As one of the goals of this work is to study the feasibility of using modulation of the isotopic mix and plasma density to control fusion heating in a burning plasma, it is important to include the effects of recycling in the model used for design and simulation. Global models of recycling, like those presented in [39, 40, 41], reduce the detailed physical description of the processes involved to a small number of physically motivated parameters, and can be used to gain a qualitative understanding of the effects of recycling on the system. In this work, we incorporate a parameterized model of coupled deuterium-tritium recycling processes that allows us to study the

performance of the proposed controller for a range of different recycling conditions. This model captures the dominant effects of recycling on the proposed isotopic fueling based control approach, that is, it captures the slowed response time of the deuterium and tritium densities to decreases in fueling and also reflects the fact that the isotopic mix of recycled material may differ from that of the exiting particle flux. Because α particle and impurity ion fluxes are much smaller than the DT flux, recycling of these species is likely to be only weakly coupled to DT recycling and have little effect on the performance of the proposed control approach. We therefore account for α-particle and impurity recycling separately through use of effective confinement times $\tau_\alpha^* > \tau_\alpha$ and $\tau_I^* > \tau_I$. This simplification makes it possible to compare the controller performance for a particular operating point using different DT recycling parameters, without having to simultaneously change the α-particle and impurity recycling conditions, which would alter the fusion power, radiative losses, etc., and significantly change the characteristics of the operating point being studied. Note that the control design approach is not dependent on this modeling choice.

The model of deuterium and tritium recycling used here is based on the following description. Upon leaving the plasma and reaching the vessel walls, a fraction f_{ref} of the exiting particles may be reflected back towards the plasma, while the remainder are either absorbed by the wall material (an effect called wall pumping), or removed from the vessel by the active pumping system. The wall pumping effect causes the development of a inventory of particles in the wall, which is, over time, re-emitted back to the confinement vessel (a small percentage of particles may be trapped more permanently through processes like codeposition [42]). To avoid the need for a complex model of wall conditions and active pumping efficiency, the amount of recycling from the plasma facing surfaces can be characterized by a global recycling coefficient $R^{eff} = S^R/S^S$, where S^R is the recycled particle flux and S^S is the particle flux

to the plasma facing surfaces. The wall inventory, and consequently the re-emitted particles, will have some isotopic mix, which we denote γ^{PFC}. The recycled (reflected or re-emitted) particles go on to fuel the plasma core with some efficiency, f_{eff}, depending on their energy and interaction with the plasma scrape-off-layer (SOL). The fraction of particles that is 'screened' by the SOL returns to the surface again to be either reflected, absorbed, or pumped out [41]. Based on this description, we can derive (see Appendix A) the following expressions for the recycled flux of deuterium and tritium:

$$\begin{aligned} S_D^R &= \frac{1}{1-f_{ref}\left(1-f_{eff}\right)}\left\{f_{ref}\frac{n_D}{\tau_D}\right. \\ &\left. +\left(1-\gamma^{PFC}\right)\left[\frac{\left(1-f_{ref}\left(1-f_{eff}\right)\right)R^{eff}}{1-R^{eff}\left(1-f_{eff}\right)}-f_{ref}\right]\left(\frac{n_D}{\tau_D}+\frac{n_T}{\tau_T}\right)\right\}, \quad (2.1) \\ S_T^R &= \frac{1}{1-f_{ref}\left(1-f_{eff}\right)}\left\{f_{ref}\frac{n_T}{\tau_T}\right. \\ &\left. +\gamma^{PFC}\left[\frac{\left(1-f_{ref}\left(1-f_{eff}\right)\right)R^{eff}}{1-R^{eff}\left(1-f_{eff}\right)}-f_{ref}\right]\left(\frac{n_D}{\tau_D}+\frac{n_T}{\tau_T}\right)\right\}, \quad (2.2) \end{aligned}$$

where τ_D and τ_T are the respective confinement times for the two species.

2.2.2 Particle and Energy Balance

The α-particle balance is given by

$$\dot{n}_\alpha = -\frac{n_\alpha}{\tau_\alpha^*} + S_\alpha, \quad (2.3)$$

where n_α is the α-particle density, τ_α^* is the effective confinement time for the α-particles, and

$$S_\alpha = \gamma\left(1-\gamma\right)n_{DT}^2\langle\sigma v\rangle, \quad (2.4)$$

is the source of α-particles from fusion. The deuterium and tritium ion densities are governed by

$$\dot{n}_D = -\frac{n_D}{\tau_D} + f_{eff} S_D^R - S_\alpha + S_D^{inj}, \tag{2.5}$$

$$\dot{n}_T = -\frac{n_T}{\tau_T} + f_{eff} S_T^R - S_\alpha + S_T^{inj}, \tag{2.6}$$

where S_D^{inj} and S_T^{inj} (controller inputs) are the deuterium and tritium injection rates, respectively.

We consider two impurity populations: $n_{I,s}$ representing impurities arising from plasma surface interaction and $n_{I,c}$ representing impurities injected for the purposes of burn control. The particle balances are given by

$$\dot{n}_{I,s} = -\frac{n_{I,s}}{\tau_{I,s}^*} + S_I^{sp}, \tag{2.7}$$

$$\dot{n}_{I,c} = -\frac{n_{I,c}}{\tau_{I,c}^*} + S_I^{inj}, \tag{2.8}$$

where $\tau_{I,s}^*$ and $\tau_{I,c}^*$ are the effective impurity confinement times, S_I^{sp} is the uncontrolled source of impurities due to sputtering, and S_I^{inj} is the controlled injection of impurities. For the purposes of this work, we model the sputtering source as

$$S_I^{sp} = \frac{f_I^{sp} n}{\tau_I^*} + f_I^{sp} \dot{n},$$

where $0 \leq f_I^{sp} \ll 1$ in order to maintain $n_{I,s} = f_I^{sp} n$ where n is the total plasma density. This simple model reflects the fact that there is typically a small uncontrolled impurity content in the plasma. To simplify presentation, we consider both impurity populations to have the same effective confinement time τ_I^*, and atomic number Z_I.

The total impurity content $n_I = n_{I,s} + n_{I,c}$ is then governed by

$$\dot{n}_I = -\frac{n_I}{\tau_I^*} + S_I^{inj} + S_I^{sp}. \tag{2.9}$$

The energy balance is given by

$$\dot{E} = -\frac{E}{\tau_E} + P_\alpha - P_{rad} + P_{aux} + P_{Ohm}, \tag{2.10}$$

where E is the plasma energy, τ_E is the energy confinement time, $P_\alpha = Q_\alpha S_\alpha$ is the alpha-heating ($Q_\alpha = 3.52$ MeV is the energy of α-particles), P_{rad} represents the radiation losses, and P_{Ohm} is the ohmic heating power. This model uses the approximation that the 3.52 MeV α-particles slow down instantaneously.

The DT reactivity $\langle\sigma\nu\rangle$ is a highly nonlinear, positive and bounded function of the plasma temperature, T, and is calculated by

$$\langle\sigma\nu\rangle = exp\left(\frac{a}{T^r} + a_2 + a_3 T + a_4 T^2 + a_5 T^3 + a_6 T^4\right), \tag{2.11}$$

where the parameters a_i and r are taken from [43]. In this work, the radiation loss P_{rad} is taken as the combination of bremsstrahlung, line, and recombination as approximated by [44]

$$P_{brem} = 4.8 \times 10^{-37} \left(n_D + n_T + 4n_\alpha + Z_I^2 n_I\right) n_e \sqrt{T(keV)}, \tag{2.12}$$

$$P_{line} = 1.8 \times 10^{-38} \left(n_D + n_T + 16n_\alpha + Z_I^4 n_I\right) n_e \left(T(keV)\right)^{-1/2}, \tag{2.13}$$

$$P_{rec} = 4.1 \times 10^{-40} \left(n_D + n_T + 64n_\alpha + Z_I^6 n_I\right) n_e \left(T(keV)\right)^{-3/2}, \tag{2.14}$$

where n_e is the electron density. The electron density is obtained from the neutrality condition $n_e = n_D + n_T + 2n_\alpha + Z_I n_I$. The effective atomic number, plasma density,

Table 2.1: ITER machine parameters [45].

Symbol	Description	Value
I	Plasma current	15.0 MA
R	Major radius	6.2 m
a	Minor radius	2.0 m
B	Magnetic field	5.3 T
κ_{95}	Elongation at 95% flux surface/separatrix	1.7
δ_{95}	Triangularity at 95% flux surface/separatrix	0.33
V	Plasma volume	837 m^3

and temperature are given by

$$\begin{aligned} Z_{eff} &= \sum_i \frac{n_i Z_i^2}{n_e} = \frac{n_D + n_T + 4n_\alpha + n_I Z_I^2}{n_e}, && (2.15) \\ n &= n_\alpha + n_D + n_T + n_I + n_e \\ &= 2n_D + 2n_T + 3n_\alpha + (Z_I + 1)\, n_I, && (2.16) \\ T &= \frac{2}{3}\frac{E}{n}, && (2.17) \end{aligned}$$

where Z_i is the atomic number of the different ion species. Note that we take $T_e = T_i = T$ as a simplification. We approximate the Ohmic heating as

$$P_{Ohm} = 2.8 \times 10^{-9} \frac{Z_{eff} I^2}{a^4 T^{3/2}}, \quad (2.18)$$

where I is in Amps and T is in keV.

The state-dependent energy confinement time is given by

$$\tau_E = 0.0562 H_H I_p^{0.93} B_T^{0.15} P^{-0.69} n_{e19}^{0.41} M^{0.19} R^{1.97} \epsilon^{0.58} \kappa_{95}^{0.78}, \quad (2.19)$$

where H_H is a scalar representing uncertainty in the scaling, I_p is the plasma current (MA), B_T is the toroidal magnetic field (T), $P = P_{aux} + P_{Ohm} + P_\alpha - P_{rad}$ is the

total power (MW), n_{e19} is the electron density ($10^{19}\mathrm{m}^{-3}$), M is the effective mass of the plasma (amu), R is the major radius (m), $\epsilon = a/R$ with a the minor radius (m), and κ_{95} is the elongation at the 95% flux surface/separatrix [45]. We utilize the main plasma parameters and dimensions given in [45] and shown in Table 2.1.

Expression (2.19) represents the H-mode confinement time and is valid when the power transported across the separatrix is greater than P_{LH} where

$$P_{LH} = 2.84 M^{-1} B_T^{0.82} n_{e20}^{0.58} R^{1.00} a^{0.81}, \tag{2.20}$$

with the units MW, amu, T, $10^{20}\mathrm{m}^{-3}$, and m.

Particle confinement times are assumed to scale with the energy confinement time, i.e.,

$$\tau_\alpha^* = k_\alpha^* \tau_E, \tag{2.21}$$

$$\tau_D = k_D \tau_E, \tag{2.22}$$

$$\tau_T = k_T \tau_E, \tag{2.23}$$

$$\tau_I^* = k_I^* \tau_I. \tag{2.24}$$

We note again that the α-particle and impurity particles balances use effective confinement times chosen to account for recycling, while the confinement times for deuterium and tritium do not, as deuterium-tritium recycling is modeled separately.

For the purposes of control, we will consider the states of the burning plasma system to be n_α, n_I, E, γ, and n. The dynamic equations for the first three have already been given in (2.3), (2.9), and (2.10), while, by noting (1.5), (1.6), and (2.16),

the remaining two equations can be written as

$$\begin{aligned}
\dot{\gamma} &= -\frac{\gamma}{\tau_T} + \frac{\gamma\left(1-\gamma\right)}{\tau_D} + \frac{\gamma^2}{\tau_T} \\
&\quad + \frac{2}{n - 3n_\alpha - \left(Z_I+1\right)n_I}\left\{f_{eff}S_T^R - S_\alpha + S_T^{inj}\right. \\
&\quad \left. -\gamma\left[f_{eff}\left(S_D^R + S_T^R\right) - 2S_\alpha + S_D^{inj} + S_T^{inj}\right]\right\}, \qquad (2.25) \\
\dot{n} &= 2\left[-\frac{n - 3n_\alpha - \left(Z_I+1\right)n_I}{2}\left(\frac{1-\gamma}{\tau_D} + \frac{\gamma}{\tau_T}\right)\right. \\
&\quad \left. + f_{eff}\left(S_D^R + S_T^R\right) - 2S_\alpha + S_D^{inj} + S_T^{inj}\right] + 3\left[-\frac{n_\alpha}{\tau_\alpha^*} + S_\alpha\right] \\
&\quad + \left(Z_I+1\right)\left[-\frac{n_I}{\tau_I^*} + S_I^{inj} + S_I^{sp}\right]. \qquad (2.26)
\end{aligned}$$

2.3 Controller Objectives

The possible steady-state operating points of the system are given by the equilibria of the dynamic equations (2.3), (2.9), (2.10), (2.25), and (2.26). If we consider no controlled injection of impurities at steady-state, i.e. $\bar{S}_I^{inj} = 0$, the equilibrium values of the fueling source terms $\bar{S}_D$, $\bar{S}_T$, and the external power $\bar{P}_{aux}$, can be determined

by solving the nonlinear algebraic equations

$$
\begin{aligned}
0 &= -\frac{\bar{n}_\alpha}{\bar{\tau}^*_\alpha} + \bar{S}_\alpha, && (2.27)\\
0 &= -\frac{\bar{\gamma}}{\bar{\tau}_T} + \frac{\bar{\gamma}\left(1-\bar{\gamma}\right)}{\bar{\tau}_D} + \frac{\bar{\gamma}^2}{\bar{\tau}_T} \\
&\quad + \frac{2}{\bar{n} - 3\bar{n}_\alpha - \left(Z_I+1\right)\bar{n}_I} \left\{ f_{eff}\bar{S}^R_T - \bar{S}_\alpha + \bar{S}^{inj}_T \right. \\
&\quad \left. -\bar{\gamma}\left[f_{eff}\left(\bar{S}^R_D + \bar{S}^R_T\right) - 2\bar{S}_\alpha + \bar{S}^{inj}_D + \bar{S}^{inj}_T \right] \right\}, && (2.28)\\
0 &= 2\left[-\frac{\bar{n} - 3\bar{n}_\alpha - \left(Z_I+1\right)\bar{n}_I}{2}\left(\frac{1-\bar{\gamma}}{\bar{\tau}_D} + \frac{\bar{\gamma}}{\bar{\tau}_T}\right) \right. \\
&\quad \left. + f_{eff}\left(\bar{S}^R_D + \bar{S}^R_T\right) - 2\bar{S}_\alpha + \bar{S}^{inj}_D + \bar{S}^{inj}_T \right] + 3\left[-\frac{\bar{n}_\alpha}{\bar{\tau}^*_\alpha} + \bar{S}_\alpha \right] \\
&\quad + \left(Z_I+1\right)\left[-\frac{\bar{n}_I}{\bar{\tau}^*_I} + \bar{S}^{inj}_I + \bar{S}^{sp}_I \right], && (2.29)\\
0 &= -\frac{\bar{E}}{\bar{\tau}_E} + \bar{P}_\alpha - \bar{P}_{rad} + \bar{P}_{aux} + \bar{P}_{Ohm}, && (2.30)\\
0 &= -\frac{\bar{n}_I}{\bar{\tau}^*_I} + \bar{S}^{sp}_I. && (2.31)
\end{aligned}
$$

A unique solution to this system can be obtained by specifying $T = \bar{T}$, $\gamma = \bar{\gamma}$, $n_I = \bar{n}_I$, and $\beta = \frac{knT}{B^2/2\mu_0} = \bar{\beta}$ where B is the magnetic field strength, μ_0 is the permeability of free space, and k is the Boltzmann constant. We assume the magnetic field B is held constant, such that $\beta \propto nT \propto E$. The objective of a burn condition controller can then be stated as regulation of E, n, γ, n_α and n_I to the chosen set of equilibrium values. We note that, as a result of regulating these values to the chosen targets, the outputs of the system, including the fusion power, will also be regulated to the value associated with that particular operating point. In this chapter, the choice of the desired operating point is considered to be made offline prior to the discharge, however, in the following chapter, a real-time optimization algorithm will be used to determine the operating point that best achieves some predetermined goal, e.g., to maximize fusion gain.

We will use the notation $\tilde{x}(t) = x(t) - \bar{x}(t)$ to represent the difference between the actual and desired states of the system. We can write the dynamics of these errors as

$$\dot{\tilde{n}}_\alpha = -\frac{n_\alpha}{\tau_\alpha^*} + S_\alpha, \tag{2.32}$$

$$\dot{\tilde{n}}_I = -\frac{\tilde{n}_I}{\tau_I^*} - \frac{\bar{n}_I}{\tau_I^*} + S_I^{inj} + S_I^{sp}, \tag{2.33}$$

$$\dot{\tilde{E}} = -\frac{\tilde{E}}{\tau_E} - \frac{\bar{E}}{\tau_E} + P_\alpha - P_{rad} + P_{Ohm} + P_{aux}, \tag{2.34}$$

$$\dot{\tilde{\gamma}} = -\frac{\tilde{\gamma}}{\tau_T} + \frac{2\left[u + (1-\gamma)\, S_T^{inj} - \gamma S_D^{inj}\right]}{n - 3n_\alpha - (Z_I+1)\, n_I}, \tag{2.35}$$

$$\dot{\tilde{n}} = -\tilde{n}\left(\frac{1-\gamma}{\tau_D} + \frac{\gamma}{\tau_T}\right) + v + 2\left(S_T^{inj} + S_D^{inj}\right), \tag{2.36}$$

where

$$\begin{aligned} u(\bar{\gamma}) &= \frac{n - 3n_\alpha - (Z_I+1)\, n_I}{2}\left[-\frac{\bar{\gamma}}{\tau_T} + \frac{\gamma\,(1-\gamma)}{\tau_D} + \frac{\gamma^2}{\tau_T} - \dot{\bar{\gamma}}\right] \\ &+ f_{eff} S_T^R - S_\alpha - \gamma\left[f_{eff}\left(S_D^R + S_T^R\right) - 2S_\alpha\right], \end{aligned} \tag{2.37}$$

$$\begin{aligned} v &= \left(-\bar{n} + 3n_\alpha + (Z_I+1)\, n_I\right)\left(\frac{1-\gamma}{\tau_D} + \frac{\gamma}{\tau_T}\right) \\ &+ 2\left[f_{eff}\left(S_D^R + S_T^R\right) - 2S_\alpha\right] + 3\left[-\frac{n_\alpha}{\tau_\alpha^*} + S_\alpha\right] \\ &+ (Z_I+1)\left[-\frac{n_I}{\tau_I^*} + S_I^{inj} + S_I^{sp}\right]. \end{aligned} \tag{2.38}$$

As noted before, our model assumes that the source of impurities from plasma facing components, S_I^{sp}, maintains $n_{I,s} = f_I n$ at steady-state. Without controlled injection of impurities, i.e., $S_I^{inj} = 0$, the content of injected impurities, $n_{I,c}$, will decay to zero such that $n_I = n_{I,s} = f_I^{sp} n$. Therefore, if we regulate the total plasma density to $\bar{n}$, we can be sure that $\tilde{n}_I \to 0$. This implies that there exists a Lyapunov function $V_I(\tilde{n}_I)$ (see Appendix B for the basics of Lyapunov stability analysis) such

that

$$V_I\Big|_{\tilde{n}=0} < 0. \tag{2.39}$$

If we consider a Lyapunov function $V_\alpha = \frac{\tilde{n}_\alpha^2}{2}$, then

$$\dot{V}_\alpha = \tilde{n}_\alpha \left(-\frac{n_\alpha}{\tau_\alpha^*} + S_\alpha \right). \tag{2.40}$$

We note that, if n_I, n, γ, and E are driven to their equilibrium values, we can write

$$S_\alpha = \left[\frac{\bar{n} - 3n_\alpha - (Z_I + 1)\,\bar{n}_I}{2} \right]^2 \bar{\gamma}\,(1 - \bar{\gamma})\,\langle \bar{\sigma v} \rangle. \tag{2.41}$$

For physically meaningful values of n_α, S_α decreases with an increase in n_α and vice versa. Also, for the confinement scaling (2.19), the term n_α/τ_α^* increases with an increase in n_α and vice versa. This allows us to write $-\frac{n_\alpha}{\tau_\alpha^*} + S_\alpha = -\tilde{n}_\alpha \phi_\alpha$ where ϕ_α is a positive continuous function and

$$\dot{V}_\alpha\Big|_{\tilde{E},\tilde{n}_I,\tilde{n},\tilde{\gamma}=0} = -\tilde{n}_\alpha^2 \phi_\alpha < 0. \tag{2.42}$$

We can therefore be sure that $\tilde{n}_\alpha$ goes to zero as long as the other states go to zero. Noting (2.39) and (2.42), we can restate the control objective as regulation of $\tilde{E}$, $\tilde{n}$, and $\tilde{\gamma}$ to zero. We will achieve this objective through control laws for the auxiliary heating P_{aux}, the fueling terms S_D^{inj} and S_T^{inj}, and the impurity injection term S_I^{inj}.

2.4 Controller Design

We begin the controller design by looking at the energy subsystem. We note that the dynamic equation (2.34) can be reduced to

$$\frac{d\tilde{E}}{dt} = -\frac{\tilde{E}}{\tau_E} - K_E\tilde{E}, \tag{2.43}$$

where $K_E > 0$ is a design constant, by satisfying the condition

$$f\left(n, E, n_\alpha, n_I, \gamma\right) = -\frac{\bar{E}}{\tau_E} + P_{Ohm} + P_\alpha - P_{rad} + P_{aux} + K_E\tilde{E} = 0. \tag{2.44}$$

The $\tilde{E}$ subsystem is then asymptotically stable since $\tau_E > 0$. The condition (2.44) can be satisfied in several different ways. The auxiliary heating term P_{aux} enters the equation directly. The actuators S_D^{inj} and S_T^{inj} can be used to change the α-heating term P_α by modulating the isotopic mix, and the impurity injection term S_I^{inj} can be used to increase the impurity content and consequently P_{rad}. Having several methods available for controlling the energy subsystem enables us to design a control scheme that can still achieve stabilization despite saturation of one or even several of the available actuators.

The control approach proposed in this work integrates all three methods, as needed. First, the algorithm attempts to control the energy through modulation of the auxiliary power. If the auxiliary power saturates, the controller identifies a trajectory γ^* for the isotopic mix that alters the fusion heating to satisfy $f = 0$. The trajectory γ^* and the equilibrium density $\bar{n}$ are then stabilized through choice of S_D^{inj} and S_T^{inj} and impurity injection is set to zero. If the system cannot meet stability or performance criteria due to fueling actuator saturation, the controller goes on to identify a trajectory n_I^* for the impurity density that can satisfy $f = 0$ and stabilizes

the trajectory using impurity injection.

Step 1: We first calculate the stabilizing value of P_{aux} as

$$P_{aux}^{unsat} = \frac{\bar{E}}{\tau_E} - Q_\alpha \bar{\gamma}(1-\bar{\gamma})\, n_{DT}^2 \langle \sigma v \rangle + P_{rad} - P_{Ohm} - K_E \tilde{E}, \tag{2.45}$$

$$P_{aux} = \text{sat}\left(\frac{P_{aux}^{unsat} - P_{aux}^{min}}{P_{aux}^{max} - P_{aux}^{min}} \right), \tag{2.46}$$

where the limit P_{aux}^{max} depends on the installed power on the tokamak and the limit $P_{aux}^{min} \geq 0$ depends on the operating scenario.

Step 2: We next find a trajectory γ^* satisfying (2.44), i.e.,

$$Q_\alpha \gamma^*(1-\gamma^*)\, n_{DT}^2 \langle \sigma \nu \rangle - P_{rad} + P_{Ohm} + P_{aux} + K_E \tilde{E} = \frac{\bar{E}}{\tau_E}. \tag{2.47}$$

Solving this equation yields

$$\gamma^*(1-\gamma^*) = \frac{\frac{\bar{E}}{\tau_E} + P_{rad} - P_{Ohm} - P_{aux} - K_E \tilde{E}}{Q_\alpha n_{DT}^2 \langle \sigma \nu \rangle} = C, \tag{2.48}$$

$$\gamma^* = \frac{1 \pm \sqrt{1-4C}}{2}, \tag{2.49}$$

We note that this equation is implicit, since C depends on τ_E, which, according to the scaling law (2.19), depends on γ through the effective mass M. To overcome this, we can use a fixed-point iteration scheme, i.e.,

$$\gamma_n^* = \frac{1 \pm \sqrt{1-4C(\gamma_{n-1}^*)}}{2}, \tag{2.50}$$

and stop the iterations once some tolerance is met. Based on numerical simulation results, very few iterations are needed to achieve convergence, in fact, there is typically little change between the first and second iteration. Note that,

if the value of P_{aux} calculated in Step 1 is not saturated, then $\gamma^* = \bar{\gamma}$. This can be shown by substituting (2.45) into (2.47). If $C \leq 0.25$, the two resulting solutions for γ^* are real and we take the tritium-lean solution, such that $\gamma^* \leq 0.5$. If $C \geq 0.25$, even the optimal isotopic mix and maximum value of auxiliary heating will not generate enough heating to satisfy $f = 0$, indicating that the requested operating point may not be achievable for the amount of auxiliary heating power installed on the device. Barring this situation, based on our choice of P_{aux} and γ^*, we have that

$$f\left(n, E, n_\alpha, n_I, \gamma^*\right) = 0. \tag{2.51}$$

This allows us to write $f = \hat{\gamma}\phi_\gamma$ where $\hat{\gamma} = \gamma - \gamma^*$ and ϕ_γ is a continuous function. Noting (2.34), (2.44), we can then write the dynamics of the energy perturbation as

$$\dot{\tilde{E}} = -\frac{\tilde{E}}{\tau_E} - K_E\tilde{E} + \hat{\gamma}\phi_\gamma, \tag{2.52}$$

and the dynamics of $\hat{\gamma}$ can be written as

$$\dot{\hat{\gamma}} \;=\; -\frac{\hat{\gamma}}{\tau_T} + \frac{2\left[u(\gamma^*) + (1-\gamma)\,S_T^{inj} - \gamma S_D^{inj}\right]}{n - 3n_\alpha - (Z_I + 1)\,n_I}. \tag{2.53}$$

Step 3: Having selected P_{aux} and γ^* in the previous steps, we must next choose S_D^{inj} and S_T^{inj} to ensure that $\tilde{E}$, $\hat{\gamma}$, and $\tilde{n}$, which are governed by (2.52), (2.53), and (2.36), are driven to zero. We consider the Lyapunov function $V_0 = V_n + V_{E,\gamma}$ where $V_n = \frac{1}{2}\tilde{n}^2$ and $V_{E,\gamma} = \frac{1}{2}k_1\tilde{E}^2 + \frac{1}{2}\hat{\gamma}^2$. It can be shown that satisfying the conditions

$$\dot{V}_n = -\tilde{n}^2\left(\frac{1-\gamma}{\tau_D} + \frac{\gamma}{\tau_T}\right) + \tilde{n}\left[v + 2\left(S_D^{inj} + S_T^{inj}\right)\right]. \tag{2.54}$$

By satisfying

$$2\left(S_T^{inj}+S_D^{inj}\right)=-v-K_n\tilde{n}, \tag{2.55}$$

where $K_n>0$, (2.54) is reduced to

$$\dot{V}_n=-\tilde{n}^2\left(\frac{1-\gamma}{\tau_D}+\frac{\gamma}{\tau_T}+K_n\right)<0, \tag{2.56}$$

guaranteeing $\tilde{n}\to 0$. We then alculate the derivative of $V_{E,\gamma}$ as

$$\begin{aligned}\dot{V}_{E,\gamma} &= k_1\tilde{E}\left[-\frac{\tilde{E}}{\tau_E}-K_E\tilde{E}+\hat{\gamma}\phi_\gamma\right]\\ &\quad+\hat{\gamma}\left\{-\frac{\hat{\gamma}}{\tau_T}+\frac{2\left[u\left(\gamma^*\right)+\left(1-\gamma\right)S_T^{inj}-\gamma S_D^{inj}\right]}{n-3n_\alpha-\left(Z_I+1\right)n_I}\right\},\\ &= -k_1\frac{\tilde{E}^2}{\tau_E}-k_1K_E\tilde{E}^2-\frac{\hat{\gamma}^2}{\tau_T}\\ &\quad+\hat{\gamma}\left\{k_1\tilde{E}\phi_\gamma+\frac{2\left[u\left(\gamma^*\right)+\left(1-\gamma\right)S_T^{inj}-\gamma S_D^{inj}\right]}{n-3n_\alpha-\left(Z_I+1\right)n_I}\right\}.\end{aligned} \tag{2.57}$$

By satisfying

$$\left(1-\gamma\right)S_T^{inj}-\gamma S_D^{inj}=-\frac{n-3n_\alpha-\left(Z_I+1\right)n_I}{2}\left(k_1\tilde{E}\phi_\gamma+K_\gamma\hat{\gamma}\right)-u, \tag{2.58}$$

where $K_\gamma>0$, we can reduce (2.57) to

$$\dot{V}_{E,\gamma}=-k_1\left(\frac{1}{\tau_E}+K_E\right)\tilde{E}^2-\left(\frac{1}{\tau_T}+K_\gamma\right)\hat{\gamma}^2<0, \tag{2.59}$$

which is negative definite, implying that $\dot{V}_0<0$. This guarantees that $\tilde{E}$, $\tilde{n}$, and $\hat{\gamma}$ will be driven to zero. The conditions (2.55) and (2.58) can be satisfied

by choosing

$$S_D^{inj} = \frac{n - 3n_\alpha - (Z_I + 1)\, n_I}{2} \left(k_1 \tilde{E} \phi_\gamma + K_\gamma \hat{\gamma} \right) + u\left(\gamma^*\right) + (1 - \gamma) \left(\frac{-v - K_n \tilde{n}}{2} \right), \tag{2.60}$$

$$S_T^{inj} = \left(\frac{-v - K_n \tilde{n}}{2} \right) - S_D^{inj}. \tag{2.61}$$

These values are subject to the constraints $0 \leq S_D^{inj} \leq S_D^{max}$ and $0 \leq S_T^{inj} \leq S_T^{max}$. If one of the fueling actuators saturates, we cannot satisfy both conditions of the control law, so we must choose to either control n or γ. If we choose to hold condition (2.58), the energy and tritium fraction subsystems will remain stable, however, the density subsystem will no longer be controlled. This could potentially lead to a violation of the density limit. To avoid this, we instead choose to maintain control of the density by satisfying (2.55). Because of fueling actuator saturation, it may be possible that $\dot{V}_{E,\gamma} > 0$, that is, we may not be able to ensure stability of the burn condition with the previously considered actuators. There are two possible situations to consider, either a thermal quench or an excursion. If the system is experiencing a quench, the controller has already increased auxiliary heating to its maximum, so the only alternative would be to change the magnetic plasma parameters to improve energy confinement (see (2.19)) or to change the reference operating point to one that is achievable. If the system is experiencing a thermal excursion, however, we can still use impurity injection to stabilize the energy subsystem, despite the heating and fueling actuator saturation. In these cases we enable the use of impurity injection by setting the control logic flag $F_{imp} = 1$ and proceeding to Step 4.

Step 4: If $F_{imp} = 1$, we use the expression for radiation losses given in (2.12) to find an impurity density trajectory n_I^* that satisfies condition (2.44). Defining the error $\hat{n}_I = n_I - n_I^*$, we can write its dynamics as

$$\dot{\hat{n}}_I = -\frac{\hat{n}_I}{\tau_I^*} - \frac{n_I^*}{\tau_I^*} + S_I^{inj} + S_I^{sp} - \dot{n}_I^*. \tag{2.62}$$

Based on the choice of n_I^*, we have that

$$f\left(n, E, n_\alpha, \gamma, n_I^*\right) \;=\; 0, \tag{2.63}$$

which allows us to write $f = \hat{n}_I \phi_I$ where ϕ_I is a continuous function. We can then rewrite (2.34) as

$$\dot{\tilde{E}} = -\frac{\tilde{E}}{\tau_E} - K_E \tilde{E} + \hat{n}_I \phi_I. \tag{2.64}$$

We take as a Lyapunov function $V_1 = V_n + V_\gamma + V_{E,I}$ where $V_\gamma = \frac{1}{2}\hat{\gamma}^2$ and $V_{E,I} = \frac{1}{2}k_3\tilde{E}^2 + \frac{1}{2}\hat{n}_I^2$.

$$\begin{aligned}
\dot{V}_{E,I} &= k_3 \tilde{E}\left[-\frac{\tilde{E}}{\tau_E} - K_E\tilde{E} + \hat{n}\phi_n\right] + \hat{n}_I\left\{-\frac{\hat{n}_I}{\tau_I^*} - \frac{n_I^*}{\tau_I^*} + S_I^{inj} + S_I^{sp} - \dot{n}_I^*\right\} \\
&= -k_3\frac{\tilde{E}^2}{\tau_E} - k_3 K_E \tilde{E}^2 - \frac{\hat{n}_I^2}{\tau_I^*} + \hat{n}_I\left\{k_3\tilde{E}\phi_I - \frac{n_I^*}{\tau_I^*} + S_I^{inj} + S_I^{sp} - \dot{n}_I^*\right\}.
\end{aligned} \tag{2.65}$$

By satisfying

$$S_I^{inj} = -k_3\tilde{E}\phi_I + \frac{n_I^*}{\tau_I^*} - S_I^{sp} + \dot{n}_I^* - K_I\hat{n}_I, \tag{2.66}$$

where $K_I > 0$, this can be reduced to

$$\dot{V}_{E,I} = -k_3\left(\frac{1}{\tau_E} + K_E\right)\tilde{E}^2 - K_I\hat{n}_I^2 < 0, \tag{2.67}$$

guaranteeing $\tilde{E}$ and $\hat{n}_I$ go to zero. We modify the tritium fraction trajectory to $\gamma^* = \gamma^*_{(\text{Step 2})} - K_S \int_{t_0}^{t} S_I^{inj} dt$ where $\gamma^*_{(\text{Step 2})}$ is the value of γ^* calculated in Step 2, $K_S > 0$, and t_0 is the time at which impurity injection was first engaged. This modification ensures that the tritium fraction is, if possible, eventually reduced to such a level that impurity injection is no longer needed, i.e., $S_I^{inj} \to 0$. Once $S_I^{inj} = 0$, we disable impurity injection in subsequent executions of the algorithm by setting $F_{imp} = 0$. By satisfying

$$\begin{aligned} 2\left(S_T^{inj} + S_D^{inj}\right) &= -v - K_n\tilde{n}, && (2.68) \\ (1-\gamma)\, S_T^{inj} - \gamma S_D^{inj} &= -\frac{n - 3n_\alpha - (Z_I+1)\, n_I}{2} K_\gamma \hat{\gamma} \\ &\quad - u(\gamma_I^*). && (2.69) \end{aligned}$$

We can ensure that $\dot{V}_n < 0$, $\dot{V}_\gamma < 0$, and therefore $\dot{V}_1 < 0$, guaranteeing stability of the system. The conditions (2.68) and (2.69) can be satisfied by choosing

$$\begin{aligned} S_D^{inj} &= \frac{n - 3n_\alpha - (Z_I+1)\, n_I}{2} K_\gamma \hat{\gamma} \\ &\quad + u(\gamma^*) + (1-\gamma)\left(\frac{-v - K_n\tilde{n}}{2}\right), && (2.70) \\ S_T^{inj} &= \left(\frac{-v - K_n\tilde{n}}{2}\right) - S_D^{inj}, && (2.71) \end{aligned}$$

which are again subject to saturation. If one of the fueling actuators saturates, we again choose to hold (2.68) to ensure stability of the density.

Through the proposed control algorithm, values for P_{aux}, S_D^{inj}, S_T^{inj}, and S_I^{inj} are found in such a way that, if possible, the energy and density are driven to the desired values. As the system approaches the desired operating point and any saturated actuators leave saturation, the trajectories γ^* and n_I^* return to $\bar{\gamma}$ and $\bar{n}_I$, respectively. Once $\tilde{E}$, $\tilde{n}$, and $\tilde{\gamma}$ go to zero, we can be sure, from (2.39) and (2.42), that the remaining states

Table 2.2: Actuator limits.

Symbol	Description	Value
P_{aux}^{max}	Maximum power	73 MW
P_{aux}^{min}	Maximum power	$5/7 \times P_{aux}^{max}$
$\dot{P}_{aux}^{max}$	Maximum power ramp rate	2.25×10^4 $\mathrm{Wm^{-3}s^{-1}}$
S_D^{max}	Maximum fueling (D)	$3 \times S_D^r$
$\dot{S}_D^{max}$	Maximum fueling (D) ramp rate	3×10^{18} $\mathrm{m^{-3}s^{-2}}$
S_T^{max}	Maximum fueling (T)	$3 \times S_T^r$
$\dot{S}_T^{max}$	Maximum fueling (T) ramp rate	3×10^{18} $\mathrm{m^{-3}s^{-2}}$

$\tilde{n}_\alpha$, and $\tilde{n}_I$ also go to zero.

2.5 Zero-Dimensional Simulation Study

In this section we study the performance of the proposed control scheme through a zero dimensional simulation study. We use the model described in Section 2.2 for the simulations. We consider magnitude and rate limits on the actuators of the form

$$\begin{aligned} x^{min} &\leq x \leq x^{max}, \\ |\dot{x}| &\leq \dot{x}^{max}, \end{aligned}$$

where x is a particular actuator. For this study, we use the limits given in Table 2.2. In addition to the actuator limits, we limit the feedforward terms $\dot{\gamma}^*$ and $\dot{n}_I^*$ to prevent the controller from reacting to strongly to step changes in these references. We also force $\phi_\gamma = 0$ when $|\hat{\gamma}| < \epsilon$ and $\phi_I = 0$ when $|\hat{n}_I| < \epsilon$, where ϵ is small, so there is no possibility of errors in precision causing ϕ_γ or ϕ_I to become unbounded.

The study is divided into two sections. The first shows how the controller can improve the response of the plasma when moving between operating points, even when the desired operating points are unstable. We then study the effect of recycling model

parameters on controller performance. Throughout the simulations, the parameters $Z_I = 4$, $k_\alpha^* = 7$, $k_I^* = 10$, and $k_D = k_T = 3$ are used.

2.5.1 Switching Between Operating Points

We begin the simulation study by comparing the open loop (uncontrolled) and closed loop (controlled) performance of the system when switching between operating points. This allows us to simultaneously test the response of the nonlinear control scheme to initial perturbations in plasma parameters and to show how, by embedding the nonlinear model of the system in the control scheme, the controller can stabilize a range of operating points. The ability to transition between operating points will be important during reactor startup and shutdown but may also be necessary during operation in order to respond to changes in power load demands or device configuration. For example, if a neutral beam injector malfunctions during operation, the reactor could switch to a different operating point that does not require as much beam power. During such transitions, it will be important to maintain stable control and to avoid large peaks in fusion power or other parameters.

2.5.1.1 Scenario 1

In this study, we started the system at a set of perturbed initial conditions and requested the plasma to move to an operating point with an auxiliary heating requirement near the power saturation limit P_{aux}^{min}, then to a second operating point with a higher fusion power and auxiliary heating requirement, and finally to a third operating point again characterized by an auxiliary heating requirement near the saturation limit.

The simulations used model parameters $f_I = 0.01$, $H_H = 1.13$, $R_{eff} = 0.9$, $\gamma^{PFC} = 0.5$, $f_{ref} = 0.7$, and $f_{eff} = 0.2$. The initial conditions were set as $n_D(0) = 1.1 \times n_D^r$,

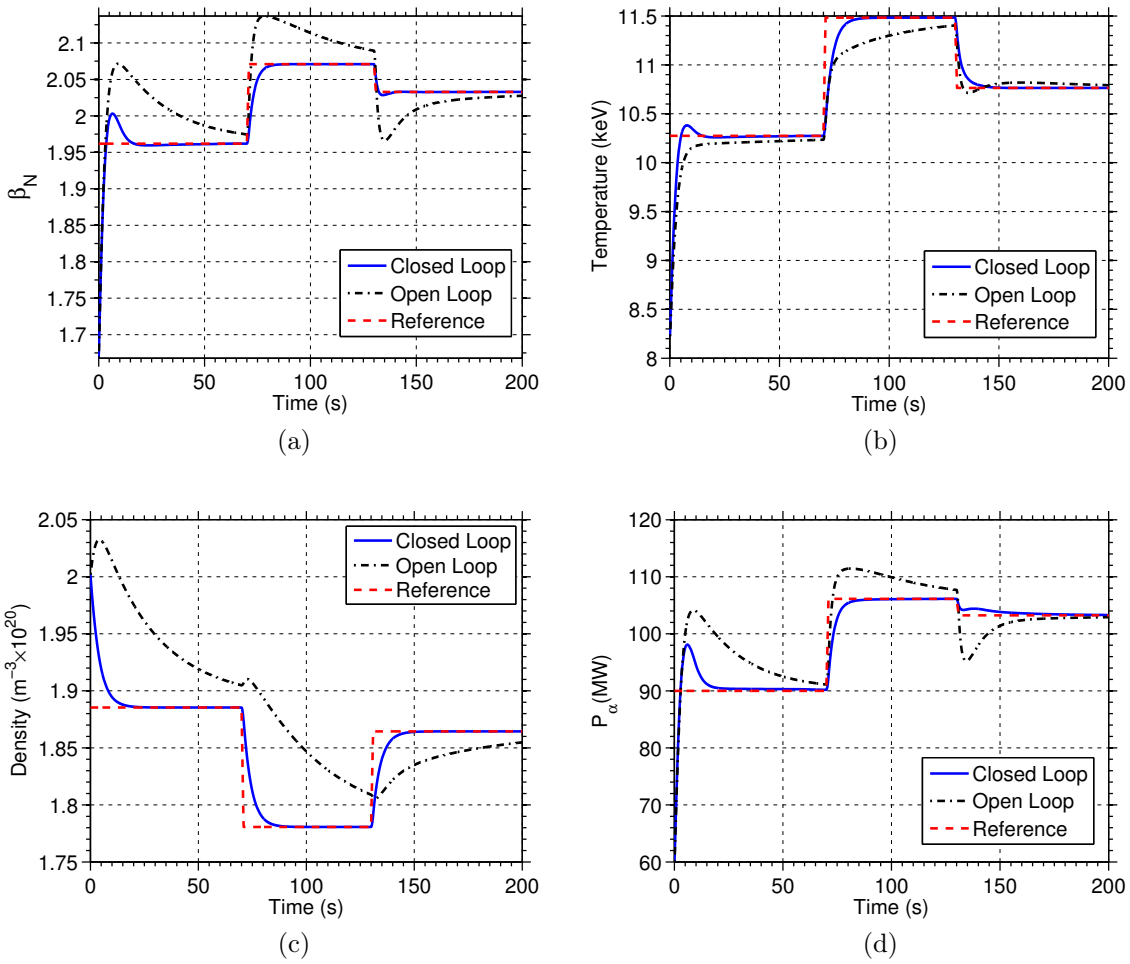

Figure 2.1: Closed loop, open loop, and desired operating point during the first simulation scenario: (a) Plasma β, (b) plasma density n, (c) temperature T, and (d) fusion heating P_α.

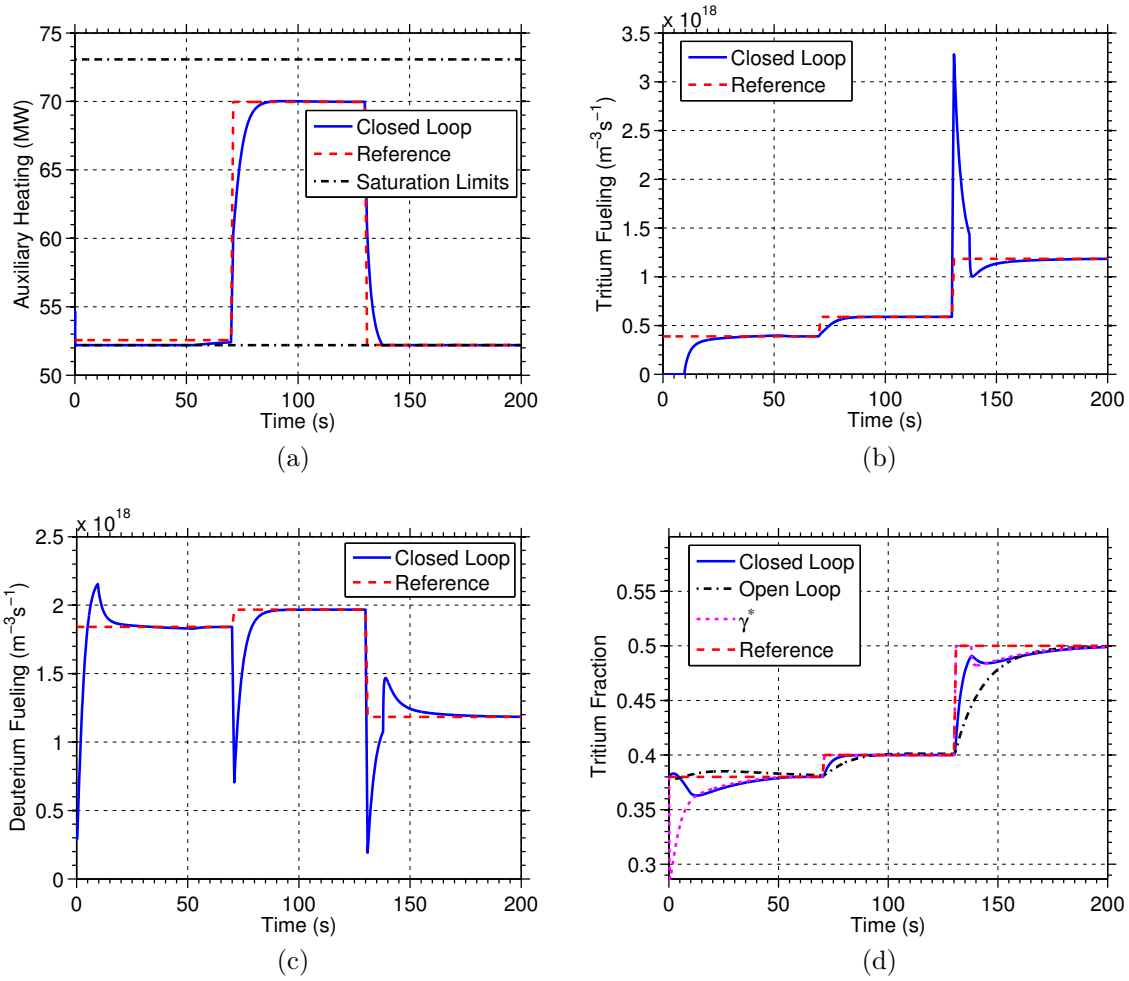

Figure 2.2: Closed loop and open loop (a) heating P_{aux}, (b) tritium fueling S_T, (c) deuterium fueling S_D, and (d) a comparison of the tritium fraction reference, closed loop and open loop results, and γ^* during the first simulation scenario.

$n_T(0) = 1.1 \times n_T^r$, $n_\alpha(0) = 0.6 \times n_\alpha^r$, $n_I(0) = n_I^r$, $E(0) = 0.85 \times E^r$.

The β_N, T, n, and P_α results for the two simulations are compared in Figure 2.1 (a), (b), (c), and (d), respectively. The auxiliary heating, tritium fueling, deuterium fueling, and tritium fraction are shown in Figure 2.2 (a), (b), (c), and (d), respectively. Due to the initial condition perturbation, there was a rapid increase in β_N initially in both the open and closed loop cases. This led to a large overshoot in both β_N and P_α in the open loop case. In the controlled case, however, the nonlinear control law was able to significantly reduce the overshoot and return the system to the desired operating point. Due to the proximity of the operating point to the auxiliary heating saturation limit, the controller was forced to reduce the tritium fraction in order to limit the severity of the excursion. This was accomplished by temporarily reducing the tritium fueling to zero. With more favorable recycling parameters, the controller could have reduced the tritium fraction more quickly and further reduced the overshoot in β_N and P_α. At $t = 70$s, the desired operating point was changed. Again, in the open loop case there was a significant overshoot in β_N and P_α, as well as a slow density and temperature response. The system response was greatly improved by the nonlinear control law. Note how the isotopic fueling capability was used to improve the response time of the isotopic mix. At $t = 130$s, the desired operating point was switched to one that required the minimum auxiliary power. The open loop case experienced an undershoot in β_N and P_α and a slow density response. The controlled case, on the other hand, quickly tracked the desired β_N, T, and n, and avoided the undershoot in P_α. Note that, because the auxiliary power saturated, the controller altered the tritium fraction to track γ^*. This was done through isotopic fuel tailoring, as seen in Figures 2.2 (b) and (c).

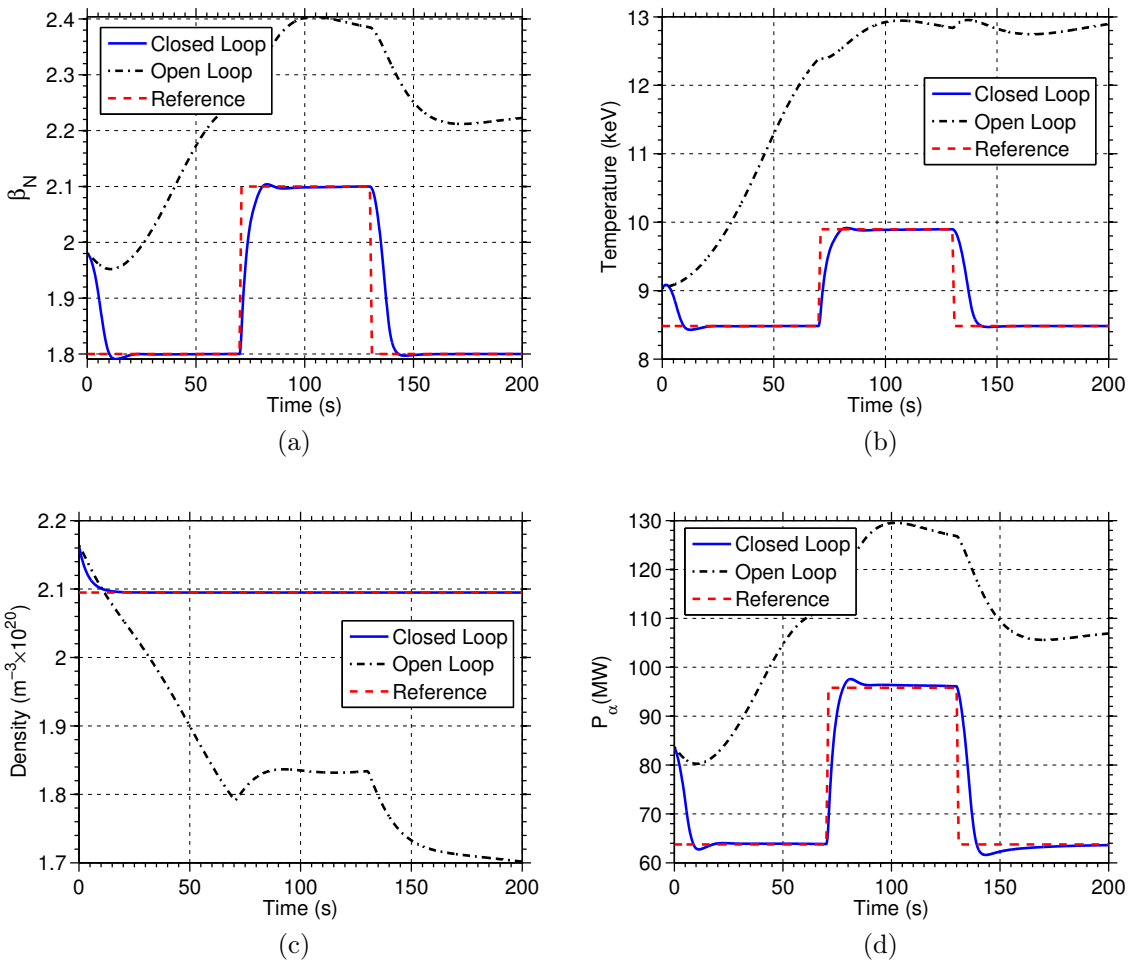

Figure 2.3: Closed loop, open loop, and desired operating point during the second simulation scenario: (a) Plasma β, (b) plasma density n, (c) temperature T, and (d) fusion heating P_α.

2.5.1.2 Scenario 2

Next, we considered a second scenario of switching between operating points, this time using an alternative confinement scaling law. For these results, the simulation and controller used the scaling law ITER90H-P [46]

$$\tau_{E,90H-P} = H_H 0.082 I^{1.02} R^{1.6} B^{0.15} M^{0.5} \kappa_{95}^{-0.19} P^{-0.47}. \tag{2.72}$$

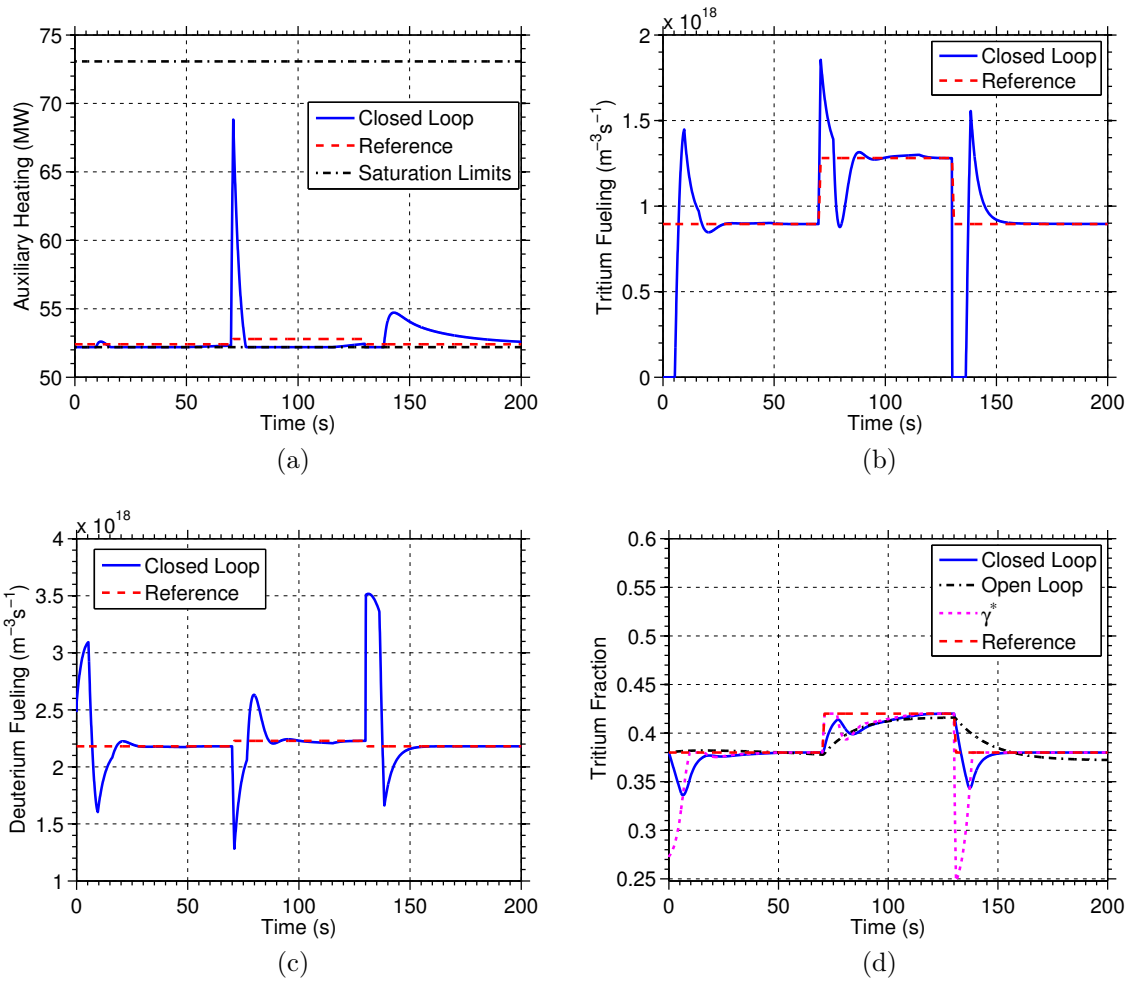

Figure 2.4: Closed loop and open loop (a) heating P_{aux}, (b) tritium fueling S_T, (c) deuterium fueling S_D, and (d) a comparison of the tritium fraction reference, closed loop and open loop results, and γ^* during the second simulation scenario.

We again started the system at a set of disturbed initial conditions and requested the plasma to move to three operating points with auxiliary heating requirements near the power saturation limit P_{aux}^{min}. The simulations used model parameters $f_I = 0.017$, $H_H = 0.75$, $R_{eff} = 0.9$, $\gamma^{PFC} = 0.4$, $f_{ref} = 0.7$, and $f_{eff} = 0.2$. The initial conditions were set as $n_D(0) = 1.05 \times n_D^r$, $n_T(0) = 1.05 \times n_T^r$, $n_\alpha(0) = 0.8 \times n_\alpha^r$, $n_I(0) = n_I^r$, $E(0) = 1.1 \times E^r$.

The β_N, T, n, and P_α results for the two simulations are compared in Figure 2.3 (a), (b), (c), and (d), respectively. The auxiliary heating, tritium fueling, deuterium fueling, and tritium fraction are shown in Figure 2.4 (a), (b), (c), and (d), respectively. Clearly, with this alternative confinement scaling, the system exhibited much worse open loop performance. The density dropped below the desired level, while β_N and T increased far beyond the requested values. This resulted in a significantly higher fusion heating than desired. These results indicate that the stability of operating points is strongly affected by the dependence of plasma confinement on changes in other parameters. In the controlled case, this nonlinear effect was accounted for and the controller was able to stabilize all three operating points and achieve excellent transient performance. Note that, because the operating points were so close to the minimum heating power, the controller often saturated the auxiliary heating actuator. The controller reduced γ^* during the heating saturation in order to maintain the reference value of E, and the isotopic fueling capability was used to track this reference. Due to particle recycling the tritium fueling actuator occasionally saturated in an effort to track γ^*, however the overall system performance was still quite good.

2.5.1.3 Scenario 3

For a third scenario, we again used the alternative scaling (2.72). In this case, however, a higher recycling rate was used, making it harder for the controller to track the

desired isotopic mix γ^*. The simulations used model parameters $f_I = 0.017$, $H_H = 0.75$, $R_{eff} = 0.95$, $\gamma^{PFC} = 0.4$, $f_{ref} = 0.7$, and $f_{eff} = 0.2$. The same initial conditions as Scenario 2 were used.

The β_N, T, n, and P_α results for the open and closed loop simulations of scenario 3 are compared in Figures 2.5 (a), (b), (c), and (d), respectively. The auxiliary heating, tritium fraction, deuterium and tritium fueling, and impurity injection/density are shown in Figures 2.6 (a), (b), (c), and (d), respectively. As in the previous case, the open loop performance was quite poor. In the closed loop simulation, the controller drove the auxiliary heating to saturation several times in order to stabilize the desired operating points. Due to the higher recycling rate, the isotopic mix could not be changed as quickly as in Scenario 2, which prompted the controller to switch to the use of impurity injection (see Figure 2.6 (b) and (d)). The injected impurities cooled the plasma and stabilized the operating points. However, because of the long confinement time of impurities, the impurity density decayed slowly and additional heating power was necessary long after the impurity injection was stopped, as seen in Figure 2.6 (a).

2.5.2 Effect of Recycling Model Parameters

The previous simulation scenario showed how, for certain values of the recycling parameters f_{ref}, f_{eff}, and R_{eff}, it can be difficult to track the stabilizing isotopic mix reference γ^* due to fueling actuator saturation, which degrades the performance of the proposed control scheme and may necessitate the use of impurity injection in some cases. Since the reference γ^* is highly dependent on the stability characteristics of the desired operating point and how close it is to the heating actuator saturation limits, any study of the effect of recycling parameters on performance will be highly scenario dependent. Nevertheless, we can get a qualitative understanding of how

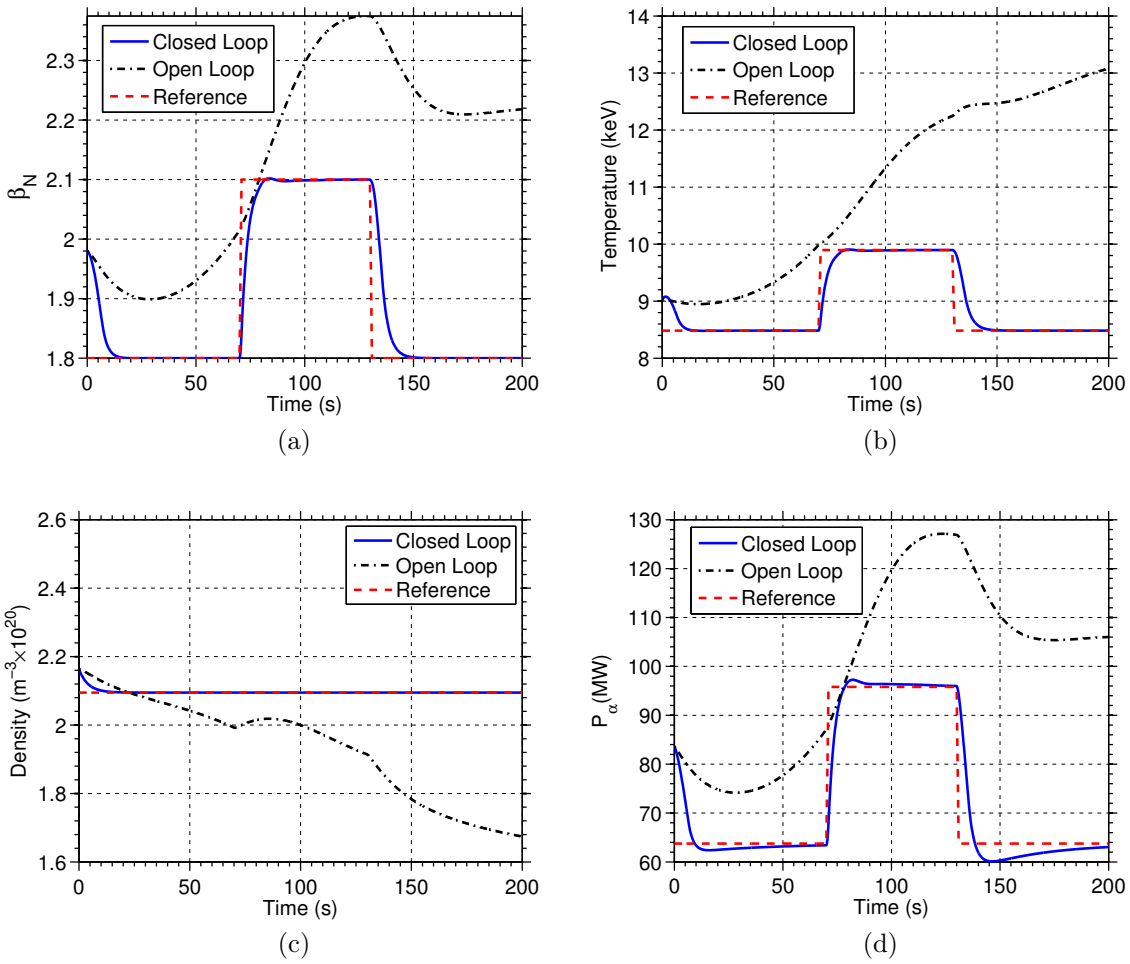

Figure 2.5: Closed loop, open loop, and desired operating point during the third simulation scenario: (a) Plasma β, (b) plasma density n, (c) temperature T, and (d) fusion heating P_α.

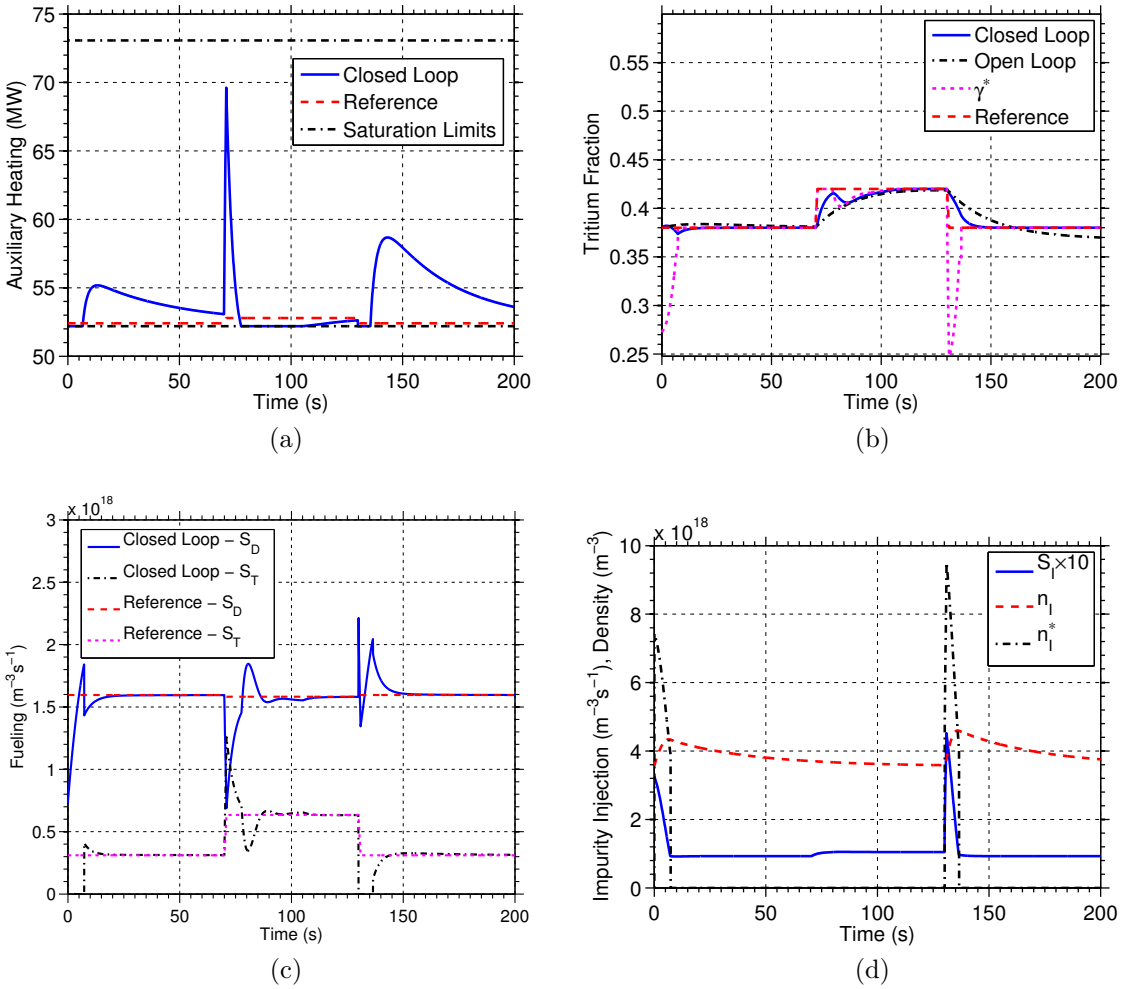

Figure 2.6: Open and closed loop (a) auxiliary heating power, (b) tritium fraction, (c) deuterium and tritium fueling, and (d) impurity injection/density during Scenario 3.

the parameters influence performance by doing a parametric study for a particular scenario and comparing controller performance metrics. For this study, we chose a scenario ($H_H = 1.1$, $\gamma^{PFC} = 0.5$, $f_I = 0.015$) in which the controller had to respond to a sudden increase in the confinement parameter H_H of 5%. The reference for the energy was chosen such that, after the confinement parameter change, the controller was forced to reduce the auxiliary heating to the minimum level and reduce the tritium fraction in order to maintain the desired energy. We used the percent overshoot (the maximum percent difference between the achieved E and the desired value E^r), 1% settling time (the time it takes the energy E to come within 1% of its final value), and steady-state error (the difference between the ultimate value of E and the desired value E^r) as the controller performance metrics to compare. We note again that, due to the nonlinearity of the system, the results of this type of study are dependent on the particular scenario studied.

Results for $R^{eff} = 0.85$, $R^{eff} = 0.90$, and $R^{eff} = 0.95$ are shown in Figure 2.9(a)-(c), (d)-(f), and (g)-(i), respectively. Each subplot depicts a particular performance metric as a function of f_{ref} and f_{eff}. It is apparent that the controller works best for low values of f_{eff} and R^{eff} coupled with high values of f_{ref}. We note that for $R^{eff} = 0.85$ there is a large region of parameter space in which there is no steady state error. The region decreases in size as R^{eff} is increased. The overshoot is most strongly dependent on R^{eff} and f_{eff}, though the dependence on f_{ref} increases for high values of f_{eff}. In the region of parameter space without steady-state error, the settling time increases with f_{eff} and decreases with f_{ref}, however, a more complex behavior occurs within the region with steady-state error. The slowest settling time occurs at high values of f_{eff} at the values of f_{ref} where steady-state error begins. In the region with steady-state error, the settling time decreases with decreasing f_{ref}. This complex dependence occurs because, although the response time of the system

is slower in this region, the final value of E is closer to the maximum overshoot, so the system takes less time to come to steady-state.

Based on these results, the controller performance can be optimized most effectively by lowering the recycling rate R_{eff} and recycled particle fueling efficiency f_{eff}. Based on experimental studies of a recycling model similar to the one used in this work [41], f_{eff} may be quite low (<0.5) for divertor configurations. Divertor designs that prevent recycled flux from escaping the divertor region could reduce f_{eff} while significant active pumping capabilities may be necessary to reduce R_{eff}. The reflectivity f_{ref} is dependent on material properties and the angle at which particles strike the surface. By operating with high reflectivity, the problem of steady-state error can be minimized because the isotopic mix of the recycled material is made less dependent on the content of the walls. We note also that, as the wall inventory exchanges with the plasma, the isotopic mix of the wall inventory γ^{PFC} may change slowly over time. This would cause the steady-state error seen in these simulations to eventually tend to zero, however, the settling time could be very long since the wall acts as a very large reservoir of particles.

2.6 One-dimensional Simulation Study

In this section, we introduce a simple one-dimensional burning plasma model of the evolution of the radial profiles of the plasma parameters. We use the one-dimensional model to study the performance of the proposed control scheme in the presence of spatially varying parameters. The model is given by the following set of coupled

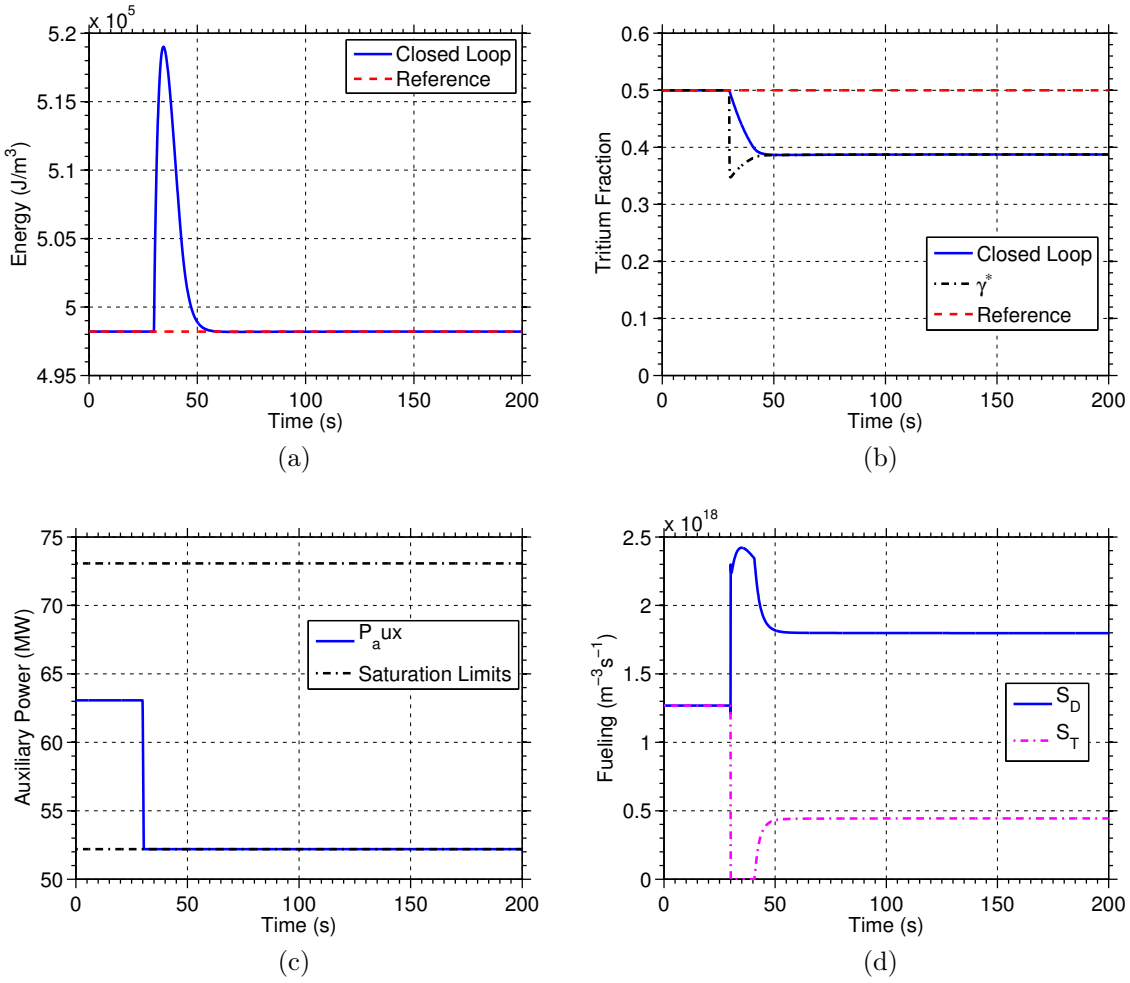

Figure 2.7: Simulation results for confinement disturbance case with $R_{eff} = 0.95$, $f_{eff} = 0.2$, $f_{ref} = 0.7$.

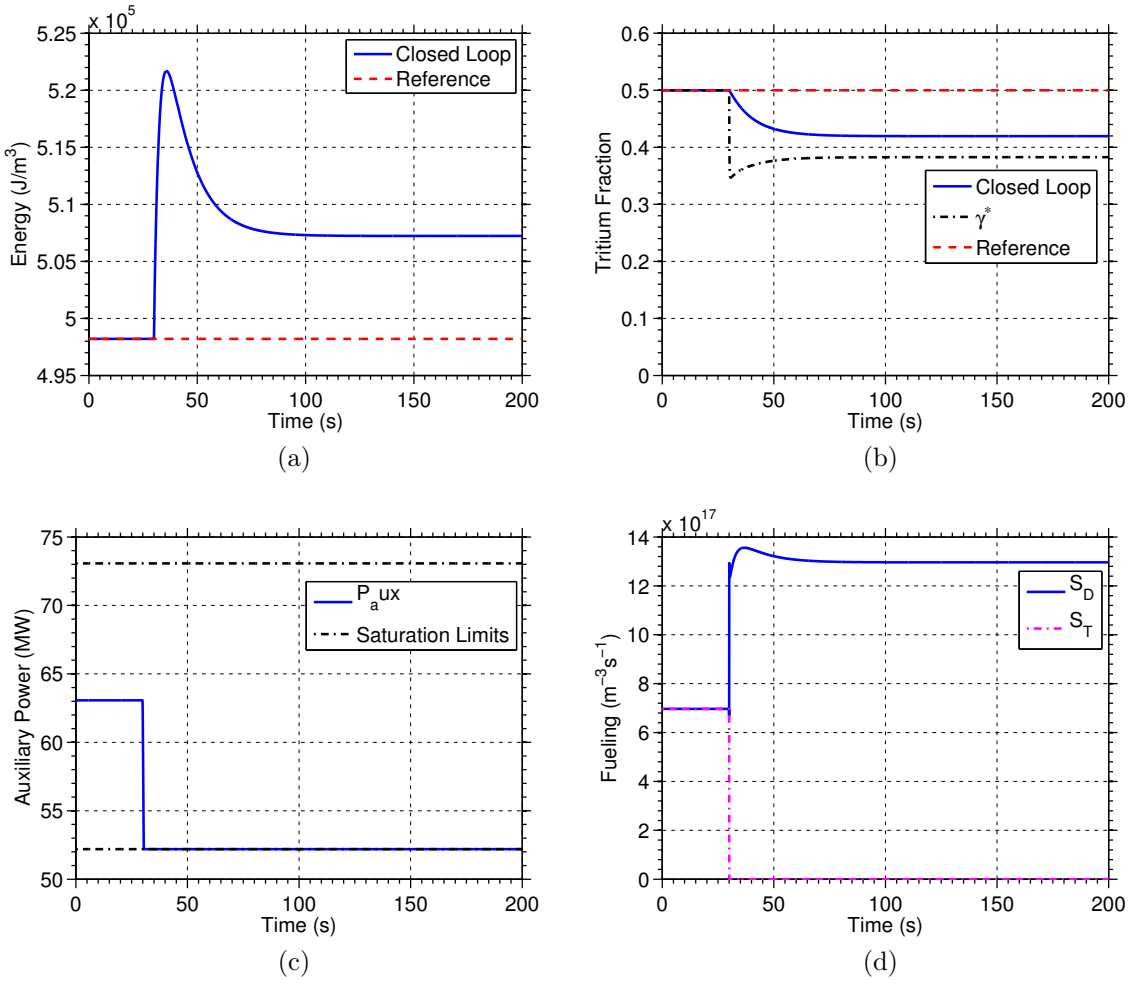

Figure 2.8: Simulation results for confinement disturbance case with $R_{eff} = 0.95$, $f_{eff} = 0.5$, $f_{ref} = 0.2$.

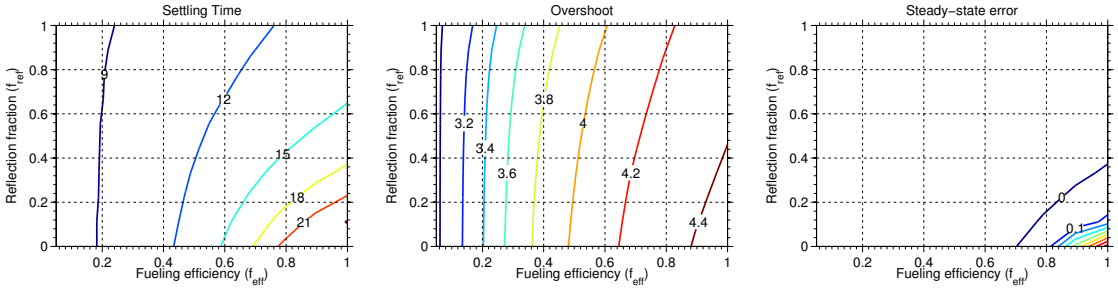

(a) $R_{eff} = 0.85$

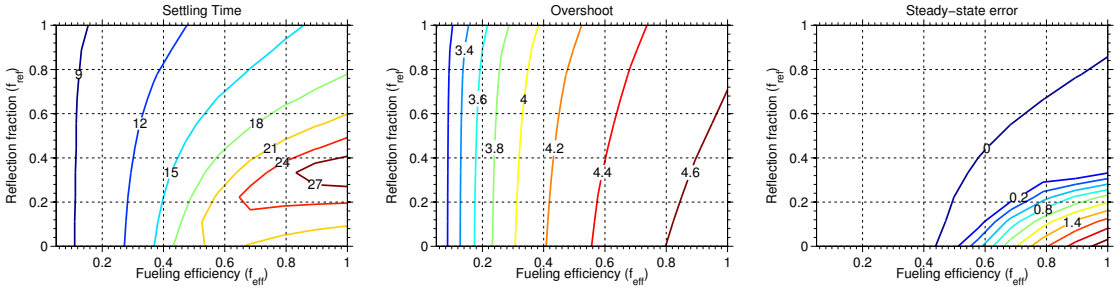

(b) $R_{eff} = 0.90$

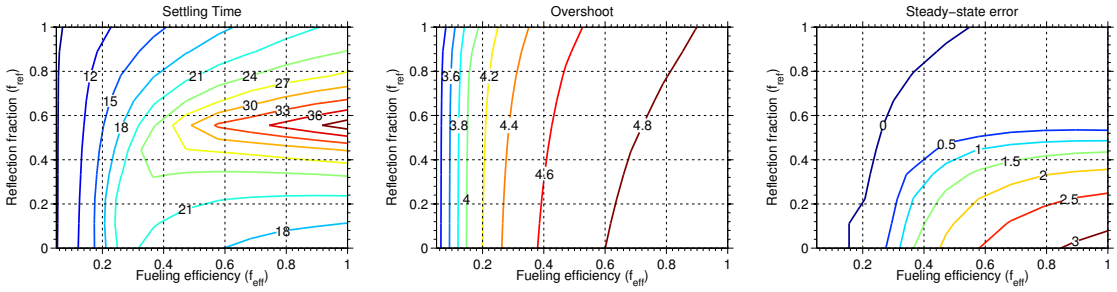

(c) $R_{eff} = 0.95$

Figure 2.9: Controller performance metrics as a function of recycling parameters for the confinement disturbance scenario with $P_{aux}^{min} = (5/7)\bar{P}_{aux}^{max}$.

nonlinear partial differential equations:

$$\begin{aligned}
\frac{\partial n_\alpha}{\partial t} &= \frac{1}{r}\frac{\partial}{\partial r} r\left(D_\alpha \frac{\partial n_\alpha}{\partial r}\right) + S_\alpha, \\
\frac{\partial n_D}{\partial t} &= \frac{1}{r}\frac{\partial}{\partial r} r\left(D_D \frac{\partial n_D}{\partial r}\right) - S_\alpha + S_D + f_{eff} S_D^R, \\
\frac{\partial n_T}{\partial t} &= \frac{1}{r}\frac{\partial}{\partial r} r\left(D_T \frac{\partial n_T}{\partial r}\right) - S_\alpha + S_T + f_{eff} S_T^R, \\
\frac{\partial n_I}{\partial t} &= \frac{1}{r}\frac{\partial}{\partial r} r\left(D_I \frac{\partial n_I}{\partial r}\right) + S_I, \\
\frac{\partial E}{\partial t} &= \frac{1}{r}\frac{\partial}{\partial r} r\left(D_E \frac{\partial E}{\partial r}\right) + Q_\alpha S_\alpha - P_{rad} + P_{Ohm} + P_{aux},
\end{aligned}$$

where $n_\alpha(r)$, $n_D(r)$, $n_T(r)$, $n_I(r)$, and $E(r)$ now represent spatially varying model states and $S_\alpha(r)$ and $P_{rad}(r)$ are calculated based on local plasma parameter values. This simple cylindrical model assumes a constant diffusivities $D_E = 0.3$, $D_D = 0.17$, $D_T = 0.14$, $D_\alpha = 0.10$, $D_I = 0.06$, and negligible pinch velocities. The heating and fueling rates are distributed throughout the plasma based on the deposition profiles of the respective actuators. We assume the shape of deposition profiles are fixed in time and only the magnitude of the actuators can be modulated by the controller, i.e.,

$$\begin{aligned}
S_D(r,t) &= \langle S_D \rangle(t) \times \hat{S}_D(r), \\
S_T(r,t) &= \langle S_T \rangle(t) \times \hat{S}_T(r), \\
S_I(r,t) &= \langle S_I \rangle(t) \times \hat{S}_I(r), \\
P_{aux}(r,t) &= \langle P_{aux} \rangle(t) \times \hat{P}_{aux}(r),
\end{aligned}$$

where $\hat{S}_D(r)$, $\hat{S}_T(r)$, $\hat{S}_I(r)$, and $\hat{P}_{aux}(r)$ are the normalized deposition profiles. The deposition profiles used in this study are shown in Figure 2.10. Profile 1 was used for $\hat{P}_{aux}(r)$, while Profile 2 was used for $\hat{S}_D(r)$, $\hat{S}_T(r)$, and $\hat{S}_I(r)$. The recycling

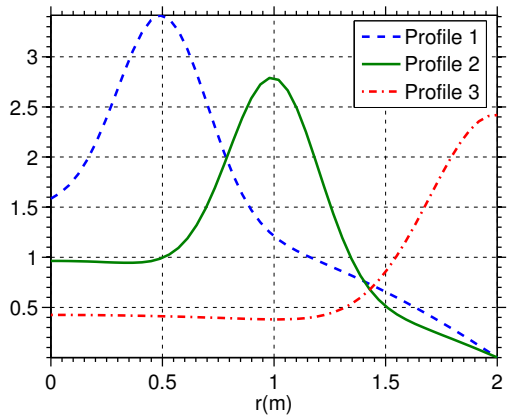

Figure 2.10: Normalized actuator deposition profiles used in the one-dimensional simulations.

model used in the zero-dimensional study is used to calculate the recycling rates of deuterium and tritium, and the recycled deuterium and tritium are assumed to fuel the plasma with time-invariant deposition profile, i.e.,

$$\begin{aligned} S_D^R(r) &= \langle S_D^R \rangle(t) \times \hat{S}_D^R(r), \\ S_T^R(r) &= \langle S_T^R \rangle(t) \times \hat{S}_T^R(r), \end{aligned}$$

where $\langle S_D^R \rangle$ and $\langle S_T^R \rangle$ are calculated using expressions (2.1) and (2.2), respectively, and $\hat{S}_D^R(r)$ and $\hat{S}_T^R(r)$ are set as Profile 3 in Figure 2.10.

Based on the cylindrical symmetry of the model, no-flux boundary conditions are

used at $r = 0$. For the set of boundary conditions at the minor radius $r = a$, we take

$$\begin{aligned}
\left.\frac{\partial n_\alpha}{\partial r}\right|_{r=a} &= -d_\alpha n_\alpha, \\
\left.\frac{\partial n_D}{\partial r}\right|_{r=a} &= -d_D n_D, \\
\left.\frac{\partial n_T}{\partial r}\right|_{r=a} &= -d_T n_T, \\
\left.\frac{\partial n_I}{\partial r}\right|_{r=a} &= -d_I n_I, \\
\left.\frac{\partial E}{\partial r}\right|_{r=a} &= -d_E E,
\end{aligned}$$

where $d_\alpha = 4.4$, $d_D = 1.2$, $d_T = 1.6$, $d_I = 1.4$, and $d_E = 4.3$.

Volume averaged quantities were obtained from the model through integration. For a quantity x, its volume average, denoted $\langle x \rangle$, is found as

$$\langle x \rangle = \frac{2\int_0^a rx dr}{a^2}.$$

Furthermore, the confinement time for the state x can be obtained by computing

$$\tau_x = -\frac{a\langle x \rangle}{2D_x \left.\frac{\partial x}{\partial r}\right|_{r=a}}. \tag{2.73}$$

During the closed loop simulation of the 1-D model, the diffusivity for each species is updated based on (2.73) such that the confinement times follow the confinement scaling (2.19) used in the zero-dimensional study.

During the simulation, the volume averages and confinement times were computed and passed as inputs to the controller, which then output the volume averages of the actuators. We assume that the volume averaged plasma parameters, including $\langle S_\alpha \rangle$, $\langle P_{rad} \rangle$, and the confinement times are all measured or estimated. To account for the

effect of the spatial distribution of parameters, the calculation of γ^* in the Step 2 of the control scheme must be modified slightly. We define $\langle\gamma\rangle = \langle n_T\rangle/(\langle n_T\rangle + \langle n_D\rangle)$ and write $\langle S_\alpha\rangle = f_p^\gamma \langle\gamma\rangle \left(1 - \langle\gamma\rangle\right) \langle n_H\rangle^2 \langle\sigma v\rangle \left(\langle T\rangle\right)$ where f_p^γ is a scale factor to account for the effects of spatial profiles. The scale factor is then used to calculate

$$\begin{aligned}
\langle\gamma^*\rangle \left(1 - \langle\gamma^*\rangle\right) &= \frac{\frac{\langle E\rangle^r}{\tau_E} + \langle P_{rad}\rangle - \langle P_{Ohm}\rangle + \langle P_{aux}\rangle}{f_p^\gamma Q_\alpha \langle n_H\rangle^2 \langle\sigma v\rangle \left(\langle T\rangle\right)} \equiv \langle C\rangle, \\
\langle\gamma^*\rangle &= \frac{1 \pm \sqrt{1 - 4\langle C\rangle}}{2},
\end{aligned}$$

The rest of the control scheme is left unchanged, aside from the $\langle\cdot\rangle$ notation, i.e.,

$$\begin{aligned}
\langle P_{aux}^{unsat}\rangle &= \frac{\langle\bar{E}\rangle}{\tau_E} - f_p^\gamma Q_\alpha \langle\gamma\rangle^r (1 - \langle\gamma\rangle^r) \langle n_{DT}\rangle^2 \langle\sigma v\rangle \left(\langle T\rangle\right) + \langle P_{rad}\rangle - \langle P_{Ohm}\rangle, \\
\langle S_D^{inj}\rangle &= \frac{\langle n\rangle - 3\langle n_\alpha\rangle - (Z_I + 1)\langle n_I\rangle}{2} \left(k_1 \langle\tilde{E}\rangle \phi_\gamma + K_\gamma \langle\hat{\gamma}\rangle\right) \\
&\quad + \langle u\left(\gamma^*\right)\rangle + \left(1 - \langle\gamma\rangle\right) \left(\frac{-\langle v\rangle - K_n \langle\tilde{n}\rangle}{2}\right), \\
\langle S_T^{inj}\rangle &= \left(\frac{-\langle v\rangle - K_n \langle\tilde{n}\rangle}{2}\right) - \langle S_D^{inj}\rangle.
\end{aligned}$$

Actuator limits in the one-dimensional simulation were the same as those used in the zero-dimensional simulation.

For the one-dimensional simulation, a low temperature operating point with an auxiliary heating requirement near the minimum auxiliary power saturation limit was chosen as a reference. Based on the chosen values of $\langle T\rangle$, $\langle\beta\rangle$, and $\langle\gamma\rangle$, as well as the actuator and recycling deposition profiles, the set of equilibrium profiles and actuator values associated with the operating point were determined. Two simulations, one using the equilibrium fueling and heating rates (open loop) and the other with the proposed controller active (closed loop), were run, both starting from a perturbed set of initial profiles. The parameters used were $H_H = 0.88$, $R_{eff} = 0.9$, $\gamma^{PFC} = 0.4$,

$f_{eff} = 1$, and $f_{ref} = 0.5$. Figure 2.11 compares the open loop and closed loop volume averages, as well as the spatiotemporal evolution of the percent error, for the (a) temperature and (b) plasma density. Figure 2.12 shows the same set of results for (a) energy and (b) fusion heating. The open loop response of the temperature and density to the perturbed initial profiles was quite slow, while in closed loop the desired temperature and density are quickly recovered. In closed loop, the profile percent error tended to zero at all spatial locations with about the same response time as the spatial average values. The energy and fusion heating averages initially responded on similar time scales in both open and closed loop. However, the open loop response exhibited an undershoot that persisted for a long time, while the closed loop system quickly reached the desired values. We see similar results in the spatiotemporal evolution of the percent error. Figure 2.13 compares the open loop and closed loop values of the actuators (a) P_{aux}, (b) S_T, and (c), S_D, as well as the (d) tritium fraction and controller requested tritium fraction γ^*. We see that, because the heating requirement for the operating point was quite close to the minimum saturation limit, the controller could not reduce heating much in response to the initial condition errors. The controller maintained control of the system by requesting a reduction in the tritium fraction γ^*, which was successfully tracked through isotopic fuel tailoring. The open loop tritium fraction did not deviate from the reference value. Finally, Figure 2.14 shows the initial, final (t=50s), and reference profiles of the states n_α, E, n_D, and n_T from the closed loop simulation, showing that, for the simple one-dimensional model used in this work, the profiles tended toward the reference magnitude and shape.

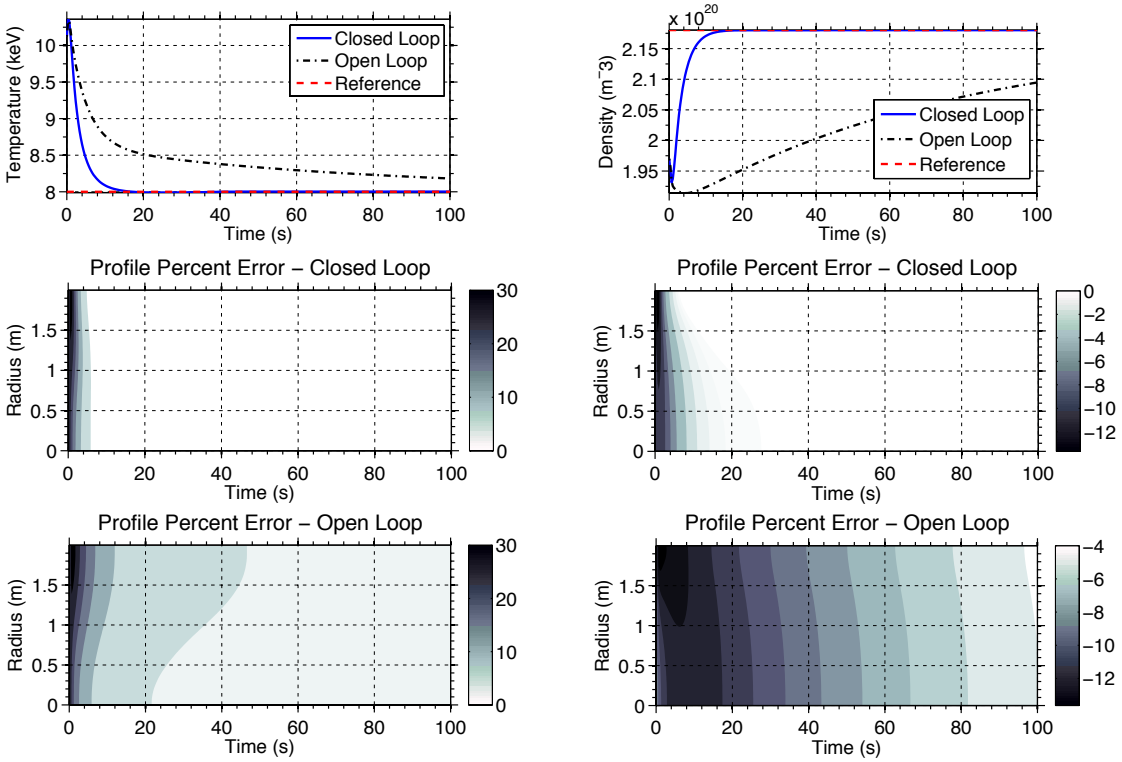

Figure 2.11: Comparison of closed loop, open loop, and reference volume averages of (a) temperature and (b) plasma density, along with contour plots depicting the closed loop and open loop spatiotemporal evolution of the percent error of each quantity.

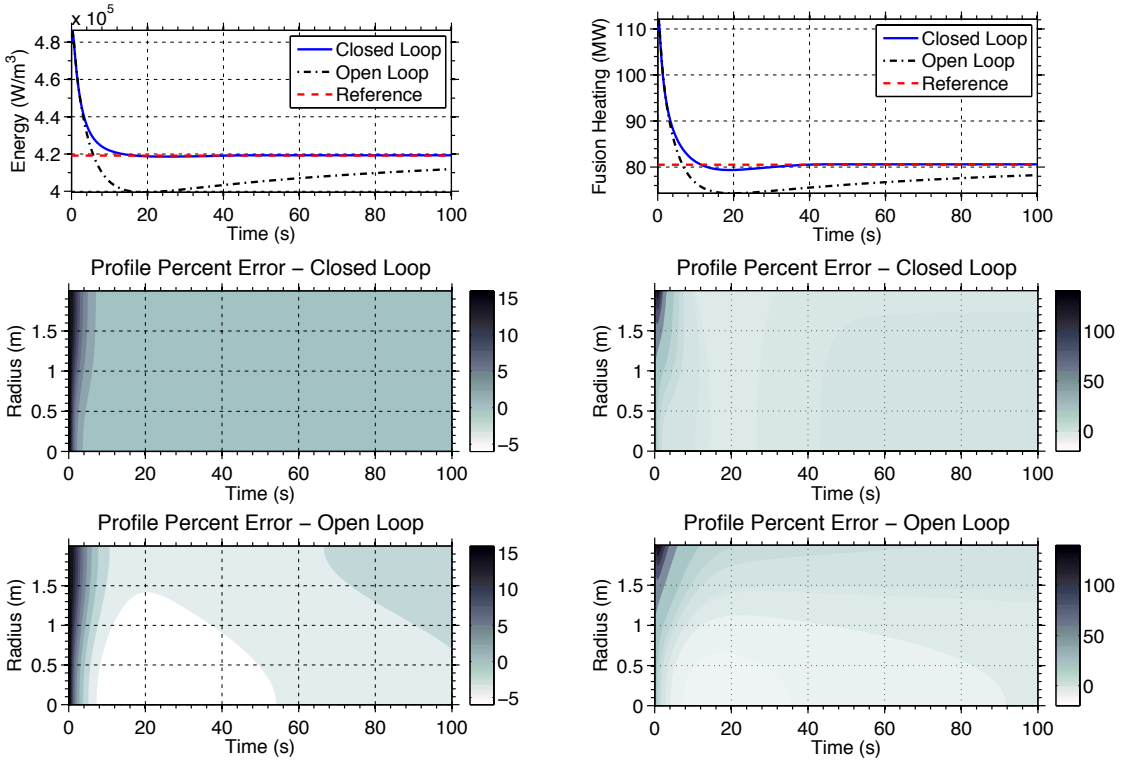

Figure 2.12: Comparison of closed loop, open loop, and reference volume averages of (a) energy and (b) fusion heating, along with contour plots depicting the closed loop and open loop spatiotemporal evolution of the percent error of each quantity.

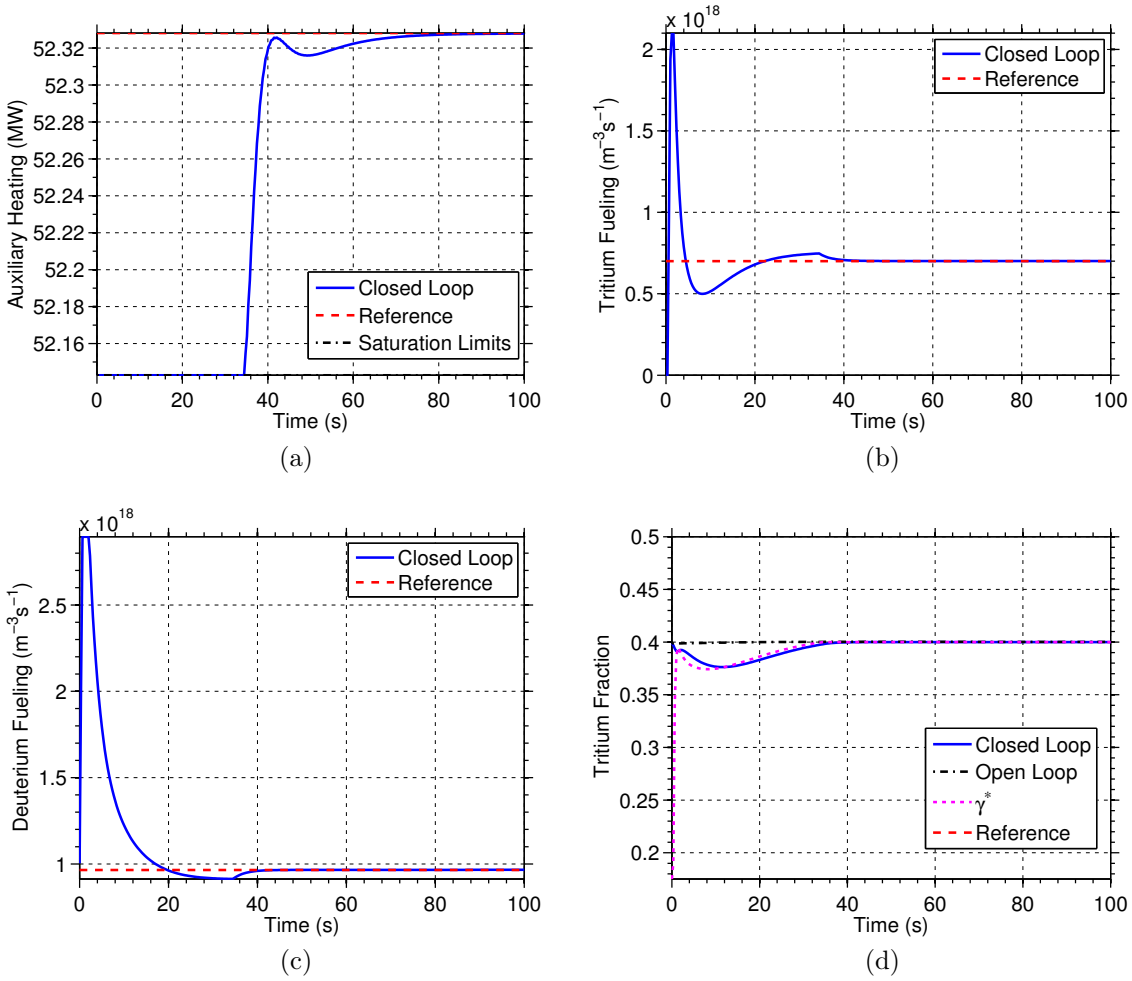

Figure 2.13: Closed loop and open loop (a) heating P_{aux}, (b) tritium fueling S_T, (c) deuterium fueling S_D, and (d) a comparison of the tritium fraction reference, closed loop and open loop results, and γ^* during the second simulation scenario.

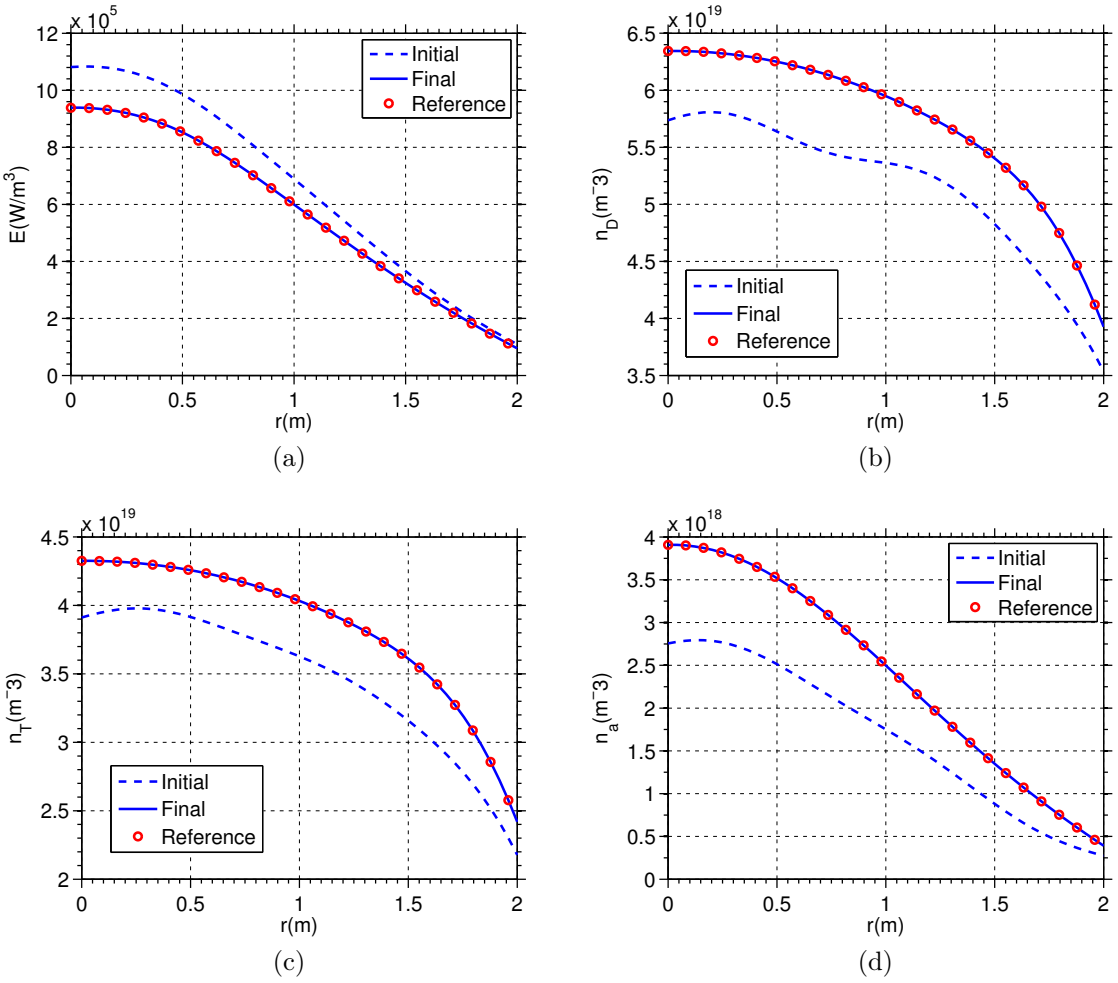

Figure 2.14: Initial, final (t=50s), and reference profiles for the one-dimensional closed loop simulation.

2.7 Conclusions

We have presented a nonlinear burn stability controller capable of rejected perturbations in the energy and ion species densities. By avoiding linearization, the controller can deal with a larger set of perturbations than previous linear controllers and the simultaneous use of multiple actuation techniques allows for the rejection of perturbations that lead to either thermal excursions or quenching. The nonlinear control law depends parametrically on the operating point, so it can be used to drive the system between different operating points. This allows for online adjustment of the power or other plasma parameters, or for transition from sub-ignition to ignition. No scheduled controllers are necessary because the control law is not designed around a particular operating point.

The deuterium and tritium ion densities are accounted for separately, allowing for control of the isotopic fuel mix within the plasma. This will be important for maintaining the desired fuel mix within the plasma core despite difference in confinement properties between the species. The isotopic fueling capability is exploited by the control scheme to help reject perturbations in the temperature when the control law for the heating reaches saturation limits. This extends the operating space of the control scheme and can help to avoid the need for impurity injection during positive temperature perturbations. We include impurity injection in the proposed scheme as a back-up actuator to handle more severe excursions.

A zero-dimensional simulation study was carried out to test the performance of the proposed control scheme. Scenarios studied included moving between various operating points, some of which were characterized by a required heating power very near the minimum power limit imposed in the scenario. Results using two different confinement scalings were shown, and the controller was shown to be capable of

stabilizing unstable points and improving the performance of the system for stable operating points. A study of the effectiveness of isotopic mix based control of the energy for a range of recycling model parameters was also presented. The study showed that the use of isotopic fueling for burn condition control purposes is most promising for low values of f_{eff} and relatively low values of R_{eff}. Such favorable conditions could be realized with appropriate divertor design and active pumping capabilities. For unfavorable recycling parameters, it is found that isotopic mix control may be too slow to be used to reject thermal excursions (due to the much faster time scale of the energy subsystem). In such cases, isotopic mix control may still be quite useful for slower time scale modulation of the burn condition and impurity injection may be necessary to reject thermal excursions. A one-dimensional simulation study was also presented to show controller performance when plasma parameters vary in space, as they would in a real tokamak. Though a very simplified one-dimensional model was used, the success of the zero-dimensional control law on the one-dimensional model is promising and motivates further testing on more sophisticated predictive codes.

It should be noted that the approach taken in this work is not restricted to the particular confinement scaling and machine parameters used here. The control design could be used in other fusion reactors with isotopic fueling capability. While many of the parameters used in the control law are either measured or well-known, some parameters, like recycling parameters are uncertain. The selection of the controller gains K_E, K_n, K_γ, and K_I, is a trade-off between the robustness of the scheme to these uncertainties and the sensitivity of the controller to noise. In order to handle the the uncertainties in a parametric way, a nonlinear adaptive control law will be synthesized. A real-time algorithm for updating the choice of operating point parameters $\bar{E}$, $\bar{n}$, and $\bar{\gamma}$ in response to changes in impurity content or confinement parameters will also be included. The optimization algorithm will be used to improve upon the response

of parameters like the fusion power and the divertor heat load, while maintaining the stability properties of the controller proposed in this work.

Chapter 3

Adaptive Nonlinear Burn Control and Online Optimization

3.1 Introduction

In the previous chapter, a nonlinear multi-input-multi-output burn control strategy capable of handling actuator saturation through the use of isotopic fueling and impurity injection was proposed. It was shown that the nonlinear controller could stabilize unstable equilibria, even in the presence of actuator saturation. A model of particle recycling was included in the burning plasma model to study the effectiveness of the proposed isotopic fueling under different recycling conditions. Despite the advantages of the proposed scheme over linear approaches, the design relies on complete knowledge of the parameters of the burning plasma model. While many of the necessary parameters are either measured or can be calculated based on first-principles equations or scaling laws, some parameters will be, in practice, uncertain or unknown. In order to handle the model uncertainty, a nonlinear adaptive control scheme is proposed in this chapter. The resulting nonlinear adaptive control scheme ensures that

the desired burn condition is still asymptotically stable despite model uncertainty.

Adaptive control design seeks to combine a control law with an online parameter estimator in order to control systems that have uncertain (or possibly time-varying) parameters. As the parameter estimates converge to the true values, the performance of the controller tends to that of a controller based on known parameters [47]. Typically, in adaptive control for linear systems, the *certainty equivalence* design approach is used, i.e., the uncertain parameters are assumed to be known to design a parameterized controller. This achieves a level of modularity, allowing any stabilizing controller design to be paired with any parameter estimation approach. For nonlinear systems, the weakness of *certainty equivalence* based control laws can allow the states of the uncertain system to become unbounded under certain conditions. Through the use of design tools like nonlinear damping in the control law, a system can be made input-to-state stable with respect to the parameter estimation error, i.e., the states remain bounded given a bounded parameter estimation error [48]. This property enables the use of modular designs, i.e., the nonlinear controller can be paired with any kind of estimator, so long as it guarantees bounded estimation errors.

While the nonlinear adaptive control scheme proposed in this chapter will drive the burn condition to the desired reference (defined by the energy, density, and tritium fraction), the model uncertainty may lead to differences between the resulting outputs, like fusion power or divertor heat load, and those predicted by the model. For example, differences in impurity or alpha particle confinement could alter radiation losses and DT fuel content in the plasma at the reference values of E, n, and γ. With large enough parameter changes, the outputs for a given reference could differ significantly from the predicted values, making it difficult to choose the controller references prior to a discharge. To overcome this issue, an online optimization scheme, similar to the general approach proposed in [49, 50] is used to alter the controller references

in real-time to minimize a cost function related to the desired reactor performance.

The chapter is organized as follows. The uncertain parametric burning plasma model used for design is given in Section 3.2. In Section 3.3, the adaptive nonlinear control design is presented, and in Section 3.4 an online optimization scheme is presented. Section 3.5 shows the results of a simulation study of the adaptive scheme alone, while simulations of the optimization scheme are presented in Section 3.6. Finally, conclusions are discussed in Section 3.7.

3.2 Uncertain Parametric Model

The burning plasma model described in Chapter 2 is again used for controller design. In practice, many of the parameters of the model may be uncertain and the control algorithm must make use of estimated model parameters. We will utilize an adaptive control approach to ensure reference tracking despite the model uncertainty. To facilitate the adaptive control design, we lump the uncertain parameters together to write the model as

$$\dot{n}_\alpha = -\theta_1 \frac{n_\alpha}{\tau_E^{sc}} + S_\alpha, \tag{3.1}$$

$$\dot{E} = -\theta_2 \frac{E}{\tau_E^{sc}} + P_\alpha - P_{rad} + P_{aux} + P_{Ohm}, \tag{3.2}$$

$$\dot{n}_I = -\theta_7 \frac{n_I}{\tau_E^{sc}} + S_I^{inj} + S_I^{sp}, \tag{3.3}$$

$$\dot{n}_D = -\theta_3 \frac{n_D}{\tau_E^{sc}} + \theta_4 \frac{n_T}{\tau_E^{sc}} - S_\alpha + S_D^{inj}, \tag{3.4}$$

$$\dot{n}_T = \theta_5 \frac{n_D}{\tau_E^{sc}} - \theta_6 \frac{n_T}{\tau_E^{sc}} - S_\alpha + S_T^{inj}, \tag{3.5}$$

where τ_E^{sc} is the energy confinement time predicted by the confinement scaling law, i.e.,

$$\tau_E^{sc} = 0.0562 I_p^{0.93} B_T^{0.15} P^{-0.69} n_{e19}^{0.41} M^{0.19} R^{1.97} \epsilon^{0.58} \kappa_{95}^{0.78},$$

and the uncertain parameters $\theta = [\theta_1, \theta_2, \ldots, \theta_7]$ are given by

$$\begin{aligned}
\theta_1 =& \frac{1}{k_\alpha^* H_H}, \\
\theta_2 =& \frac{1}{H_H}, \\
\theta_3 =& \frac{1}{k_D H_H} - \frac{f_{eff}}{k_D H_H \left[1 - f_{ref}\left(1 - f_{eff}\right)\right]} \left\{ f_{ref} \right. \\
& \left. + \left(1 - \gamma^{PFC}\right) \left[\frac{\left(1 - f_{ref}\left(1 - f_{eff}\right)\right) R^{eff}}{1 - R^{eff}\left(1 - f_{eff}\right)} - f_{ref} \right] \right\}, \\
\theta_4 =& \frac{f_{eff}\left(1 - \gamma^{PFC}\right)}{k_T H_H \left[1 - f_{ref}\left(1 - f_{eff}\right)\right]} \times \\
& \left[\frac{\left(1 - f_{ref}\left(1 - f_{eff}\right)\right) R^{eff}}{1 - R^{eff}\left(1 - f_{eff}\right)} - f_{ref} \right], \\
\theta_5 =& \frac{f_{eff}\gamma^{PFC}}{k_D H_H \left[1 - f_{ref}\left(1 - f_{eff}\right)\right]} \times \\
& \left[\frac{\left(1 - f_{ref}\left(1 - f_{eff}\right)\right) R^{eff}}{1 - R^{eff}\left(1 - f_{eff}\right)} - f_{ref} \right], \\
\theta_6 =& \frac{1}{k_T H_H} - \frac{f_{eff}}{k_T H_H \left[1 - f_{ref}\left(1 - f_{eff}\right)\right]} \times \\
& \left\{ f_{ref} + \gamma^{PFC} \left[\frac{\left(1 - f_{ref}\left(1 - f_{eff}\right)\right) R^{eff}}{1 - R^{eff}\left(1 - f_{eff}\right)} - f_{ref} \right] \right\}, \\
\theta_7 =& \frac{1}{k_I^* H_H}.
\end{aligned}$$

Using these expressions, the equations (2.25) and (2.26) can be written in the form

$$\begin{aligned}\dot{n} =& 2\left[(\theta_5-\theta_3)\frac{n_D}{\tau_E^{sc}}+(\theta_4-\theta_6)\frac{n_T}{\tau_E^{sc}}-2S_\alpha+S_D^{inj}+S_T^{inj}\right]\\ &+3\left[-\theta_1\frac{n_\alpha}{\tau_E^{sc}}+S_\alpha\right]+(Z_I+1)\left[-\theta_7\frac{n_I}{\tau_E^{sc}}+S_I^{inj}+S_I^{sp}\right], \qquad (3.6)\\ \dot{\gamma} =& \frac{1}{n_{DT}}\left\{\theta_5\frac{n_D}{\tau_E^{sc}}-\theta_6\frac{n_T}{\tau_E^{sc}}-S_\alpha+S_T^{inj}\right.\\ &\left.-\gamma\left[(\theta_5-\theta_3)\frac{n_D}{\tau_E^{sc}}+(\theta_4-\theta_6)\frac{n_T}{\tau_E^{sc}}-2S_\alpha+S_D^{inj}+S_T^{inj}\right]\right\}. \qquad (3.7)\end{aligned}$$

We consider the model parameters to be bounded, i.e.,

$$\begin{aligned} 2 \le k_\alpha \le 10, \qquad & 0.1 \le f_{eff} \le 0.5,\\ 2 \le k_D \le 5, \qquad & 0.2 \le f_{ref} \le 0.9,\\ 2 \le k_T \le 5, \qquad & 0.8 \le R_{eff} \le 0.95,\\ 2 \le k_I \le 10, \qquad & 0.1 \le \gamma^{PFC} \le 0.5,\\ .75 \le H_H \le 1.25. & \end{aligned}$$

Note that, although the existence of bounds is necessary for the stability analysis, the control design is not dependent on the particular values of the bounds. The above bounds are only considered for the purpose of simulation. With these constraints, we can determine bounds on the uncertain parameters. For the limits considered in this

work, the uncertain parameters lie within the bounds

$$\begin{aligned} 0.08 \leq \theta_1 \leq 0.6, \qquad & 0 \leq \theta_5 \leq 0.2647, \\ 0.75 \leq \theta_2 \leq 1.25, \qquad & 0.0222 \leq \theta_6 \leq 0.6330, \\ 0.0175 \leq \theta_3 \leq 0.5633, \qquad & 0.08 \leq \theta_7 \leq 0.6, \\ 0 \leq \theta_4 \leq 0.4765. & \end{aligned}$$

These bounds were established by using the constrained nonlinear minimization function *fmincon* in MatLab. In addition to the above model parameter constraints, θ_4 and θ_5 were restricted to being positive semi-definite to ensure that the desorbed flux from the plasma facing components, S^{PFC}, is always positive semi-definite. For the range of model parameters considered, it is always the case that $\theta_3 > \theta_5$, $\theta_6 > \theta_4$, and the eigenvalues of the matrix $\begin{bmatrix} \theta_3 & \theta_4 \\ \theta_5 & \theta_6 \end{bmatrix}$ are positive definite. We can exploit our knowledge of parameter bounds in our estimation strategy by projecting the estimated parameters generated by the adaptive laws onto the subspace of possible parameter values.

We can write the dynamics of the error variables $\tilde{E} = E - E^r$, $\tilde{n} = n - n^r$, and $\tilde{\gamma} = \gamma - \gamma^r$ as

$$\dot{\tilde{E}} = -\theta_2 \frac{\tilde{E}}{\tau_E^{sc}} - \theta_2 \frac{E^r}{\tau_E^{sc}} + P_\alpha - P_{rad} + P_{Ohm} + P_{aux} - \dot{E}^r, \tag{3.8}$$

$$\dot{\tilde{\gamma}} = -\theta_6 \frac{\tilde{\gamma}}{\tau_E^{sc}} + \frac{2\left[u(\gamma^r) + (1-\gamma)\, S_T^{inj} - \gamma S_D^{inj}\right]}{n - 3n_\alpha - (Z_I + 1)\, n_I}, \tag{3.9}$$

$$\dot{\tilde{n}} = -\tilde{n}\left[-\left(\theta_5 - \theta_3\right)\frac{(1-\gamma)}{\tau_E^{sc}} - \left(\theta_4 - \theta_6\right)\frac{\gamma}{\tau_E^{sc}}\right] \tag{3.10}$$

$$+ v - \dot{n}^r + 2\left(S_D^{inj} + S_T^{inj}\right), \tag{3.11}$$

where

$$u(\gamma^r) = \frac{n-3n_\alpha-(Z_I+1)\,n_I}{2}\left[\theta_5\frac{(1-\gamma)}{\tau_E^{sc}} - \theta_6\frac{\gamma^r}{\tau_E^{sc}} - \dot{\gamma}^r \right.$$
$$\left. - (\theta_5-\theta_3)\,\frac{(\gamma-\gamma^2)}{\tau_E^{sc}} - (\theta_4-\theta_6)\,\frac{\gamma^2}{\tau_E^{sc}}\right] + (2\gamma-1)\,S_\alpha, \tag{3.12}$$

$$v = [-n^r + 3n_\alpha + (Z_I+1)\,n_I]\left[-(\theta_5-\theta_3)\,\frac{(1-\gamma)}{\tau_E^{sc}}\right.$$
$$\left. - (\theta_4-\theta_6)\,\frac{\gamma}{\tau_E^{sc}}\right] - 4S_\alpha + 3\left[-\theta_1\frac{n_\alpha}{\tau_E^{sc}} + S_\alpha\right]$$
$$+ (Z_I+1)\left[-\theta_7\frac{n_I}{\tau_E^{sc}} + S_I^{inj} + S_I^{sp}\right]. \tag{3.13}$$

The objective of the controller designed in the following section is to ensure the stability of the origin for this dynamic system.

3.3 Controller Design

3.3.1 Nominal Control Design

We first consider the design of a nominal controller, i.e., we assume the uncertain parameters are exactly known. In the subsequent sections, the design will be augmented to ensure stability and regulation despite model uncertainties. We begin the nominal controller design by looking at the energy subsystem (3.8). We note that $\tilde{E}$ can be driven to zero by satisfying the condition

$$f(n,E,n_\alpha,n_I,\gamma) = -\theta_2\frac{E^r}{\tau_E^{sc}} + P_{Ohm} + P_\alpha - P_{rad} + P_{aux} - \dot{E}^r + K_E\tilde{E} = 0. \tag{3.14}$$

The condition (3.14) can be satisfied in several different ways. The auxiliary heating term P_{aux} enters the equation directly, the actuators S_D^{inj} and S_T^{inj} can be used to change the α-heating term P_α by modulating the tritium fraction, and the impurity

injection term S_I^{inj} can be used to increase the impurity content and consequently P_{rad}. Having several methods available for controlling the energy subsystem enables us to design a control scheme that can still achieve stabilization despite saturation of one or even several of the available actuators.

Step 1: We first calculate the P_{aux} as

$$P_{aux}^{unsat} = \theta \frac{E^r}{\tau_E^{sc}} - Q_\alpha \gamma^r (1-\gamma^r)\, n_{DT}^2 \langle \sigma v \rangle + P_{rad} - P_{Ohm} + \dot{E}^r - K_E \tilde{E}, \tag{3.15}$$

$$P_{aux} = \text{sat}\left(\frac{P_{aux}^{unsat} - P_{aux}^{min}}{P_{aux}^{max} - P_{aux}^{min}} \right), \tag{3.16}$$

where the limit P_{aux}^{max} depends on the installed power on the tokamak and the limit $P_{aux}^{min} \geq 0$ depends on the operating scenario. For example, some minimum amount of power may be needed to maintain the required amount of non-inductive current drive during a particular discharge since some sources of power (neutral beam injection, electron-cyclotron current drive, etc.) double as sources of plasma current.

Step 2: We next find a trajectory γ^* satisfying (3.14), i.e.,

$$Q_\alpha \gamma^* (1-\gamma^*)\, n_{DT}^2 \langle \sigma \nu \rangle = P_{rad} - P_{Ohm} - P_{aux} + \theta_2 \frac{E^r}{\tau_E^{sc}} + \dot{E}^r - K_E \tilde{E}, \tag{3.17}$$

Solving this equation yields

$$\gamma^* (1-\gamma^*) = \frac{1}{Q_\alpha n_{DT}^2 \langle \sigma \nu \rangle} \left[\theta_2 \frac{E^r}{\tau_E^{sc}} + P_{rad} - P_{Ohm} - P_{aux} + \dot{E}^r - K_E \tilde{E} \right] = C, \tag{3.18}$$

$$\gamma^* = \frac{1 \pm \sqrt{1-4C}}{2}. \tag{3.19}$$

Note that, if the value of P_{aux} calculated in Step 1 is not saturated, then $\gamma^* = \gamma^r$. This can be shown by substituting (3.15) into (3.17). If $C \leq 0.25$, the two resulting solutions for γ^* are real and we take the tritium-lean solution, such that $\gamma^* \leq 0.5$. If

$C \geq 0.25$, even the optimal isotopic mix and maximum value of auxiliary heating will not generate enough heating to satisfy $f = 0$, indicating that the requested operating point may not be achievable for the amount of auxiliary heating power installed on the device. Barring this situation, based on our choice of P_{aux} and γ^*, we have that

$$f\left(n, E, n_\alpha, n_I, \gamma^*\right) = 0. \tag{3.20}$$

This allows us to write $f = \hat{\gamma}\phi_\gamma$ where $\hat{\gamma} = \gamma - \gamma^*$ and ϕ_γ is a continuous function. Noting (3.8), (3.14), we can then write the dynamics of the energy perturbation as

$$\dot{\tilde{E}} = -\theta_2 \frac{\tilde{E}}{\tau_E^{sc}} - K_E \tilde{E} + \hat{\gamma}\phi_\gamma, \tag{3.21}$$

and the dynamics of $\hat{\gamma}$ can be written as

$$\dot{\hat{\gamma}} = -\theta_6 \frac{\hat{\gamma}}{\tau_E^{sc}} + \frac{2\left[u(\gamma^*) + (1-\gamma)\, S_T^{inj} - \gamma S_D^{inj}\right]}{n - 3n_\alpha - (Z_I + 1)\, n_I}. \tag{3.22}$$

Step 3: Having selected P_{aux} and γ^* in the previous steps, we must next choose S_D^{inj} and S_T^{inj} to ensure that $\tilde{E}$, $\hat{\gamma}$, and $\tilde{n}$, which are governed by (3.21), (3.22), and (3.11), are driven to zero. We consider the Lyapunov function $V_0 = V_n + V_{E,\gamma}$ where $V_n = \frac{1}{2}\tilde{n}^2$ and $V_{E,\gamma} = \frac{1}{2}k_1\tilde{E}^2 + \frac{1}{2}\hat{\gamma}^2$. It can be shown that satisfying the conditions

$$2\left(S_T^{inj} + S_D^{inj}\right) = -\upsilon - K_n\tilde{n} + \dot{n}^r, \tag{3.23}$$

$$\begin{aligned}(1-\gamma)\, S_T^{inj} - \gamma S_D^{inj} = &-\frac{n - 3n_\alpha - (Z_I+1)\, n_I}{2} \\ &\times \left(k_1\tilde{E}\phi_\gamma + K_\gamma\hat{\gamma}\right) - u(\gamma^*),\end{aligned} \tag{3.24}$$

where $K_n > 0$ and $K_\gamma > 0$ results in

$$\dot{V}_n = -\tilde{n}^2 \left(-\left(\theta_5 - \theta_3\right) \frac{\left(1-\gamma\right)}{\tau_E^{sc}} - \left(\theta_4 - \theta_6\right) \frac{\gamma}{\tau_E^{sc}} + K_n \right) < 0, \tag{3.25}$$

$$\dot{V}_{E,\gamma} = -k_1 \theta_2 \frac{\tilde{E}^2}{\tau_E^{sc}} - k_1 K_E \tilde{E}^2 - \left(\frac{1}{\tau_T} + K_\gamma \right) \hat{\gamma}^2 < 0, \tag{3.26}$$

such that $\dot{V}_0 < 0$, guaranteeing asymptotic stability of the system. The conditions (3.23) and (3.24) can be satisfied by choosing

$$\begin{aligned} S_D^{inj} = & \frac{n - 3n_\alpha - \left(Z_I + 1\right) n_I}{2} \left(k_1 \tilde{E} \phi_\gamma + K_\gamma \hat{\gamma} \right) \\ & + u(\gamma^*) + \left(1 - \gamma\right) \left(\frac{-v - K_n \tilde{n} + \dot{n}^r}{2} \right), \end{aligned} \tag{3.27}$$

$$S_T^{inj} = \left(\frac{-v - K_n \tilde{n} + \dot{n}^r}{2} \right) - S_D^{inj}. \tag{3.28}$$

These values are subject to the constraints $0 \leq S_D^{inj} \leq S_D^{inj,max}$ and $0 \leq S_T^{inj} \leq S_T^{inj,max}$. If one of the fueling actuators saturates, we cannot satisfy both conditions of the control law, so we must choose to either control n or γ. If we choose to hold condition (3.24), the energy and tritium fraction subsystems will remain stable, however, the density subsystem will no longer be controlled. This could potentially lead to a violation of the density limit. To avoid this, we instead choose to maintain control of the density by satisfying (3.23).

Because of fueling actuator saturation, it may be possible that $\dot{V}_{E,\gamma} > 0$, that is, we may not be able to ensure stability of the burn condition with the previously considered actuators. There are two possible situations to consider, either a thermal quench or an excursion. If the system is experiencing a quench, the controller has already increased auxiliary heating to its maximum, so the only alternative would be to change the magnetic plasma parameters to improve energy confinement (see (2.19)) or to change the reference operating point to one that is achievable. If the system

is experiencing a thermal excursion, however, we can still use impurity injection to stabilize the energy subsystem, despite the heating and fueling actuator saturation. In these cases we enable the use of impurity injection by setting the flag $F_{imp} = 1$ and proceeding to Step 4.

Step 4: If $F_{imp} = 1$, we use the expression for radiation losses given in (2.12) to find an impurity density trajectory n_I^* that satisfies condition (3.14). Defining the error $\hat{n}_I = n_I - n_I^*$, we can write its dynamics as

$$\dot{\hat{n}}_I = -\theta_7 \frac{\hat{n}_I}{\tau_E^{sc}} - \theta_7 \frac{n_I^*}{\tau_E^{sc}} + S_I^{inj} + S_I^{sp} - \dot{n}_I^*. \tag{3.29}$$

Based on the choice of n_I^*, we have that

$$f\left(n, E, n_\alpha, \gamma, n_I^*\right) \;\; = \;\; 0, \tag{3.30}$$

which allows us to write $f = \hat{n}_I \phi_I$ where ϕ_I is a continuous function. We can then rewrite (3.8) as

$$\dot{\tilde{E}} = -\theta_2 \frac{\tilde{E}}{\tau_E^{sc}} - K_E \tilde{E} + \hat{n}_I \phi_I. \tag{3.31}$$

We take as a Lyapunov function $V_1 = V_n + V_\gamma + V_{E,I}$ where $V_\gamma = \frac{1}{2}\hat{\gamma}^2$ and $V_{E,I} = \frac{1}{2}k_3\tilde{E}^2 + \frac{1}{2}\hat{n}_I^2$. By satisfying

$$S_I^{inj} = -k_3 \tilde{E} \phi_I + \theta_7 \frac{n_I^*}{\tau_E^{sc}} - S_I^{sp} + \dot{n}_I^* - K_I \hat{n}_I, \tag{3.32}$$

where $K_I > 0$, the derivative of $V_{E,I}$ can be reduced to

$$\dot{V}_{E,I} = -k_3\theta_2 \frac{\tilde{E}^2}{\tau_E^{sc}} - k_3 K_E \tilde{E}^2 - K_I \hat{n}_I^2 < 0. \tag{3.33}$$

We modify the tritium fraction trajectory to $\gamma^* = \gamma^*_{(\text{Step 2})} - K_S \int_{t_0}^{t} S_I^{inj} dt$ where

$\gamma^*_{(\text{Step 2})}$ is the value of γ^* calculated in Step 2, $K_S > 0$, and t_0 is the time at which impurity injection was first engaged. This modification ensures that the tritium fraction is, if possible, eventually reduced to such a level that impurity injection is no longer needed, i.e., $S_I^{inj} \to 0$. Once $S_I^{inj} = 0$, we disable impurity injection in subsequent executions of the algorithm by setting $F_{imp} = 0$. By satisfying

$$2\left(S_T^{inj} + S_D^{inj}\right) = -v - K_n\tilde{n}, \tag{3.34}$$

$$\begin{aligned}(1-\gamma)\, S_T^{inj} - \gamma S_D^{inj} = &-\frac{n - 3n_\alpha - (Z_I+1)\, n_I}{2} K_\gamma \hat{\gamma} \\ &- u(\gamma_I^*).\end{aligned} \tag{3.35}$$

We can ensure that $\dot{V}_n < 0$, $\dot{V}_\gamma < 0$, and therefore $\dot{V}_1 < 0$, guaranteeing stability of the system. The conditions (3.34) and (3.35) can be satisfied by choosing

$$\begin{aligned}S_D^{inj} = &\frac{n - 3n_\alpha - (Z_I+1)\, n_I}{2} K_\gamma \hat{\gamma} \\ &+ u(\gamma^*) + (1-\gamma)\left(\frac{-v - K_n\tilde{n}}{2}\right),\end{aligned} \tag{3.36}$$

$$S_T^{inj} = \left(\frac{-v - K_n\tilde{n}}{2}\right) - S_D^{inj}, \tag{3.37}$$

which are again subject to saturation. If one of the fueling actuators saturates, we again choose to hold (3.34) to ensure stability of the density.

3.3.2 ISS Controller for Uncertain Model

Having designed a nominal controller that stabilizes the system, we now consider the effects of uncertainty in the model parameters θ. In practice, the nominal controller must utilize estimated parameters $\hat{\theta} = \theta - \tilde{\theta}$, where $\hat{\theta} = \left[\hat{\theta}_1, \hat{\theta}_2, \hat{\theta}_3, \hat{\theta}_4, \hat{\theta}_5, \hat{\theta}_6, \hat{\theta}_7\right]^T$ and $\tilde{\theta} = \left[\tilde{\theta}_1, \tilde{\theta}_2, \tilde{\theta}_3, \tilde{\theta}_4, \tilde{\theta}_5, \tilde{\theta}_6, \tilde{\theta}_7\right]^T$ is the estimation error. Knowing *a priori* bounds on

θ allows us to restrict our estimates to within these bounds, guaranteeing that the estimation error will have a known bound. In this section, we show that the closed loop system can be rendered input-to-state-stable (ISS) [51] with respect to the estimation errors. We exploit this fact in the design of adaptive parameter estimation update laws in the sequel.

We begin by considering the results of Step 3. The control laws are calculated using estimated model parameters, which, upon substitution, results in

$$\begin{aligned}\dot{V}_n =& \tilde{n}^2 \left[(\theta_5 - \theta_3) \frac{(1-\gamma)}{\tau_E^{sc}} + (\theta_4 - \theta_6) \frac{\gamma}{\tau_E^{sc}} - K_n \right] \\ &+ \tilde{n}\tilde{v}, \end{aligned} \tag{3.38}$$

$$\begin{aligned}\dot{V}_{E,\gamma} =& - k_1\theta_2 \frac{\tilde{E}^2}{\tau_E^{sc}} - k_1 K_E \tilde{E}^2 - k_1 \tilde{E} \left[\tilde{\theta}_2 \frac{E^r}{\tau_E^{sc}} \right] \\ &- \left(\frac{\theta_6}{\tau_E^{sc}} + K_\gamma \right) \hat{\gamma}^2 + \hat{\gamma}\tilde{u}, \end{aligned} \tag{3.39}$$

where

$$\begin{aligned}\tilde{u}(\gamma^r) =& \left[\tilde{\theta}_5 \frac{(1-\gamma)}{\tau_E^{sc}} - \tilde{\theta}_6 \frac{\gamma^r}{\tau_E^{sc}} - \left(\tilde{\theta}_5 - \tilde{\theta}_3 \right) \frac{(\gamma - \gamma^2)}{\tau_E^{sc}} \right. \\ &\left. - \left(\tilde{\theta}_4 - \tilde{\theta}_6 \right) \frac{\gamma^2}{\tau_E^{sc}} \right] \frac{n - 3n_\alpha - (Z_I+1)\, n_I}{2}, \end{aligned} \tag{3.40}$$

$$\begin{aligned}\tilde{v} =& \left[-n^r + 3n_\alpha + (Z_I+1)\, n_I \right] \left[- \left(\tilde{\theta}_5 - \tilde{\theta}_3 \right) \frac{(1-\gamma)}{\tau_E^{sc}} \right. \\ &\left. - \left(\tilde{\theta}_4 - \tilde{\theta}_6 \right) \frac{\gamma}{\tau_E^{sc}} \right] + 3 \left[-\tilde{\theta}_1 \frac{n_\alpha}{\tau_E^{sc}} \right] \\ &+ (Z_I + 1) \left[-\tilde{\theta}_7 \frac{n_I}{\tau_E^{sc}} \right]. \end{aligned} \tag{3.41}$$

We note that the uncertain terms are bounded, i.e.,

$$\begin{aligned}
|\tilde{v}| = \quad & 2 \quad n_{DT}\left[\left|\tilde{\theta}_5-\tilde{\theta}_3\right|\frac{(1-\gamma)}{\tau_E^{sc}}+\left|\tilde{\theta}_4-\tilde{\theta}_6\right|\frac{\gamma}{\tau_E^{sc}}\right] \\
& + \quad 3\left|\tilde{\theta}_1\right|\frac{n_\alpha}{\tau_E^{sc}}+(Z_I+1)\left|\tilde{\theta}_7\right|\frac{n_I}{\tau_E^{sc}} \\
& + \quad |\tilde{n}|\left[\left|\tilde{\theta}_5-\tilde{\theta}_3\right|\frac{(1-\gamma)}{\tau_E^{sc}}+\left|\tilde{\theta}_4-\tilde{\theta}_6\right|\frac{\gamma}{\tau_E^{sc}}\right] \\
\leq \quad & 2 \quad \left|\tilde{\theta}_{max}\right|\frac{n+|\tilde{n}|}{\tau_E^{sc}} \\
|\tilde{u}| \leq \quad & 4 \quad |\tilde{\theta}_{max}|\frac{n_{DT}}{\tau_E^{sc}},
\end{aligned}$$

If we choose $K_n = C_n\frac{n+|\tilde{n}|}{\tau_E^{sc}}$, $K_E = C_E\frac{E^r}{\tau_E^{sc}}$, and $K_\gamma = C_\gamma\frac{n_{DT}}{\tau_E^{sc}}$ where C_n , C_E, and C_γ are positive constants, it can then be shown that the negative definite term $-K_n\tilde{n}^2$ is guaranteed to dominate the indefinite term $\tilde{n}\tilde{v}$ whenever

$$|\tilde{n}| \geq 2\frac{\left|\tilde{\theta}_{max}\right|}{C_n}.$$

Furthermore, the indefinite terms $-k_1\tilde{E}\left[\tilde{\theta}_2\frac{E^r}{\tau_E^{sc}}\right]$ and $\hat{\gamma}\tilde{u}$ are dominated by $-k_1K_E\tilde{E}^2$ and $-K_\gamma\hat{\gamma}^2$, respectively, whenever conditions

$$\begin{aligned}
\left|\tilde{E}\right| \quad & \geq \quad \frac{\left|\tilde{\theta}_2\right|}{C_E}, \\
|\hat{\gamma}| \quad & \geq \quad \frac{4\left|\tilde{\theta}_{max}\right|}{C_\gamma},
\end{aligned}$$

are satisfied. This implies that the system is ISS with respect to the model uncertainty. A similar analysis can be completed for the results of Step 4.

3.3.3 Adaptive Parameter Update Laws

The use of a controller that renders the system ISS with respect to bounded uncertainties allows us to design an adaptive parameter estimation update law separately from the controller [48]. This simplifies the design and analysis, gives us freedom to choose from among the various types of adaptive laws that are available, and enables the incorporation of techniques that make the adaptive system robust to disturbances and unmodeled dynamics. In order to identify the uncertain parameters, we will construct an observer for the burning plasma system based on the estimated model parameters, and render the prediction error of this system asymptotically stable through choice of parameter update laws. We define the observer for the system as

$$
\begin{aligned}
\dot{n}_{\alpha}^{ob} =& -\hat{\theta}_1 \frac{n_{\alpha}}{\tau_E^{sc}} + S_{\alpha} - K_{\alpha}^{ob}\left(n_{\alpha}^{ob} - n_{\alpha}\right), \\
\dot{E}^{ob} =& -\hat{\theta}_2 \frac{E}{\tau_E^{sc}} + P_{\alpha} - P_{rad} \\
&+ P_{aux} + P_{Ohm} - K_E^{ob}\left(E^{ob} - E\right), \\
\dot{n}_I^{ob} =& -\hat{\theta}_7 \frac{n_I}{\tau_E^{sc}} + S_I^{inj} + S_I^{sp} - K_I^{ob}\left(n_I^{ob} - n_I\right), \\
\dot{n}_D^{ob} =& -\hat{\theta}_3 \frac{n_D}{\tau_E^{sc}} + \hat{\theta}_4 \frac{n_T}{\tau_E^{sc}} - S_{\alpha} + S_D^{inj} - K_D^{ob}\left(n_D^{ob} - n_D\right), \\
\dot{n}_T^{ob} =& \hat{\theta}_5 \frac{n_D}{\tau_E^{sc}} - \hat{\theta}_6 \frac{n_T}{\tau_E^{sc}} - S_{\alpha} + S_T^{inj} - K_T^{ob}\left(n_T^{ob} - n_T\right),
\end{aligned}
$$

where n_{α}^{ob}, E^{ob}, n_I^{ob}, n_D^{ob}, and n_T^{ob} are the states of the observer, $\hat{\theta}$ represents model parameter estimates, and K_{α}^{ob}, K_E^{ob}, K_I^{ob}, K_D^{ob}, and K_T^{ob} are observer gains. If we define the observer error $\tilde{n}_{\alpha}^{ob} = n_{\alpha}^{ob} - n_{\alpha}$, $\tilde{E}^{ob} = E^{ob} - E$, $\tilde{n}_I^{ob} = n_I^{ob} - n_I$, $\tilde{n}_D^{ob} = n_D^{ob} - n_D$, and

$\tilde{n}_T^{ob} = n_T^{ob} - n_T$, the dynamics of the error can be expressed as

$$\begin{aligned}
\dot{\tilde{n}}_\alpha^{ob} =& -\tilde{\theta}_1 \frac{n_\alpha}{\tau_E^{sc}} - K_\alpha^{ob} \tilde{n}_\alpha^{ob}, \\
\dot{\tilde{E}}^{ob} =& -\tilde{\theta}_2 \frac{E}{\tau_E^{sc}} - K_E^{ob} \tilde{E}^{ob}, \\
\dot{\tilde{n}}_I^{ob} =& -\tilde{\theta}_7 \frac{n_I}{\tau_E^{sc}} - K_I^{ob} \tilde{n}_I^{ob}, \\
\dot{\tilde{n}}_D^{ob} =& -\tilde{\theta}_3 \frac{n_D}{\tau_E^{sc}} + \tilde{\theta}_4 \frac{n_T}{\tau_E^{sc}} - K_D^{ob} \tilde{n}_D^{ob}, \\
\dot{\tilde{n}}_T^{ob} =& \tilde{\theta}_5 \frac{n_D}{\tau_E^{sc}} - \tilde{\theta}_6 \frac{n_T}{\tau_E^{sc}} - K_T^{ob} \tilde{n}_T^{ob}.
\end{aligned}$$

To study the stability of the system, we consider the Lyapunov function

$$\begin{aligned}
V^{ob} =& \frac{1}{2} \left(\tilde{n}_\alpha^{ob}\right)^2 + \frac{1}{2} \left(\tilde{E}^{ob}\right)^2 + \frac{1}{2} \left(\tilde{n}_I^{ob}\right)^2 \\
&+ \frac{1}{2} \left(\tilde{n}_D^{ob}\right)^2 + \frac{1}{2} \left(\tilde{n}_T^{ob}\right)^2 + \frac{1}{2} \tilde{\theta} \Gamma^{-1} \tilde{\theta},
\end{aligned}$$

where Γ is a positive definite diagonal matrix of design parameters, and calculate its derivative as

$$\begin{aligned}
\dot{V}^{ob} =& - K_\alpha^{ob} \left(\tilde{n}_\alpha^{ob}\right)^2 - K_E^{ob} \left(E^{ob}\right)^2 - K_I^{ob} \left(\tilde{n}_I^{ob}\right)^2 \\
&- K_D^{ob} \left(\tilde{n}_D^{ob}\right)^2 - K_T^{ob} \left(\tilde{n}_T^{ob}\right)^2 - \tilde{\theta}_1 \tilde{n}_\alpha^{ob} \frac{n_\alpha}{\tau_E^{sc}} - \tilde{\theta}_2 \tilde{E}^{ob} \frac{E}{\tau_E^{sc}} \\
&- \tilde{\theta}_7 \tilde{n}_I^{ob} \frac{n_I}{\tau_E^{sc}} - \tilde{\theta}_3 \tilde{n}_D^{ob} \frac{n_D}{\tau_E^{sc}} + \tilde{\theta}_4 \tilde{n}_D^{ob} \frac{n_T}{\tau_E^{sc}} + \tilde{\theta}_5 \tilde{n}_T^{ob} \frac{n_D}{\tau_E^{sc}} \\
&- \tilde{\theta}_6 \tilde{n}_T^{ob} \frac{n_T}{\tau_E^{sc}} + \tilde{\theta} \Gamma^{-1} \dot{\tilde{\theta}}.
\end{aligned}$$

We can render this expression negative definite by choosing the adaptive update laws

$$\dot{\hat{\theta}} = \frac{1}{\tau_E^{sc}}\Gamma \begin{bmatrix} \tilde{n}_\alpha^{ob} n_\alpha \\ \tilde{E}^{ob} E \\ \tilde{n}_D^{ob} n_D \\ -\tilde{n}_D^{ob} n_T \\ -\tilde{n}_T^{ob} n_D \\ \tilde{n}_T^{ob} n_T \\ \tilde{n}_I^{ob} n_I \end{bmatrix}.$$

3.3.4 Supervisory Control

Because small prediction errors corrupted by measurement noise have a very low signal to noise ratio, they contain inaccurate information that can negatively impact the online model identification process. In general, this can lead to phenomena such as parameter drift and bursting, potentially causing instabilities or performance degradation [47]. The problem can be avoided by using sufficiently exciting input signals that provide useful data to the model identification scheme at all times. However, to overcome the effect of noise, the amplitude of the reference modulation may need to be quite large, which could cause a reduction in closed loop performance.

An alternative approach is to utilize a supervisory scheme to monitor the performance of the adaptive update law. One such scheme, called a deadzone, switches the model identification scheme on or off based on the size of the model prediction error. If the prediction error is smaller than some specified threshold value (an *a priori* estimate of the unknown output disturbance), the signal-to-noise ratio is assumed to be too low for the information to be useful and identification is halted. Once the prediction error exceeds the threshold, identification is resumed. In the dual-model

approach [52], two parameter estimators are used, one generating θ_C, used in the controller, and another generating θ_S, used only by the supervisory scheme. The control parameters are only updated if the state prediction of the model using θ_C is worse than that of the model based on θ_S, with some prescribed threshold.

3.4 Online Operating Point Optimization

Since a given reference for the controlled states $r = [E^r, n^r, \gamma^r]^T$ determines the steady-state fusion power, temperature, and all other plasma parameters that may be of interest during operation, part of the burn control problem is the selection of r in such a way that a particular figure of merit for reactor performance is optimized. In this work, we consider a convex (at least locally) cost function $p(r, x, \hat{\theta})$ where $x = [n_\alpha, n_I]^T$. We assume the states of the system to be constrained within a region of parameter space over which the cost function is convex, guaranteeing a unique minimum.

Following an approach similar to the one used in [53, 49, 50], we take as a Lyapunov function

$$V_r = \frac{1}{2}\left(\frac{\partial p(r, x, \hat{\theta})}{\partial r}\right)^T \frac{\partial p(r, x, \hat{\theta})}{\partial r}. \tag{3.42}$$

By taking the time derivative of V_r, we obtain

$$\dot{V}_r = \left(\frac{\partial p}{\partial r}\right)^T \left[\frac{\partial^2 p}{\partial r^2}\dot{r} + \frac{\partial^2 p}{\partial r \partial x}\dot{x} + \frac{\partial^2 p}{\partial r \partial \hat{\theta}}\dot{\hat{\theta}}\right]. \tag{3.43}$$

We can then choose as an update law

$$\dot{r} = -\left(\frac{\partial^2 p}{\partial r^2}\right)^{-1} \left[K_{RTO}\frac{\partial p}{\partial r} + \frac{\partial^2 p}{\partial r \partial x}\dot{x} + \frac{\partial^2 p}{\partial r \partial \hat{\theta}}\dot{\hat{\theta}}\right], \tag{3.44}$$

where K_{RTO} is a diagonal positive definite matrix, leading to

$$\dot{V}_r \leq -\left(\frac{\partial p}{\partial r}\right)^T K_{RTO} \frac{\partial p}{\partial r}. \tag{3.45}$$

This implies that $\frac{\partial p}{\partial r} \to 0$ and, therefore, r is driven toward the optimal x-dependent and $\hat{\theta}$-dependent set point, r^*.

3.4.1 Constrained Optimization

It is important to include constraints in the optimization problem for several reasons. First, there are MHD stability limits that must be avoided, including the β limit and the Greenwald density limit. Violating these constraints could cause plasma disruptions and potentially damage the confinement vessel. Additionally, the optimized references should respect the physical limitations of the available actuators. If these limits are not considered, the optimization scheme may converge to a set of references that are not physically achievable and the burning plasma system will converge to a different (possibly far from optimal) operating point. By considering the limitations, the optimization scheme will converge to the optimal physically achievable reference. This approach could enable the control system to respond to actuator faults (e.g., loss of a beam) and find new optimal operating points. Finally, upper and lower bounds on the references can be included in the scheme to 'supervise' the optimization process and prevent unreasonable references from being selected. In order to include these constraints in the optimization scheme, they are first written in the form $g_i(E, n, \gamma, n_\alpha, n_I) \leq 0$, where $i \in (1, K)$ and K is the number of constraints. The interior point barrier function method to constrained optimization is used, i.e.,

an augmented cost function is written in the form

$$p_c = p - \frac{1}{\eta_c} \sum_{i=1}^{K} \ln(-g_i). \tag{3.46}$$

The optimization scheme must be initialized at a feasible point (one that does not violate the constraints), but is otherwise unchanged.

3.5 Simulation of Adaptive Control Scheme

3.5.1 Comparison of Static and Adaptive Controllers

In this section, the results of two closed loop simulations, one with $\Gamma = 0$, i.e without adaptation, and one with

$$\Gamma = \text{diag}(0.08\text{E-}36, 0.02\text{E-}10, 0.05\text{E-}38, 0.05\text{E-}38, 0.05\text{E-}38, 0.05\text{E-}38, 0.08\text{E-}36),$$

i.e., with adaptation, are compared. The simulations considered a nominal impurity content of $1 \times 10^{18} \#/\text{m}^3$, and the atomic number of the impurity species was taken to be $Z_I = 6$. The confinement scaling parameters were taken to be $H_H = 1.1$, $k_\alpha^* = k_D = k_T = 3$, and $k_I^* = 10$. We considered an installed ICRH power $P_{ICRH}^{max} = 20$ MW and a constant power from the current drive sources, $P_{cd} = 53$ MW. The recycling model parameters used were $\gamma^{PFC} = 0.5$, $f_{eff} = 0.3$, $f_{ref} = 0.5$, and $R^{eff} = 0.9$. During the adaptive simulation, the parameters $K_\alpha^{ob} = K_E^{ob} = K_D^{ob} = K_T^{ob} = K_I^{ob} = 0.03$ were used.

The results of the simulations are shown in Figure 3.1. While the static (non-adaptive) controller resulted in a steady-state error in the energy, density, and tritium fraction, as seen in Figures 3.1 (a-c), the adaptive simulation was able to achieve

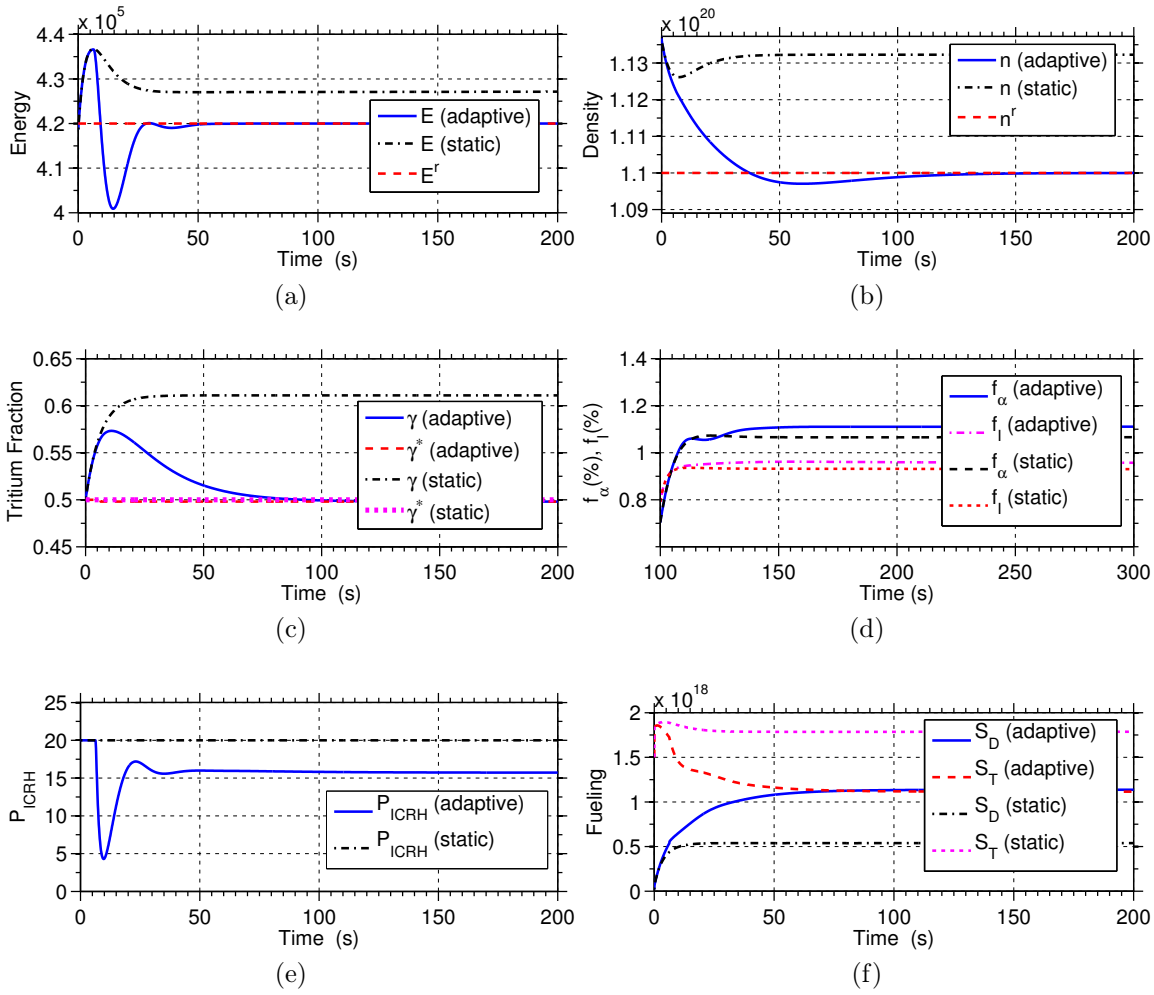

Figure 3.1: Comparison of states (a-d) and actuator trajectories (e,f) in static and adaptive control simulations.

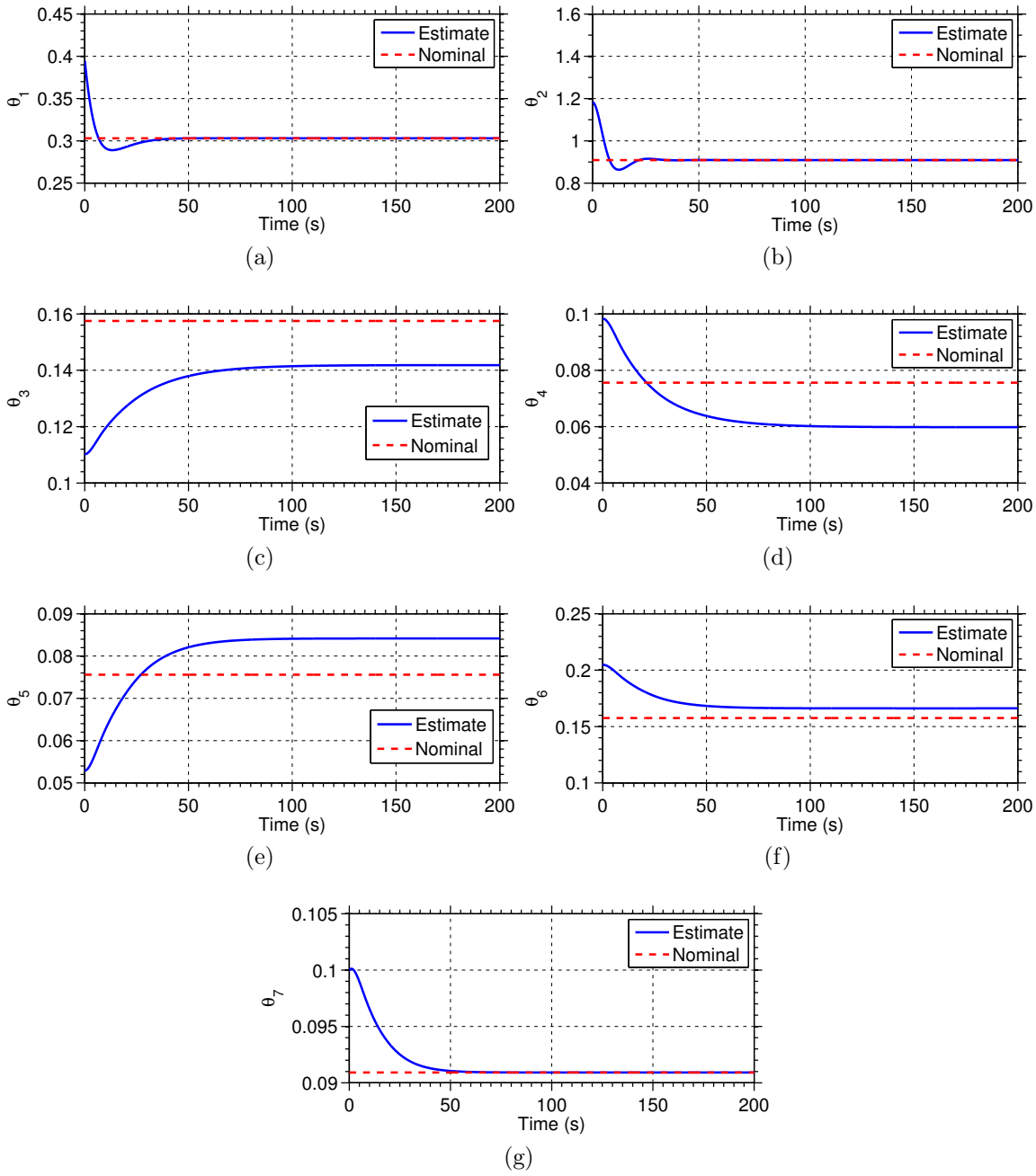

Figure 3.2: Comparison of estimated and nominal model parameters during the adaptive control simulation.

asymptotic stability of the desired equilibrium. Differences in the evolution of impurities and alpha-particles, as well as the actuator responses, are apparent in Figures 3.1 (d-f). The initial oscillations present during the adaptive simulation occur as the parameter estimator converges to constant estimates of the uncertain model parameters. The parameter estimates are compared with their respective nominal values in Figure 3.2. The transient response can be adjusted through choice of the design parameters.

3.5.2 Adaptive Control with Noisy Measurements

In this section, the same simulation scenario is considered, with the addition of white noise disturbances in the measurements sent to the adaptive controller. The variance of the noise was in the range of 5-10% of the nominal signal level for each measurement. The supervisory control strategy discussed in Section 3.3.4 was used during the simulation to supervise the parameter estimation.

Results of the simulation are shown in Figure 3.3. As shown in Figures 3.3a-d, the states of the system asymptotically track the references E^r, n^r, and γ^r, and the impurity and alpha-particle fractions settle to constant values within 100s. The noisy measurements cause the actuator signals, shown in Figures 3.3e and f to be noisy (since the measurements enter the control laws directly), however, the noise is attenuated by the plasma model, as made evident by the fairly noise-free evolution of states during the simulation. As it is possible that unmodeled dynamics could be excited by the high-frequency actuation, it is advisable to filter the measurements used by the controller in some way if high noise levels are expected. Time traces of the parameter estimates used by the controller (in blue) and those used by the supervisory strategy (denoted with an S and shown as black-dashed lines), are compared with the nominal model parameters in Figure 3.4. Due to the presence of noise, the parameters

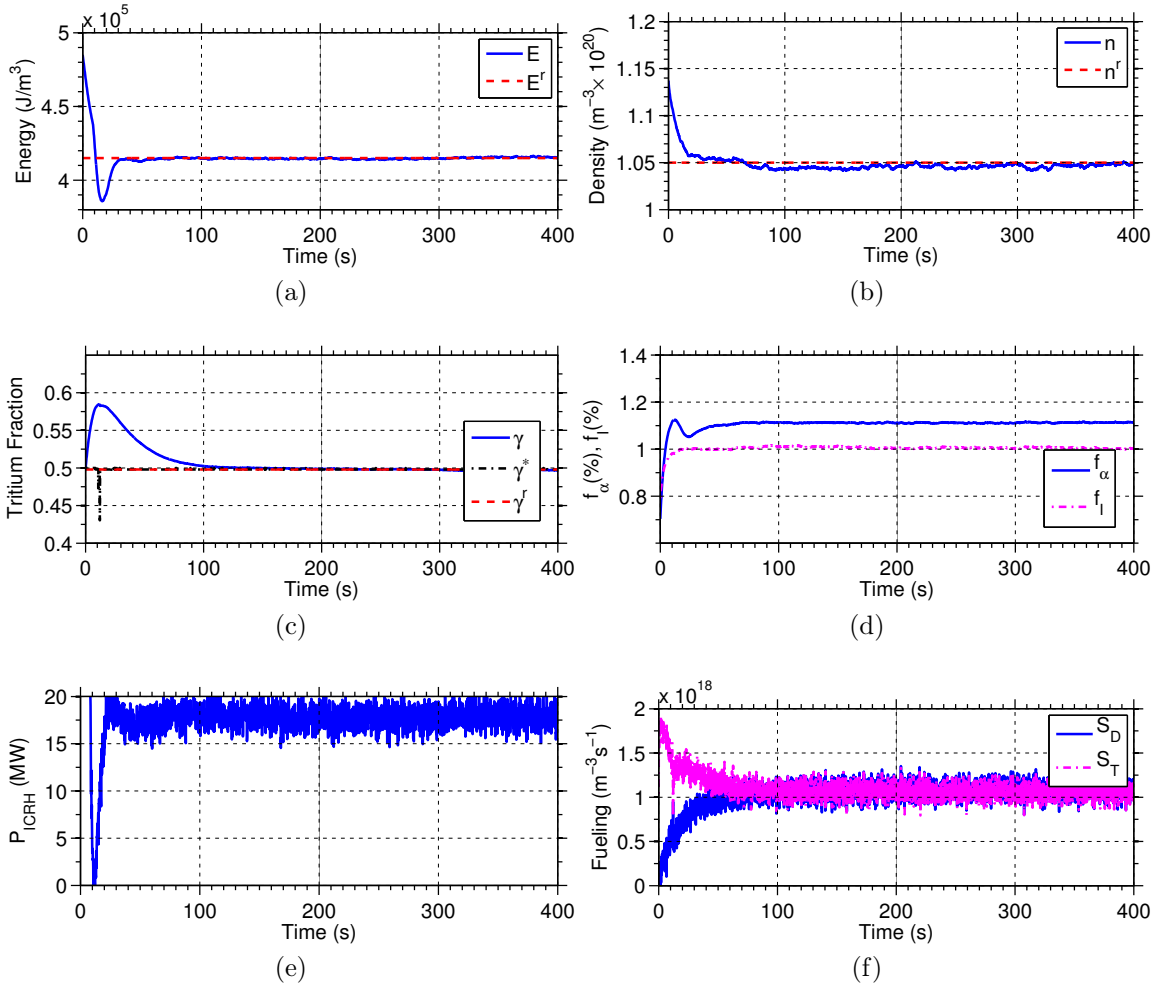

Figure 3.3: Comparison of states (a-d) and actuator trajectories (e,f) in the adaptive control simulation with noise.

θ_S are more noisy than the estimates in the previous noise-free simulation, and in the case of θ_3, θ_4, θ_5, and θ_6, begin to drift slowly over time. Through the use of the supervisory control strategy, the parameters used by the controller, $\hat{\theta}_C$, were only updated when the model prediction using $\hat{\theta}_C$ was 1.15 times worse than the model prediction by $\hat{\theta}_S$. As a result, the parameters $\hat{\theta}_C$ evolve more closely to the way the parameter estimates evolved in the previous noise-free simulation.

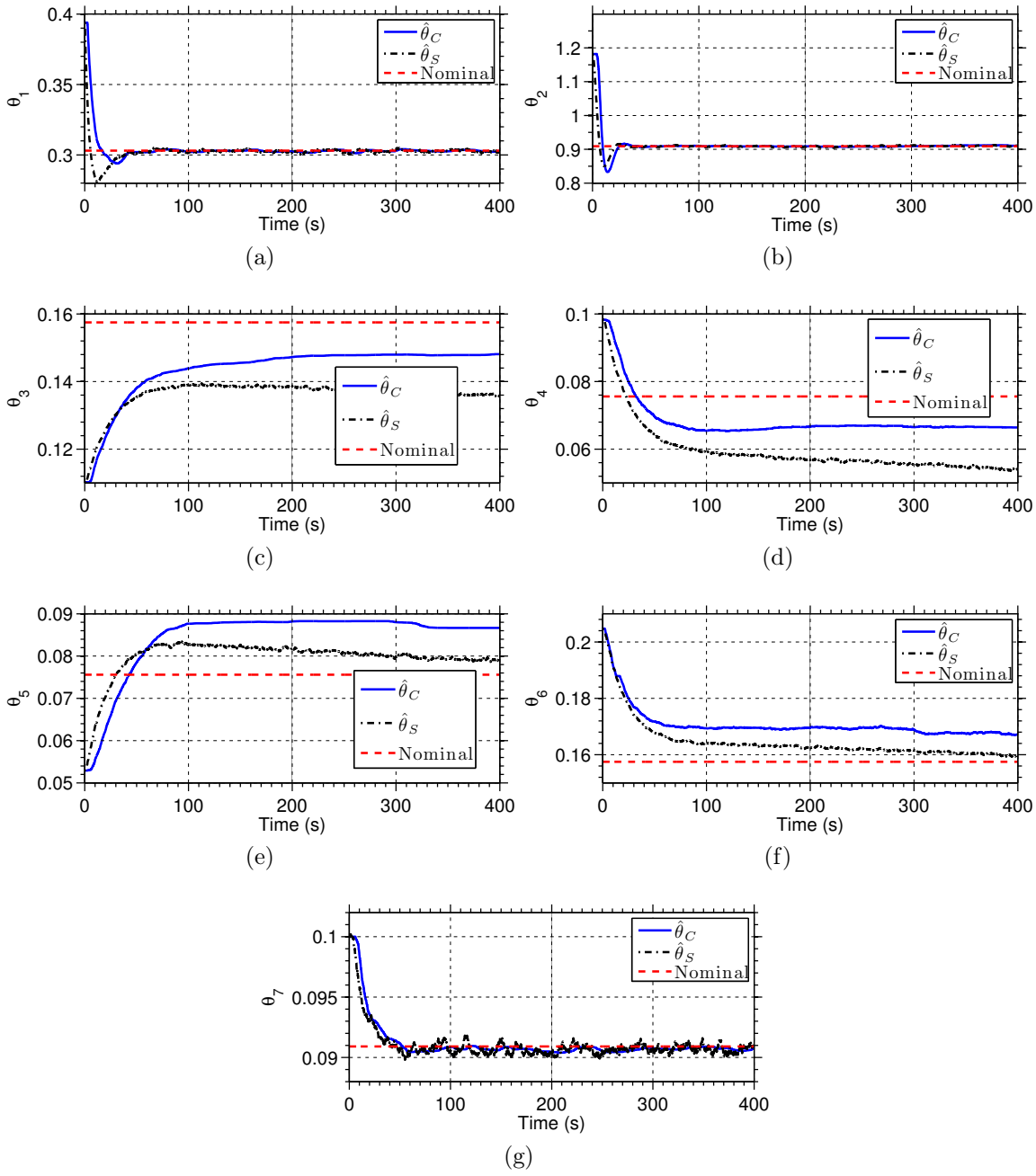

Figure 3.4: Comparison of estimated parameters used in the controller, those estimated by the adaptive control supervisor, and the nominal parameters.

3.6 Simulation of Online Optimization Scheme

In this section, the results of a simulation study of the online optimization scheme are presented. The simulations use a cost function given by

$$p = \frac{w_T}{2}\left(T - T^p\right)^2 + \frac{w_{P_\alpha}}{2}\left(P_\alpha - P_\alpha^p\right)^2 + \frac{w_\gamma}{2}\left(\gamma - \gamma^p\right)^2 - \frac{1}{\eta_c}\sum_{i=1}^{K}\ln(-g_i). \tag{3.47}$$

where T^p, P_α^p , and γ^p are references for temperature, alpha-heating, and tritium fraction, and the tracking errors are weighted by constants w_T, w_{P_α}, and w_γ. By altering the references and weights in this general cost function, many different scenarios can be tested. The last term represents the barrier functions for constraints. The constraints considered in these simulations include

$$\begin{aligned} &n_e < n_{GW}, && P_{ICRH} < P_{ICRH}^{max}, \\ &\beta_N < \beta_N^{max}, && P_{ICRH} > 0, \\ &\frac{E}{\tau_E} < Q_{div}^{max}, \end{aligned}$$

where n_{GW} is the Greenwald density limit, β_N is the Troyon β limit, Q_{div}^{max} is the maximum allowed heat load to the divertor. Note that the optimization approach is general and could be applied to other general cost functions.

3.6.1 Scenario 1

In the following results, the controller was initialized with arbitrary references E^r and n^r, which were modified in real-time to minimize the cost function p. The reference $\gamma^r = 0.5$ was kept constant throughout this simulation, i.e., it was not modified by the real-time extremum-seeking algorithm, and w_γ was taken as zero. The other weights were taken as $w_T = 0.1$ and $w_{P_\alpha} = 1$. Constraints were not considered in

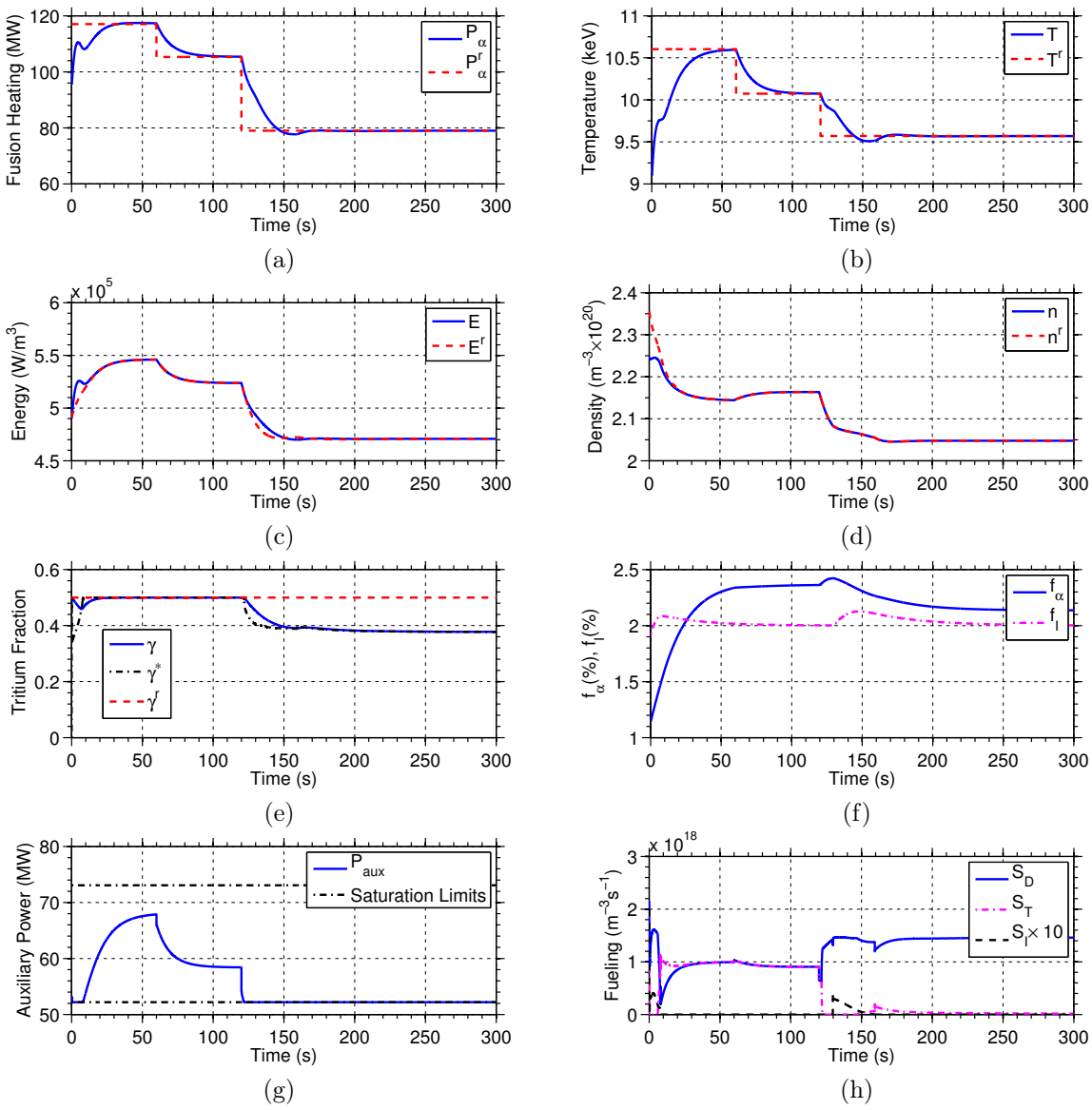

Figure 3.5: Closed loop evolution of (a) fusion heating, (b) temperature, (c) energy, (d) density, (e) tritium fraction, (f) alpha-fraction, and impurity fraction, along with closed loop response of (g) auxiliary heating and (h) fueling actuators during the simulation of Scenario 1.

the cost function. The references for fusion heating and temperature, P_α^p and T^p, which enter into the cost function, were modified twice during the simulation (at $t = 60s$ and $t = 120s$) to show the ability of the scheme to move the system between operating points. The simulation considered a fractional content of impurities of 2%, i.e., $f_I^{sp} = 0.02$, and the atomic number of the impurity species was taken to be $Z_I = 4$. The confinement scaling parameters were taken to be $k_\alpha^* = 7$, $k_D = k_T = 3$, and $k_I^* = 10$. We considered an installed heating power $P_{aux}^{max} = 73$ MW with the additional constraint $P_{aux}^{min} = \frac{5}{7}P_{aux}^{max}$. The recycling model parameters used were $\gamma^{PFC} = 0.5$, $f_{eff} = 0.3$, $f_{ref} = 0.5$, and $R^{eff} = 0.95$, which represent unfavorable conditions for control of the tritium fraction. These parameters were selected to ensure that impurity injection was required during the simulation so that all aspects of the control scheme could be illustrated. Actual recycling parameters in machines like ITER may be more favorable for control such that tritium fraction control may be more effective in experiments than it is in the results shown here.

The results of the simulation are shown in Figure 3.5. The fusion heating and temperature are compared with their respective references in Figures 3.5a and 3.5b, while the system states E, n, and γ are depicted in Figures 3.5c, 3.5d and 3.5e. The fractional content of alpha-particles and impurities are shown in Figure 3.5f and the actuators are given in Figures 3.5g and 3.5h. Because the initial operating point was not optimal, the optimization scheme immediately began to adjust the references E^r and n^r to move the system towards an optimal point. Due to the initial conditions of the system, a significant reduction in heating was required to track the reference E^r at $t = 0$, causing the auxiliary power to saturate. In order to achieve the necessary reduction in heating, the requested tritium fraction trajectory γ^* was reduced, however, the unfavorable particle recycling conditions in the simulation caused the fueling actuators to saturate and the actual tritium fraction could not

track the request. To overcome this, impurity injection was enabled and used to cool the plasma. The impurity content increased for a short time until around $t = 10s$, at which point, due to the increasing reference E^r, additional auxiliary heating was required and impurity injection was disabled. The tritium fraction then returned to its reference value and the impurity content slowly decayed back to its nominal level $f_I = f_I^{sp} = 0.02$. By around $t = 40s$, the scheme successfully forced the system to the optimal operating point, achieving the desired fusion heating and temperature. At $t = 60s$ the requested fusion heating and temperature were changed and the optimization scheme adjusted the references E^r and n^r accordingly. These requests were successfully tracked by the nonlinear control scheme through a reduction in heating and fueling, and the desired fusion heating and temperature were achieved by around $t = 100s$. At $t = 120s$, the references were changed again. The reference E^r was driven down significantly by the optimization scheme and, as a result, the auxiliary power saturated at its minimum. Again, the request γ^* was reduced and, although the actual tritium fraction began to follow the request this time, impurity injection was still needed to cool the plasma initially. By around $t = 150s$, the tritium fraction reached the requested value γ^* and impurity injection was disabled. At about the same time, the fusion heating and temperature reached the desired values and the controller regulated the system at this operating point throughout the remainder of the simulation. Over time, the fractional content of impurities decayed back to its intrinsic level $f_I = f_I^{sp} = 0.02$ and the alpha particle content converged to its steady-state value.

3.6.2 Scenario 2

In the following, the controller was initialized with arbitrary references E^r, n^r, and γ^r which were modified in real-time to minimize the cost function p (with $w_T = 0.1$,

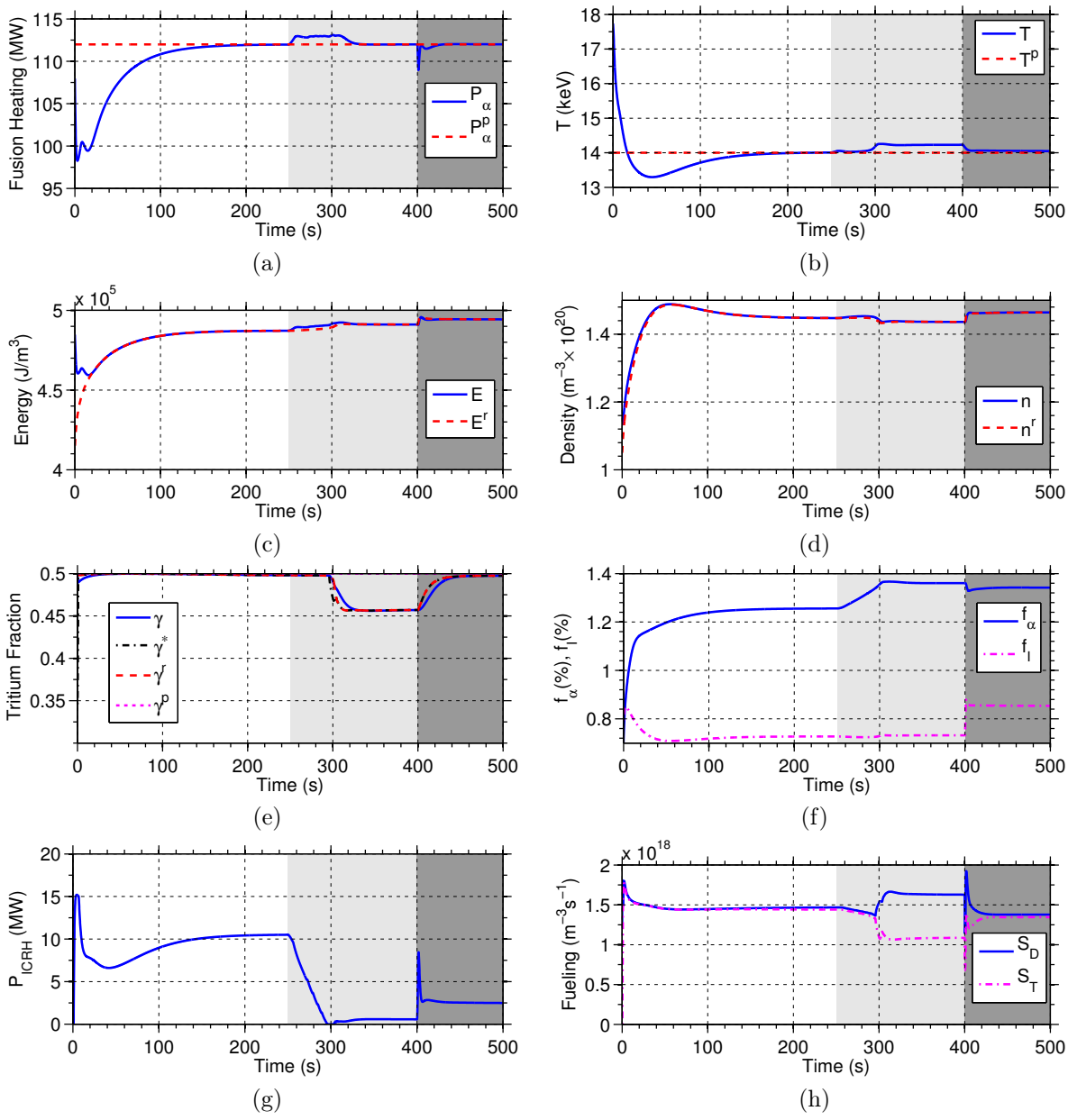

Figure 3.6: Closed loop evolution of (a) fusion heating, (b) temperature, (c) energy, (d) density, (e) tritium fraction, (f) alpha-fraction, and impurity fraction, along with closed loop response of (g) auxiliary heating and (h) fueling actuators. The shaded light gray region indicates the time interval in which the confinement disturbance was introduced, and the dark gray region indicates the impurity disturbance.

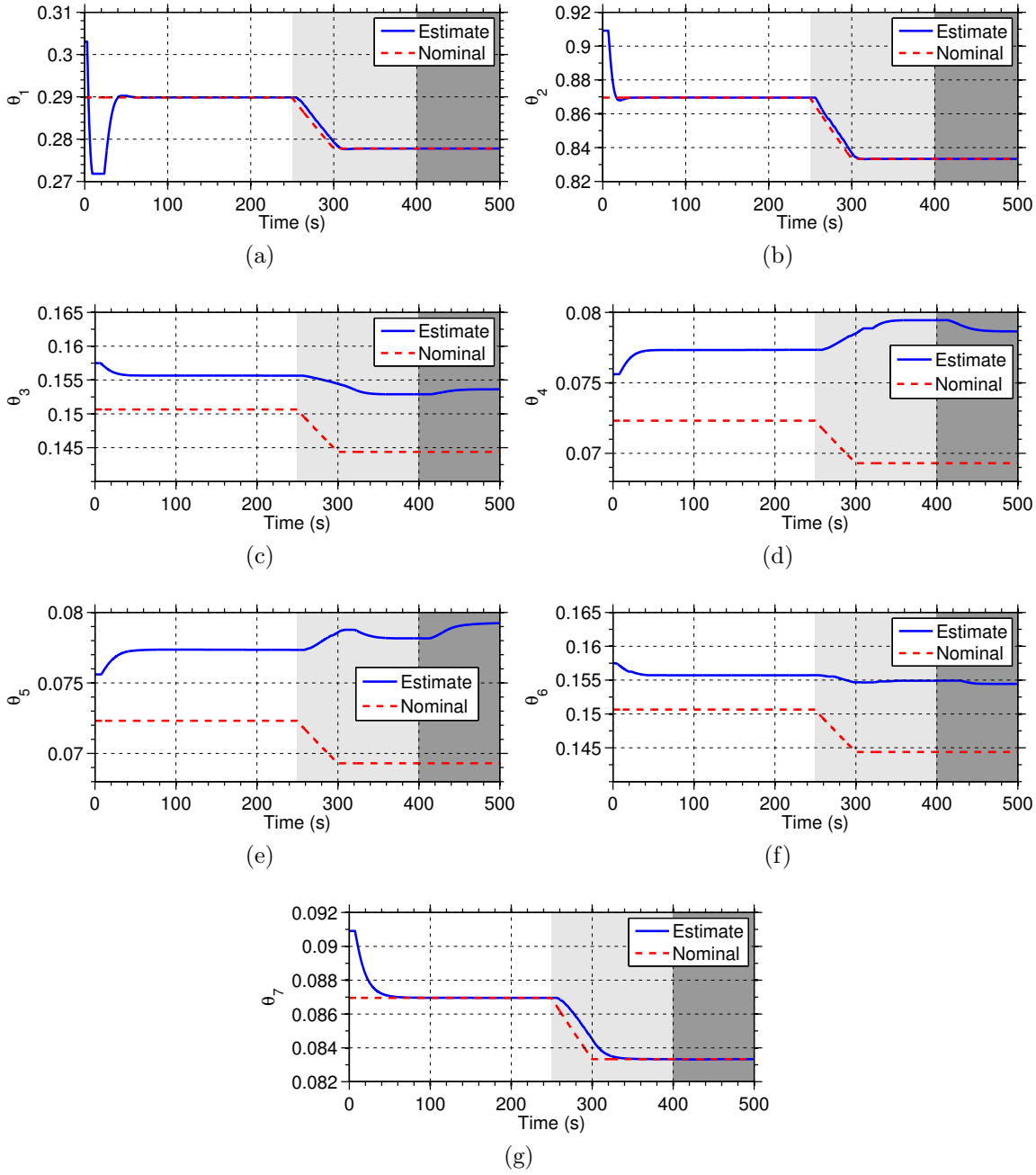

Figure 3.7: Comparison of estimated and nominal model parameters during the simulation of Scenario 2.

$w_{P_\alpha} = 1$, and $w_\gamma = 1$, and constraints on ICRH heating power active). This time, the cost function references for fusion heating, temperature, and tritium fraction, P_α^p, T^p, and γ^p, were kept constant throughout the simulation, however, disturbances were introduced to the system, to illustrate the controller's ability to cope with changing plasma conditions. Between $t = 350$s and $t = 400$s, the confinement factor H_H was ramped from 1.15 to 1.2 and held there throughout the discharge. At $t = 500$s, the impurity content was increased by a value of $2\times10^{17}\#/\mathrm{m}^3$. The simulation considered a nominal impurity content of $1 \times 10^{18}\#/\mathrm{m}^3$, and the atomic number of the impurity species was taken to be $Z_I = 6$. The confinement scaling parameters were taken to be $k_\alpha^* = k_D = k_T = 3$, and $k_I^* = 10$. An installed ICRH power $P_{ICRH}^{max} = 20$ MW and a constant power from the current drive sources of $P_{cd} = 53$ MW was considered. The recycling model parameters $\gamma^{PFC} = 0.5$, $f_{eff} = 0.3$, $f_{ref} = 0.5$, and $R^{eff} = 0.9$ were used.

The results of the simulation are shown in Figures 3.6 and 3.7. The fusion heating and temperature, the components of the cost function (3.47), are shown in Figures 3.6a and 3.6b, while the system states E, n, and γ are depicted in Figures 3.6c, 3.6d and 3.6e. The fractional content of alpha-particles and impurities are shown in Figure 3.6f and the actuators are given in Figures 3.6g and 3.6h. Finally, the nominal and estimated model parameters are compared in Figure 3.7. The initial operating point was again not optimal, and the optimization scheme adjusted the references E^r, n^r, and γ^r, as seen in Figures 3.6c, 3.6d and 3.6e, in order to reduce the cost function. Despite initial condition errors, these requests were successfully tracked by the nonlinear control scheme through modulation of the heating and fueling, and the optimal operating point, producing the desired fusion heating and temperature, was achieved by around $t = 200s$. At $t = 350s$, the confinement disturbance was ramped up, forcing the adaptive parameter estimation scheme to update its estimates, as seen

in Figure 3.7. During the transient part of the disturbance, small tracking errors can be noted in Figures 3.6c and 3.6d. The increase in confinement caused the controller to ramp down the ICRH power, eventually reaching saturation (Figure 3.6g). The constrained online optimization scheme responded to the saturation by decreasing the reference γ^r, as seen in Figure 3.6e, resulting in an operating point that could be stabilized without ICRH heating, while still remaining close to the desired temperature and fusion power, i.e., the optimal feasible operating point. The desired fusion power was achieved by around $t = 320$s, while a slight deviation from the reference temperature remained (Figure 3.6b) due to the fact that the optimization scheme was constrained by the saturation of the ICRH power (recall that the cost function weight on fusion heating tracking error was significantly higher than that placed on the temperature tracking error). As seen in Figure 3.6f, the impurity disturbance was introduced at $t = 500$s, which increased radiation losses and diluted the fusion fuel, causing a reduction in temperature and fusion heating. The optimization scheme responded by increasing all three controller references, and the nonlinear controller was able to track them and regulate the optimal operating point. Due to the increased impurity level, the ICRH power was increased out of saturation and the optimization scheme was able to drive the system to the optimal point, achieving the desired values P_α^p, T^p, and γ^p, as shown in Figures 3.6c, 3.6d and 3.6e. Turning to the model parameter estimates, it should be noted that only θ_2 affects the cost function (through its influence on the constrained input P_{ICRH}). Despite the fact that the nominal parameter changed during the simulation, the parameter estimation scheme was able to keep the estimated value close to the true value, as seen Figure 3.7b. After the confinement disturbance, the estimates of θ_3, θ_4, θ_5, and θ_6, shown in Figures 3.7c, 3.7d, 3.7e, and 3.7f, do not converge to the true values, due to a lack of persistent excitation. However, this does not influence the tracking performance of the control,

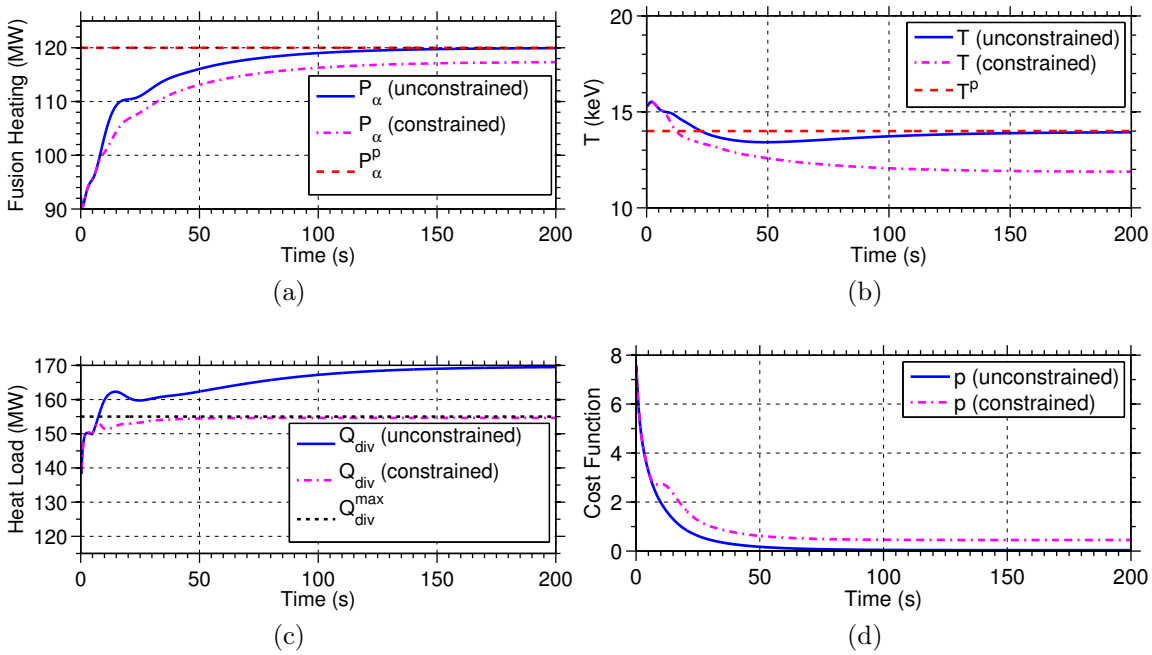

Figure 3.8: Comparison of (a) fusion heating, (b) temperature, (c) divertor heat load, and (d) the cost function p during simulations of Scenario 3 using both constrained and unconstrained optimization.

nor does it affect the optimization scheme, as these parameters do not enter into the calculation of the cost function.

3.6.3 Scenario 3

In the following, the cost function from the previous section was considered, and the references for fusion heating, temperature, and tritium fraction, $P_\alpha^p = 120$, $T^p = 14$, and $\gamma^p = 0.5$, were kept constant throughout the simulation. However, this time a constraint on the divertor heat load was added, i.e., $Q_{div} < Q_{div}^{max}$, where Q_{div}^{max} was set to 155 MW, to illustrate the controller's ability to cope with constraints. The simulation considered a nominal impurity content of $1 \times 10^{18}\#/\mathrm{m}^3$, and the atomic number of the impurity species was taken to be $Z_I = 6$. The confinement scaling parameters were taken to be $k_\alpha^* = k_D = k_T = 3$, and $k_I^* = 10$, while the confinement

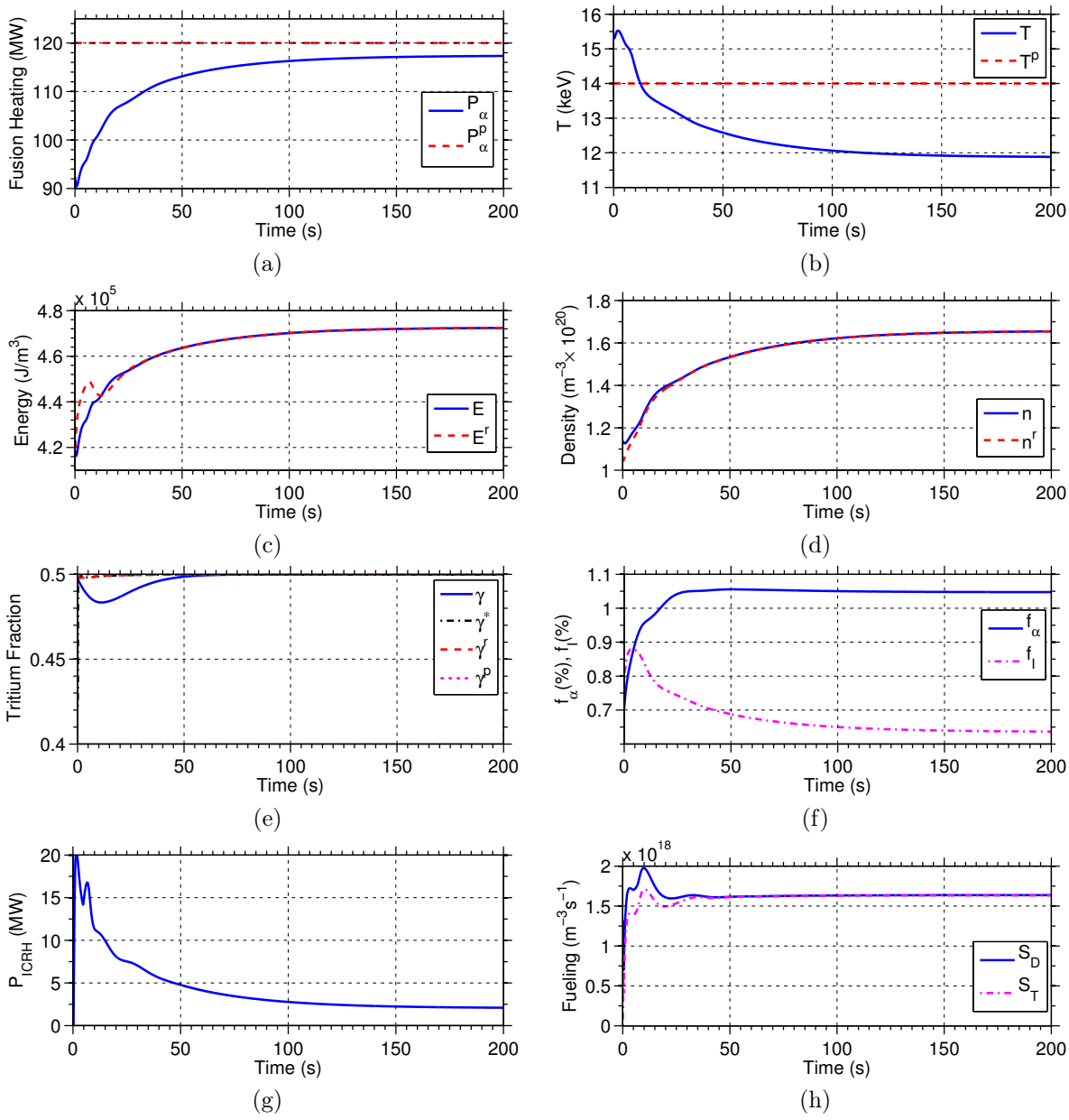

Figure 3.9: Closed loop evolution of (a) fusion heating, (b) temperature, (c) energy, (d) density, (e) tritium fraction, (f) alpha-fraction, and impurity fraction, along with closed loop response of (g) auxiliary heating and (h) fueling actuators during the simulation of Scenario 3. The shaded light gray region indicates the time interval in which the confinement disturbance was introduced, and the dark gray region indicates the impurity disturbance.

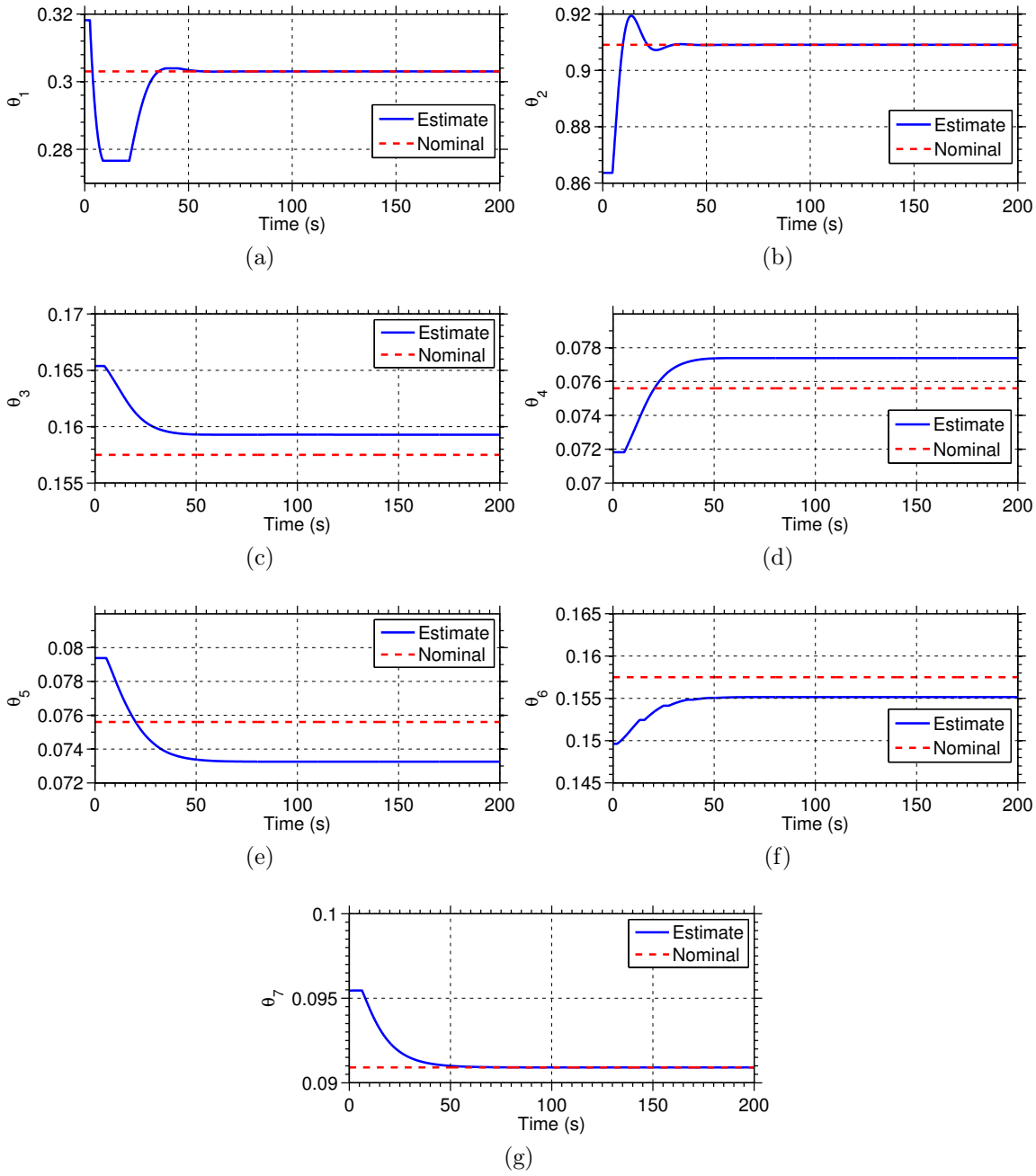

Figure 3.10: Comparison of estimated and nominal model parameters during the simulation of Scenario 3.

factor was taken as $H_H = 1.1$ throughout the discharge. An installed ICRH power $P_{ICRH}^{max} = 20$ MW and a constant power from the current drive sources, $P_{cd} = 53$ MW, were considered. The recycling model parameters used were again $\gamma^{PFC} = 0.5$, $f_{eff} = 0.3$, $f_{ref} = 0.5$, and $R^{eff} = 0.9$.

Figure 3.8 compares the fusion power, temperature, heat load, and cost function during the constrained simulation with the results of an unconstrained simulation. The remaining plasma parameters during the constrained simulation are shown in Figures 3.9 and 3.10. The fusion heating and temperature, the components of the cost function (3.47), are shown in Figures 3.9a and 3.9b, while the system states E, n, and γ are depicted in Figures 3.9c, 3.9d and 3.9e. The fractional content of alpha-particles and impurities are shown in Figure 3.9f and the actuators are given in Figures 3.9g and 3.9h. The nominal and estimated model parameters are compared in Figure 3.10.

Comparing the results of the constrained simulation with an unconstrained one, it can be seen that the fusion power and temperature settle to values lower than the requested ones in the constrained case, while the request values are achieved in the unconstrained case. This results in a slightly higher value of the cost function in the constrained case, as seen in Figure 3.8d. In Figure 3.8c, it can be seen that, while the the unconstrained optimization scheme violates the divertor heat load constraint, the constrained version keeps the heat load below the specified limit by driving the system to the optimal feasible point. As seen in Figures 3.6c, 3.6d and 3.6e, the optimization scheme adjusted the references E^r, n^r, and γ^r to achieve the optimal operating point. Reference tracking errors can been seen decaying away in the first 50s as the parameter estimations, shown in Figure 3.10, converged toward a constant set of model parameter estimates.

3.7 Conclusions

The nonlinear burn control law designed in Chapter 2 has been augmented with an adaptive control scheme to ensure reference tracking despite uncertainty in the parameters of the model used for control design. A dual model supervisory strategy has also been proposed to oversee the adaptive controller to avoid parameter drift due to noisy measurements. In addition, an online optimization scheme has been proposed to modify the controller references in real-time to minimize a given cost function in response to changes in n_α and n_I, and to make use of the improved model parameters arrived at through adaptive update laws. Constraints are included in the optimization scheme through the use of barrier functions in the cost function. Simulations show the ability of the adaptive optimization scheme to move the system between operating points, handle uncertainty and disturbances, and respect state/input constraints.

Chapter 4

Nonlinear Burn Control With Output Feedback

4.1 Introduction

Due to the extreme conditions in fusion reactors, as well as economic considerations, diagnostic systems for measuring plasma parameters may be limited. The proposed nonlinear burn control control approach, which relies on knowledge of the states of the system to calculate actuator trajectories (state feedback), may not, therefore, be directly implementable. To overcome this obstacle, an observer, a computer-implemented dynamic system that combines knowledge from the mathematical model of the system with the available real-time output measurements to estimate the system states, will likely be necessary in practice. For linear systems, observers typically take the form of a copy of the plant dynamics with the addition of output error injection

terms, i.e., for the general system

$$\dot{x} = Ax + Bu$$
$$y = Cx + Du,$$

the observer would take the form

$$\dot{\hat{x}} = A\hat{x} + Bu + L\left(\hat{y} - y\right)$$
$$\hat{y} = C\hat{x} + Du.$$

Through proper choice of the gain L, the state estimation error (the difference between x and $\hat{x}$) can be quickly driven to zero. For linear systems, the separation principle makes it possible to separately design the control law for the input u and the output injection gain L. Observer design for the burning plasma system is complicated by the presence of modeling uncertainties, the nonlinearity of the state dynamics, and the fact that the output map is, in general, nonlinearly dependent on the states of the system. Because each nonlinear system is unique, no general approach to nonlinear observer design exists (see [54] for a survey of nonlinear observer approaches). Designs for particular types of systems with nonlinear dynamics and output maps have been proposed based on coordinate transformations and local linearization of the nonlinear system [55, 56]. It so happens that, based on the dynamics and available diagnostics for ITER, an observer design approach similar to that used in [55] for a steel converter process, can be taken here.

The nonlinear observer proposed in this work makes use of the concept of a proportional-integral observer. PIO designs differ from the previously cited observers by the presence of an integral component in the output injection term, which pro-

vides an additional degree of freedom that can be used to decrease sensitivity to model uncertainties and disturbances. Output feedback controllers with PIOs have been proposed for general linear systems [57, 58] and have more recently been applied to certain nonlinear systems [59, 60]. For the nominal burning plasma system, the nonlinear PIO design proposed in this work is stable for suitably small state estimation errors or observer gains. The state estimation error is ISS with respect to the considered set of uncertain model parameters, and, due to the inclusion of an integral output injection term, the output estimation error converges to zero asymptotically. A simulation study is presented showing the performance of the output feedback scheme for a particular diagnostic set expected to be available on ITER. A list of the ITER diagnostic systems that are relevant to the problem of burn control, adapted from [61], is provided in Table 4.1.

This chapter is organized as follows. The design of a nonlinear controller and proportional-integral observer is presented in Section 4.2. The scheme is augmented with adaptive parameter update laws to estimate uncertain model parameters in Section 4.3, and the design of an output feedback based real-time optimization scheme is provided in Section 4.4. A simulation study of the output feedback control scheme is presented in Section 4.5. Finally, conclusions and possible extensions to this work are discussed in Section 4.6.

Table 4.1: Relevant ITER diagnostic systems, the parameter they measure, range, time resolution, spatial resolution, and accuracy [61].

Diagnostic	Parameter	Range	Time Resolution	Spatial Resolution	Accuracy
Neutron flux monitors	Fusion power	100 kW-1.5 GW	1 ms	Integral	10%
Neutron spectrometer	Fuel ratio in core	0.01-10	100 ms	$a/10$	0.2
Interferometer/ polarimeter	Line-averaged electron density	1E18-4E20 m^{-3}	1 ms	Integral	1%
Bolometers	Radiated power	0.1 MW - 1 GW	1 ms	Integral	10%
CXRS	Effective atomic number	1-5	10 ms	Integral	20%
Impurity influx monitor	Impurity/D/T influx in divertor	1E19-1E25 at s^{-1}	1 ms	50 mm	0.3
CXRS	Core He density	1-20%	100 ms	$a/10$	0.1
Diamagnetic loop	Plasma energy (β_p)	0.01-5	1 μs	Integral	5%
In-vessel magnetics	Plasma current	1-17.5 MA	1 ms	Integral	1%
In-vessel magnetics	Plasma position/shape	-	10 ms	-	10 mm
Neutron camera	Neutron- and $\alpha-$source profile	1E14-6E18 $nm^{-3}s^{-1}$	1 ms	$a/10$	10%
Thomson scattering	Electron temperature profile	0.5-40 keV	10 ms	$a/30$	0.1
Thomson scattering	Electron density profile	3E19-3E20 m^{-3}	10 ms	$a/30$	0.05
X-ray crystal spectrometer	Ion temperature profile	0.5-40 keV	100 ms	$a/30$	0.1
IR thermography	Heat load in divertor	0.1-25 MW m^{-2}	2 ms	3 mm	0.1

4.2 Controller and Observer Design

We consider an observer of the form

$$\dot{\mathring{n}}_\alpha = -\hat{\theta}_1 \frac{\mathring{n}_\alpha}{\tau_E^{sc}} + S_\alpha + L_\alpha, \tag{4.1}$$

$$\dot{\mathring{E}} = -\hat{\theta}_2 \frac{\mathring{E}}{\tau_E^{sc}} + P_\alpha - P_{rad} + P_{aux} + P_{Ohm} + L_E, \tag{4.2}$$

$$\dot{\mathring{n}}_I = -\hat{\theta}_7 \frac{\mathring{n}_I}{\tau_E^{sc}} + S_I^{inj} + S_I^{sp} + L_I, \tag{4.3}$$

$$\dot{\mathring{n}}_D = -\hat{\theta}_3 \frac{\mathring{n}_D}{\tau_E^{sc}} + \hat{\theta}_4 \frac{\mathring{n}_T}{\tau_E^{sc}} - S_\alpha + S_D^{inj} + L_D, \tag{4.4}$$

$$\dot{\mathring{n}}_T = \hat{\theta}_5 \frac{\mathring{n}_D}{\tau_E^{sc}} - \hat{\theta}_6 \frac{\mathring{n}_T}{\tau_E^{sc}} - S_\alpha + S_T^{inj} + L_T, \tag{4.5}$$

where L_α, L_E, L_I, L_D, and L_T are to-be-designed output injection terms. The terms S_α, P_α, P_{rad}, P_{Ohm}, and S_I^{sp} are considered to be measured, based on the diagnostic systems planned for ITER [61] (if unavailable, these terms could always be estimated based on the observer state estimates). The output map is considered to be of the form

$$y = h(n_\alpha, E, n_I, n_D, n_T).$$

The system is augmented with an additional state, $\check{z}$, governed by

$$\dot{\check{z}} = \mathring{y} - y = \check{y}, \tag{4.6}$$

where $\mathring{y} = h(\mathring{n}_\alpha, \mathring{E}, \mathring{n}_I, \mathring{n}_D, \mathring{n}_T)$.

For the purposes of control design, we consider the estimated states $\mathring{n}$ and $\mathring{\gamma}$, which are governed by

$$\dot{\mathring{n}} = 2\left[\left(\hat{\theta}_5 - \hat{\theta}_3\right)\frac{\mathring{n}_D}{\tau_E^{sc}} + \left(\hat{\theta}_4 - \hat{\theta}_6\right)\frac{\mathring{n}_T}{\tau_E^{sc}} - 2S_\alpha + S_D^{inj} + S_T^{inj} + L_D + L_T\right] + 3\left[-\hat{\theta}_1\frac{\mathring{n}_\alpha}{\tau_E^{sc}} + S_\alpha + L_\alpha\right] + (Z_I + 1)\left[-\hat{\theta}_7\frac{\mathring{n}_I}{\tau_E^{sc}} + S_I^{inj} + S_I^{sp} + L_I\right], \tag{4.7}$$

$$\dot{\mathring{\gamma}} = \frac{1}{\mathring{n}_{DT}}\left\{\hat{\theta}_5\frac{\mathring{n}_D}{\tau_E^{sc}} - \hat{\theta}_6\frac{\mathring{n}_T}{\tau_E^{sc}} - S_\alpha + S_T^{inj} + L_T - \mathring{\gamma}\left[\left(\hat{\theta}_5 - \hat{\theta}_3\right)\frac{\mathring{n}_D}{\tau_E^{sc}} + \left(\hat{\theta}_4 - \hat{\theta}_6\right)\frac{\mathring{n}_T}{\tau_E^{sc}} - 2S_\alpha + S_D^{inj} + S_T^{inj} + L_D + L_T\right]\right\}. \tag{4.8}$$

We define the errors $\tilde{E} = \mathring{E} - E^r$, $\tilde{\gamma} = \mathring{\gamma} - \gamma^r$, and $\tilde{n} = \mathring{n} - n^r$ to write

$$\dot{\tilde{E}} = -\hat{\theta}_2\frac{\tilde{E}}{\tau_E^{sc}} - \hat{\theta}_2\frac{E^r}{\tau_E^{sc}} + P_\alpha - P_{rad} + P_{aux} + P_{Ohm} + L_E - \dot{E}^r, \tag{4.9}$$

$$\dot{\tilde{\gamma}} = -\hat{\theta}_6\frac{\tilde{\gamma}}{\tau_E^{sc}} + \frac{2\left[u(\gamma^r) + (1 - \mathring{\gamma})\, S_T^{inj} - \mathring{\gamma} S_D^{inj}\right]}{\mathring{n} - 3\mathring{n}_\alpha - (Z_I + 1)\,\mathring{n}_I}, \tag{4.10}$$

$$\dot{\tilde{n}} = -\tilde{n}\left[-\left(\hat{\theta}_5 - \hat{\theta}_3\right)\frac{(1 - \mathring{\gamma})}{\tau_E^{sc}} - \left(\hat{\theta}_4 - \hat{\theta}_6\right)\frac{\mathring{\gamma}}{\tau_E^{sc}}\right] + v - \dot{n}^r + 2\left(S_D^{inj} + S_T^{inj}\right), \tag{4.11}$$

where

$$u(\gamma^r) = \frac{\mathring{n} - 3\mathring{n}_\alpha - (Z_I + 1)\,\mathring{n}_I}{2}\left[\hat{\theta}_5\frac{(1 - \mathring{\gamma})}{\tau_E^{sc}} - \hat{\theta}_6\frac{\gamma^r}{\tau_E^{sc}} - \dot{\gamma}^r - \left(\hat{\theta}_5 - \hat{\theta}_3\right)\frac{(\mathring{\gamma} - \mathring{\gamma}^2)}{\tau_E^{sc}} - \left(\hat{\theta}_4 - \hat{\theta}_6\right)\frac{\mathring{\gamma}^2}{\tau_E^{sc}}\right] + (2\mathring{\gamma} - 1)\, S_\alpha + (1 - \mathring{\gamma})\, L_T - \mathring{\gamma} L_D, \tag{4.12}$$

$$v = \left[-n^r + 3\mathring{n}_\alpha + (Z_I + 1)\,\mathring{n}_I\right]\left[-\left(\hat{\theta}_5 - \hat{\theta}_3\right)\frac{(1 - \mathring{\gamma})}{\tau_E^{sc}} - \left(\hat{\theta}_4 - \hat{\theta}_6\right)\frac{\mathring{\gamma}}{\tau_E^{sc}}\right] - 4S_\alpha + 3\left[-\hat{\theta}_1\frac{\mathring{n}_\alpha}{\tau_E^{sc}} + S_\alpha + L_\alpha\right] + (Z_I + 1)\left[-\hat{\theta}_7\frac{\mathring{n}_I}{\tau_E^{sc}} + S_I^{inj} + S_I^{sp} + L_I\right] + 2\left(L_D + L_T\right). \tag{4.13}$$

Note that, if no controlled impurity injection at steady-state is considered, the ref-

erence $r = [E^r, n^r, \gamma^r]$ uniquely determines the equilibrium values of n_α and n_I, and these states remain bounded if r is stabilized. We therefore make regulation of r the objective of the control design.

4.2.1 Controller Design

We note that $\tilde{E}$ can be driven to zero by satisfying the condition

$$\begin{aligned} f(n,E,n_\alpha,n_I,\gamma) =& -\hat{\theta}_2 \frac{E^r}{\tau_E^{sc}} + P_{Ohm} + P_\alpha - P_{rad} + P_{aux} + L_E - \dot{E}^r \\ &+ K_E \tilde{E} = 0, \end{aligned} \tag{4.14}$$

The condition (4.14) can be satisfied in several different ways. The auxiliary heating term P_{aux} enters the equation directly, the actuators S_D^{inj} and S_T^{inj} can be used to change the α-heating term P_α by modulating the tritium fraction, and the impurity injection term S_I^{inj} can be used to increase the impurity content and consequently P_{rad}. Having several methods available for controlling the energy subsystem enables us to design a control scheme that can still achieve stabilization despite saturation of one or even several of the available actuators.

Step 1: We first calculate the P_{aux} as

$$\begin{aligned} P_{aux}^{unsat} =& \hat{\theta} \frac{E^r}{\tau_E^{sc}} - \gamma^r \left(1 - \gamma^r\right) \frac{P_\alpha}{\mathring{\gamma}\left(1 - \mathring{\gamma}\right)} + P_{rad} \\ &- P_{Ohm} - L_E + \dot{E}^r - K_E \tilde{E}, \end{aligned} \tag{4.15}$$

$$P_{aux} = \text{sat}\left(\frac{P_{aux}^{unsat} - P_{aux}^{min}}{P_{aux}^{max} - P_{aux}^{min}} \right), \tag{4.16}$$

where $P_\alpha / \left[\mathring{\gamma}\left(1 - \mathring{\gamma}\right)\right]$ is an estimate of $Q_\alpha n_{DT}^2 \langle \sigma\nu \rangle$, the limit P_{aux}^{max} depends on the installed power on the tokamak, and the limit $P_{aux}^{min} \geq 0$ depends on the operating

scenario. For example, some minimum amount of power may be needed to maintain the required amount of non-inductive current drive during a particular discharge since some sources of power (neutral beam injection, electron-cyclotron current drive, etc.) double as sources of plasma current.

Step 2: We next find a trajectory γ^* satisfying (4.14), i.e.,

$$\gamma^*(1-\gamma^*)\frac{P_\alpha}{\mathring{\gamma}\left(1-\mathring{\gamma}\right)} = P_{rad} - P_{Ohm} - P_{aux} - L_E + \hat{\theta}_2 \frac{E^r}{\tau_E^{sc}} + \dot{E}^r - K_E \tilde{E}. \tag{4.17}$$

Solving this equation yields

$$\gamma^*\left(1-\gamma^*\right) = \frac{\mathring{\gamma}\left(1-\mathring{\gamma}\right)}{P_\alpha}\left[\hat{\theta}_2 \frac{E^r}{\tau_E^{sc}} + P_{rad} - P_{Ohm} - P_{aux} - L_E + \dot{E}^r - K_E \tilde{E}\right] = C, \tag{4.18}$$

$$\gamma^* = \frac{1 \pm \sqrt{1-4C}}{2}. \tag{4.19}$$

Note that, if the value of P_{aux} calculated in Step 1 is not saturated, then $\gamma^* = \gamma^r$. This can be shown by substituting (4.16) into (4.17). If $C \leq 0.25$, the two resulting solutions for γ^* are real and we take the tritium-lean solution, such that $\gamma^* \leq 0.5$. If $C \geq 0.25$, even the optimal isotopic mix and maximum value of auxiliary heating will not generate enough heating to satisfy $f = 0$, indicating that the requested operating point may not be achievable for the amount of auxiliary heating power installed on the device. Barring this situation, based on our choice of P_{aux} and γ^*, we have that

$$f\left(n, E, n_\alpha, n_I, \gamma^*\right) = 0. \tag{4.20}$$

This allows us to write $f = \hat{\gamma}\phi_\gamma$ where $\hat{\gamma} = \mathring{\gamma} - \gamma^*$ and ϕ_γ is a continuous function. Noting (4.9), (4.14), we can then write the dynamics of the energy perturbation as

$$\dot{\tilde{E}} = -\hat{\theta}_2 \frac{\tilde{E}}{\tau_E^{sc}} - K_E \tilde{E} + \hat{\gamma}\phi_\gamma, \tag{4.21}$$

and the dynamics of $\hat{\gamma}$ can be written as

$$\dot{\hat{\gamma}} = -\hat{\theta}_6 \frac{\hat{\gamma}}{\tau_E^{sc}} + \frac{2\left[u(\gamma^*) + (1-\mathring{\gamma})\, S_T^{inj} - \mathring{\gamma} S_D^{inj}\right]}{\mathring{n} - 3\mathring{n}_\alpha - (Z_I + 1)\,\mathring{n}_I}. \tag{4.22}$$

Step 3: Having selected P_{aux} and γ^* in the previous steps, we must next choose S_D^{inj} and S_T^{inj} to ensure that $\tilde{E}$, $\hat{\gamma}$, and $\tilde{n}$, which are governed by (4.21), (4.22), and (4.11), are driven to zero. We consider the Lyapunov function $V_0 = V_n + V_{E,\gamma}$ where $V_n = \frac{1}{2}\tilde{n}^2$ and $V_{E,\gamma} = \frac{1}{2}k_1\tilde{E}^2 + \frac{1}{2}\hat{\gamma}^2$. It can be shown that satisfying the conditions

$$2\left(S_T^{inj} + S_D^{inj}\right) = -v - K_n\tilde{n} + \dot{n}^r, \tag{4.23}$$

$$\begin{aligned}(1-\mathring{\gamma})\, S_T^{inj} - \mathring{\gamma} S_D^{inj} = &-\frac{\mathring{n} - 3\mathring{n}_\alpha - (Z_I+1)\,\mathring{n}_I}{2} \\ &\times \left(k_1\tilde{E}\phi_\gamma + K_\gamma\hat{\gamma}\right) - u(\gamma^*),\end{aligned} \tag{4.24}$$

where $K_n > 0$ and $K_\gamma > 0$ results in

$$\dot{V}_n = -\tilde{n}^2\left(-\left(\hat{\theta}_5 - \hat{\theta}_3\right)\frac{(1-\mathring{\gamma})}{\tau_E^{sc}} - \left(\hat{\theta}_4 - \hat{\theta}_6\right)\frac{\mathring{\gamma}}{\tau_E^{sc}} + K_n\right) < 0, \tag{4.25}$$

$$\dot{V}_{E,\gamma} = -k_1\hat{\theta}_2\frac{\tilde{E}^2}{\tau_E^{sc}} - k_1 K_E\tilde{E}^2 - \left(\frac{1}{\tau_T} + K_\gamma\right)\hat{\gamma}^2 < 0, \tag{4.26}$$

such that $\dot{V}_0 < 0$, guaranteeing asymptotic stability of the system. The conditions (4.23) and (4.24) can be satisfied by choosing

$$S_D^{inj} = \frac{\mathring{n} - 3\mathring{n}_\alpha - (Z_I + 1)\,\mathring{n}_I}{2}\left(k_1 \tilde{E}\phi_\gamma + K_\gamma \hat{\gamma}\right) + u(\gamma^*) + (1 - \mathring{\gamma})\left(\frac{-v - K_n\tilde{n} + \dot{n}^r}{2}\right), \tag{4.27}$$

$$S_T^{inj} = \left(\frac{-v - K_n\tilde{n} + \dot{n}^r}{2}\right) - S_D^{inj}. \tag{4.28}$$

These values are subject to the constraints $0 \leq S_D^{inj} \leq S_D^{inj,max}$ and $0 \leq S_T^{inj} \leq S_T^{inj,max}$. If one of the fueling actuators saturates, we cannot satisfy both conditions of the control law, so we must choose to either control $\mathring{n}$ or $\mathring{\gamma}$. If we choose to hold condition (4.24), the energy and tritium fraction subsystems will remain stable, however, the density subsystem will no longer be controlled. This could potentially lead to a violation of the density limit. To avoid this, we instead choose to maintain control of the density by satisfying (4.23).

Because of fueling actuator saturation, it may be possible that $\dot{V}_{E,\gamma} > 0$, that is, we may not be able to ensure stability of the burn condition with the previously considered actuators. There are two possible situations to consider, either a thermal quench or an excursion. If the system is experiencing a quench, the controller has already increased auxiliary heating to its maximum, so the only alternative would be to change the magnetic plasma parameters to improve energy confinement (see (2.19)) or to change the reference operating point to one that is achievable. If the system is experiencing a thermal excursion, however, we can still use impurity injection to stabilize the energy subsystem, despite the heating and fueling actuator saturation. In these cases we enable the use of impurity injection by setting the flag $F_{imp} = 1$ and proceeding to Step 4.

Step 4: If $F_{imp} = 1$, we use the expression for radiation losses given in (2.12)

to find an impurity density trajectory n_I^* that satisfies condition (4.14). Defining the error $\hat{n}_I = \mathring{n}_I - n_I^*$, we can write its dynamics as

$$\dot{\hat{n}}_I = -\hat{\theta}_7 \frac{\hat{n}_I}{\tau_E^{sc}} - \hat{\theta}_7 \frac{n_I^*}{\tau_E^{sc}} + S_I^{inj} + S_I^{sp} - \dot{n}_I^*. \tag{4.29}$$

Based on the choice of n_I^*, we have that

$$f\left(n, E, n_\alpha, \gamma, n_I^*\right) \;\; = \;\; 0, \tag{4.30}$$

which allows us to write $f = \hat{n}_I \phi_I$ where ϕ_I is a continuous function. We can then rewrite (4.9) as

$$\dot{\tilde{E}} = -\hat{\theta}_2 \frac{\tilde{E}}{\tau_E^{sc}} - K_E \tilde{E} + \hat{n}_I \phi_I. \tag{4.31}$$

We take as a Lyapunov function $V_1 = V_n + V_\gamma + V_{E,I}$ where $V_\gamma = \frac{1}{2}\hat{\gamma}^2$ and $V_{E,I} = \frac{1}{2}k_3\tilde{E}^2 + \frac{1}{2}\hat{n}_I^2$. By satisfying

$$S_I^{inj} = -k_3 \tilde{E} \phi_I + \hat{\theta}_7 \frac{n_I^*}{\tau_E^{sc}} - S_I^{sp} + \dot{n}_I^* - K_I \hat{n}_I, \tag{4.32}$$

where $K_I > 0$, the derivative of $V_{E,I}$ can be reduced to

$$\dot{V}_{E,I} = -k_3 \hat{\theta}_2 \frac{\tilde{E}^2}{\tau_E^{sc}} - k_3 K_E \tilde{E}^2 - K_I \hat{n}_I^2 < 0. \tag{4.33}$$

We modify the tritium fraction trajectory to $\gamma^* = \gamma^*_{(\text{Step 2})} - K_S \int_{t_0}^{t} S_I^{inj} dt$ where $\gamma^*_{(\text{Step 2})}$ is the value of γ^* calculated in Step 2, $K_S > 0$, and t_0 is the time at which impurity injection was first engaged. This modification ensures that the tritium fraction is, if possible, eventually reduced to such a level that impurity injection is no longer needed, i.e., $S_I^{inj} \to 0$. Once $S_I^{inj} = 0$, we disable impurity injection in

subsequent executions of the algorithm by setting $F_{imp} = 0$. By satisfying

$$2\left(S_T^{inj} + S_D^{inj}\right) = -v - K_n\tilde{n}, \tag{4.34}$$

$$\begin{aligned}(1-\mathring{\gamma})\, S_T^{inj} - \mathring{\gamma} S_D^{inj} = &- \frac{\mathring{n} - 3\mathring{n}_\alpha - (Z_I+1)\,\mathring{n}_I}{2} K_\gamma \hat{\gamma} \\ &- u(\gamma_I^*).\end{aligned} \tag{4.35}$$

We can ensure that $\dot{V}_n < 0$, $\dot{V}_\gamma < 0$, and therefore $\dot{V}_1 < 0$, guaranteeing stability of the system. The conditions (4.34) and (4.35) can be satisfied by choosing

$$\begin{aligned}S_D^{inj} = &\frac{\mathring{n} - 3\mathring{n}_\alpha - (Z_I+1)\,\mathring{n}_I}{2} K_\gamma \hat{\gamma} \\ &+ u(\gamma^*) + (1-\mathring{\gamma})\left(\frac{-v - K_n\tilde{n}}{2}\right),\end{aligned} \tag{4.36}$$

$$S_T^{inj} = \left(\frac{-v - K_n\tilde{n}}{2}\right) - S_D^{inj}, \tag{4.37}$$

which are again subject to saturation. If one of the fueling actuators saturates, we again choose to hold (4.34) to ensure stability of the density.

4.2.2 Observer Design

The dynamics of the estimation error can be shown to be governed by

$$\dot{\tilde{n}}_\alpha = -\tilde{\theta}_1 \frac{\mathring{n}_\alpha}{\tau_E^{sc}} - \theta_1 \frac{\check{n}_\alpha}{\tau_E^{sc}} + L_\alpha, \tag{4.38}$$

$$\dot{\tilde{E}} = -\tilde{\theta}_2 \frac{\mathring{E}}{\tau_E^{sc}} - \theta_2 \frac{\check{E}}{\tau_E^{sc}} + L_E, \tag{4.39}$$

$$\dot{\tilde{n}}_I = -\tilde{\theta}_7 \frac{\mathring{n}_I}{\tau_E^{sc}} - \theta_7 \frac{\check{n}_I}{\tau_E^{sc}} + L_I, \tag{4.40}$$

$$\dot{\tilde{n}}_D = -\tilde{\theta}_3 \frac{\mathring{n}_D}{\tau_E^{sc}} - \theta_3 \frac{\check{n}_D}{\tau_E^{sc}} + \tilde{\theta}_4 \frac{\mathring{n}_T}{\tau_E^{sc}} + \theta_4 \frac{\check{n}_T}{\tau_E^{sc}} + L_D, \tag{4.41}$$

$$\dot{\tilde{n}}_T = \tilde{\theta}_5 \frac{\mathring{n}_D}{\tau_E^{sc}} + \theta_5 \frac{\check{n}_D}{\tau_E^{sc}} - \tilde{\theta}_6 \frac{\mathring{n}_T}{\tau_E^{sc}} - \theta_6 \frac{\check{n}_T}{\tau_E^{sc}} + L_T, \tag{4.42}$$

or, in a more compact form,

$$\dot{\check{x}} = A\check{x} + L + \Phi\Theta,$$

where $\check{x} = \left[\check{n}_\alpha, \check{E}, \check{n}_D, \check{n}_T, \check{n}_I\right]^T$, $L = [L_\alpha, L_E, L_D, L_{T,} L_I]^T$, $\Theta = \left[\tilde{\theta}_1, \tilde{\theta}_2, \tilde{\theta}_3, \tilde{\theta}_4, \tilde{\theta}_5, \tilde{\theta}_6, \tilde{\theta}_7\right]^T$, and

$$\Phi = -\frac{1}{\tau_E^{sc}} \begin{bmatrix} \mathring{n}_\alpha & 0 & 0 & 0 & 0 & 0 & 0 \\ 0 & \mathring{E} & 0 & 0 & 0 & 0 & 0 \\ 0 & 0 & \mathring{n}_D & -\mathring{n}_T & 0 & 0 & 0 \\ 0 & 0 & 0 & 0 & -\mathring{n}_D & \mathring{n}_T & 0 \\ 0 & 0 & 0 & 0 & 0 & 0 & \mathring{n}_I \end{bmatrix}, \tag{4.43}$$

$$A = -\frac{1}{\tau_E^{sc}} \begin{bmatrix} \theta_1 & 0 & 0 & 0 & 0 \\ 0 & \theta_2 & 0 & 0 & 0 \\ 0 & 0 & \theta_3 & \theta_4 & 0 \\ 0 & 0 & \theta_5 & \theta_6 & 0 \\ 0 & 0 & 0 & 0 & \theta_7 \end{bmatrix}. \tag{4.44}$$

We consider the Lyapunov function

$$\check{V} = \frac{1}{2}\check{x}^T Q\check{x} + \frac{1}{2}\check{z}^T K_I \check{z}, \tag{4.45}$$

where $\check{z}$ is the integral of the output error, given by (4.6), and calculate the time derivative of $\check{V}$ as

$$\dot{\check{V}} = \check{x}^T \left[QA\check{x} + QL + Q\Phi\Theta\right] + \check{z}^T K_I \check{y}. \tag{4.46}$$

Noting that the output error can be written as

$$\check{y} = \left.\frac{\partial h}{\partial x}\right|_{x=\mathring{x}} \check{x} + H.O.T., \tag{4.47}$$

and that the scalar term $\check{z}^T K_I \check{y}$ is equivalent to $\check{y}^T K_I^T \check{z}$, we can write

$$\dot{\check{V}} = \check{x}^T Q \left[A\check{x} + L + \Phi\Theta + Q^{-1} \frac{\partial h}{\partial x}\bigg|_{x=\mathring{x}}^{T} K_I^T \check{z} \right] + (H.O.T.)\, K_I^T \check{z}. \tag{4.48}$$

By choosing

$$\begin{aligned} L &= -Q^{-1} \frac{\partial h}{\partial x}\bigg|_{x=\mathring{x}}^{T} K_I^T \check{z} + A_0 \frac{\partial h}{\partial x}\bigg|_{x=\mathring{x}}^{T} \check{y} \\ &= -Q^{-1} \frac{\partial h}{\partial x}\bigg|_{x=\mathring{x}}^{T} K_I^T \check{z} + A_0 \frac{\partial h}{\partial x}^{T}\bigg|_{x=\mathring{x}} \left(\frac{\partial h}{\partial x}\bigg|_{x=\mathring{x}} \check{x} + H.O.T. \right), \end{aligned} \tag{4.49}$$

where A_0 is a Hurwitz matrix, we have that

$$\begin{aligned} \dot{\check{V}} =& \check{x}^T Q \left[A\check{x} + A_0 h'(\mathring{x})^T h'(\mathring{x}) \check{x} + \Phi\Theta \right] \\ &+ Q A_0 h'(\mathring{x})^T (H.O.T) + (H.O.T.)\, K_I^T \check{z}. \end{aligned} \tag{4.50}$$

If θ is known exactly, then $\Theta = 0$ and we have that $\dot{\check{V}} \leq 0$ for sufficiently small state estimation errors or observer gains. It can also be shown that, the system is ISS with respect to the parameter estimation errors, Θ, implying that the estimation error $\check{x}$ will be bounded for bounded parameter estimation errors. Furthermore, since $\check{z}$ is bounded and $\check{z} = \int_0^t (\mathring{y} - y)\, d\tau$, we can be sure that the estimated output asymptotically converges to the measured output. This implies that, despite possible uncertainty in the actual states of the system, as long as the references E^r, γ^r, and n^r are chosen in such a way that the observed output tracks a desired reference, the measured output will converge to the same reference.

4.3 Adaptive Output Feedback

Because the closed loop output feedback system is ISS with respect to the uncertain model parameters, the scheme can be augmented with an online estimation scheme with parameter projection. To estimate the unknown parameters, a second observer is constructed of the form

$$\dot{n}_\alpha^{ob} = -\hat{\theta}_1 \frac{n_\alpha^{ob}}{\tau_E^{sc}} + S_\alpha, \tag{4.51}$$

$$\dot{E}^{ob} = -\hat{\theta}_2 \frac{E^{ob}}{\tau_E^{sc}} + P_\alpha - P_{rad} + P_{aux} + P_{Ohm}, \tag{4.52}$$

$$\dot{n}_I^{ob} = -\hat{\theta}_7 \frac{n_I^{ob}}{\tau_E^{sc}} + S_I^{inj} + S_I^{sp}, \tag{4.53}$$

$$\dot{n}_D^{ob} = -\hat{\theta}_3 \frac{n_D^{ob}}{\tau_E^{sc}} + \hat{\theta}_4 \frac{n_T^{ob}}{\tau_E^{sc}} - S_\alpha + S_D^{inj}, \tag{4.54}$$

$$\dot{n}_T^{ob} = \hat{\theta}_5 \frac{n_D^{ob}}{\tau_E^{sc}} - \hat{\theta}_6 \frac{n_T^{ob}}{\tau_E^{sc}} - S_\alpha + S_T^{inj}. \tag{4.55}$$

The dynamics of the observer error $n_\alpha^{ob} - n_\alpha$ are given by

$$\dot{\tilde{n}}_\alpha^{ob} = -\theta_1 \frac{\tilde{n}_\alpha^{ob}}{\tau_E^{sc}} - \tilde{\theta}_1 \frac{n_\alpha^{ob}}{\tau_E^{sc}}, \tag{4.56}$$

$$\dot{\tilde{E}}^{ob} = -\theta_2 \frac{\tilde{E}^{ob}}{\tau_E^{sc}} - \tilde{\theta}_2 \frac{E^{ob}}{\tau_E^{sc}}, \tag{4.57}$$

$$\dot{\tilde{n}}_I^{ob} = -\theta_7 \frac{\tilde{n}_I^{ob}}{\tau_E^{sc}} - \tilde{\theta}_7 \frac{n_I^{ob}}{\tau_E^{sc}}, \tag{4.58}$$

$$\dot{\tilde{n}}_D^{ob} = -\theta_3 \frac{\tilde{n}_D^{ob}}{\tau_E^{sc}} + \theta_4 \frac{\tilde{n}_T^{ob}}{\tau_E^{sc}} - \tilde{\theta}_3 \frac{n_D^{ob}}{\tau_E^{sc}} + \tilde{\theta}_4 \frac{n_T^{ob}}{\tau_E^{sc}}, \tag{4.59}$$

$$\dot{\tilde{n}}_T^{ob} = \theta_5 \frac{\tilde{n}_D^{ob}}{\tau_E^{sc}} - \theta_6 \frac{\tilde{n}_T^{ob}}{\tau_E^{sc}} + \tilde{\theta}_5 \frac{n_D^{ob}}{\tau_E^{sc}} - \tilde{\theta}_6 \frac{n_T^{ob}}{\tau_E^{sc}}, \tag{4.60}$$

or in a more compact form $\dot{\tilde{x}}^{ob} = A\tilde{x}^{ob} + \Phi^{ob}\Theta$ where $\tilde{x}^{ob} = \left[\tilde{n}_{\alpha}^{ob}, \tilde{E}^{ob}, \tilde{n}_{I}^{ob}, \tilde{n}_{D}^{ob}, \tilde{n}_{t}^{ob}\right]$ and

$$\Phi^{ob} = -\frac{1}{\tau_E^{sc}} \begin{bmatrix} n_{\alpha}^{ob} & 0 & 0 & 0 & 0 & 0 & 0 \\ 0 & E^{ob} & 0 & 0 & 0 & 0 & 0 \\ 0 & 0 & n_D^{ob} & -n_T^{ob} & 0 & 0 & 0 \\ 0 & 0 & 0 & 0 & -n_D^{ob} & n_T^{ob} & 0 \\ 0 & 0 & 0 & 0 & 0 & 0 & n_I^{ob} \end{bmatrix}. \tag{4.61}$$

We consider the Lyapunov function $V^{ob} = \frac{1}{2}\left(\tilde{x}^{ob}\right)^T Q\tilde{x}^{ob} + \Theta^T\Gamma\Theta$. The derivative can be calculated as

$$\dot{V}^{ob} = \left(\tilde{x}^{ob}\right)^T QA\tilde{x}^{ob} + \Theta^T\left(\Phi^T Q^T\tilde{x}^{ob} + \Gamma\dot{\Theta}\right), \tag{4.62}$$

If the states were all measured, the observer error could be asymptotically stabilized by choosing

$$\dot{\Theta} = -\Gamma^{-1}\left(\Phi^{ob}\right)^T Q^T\tilde{x}^{ob}. \tag{4.63}$$

However, since the states are not measured, we must approximate the parameter update law using the estimated states $\mathring{x}$. We note that $\tilde{x}^{ob} = x^{ob} - x = x^{ob} - \mathring{x} + \check{x}$, and choose the parameter update law

$$\dot{\Theta} = -\Gamma^{-1}\left(\Phi^{ob}\right)^T Q^T\left(x^{ob} - \mathring{x}\right), \tag{4.64}$$

resulting in

$$\dot{V}^{ob} = \left(\tilde{x}^{ob}\right)^T QA\tilde{x}^{ob} + \Theta^T\left(\Phi^{ob}\right)^T Q^T\check{x}. \tag{4.65}$$

This can be shown to be ISS with respect to the bounded uncertainties Θ^T and $\check{x}$. If $\check{x} \to 0$ (which can be guaranteed with a suitably chosen set of output measurements),

the second term vanishes and the observer error is rendered asymptotically stable. Given persistent excitation of the references, the parameter estimation error Θ will be driven to zero.

4.4 Online Operating Point Optimization

Noting that the nonlinear output feedback controller drives the states of the observer to the reference $r = [E^r, n^r, \gamma^r]$, and that, even in the presence of model uncertainty, the proportional-integral observer guarantees convergence of the observer outputs to the measured ones, the task remains to choose r such that the achieved outputs are those desired by the operator. To this end, the reference optimization scheme presented in Chapter 3 can be adapted to the output feedback case. We again consider a convex cost function $p(r, x, \hat{\theta})$ where, in this case, $x = [\mathring{n}_\alpha, \mathring{n}_I]^T$. We again consider the references to be constrained within a certain region of parameter space over which the cost function is convex, guaranteeing a unique minimum. The update law for the reference is again given by

$$\dot{r} = -\left(\frac{\partial^2 p}{\partial r^2}\right)^{-1}\left[K_{RTO}\frac{\partial p}{\partial r} + \frac{\partial^2 p}{\partial r \partial x}\dot{x} + \frac{\partial^2 p}{\partial r \partial \hat{\theta}}\dot{\hat{\theta}}\right], \tag{4.66}$$

where K_{RTO} is a diagonal positive definite matrix. The update law drives $\frac{\partial p}{\partial r}$ to 0, i.e., r is driven toward the optimal x-dependent and $\hat{\theta}$-dependent set point, r^*.

4.5 Simulation Study

In this section, we show results from a simulation study of the proposed output feedback burn control scheme. The nominal confinement scaling parameters were taken to be $k_\alpha^* = k_D = k_T = 3$, and $k_I^* = 10$. $Z_{imp} = 6$. An installed ICRH heating

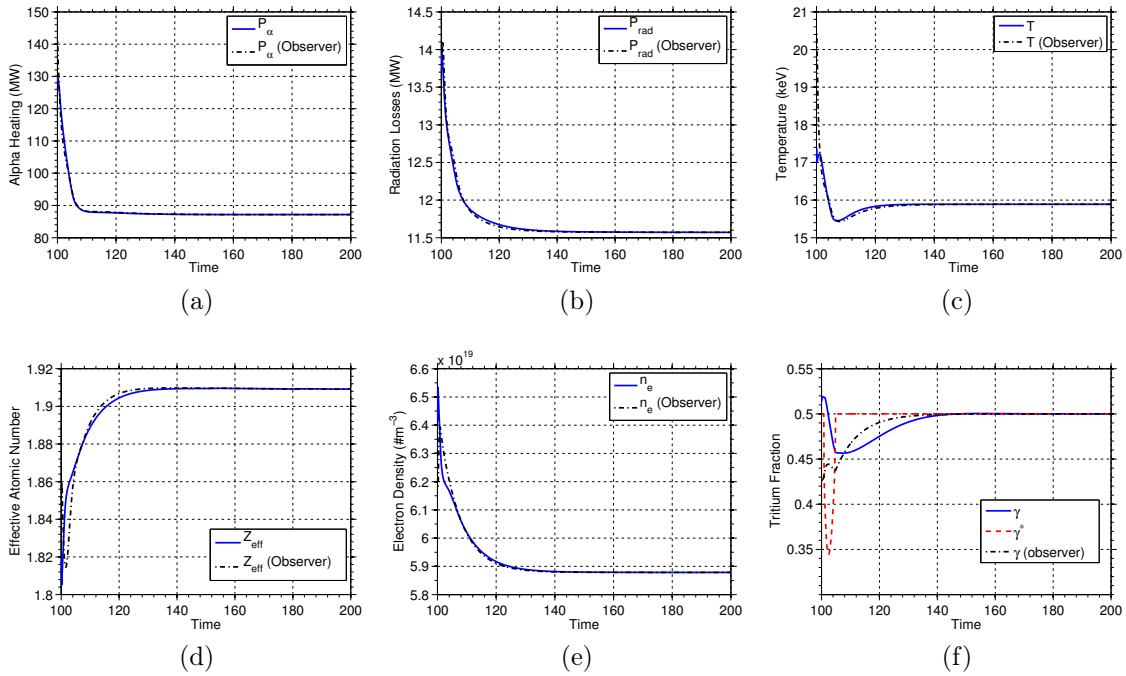

Figure 4.1: Comparison of measured outputs to the values calculated from the states of the observer during the output feedback simulation using the nominal model. The desired tritium ratio, γ^*, is shown in (f).

power $P_{ICRH}^{max} = 20$ MW was considered for feedback actuation, and the other sources of power were held constant at $P_{cd} = 53$MW. The recycling model parameters used were $\gamma^{PFC} = 0.5$, $f_{eff} = 0.3$, $f_{ref} = 0.5$, and $R^{eff} = 0.9$.

4.5.1 Scenario 1

As a first test of the performance of the proposed output feedback control scheme, a simulation was conducted using an observer and controller designed with the nominal model. The initial conditions of the observer states were made to differ from the initial conditions of the simulation states. Figure 4.1 compares the output measurements during the simulation to the values calculated from the estimated states predicted by the observer. The observed outputs converged to the measured values,

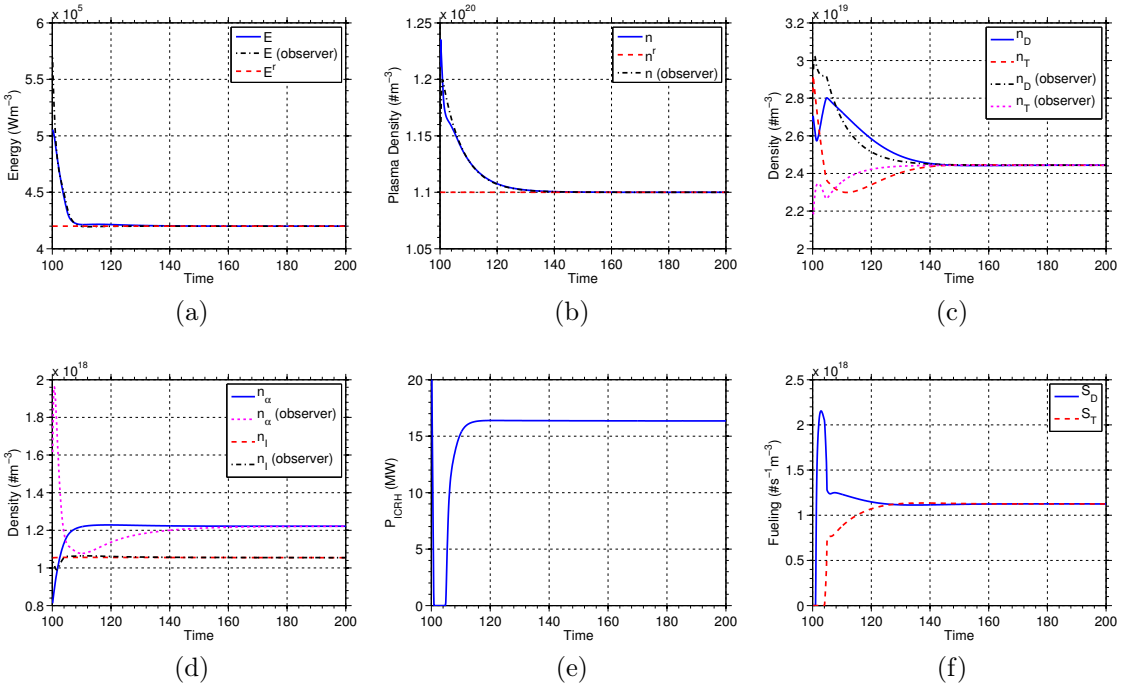

Figure 4.2: Comparison of state estimations to actual values (a-d) and actuator trajectories (e,f) during the output feedback simulation with the nominal model.

and indeed remained very close to the measured values throughout the simulation. The states of the system are compared with the estimated states in Figures 4.2a-d. As expected based on the exponential stability of the state estimation error dynamics for the nominal system, the estimated states converged to the actual values over time. Despite the absence of direct state measurements and uncertain initial conditions, the proposed scheme was able to drive the energy, density, and tritium fraction to their respective desired references, as shown in Figures 4.2a, 4.2b, and 4.1f. The feedback controlled actuator trajectories, which were calculated based on the estimated states, are shown in Figures 4.2e and 4.2f.

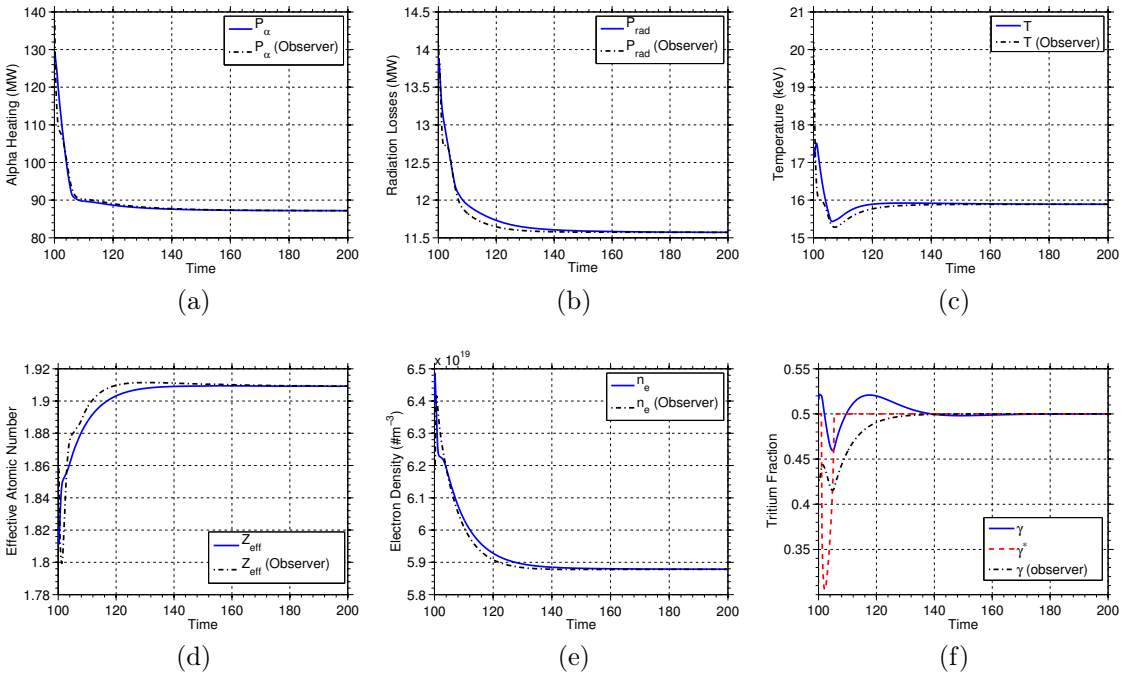

Figure 4.3: Comparison of measured outputs to the values calculated from the states of the observer during the output feedback simulation using the uncertain model. The desired tritium ratio, γ^*, is shown in (f).

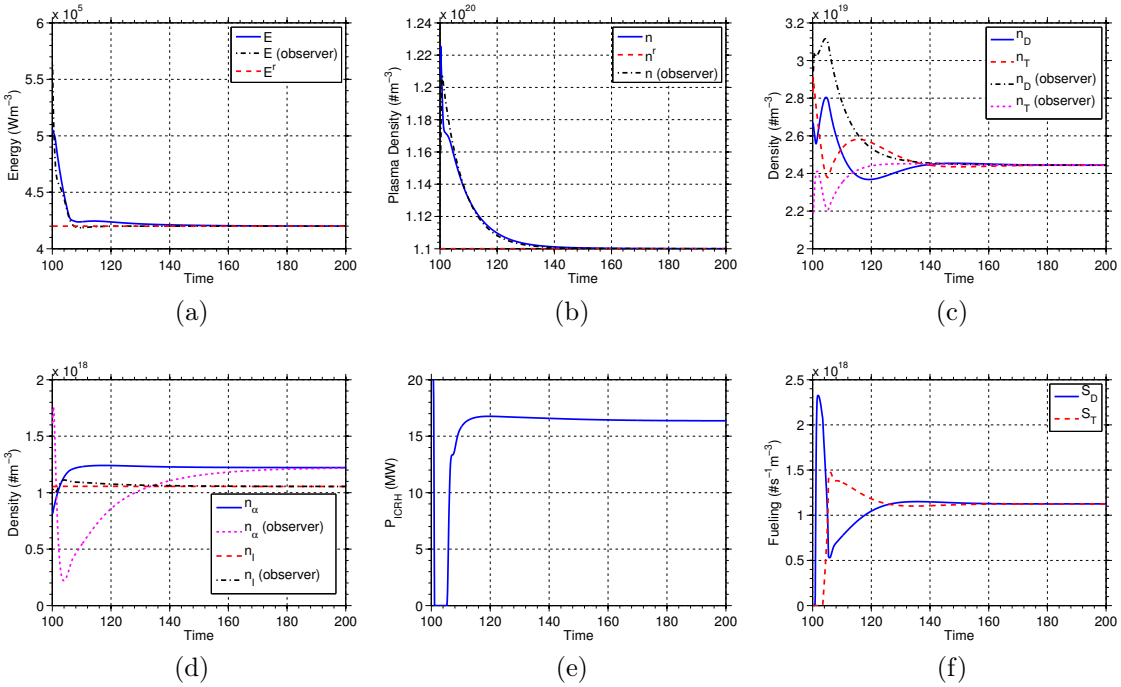

Figure 4.4: Comparison of state estimations to actual values (a-d) and actuator trajectories (e,f) during the output feedback simulation with the uncertain model.

4.5.2 Scenario 2

As a second test of the proposed scheme, the model parameters used in the controller and observer design were significantly perturbed. The parameter estimates used in the simulation were $\hat{\theta}_1 = 1.3\theta_1$, $\hat{\theta}_2 = 1.3\theta_2$, $\hat{\theta}_3 = 0.7\theta_3$, $\hat{\theta}_4 = 1.3\theta_4$, $\hat{\theta}_5 = 0.7\theta_5$, $\hat{\theta}_6 = 1.3\theta_6$, $\hat{\theta}_7 = 1.1\theta_7$. The initial conditions of the observer states were again made to differ from the initial conditions of the simulation states. Figure 4.3 compares the output measurements during the simulation to the values calculated from the estimated states predicted by the observer. Despite the model uncertainty, the observed outputs again converged to the measured values due to the presence of an integral output injection term in the observer. The estimated states of the system, compared with the estimated states in Figure 4.4a-d, also converged to the actual values over time. Though the convergence of the actual and estimated states is not,

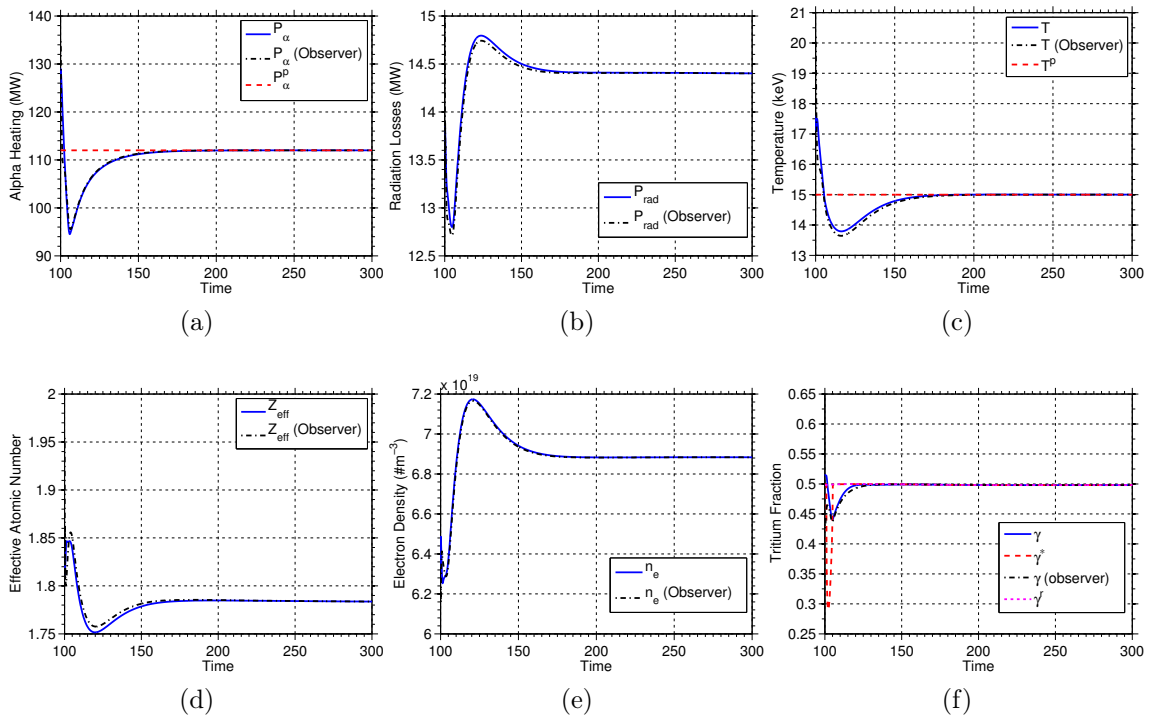

Figure 4.5: Comparison of measured outputs to the values calculated from the states of the observer during the output feedback online optimization simulation using the uncertain model. The desired and controller requested tritium ratios, γ^p and γ^*, respectively, are also shown in (f).

in general, guaranteed for an uncertain model, the set of diagnostics considered in this work results in state convergence. The proposed scheme is again shown to be able to drive energy, density, and tritium fraction states to their respective desired references, as seen in Figures 4.4a, 4.4b, and 4.3f. Finally, the feedback controlled actuator trajectories are shown in Figures 4.4e and 4.4f.

4.5.3 Scenario 3

In this simulation, online optimization of the reference r was used to minimize the cost function p. The cost function parameters $w_T = 0.1$, $w_{P_\alpha} = 1$, $w_\gamma = 1$, $T^p = 15$ keV, $P_\alpha^p = 112$ MW, and $\gamma^p = 0.5$ were used. The initial conditions of the observer states

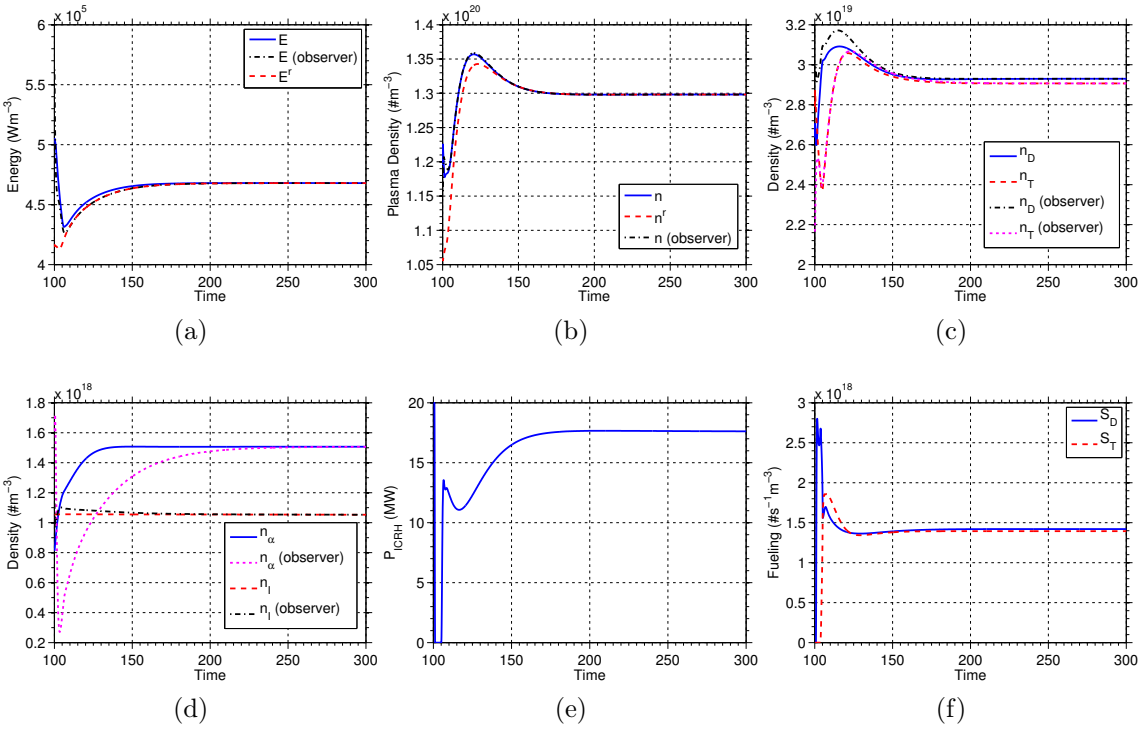

Figure 4.6: Comparison of state estimations to actual values (a-d) and actuator trajectories (e,f) during the output feedback online optimization simulation using the uncertain model.

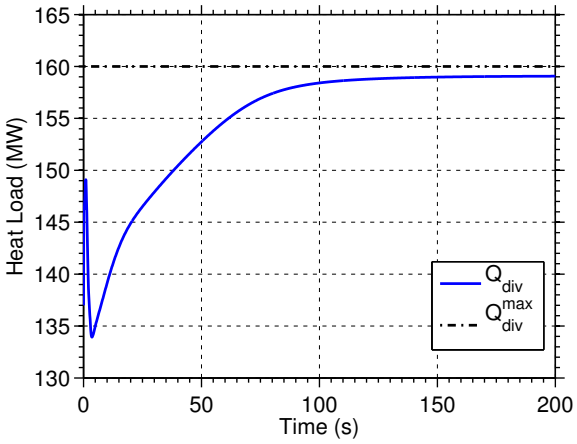

Figure 4.7: Achieved heat load in the constrained optimization simulation using adaptive output feedback compared with the limit.

were again made to differ from the initial conditions of the simulation states. Figure 4.5 compares the output measurements during the simulation to the values calculated from the estimated states predicted by the observer. Due to the integral action of the nonlinear proportional-integral observer, the observed outputs quickly converge to the measured values. In addition, Figures 4.1a, 4.1c, and 4.1f show that the fusion heating, plasma temperature, and tritium fraction converge to the desired values specified in the cost function, (P_α^p, T^p, and γ^p) as a result of the online optimization scheme. The states of the system are compared with the estimated states in Figure 4.6. The estimated states again converged to the actual values over time, and the output feedback scheme was able to drive the energy, density, and tritium fraction to their respective desired references. The optimization of the references E^r and n^r over time is clear in Figures 4.6a and 4.6b. Finally, the feedback controlled actuators are shown in Figures 4.6e and 4.6f.

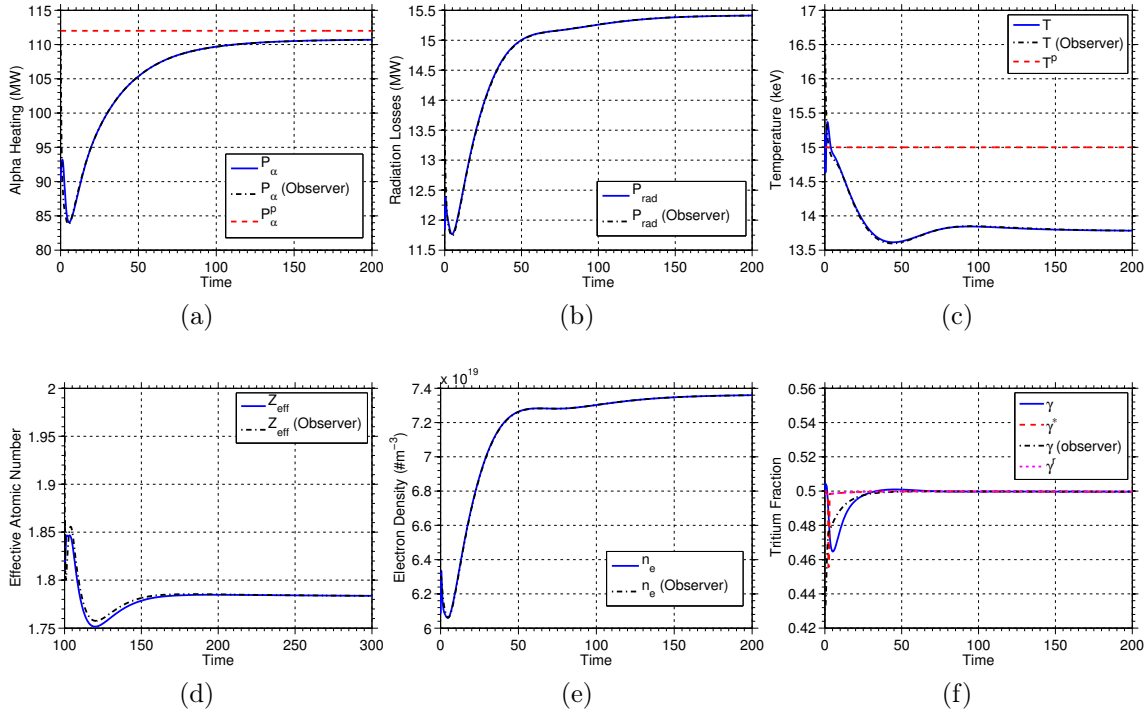

Figure 4.8: Comparison of measured outputs to the values calculated from the states of the observer during the constrained optimization simulation using adaptive output feedback. The desired and controller requested tritium ratios, γ^r and γ^*, respectively, are also shown in (f).

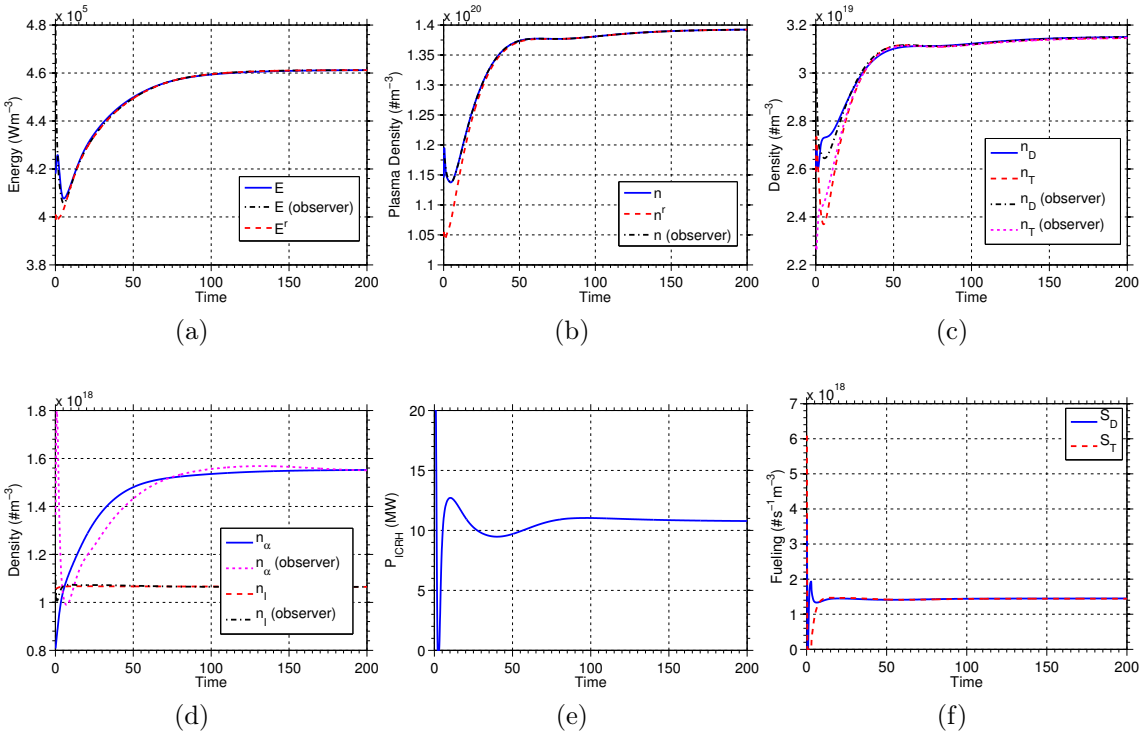

Figure 4.9: Comparison of state estimations to actual values (a,d) and actuator trajectories (e,f) during the constrained optimization simulation using adaptive output feedback.

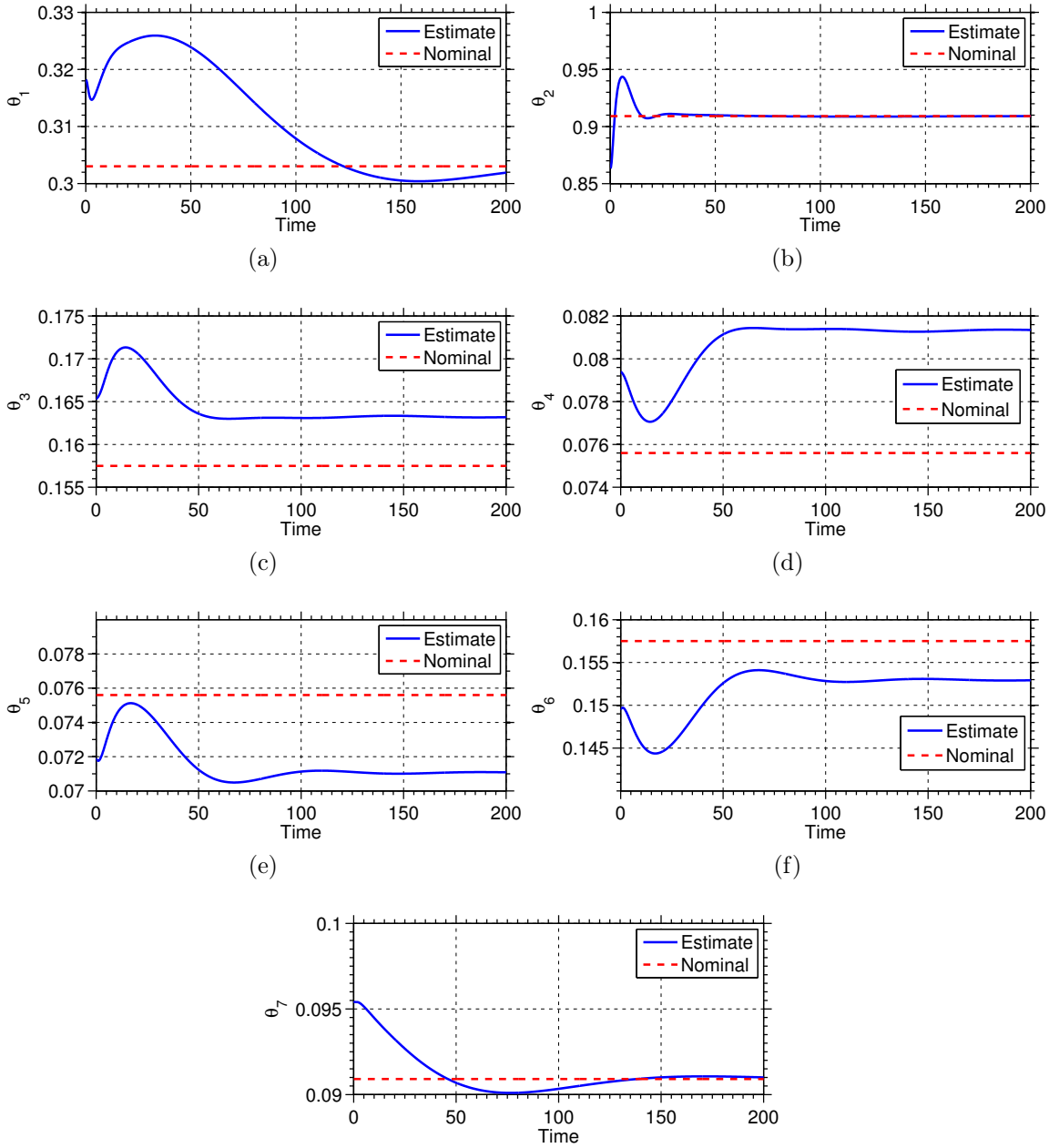

Figure 4.10: Comparison of estimated and nominal model parameters during the constrained optimization simulation using adaptive output feedback.

4.5.4 Scenario 4

In this simulation, the uncertain model parameters were estimated online using the adaptive update law (4.64), and online optimization of the reference r was used to minimize the cost function p. The cost function parameters $w_T = 0.1$, $w_{P_\alpha} = 1$, $w_\gamma = 1$, $T^p = 15$ keV, $P_\alpha^p = 112$ MW, and $\gamma^p = 0.5$ were used. A constraint on the maximum heat load to the divertor of $Q_{div}^{max} = 160$ MW was also considered. Note that the uncertain parameter θ_2 enters into the cost function through the calculation of the divertor heat load, i.e., $Q_{div} = \theta_2 E/\tau_E^{sc}$. Figure 4.7 shows that the controller is able to respect the heat load constraint throughout the simulation by considering the constraint in the online set point optimization scheme. Figures 4.8 compares the output measurements during the simulation to the values calculated from the estimated states predicted by the observer. The observed outputs converge to the measured values, and indeed remain very close to the measured values throughout the simulation. In addition, Figures 4.8a, c, and f show that the fusion heating, plasma temperature, and tritium fraction converge to constant values close to the desired values specified in the cost function, (P_α^p, T^p, and γ^p). Unlike the previous scenario, the desired values are not achieved due to the presence of the constraint on the divertor heat load. The online optimization instead drove the system to the optimal feasible operating point. The states of the system are compared with the estimated states in Figure 4.9. The estimated states converged to the actual values over time, and the output feedback scheme successfully drove the energy, density, and tritium fraction to their respective references. The optimization of the references E^r and n^r over time is clear in Figures 4.9a and b. The feedback controlled actuators are shown in Figures 4.9e and f. Finally, the estimated and nominal model parameters are compared in Figure 4.10. Recall that the constraint on the heat load depends on the parameter θ_2, the estimate of which is shown to quickly converge to the nominal

value in Figure 4.10b.

4.6 Conclusions

A nonlinear output feedback control scheme for tracking a desired burn condition in tokamak fusion reactors has been presented. The proposed scheme utilizes a nonlinear proportional-integral observer that guarantees that the observer estimates converge to the actual values for the nominal system. When model uncertainty is present, the state estimation errors are bounded and the predicted output converges to the measured values. Through the use of adaptive parameter estimation and online constrained optimization, the nonlinear output feedback controller is able drive the burning plasma system to feasible operating point that optimizes a particular figure of merit. A simulation study shows the effectiveness of the output feedback scheme, even when significant initial estimation errors and model uncertainties are present.

Chapter 5

Study of Nonlinear Burn Control Strategies Using METIS

5.1 Introduction

Thus far, the burn control strategies developed in this work have been tested by simulating the closed loop system resulting from a feedback interconnection of the controllers with the simplified burning plasma model used for control design. The use of simplified models in simulation is useful for preliminary implementation testing and controller tuning, since the simplified model can be simulated quite quickly. To some degree, robustness of the control strategies to parametric model uncertainty, noise, and disturbances can also be assessed using simplified models. However, in all control engineering applications, it is critical to understand how control laws will affect (or be affected by) the complex physical processes neglected by the design model. While experimental implementation is the best test of controller performance, the expense of fusion experiments and the potential for poorly performing controllers to trigger MHD or thermal instabilities motivate an intermediate validation step in which control laws

designed with simplified models are tested with increasingly complex simulation codes.

Complex integrated tokamak modeling codes seek to model the numerous physical systems within a tokamak to either predict performance based on prescribed actuators, or interpret the results of experiments through reconstruction of unmeasured quantities of interest based on available measurements. These codes are typically made up of smaller modules, each tailored to accurately model specific physical processes. Examples of integrated modeling codes include PTRANSP [62], developed at Princeton Plasma Physics Laboratory, and CRONOS [63], developed by the Commissariat à l'Énergie Atomique (CEA) in France.

While very accurate integrated modeling codes can be useful tools for predicting tokamak performance and making detailed analysis of experimental results, the complexity of the codes leads to very long computation times. For certain purposes, including conceptual feedback control design studies, the detailed and computationally intensive calculations done in codes like PTRANSP and CRONOS are not necessary, making simpler, faster running codes a desirable alternative. The METIS (**M**inute **E**mbedded **T**okamak **I**ntegrated **S**imulator) code, developed by researchers at the Commissariat à l'Énergie Atomique (CEA) in France, is an alternative simulation tool that combines information from scaling laws and simplified models to quickly predict the evolution of tokamak plasmas based on a set of prescribed input trajectories. It is a tool in the CRONOS suite of simulation codes designed to enable fast processing of experimental data for analysis of shots, preparation of experimental scenarios and CRONOS simulations, and, in conjunction with Simulink, development of feedback control schemes. In this chapter, a framework for testing burn control strategies in METIS is presented and several simulation scenarios are shown that demonstrate the potential effectiveness of the control schemes proposed in the previous chapters. This work represents the preliminary steps toward the rigorous testing

and analysis of comprehensive burn control strategies required before implementation in ITER experiments.

This chapter is organized as follows. In Section 5.2, the models used in the METIS code are briefly described, while in Section 5.3 the framework used to implement and simulate burn control strategies is discussed. The results of simulations using the METIS simulation framework are presented in Section 5.4. Finally, conclusions are given in Section 5.5.

5.2 Overview of METIS Calculations

A diagram of the coupling of the various modules of the METIS code is given in Figure 5.1. The models used within each module are chosen to provide a suitable trade-off between precision and computation time. In the following, a brief overview of the various models is provided, focusing on the calculations that are relevant to burn control studies.

5.2.1 Geometry and Magnetohydrodynamic Equilibrium

While full magnetic equilibrium calculations are used in CRONOS to describe the geometry of the plasma, METIS uses a simplified description. The plasma is assumed to be symmetric about the $Z = Z_{ref}$ plane, where Z is the vertical axis of the tokamak, and the last closed flux surface is described by time varying parameters, including the minor radius, major radius, elongation, and triangularity. The complete MHD equilibrium is calculated using Shafranov shift, ellipticity, and triangularity profiles, determined from moment equations [64].

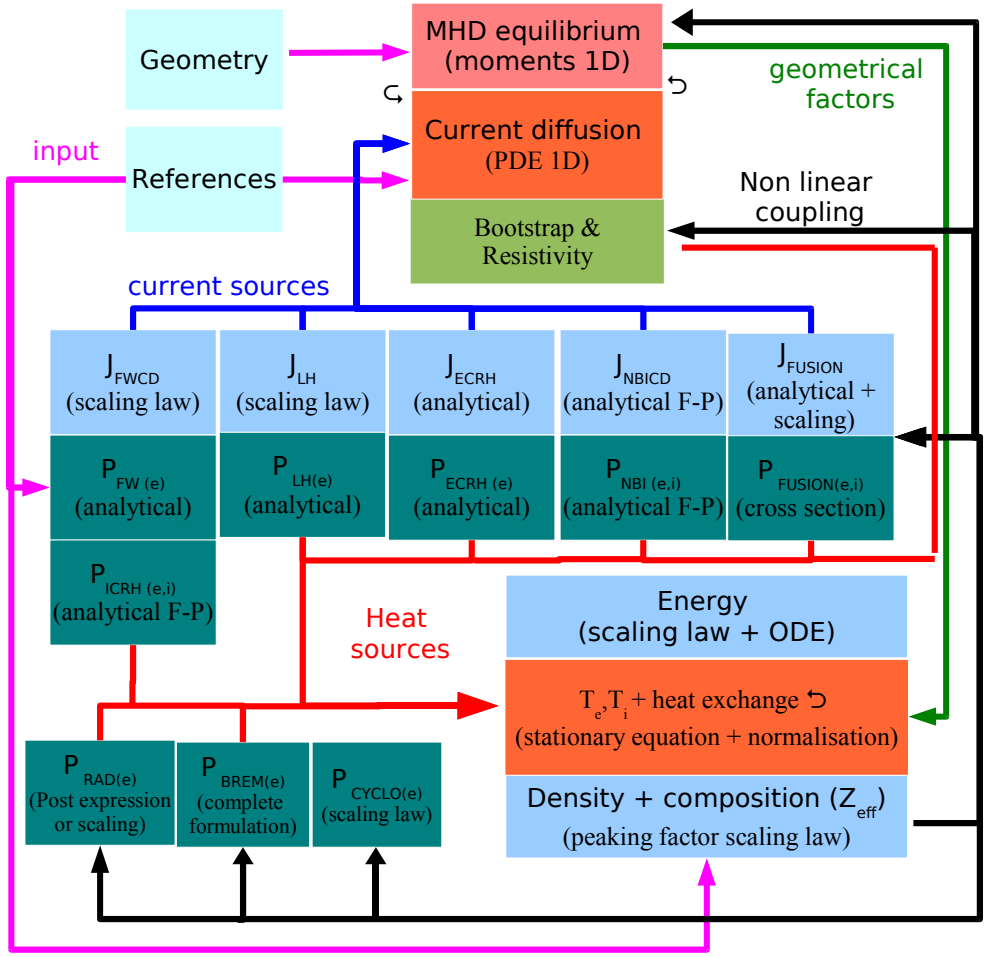

Figure 5.1: Schematic of the METIS code depicting the interconnection of modules. (Source: CEA).

5.2.2 Power Sources and Sinks

For ITER, the auxiliary heating and current drive (H&CD) is provided by ion cyclotron and electron cyclotron radio frequency H&CD, as well as neutral beam H&CD. For each source, the total heating and current drive efficiencies and spatial distribution profiles are calculated separately in METIS based on different formulations chosen to provide the best trade-off in terms of computational complexity and precision.

Fusion power calculations include the dominant DT reactions, the less significant DD reactions within the plasma, as well as reactions involving the fast ions from neutral beam injection. DT fusion calculations are based on the deuterium and tritium density profiles, and the ion temperature profile, which is used to determine the reactivity. Ohmic heating is also calculated based on the current density and plasma resistivity.

Radiative power losses represent a major energy sink in tokamak discharges. In METIS, the total line transition and thermal bremsstrahlung radiation are calculated based on the temperature, density, and composition profiles of the plasma by using the radiative collisional equilibrium [65]. The bremsstrahlung losses are calculated using an expression given in [66], and the line radiation is inferred from the difference between the total losses and the bremsstrahlung losses. Electron cyclotron radiative losses are also calculated using a scaling law [67].

5.2.3 Kinetic Profiles

In METIS, the PDE describing the dynamics of the current profile, commonly referred to as the magnetic diffusion equation, is solved using the Crank-Nicholson method on a spatial grid of 21 points. The boundary conditions are given by a no-flux boundary condition in the center of the plasma, and either prescribed plasma current, loop

voltage, or edge flux. The resistivity and bootstrap current, both calculated using the Sauter model [68], the auxiliary current drive sources, and geometric factors calculated from the plasma equilibrium are combined with the boundary conditions to calculate the current profile evolution.

The dynamics of the plasma stored energy are treated with a 0-D (volume averaged) energy balance model that uses scaling laws to determine the energy confinement. The line averaged density, tritium fraction, and effective atomic number, which are time-varying inputs to the METIS code, are combined with peaking factor and edge density scaling laws to determine the density profiles of each ion species (deuterium, tritium, alpha particles, and impurities). The ion and electron temperature profiles are calculated by solving the steady-state temperature transport equations, using the distributed heating sources and sinks (fusion, NBI, radiative losses, etc.), with a no-flux boundary condition at the magnetic axis and the edge temperature (calculated from scaling laws) as the outer boundary condition. The thermal conductivities, κ_e and κ_i, are assumed to have fixed spatial profiles, and it is assumed that $\kappa_i = \mu_{e,i}\kappa_e$, where $\mu_{e,i}$ can be prescribed or obtained from scaling laws. The magnitude of the thermal conductivity is iteratively changed until the calculated temperature profiles result in a volume averaged stored energy matching the results of the dynamic 0D stored energy calculation. Through additional scaling laws that modify the confinement and shape of conductivity profiles, magnetohydrodynamic (MHD) effects and internal transport barriers are approximately taken into account.

5.3 Burn Control Simulation Framework

The METIS code is typically run in an open loop mode, i.e., inputs are prescribed prior to running the model. In order to test control laws and run in closed loop, the

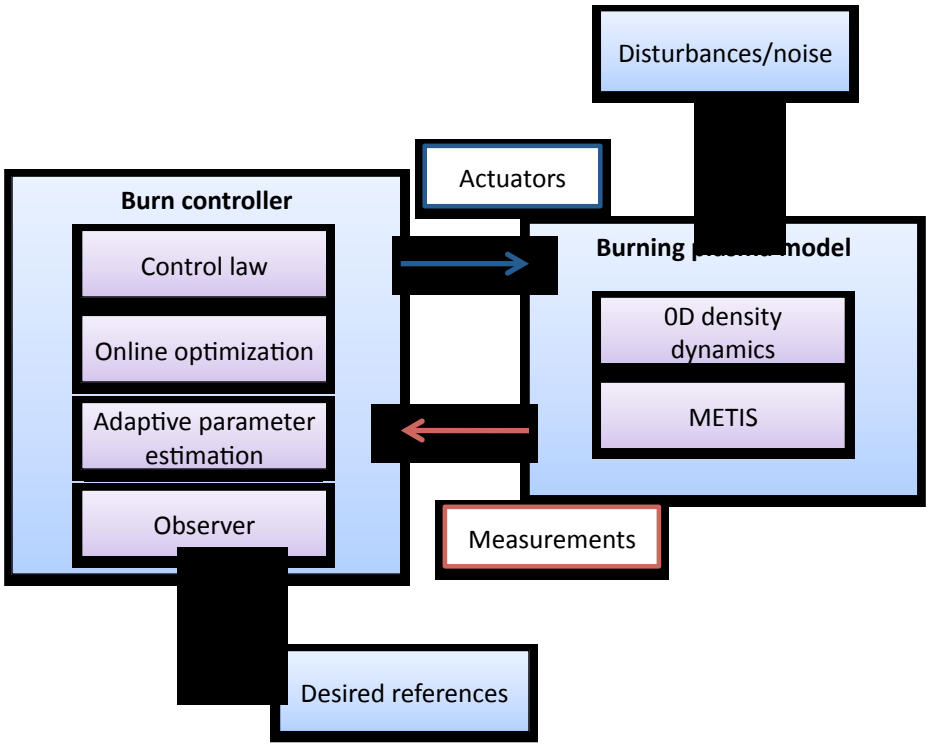

Figure 5.2: Framework used for simulating burn control algorithms with METIS.

METIS code has been embedded within a Simulink S-function block. At each time step in a simulation, measured outputs from the METIS block are sent to blocks containing feedback control laws, and the resulting actuator requests are subsequently sent through input channels. These inputs are then used by the METIS model to calculate the states of the burning plasma system at the next time step of the simulation. To test controller robustness, disturbances and noise can be added to the measurements or actuator signals.

While the METIS code provides an integrated model of many of the physical processes contributing to the evolution of tokamak plasma discharges, some processes are not handled in a way that is appropriate for the study of burn control strategies. For example, the plasma density, fuel composition, and effective atomic number are considered inputs to the METIS model, while they are in reality dynamic states

of the system governed by fueling, particle losses, and recycling. To overcome this limitation, the particle balance model, described in Chapter 2, was implemented in a Matlab S-function. The inputs to the function include the fueling rates, energy confinement time, alpha-particle generation rate, and impurity injection rates. The outputs of the density dynamic model, the effective atomic number, line averaged density, and isotopic mix, are then routed to the respective inputs of the METIS model. The complete METIS simulation framework for burn control studies is depicted in Figure 5.2.

5.4 Simulation Results

In this section, results of a simulation study using the METIS framework are presented.

5.4.1 Scenario 1

In this scenario, the adaptive controller with online optimization from Chapter 3 was tested. The adaptive controller was activated near the start of the burn ramp-up, $t = 50s$ (pre-programmed actuator trajectories were used during the non-burning early ramp-up phase of the discharge). Preprogrammed time-varying references E^r and n^r were used from $t = 50$s to $t = 100$s, that is, no online optimization was used. At $t = 100$s, the online optimization scheme was activated in order to move the system to an operating point optimizing the cost function (3.47) with $w_{P_\alpha} = 1$, $w_T = 0.1$, $P_\alpha^p = 98MW$, and $T^p = 13$keV. The reference for the isotopic mix was held fixed at $\gamma^r = 0.5$.

During the simulation, the volume averaged plasma parameters, including $\langle S_\alpha \rangle$, $\langle P_\alpha \rangle$, and $\langle P_{rad} \rangle$, where $\langle \cdot \rangle$ is used to distinguish the volume average from spatially

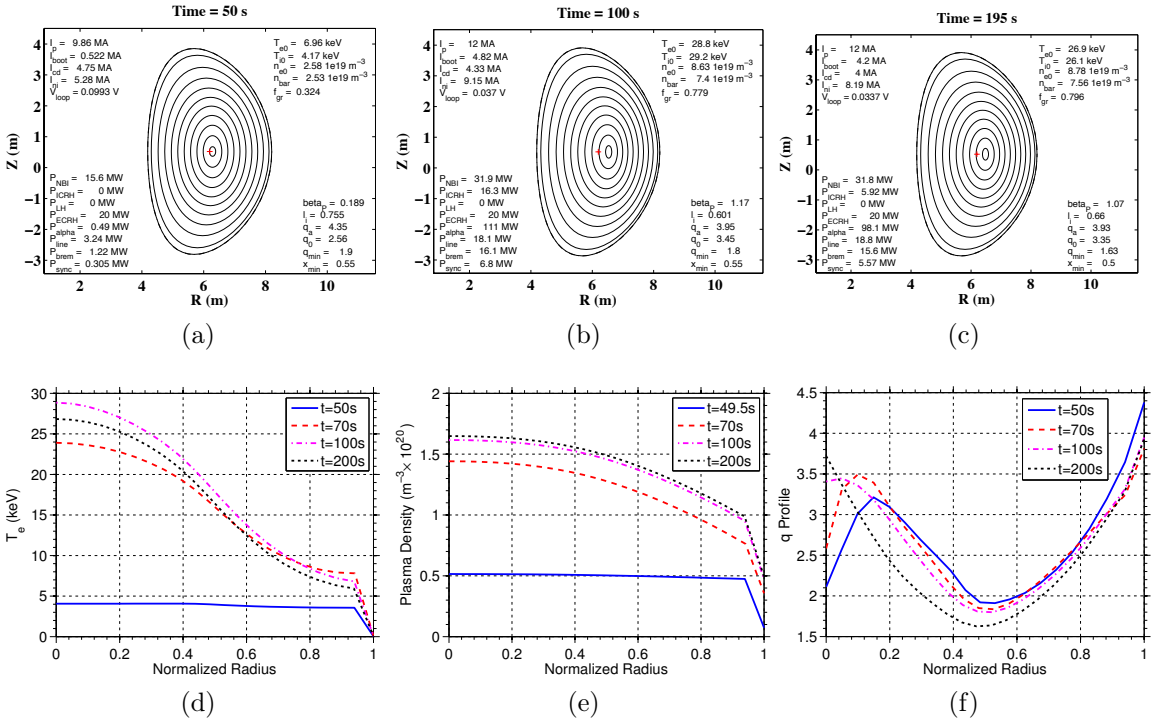

Figure 5.3: Evolution of the plasma cross-sectional shape (a-c) and parameter profiles (d-f) during Scenario 1.

varying profiles, were assumed to be measured. As was done in the one-dimensional simulations of the nonlinear controller proposed in Chapter 2 (see Section 2.6), a slight modification to the calculation of γ^* in Step 2 of the control scheme is made to account for the effect of the spatial distribution of parameters. We define $\langle\gamma\rangle = \langle n_T\rangle/(\langle n_T\rangle + \langle n_D\rangle)$ and write $\langle S_\alpha\rangle = f_p^\gamma\langle\gamma\rangle\left(1-\langle\gamma\rangle\right)\langle n_H\rangle^2\langle\sigma v\rangle\left(\langle T\rangle\right)$ where f_p^γ is a scale factor used to account for the effects of spatial profiles that is calculated in real-time based on measurements of the volume averaged states and fusion heating. The scale factor is then used to calculate

$$\langle\gamma^*\rangle\left(1-\langle\gamma^*\rangle\right) = \frac{\left[\theta_2\frac{\langle E\rangle^r}{\tau_E^{sc}} + \langle P_{rad}\rangle - \langle P_{Ohm}\rangle - \langle P_{aux}\rangle + \langle\dot{E}\rangle^r - K_E\langle\tilde{E}\rangle\right]}{Q_\alpha f_p^\gamma\langle\gamma\rangle\left(1-\langle\gamma\rangle\right)\langle n_H\rangle^2\langle\sigma v\rangle\left(\langle T\rangle\right)} = C, \quad (5.1)$$

$$\langle\gamma^*\rangle = \frac{1\pm\sqrt{1-4C}}{2}. \quad (5.2)$$

A similar modification is made to calculate the required impurity density in Step 4. Aside from these modifications and the notational change, i.e., the use of $\langle\cdot\rangle$, the control laws are unchanged. The peaking factors for the other measured plasma parameters were also used in the online optimization scheme to calculate the optimal operating point.

In Figures 5.3a-c, the poloidal cross-section of the plasma is compared at various times during the controlled discharge. As the density and temperature were ramped up, the shape changed slightly, however, it remained fairly constant for most of the discharge. The spatial profiles of electron temperature T_e, plasma density n, and safety factor q (a quantity related to the current profile), are depicted in Figures 5.3d-f at various times during the simulation. The H-mode pedestal can be noted at a normalized radius of 0.95 in Figures 5.3d and 5.3e. Note that the temperature and density profiles changed significantly during the early part of the simulation (between $t = 50$s and $t = 70$s, but the shape of the profiles did not change significantly after

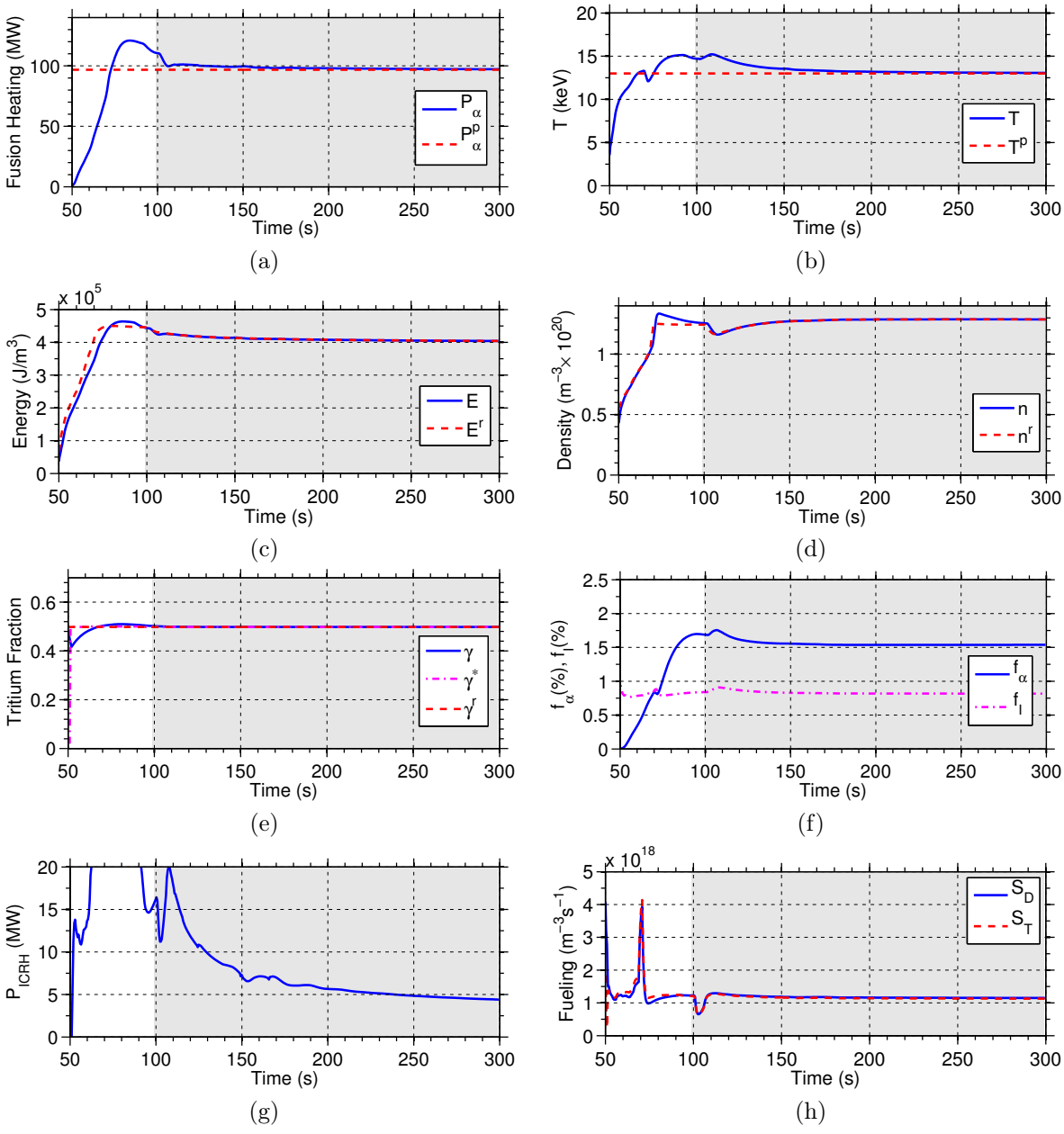

Figure 5.4: Closed loop evolution of (a) fusion heating, (b) temperature, (c) energy, (d) density, (e) tritium fraction, (f) alpha-fraction, and impurity fraction, along with closed loop response of (g) auxiliary heating and (h) fueling actuators during the simulation of Scenario 1. The online optimization scheme was active during the shaded time interval.

$t = 100$s. Only a change in magnitude is seen between $t = 100$s and $t = 200$s. The q profile, shown in Figure 5.3f, evolves at a much slower rate than the other kinetic variables and did not reach a steady state during the simulation.

The output, state, and actuator trajectories during the simulation are compared in Figure 5.4. Figures 5.4a and b show that between $t = 50$s and $t = 100$s, the fusion power and temperature are ramped up, eventually exceeding the desired values (recall that online optimization of the operating point was not active during this time interval, i.e., a preprogrammed, non-optimal reference was being tracked by the controller). At $t = 100$s, the online optimization scheme was activated and was able to quickly drive the fusion heating and temperature toward the targets. The time-varying pre-programmed references for energy and density can be noted between $t = 50$s and $t = 100$s in Figures 5.4c and d. The references were tracked quite well, though some tracking error can be noted as the adaptive parameter update laws responded to the changing model parameter values. The adjustment of the references E^r and n^r by the online optimization scheme can be seen after $t = 100$s. The constant reference for the tritium fraction was regulated after initial tracking errors due to parameter uncertainty, as seen in Figure 5.4e. The alpha particle and impurity densities, shown in Figure 5.4f, settled to constant values over time. Finally, the actuators, modified by the nonlinear controller to track the time-varying references for energy, density, and tritium fraction, are shown in Figures 5.4g and h. It can be noted that, to some degree, the energy tracking error during the ramp-up can be attributed to saturation of the ICRH heating power.

The estimated model parameters are compared to the nominal values in Figure 5.5. Between roughly $t = 50$s and $t = 100$s, the parameter estimates changed over time, eventually settling to a constant set of estimates. The estimates of θ_1 and θ_7 (Figure 5.5a and 5.5g, respectively) converged to their nominal values. The value

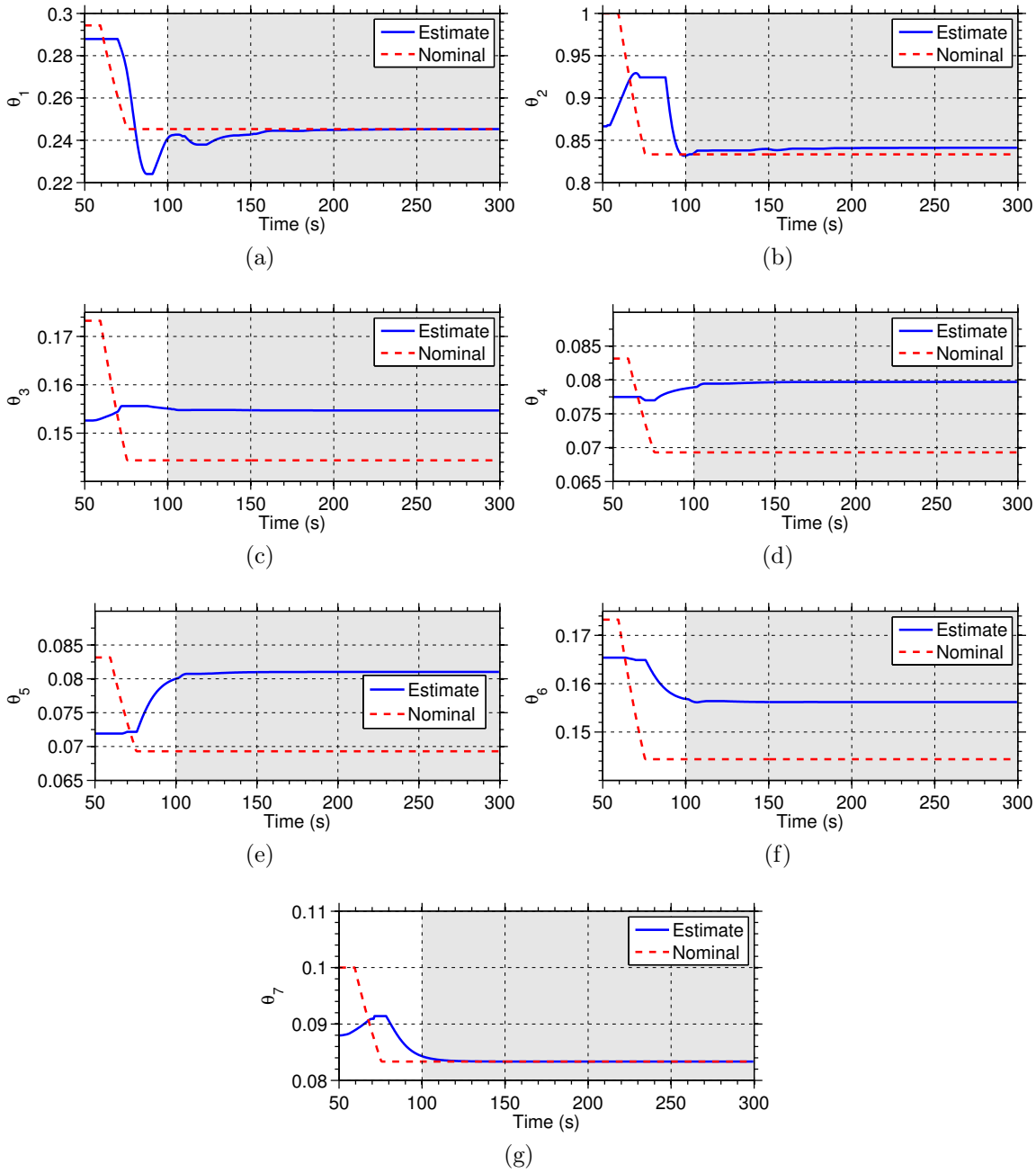

Figure 5.5: Comparison of estimated and nominal model parameters during the METIS simulation of Scenario 1.

of θ_2, shown in Figure 5.5b, did not quite converge to its nominal value. This is because, while METIS considers the fact that not all power delivered by the various heating sources is actually absorbed by the plasma, the model used for control design assumes the sources to have unity efficiency. As was the case in previous simulations, the remaining model parameters did not converge to the nominal values due to a lack of sufficient excitation, however, this does not effect the tracking performance of the adaptive control scheme.

5.4.2 Scenario 2

In this scenario, the output feedback controller from Chapter 4 was tested. The observer was initiated at $t = 50$s with incorrect initial state estimates, as well as incorrect model parameters given by $\hat{\theta} = [1.05\theta_1, 0.92\theta_2, 1.1\theta_3, 0.95\theta_4, 0.95\theta_5, 1.1\theta_6, 0.95\theta_7]$. A preprogrammed time-varying reference for the energy and density was used from $t = 50$s to $t = 100$s, that is, no online optimization was used. At $t = 100$s, the online optimization scheme was activated in order to drive the system to an operating point optimizing the cost function (3.47) with $w_{P_\alpha} = 1$, $w_T = 0.1$, $P_\alpha^p = 98MW$, and $T^p = 13$keV. The reference for the isotopic mix was held fixed at $\gamma^r = 0.5$. Since the output feedback scheme relies on knowledge of how the measured volume averaged outputs depend on the volume averaged states of the system, the peaking factors associated with each output are needed to account for the distributed nature of the kinetic variables. However, since measurements of the volume averaged states were considered to be unavailable in this test of the output feedback scheme, it was not possible to calculate these peaking factors in real-time, as was possible in the previous state feedback scenario. To overcome this issue for this preliminary test case, it is assumed that the peaking factors are well-known ahead of time, or can be calculated based on measured or estimated spatial distribution profile measurements.

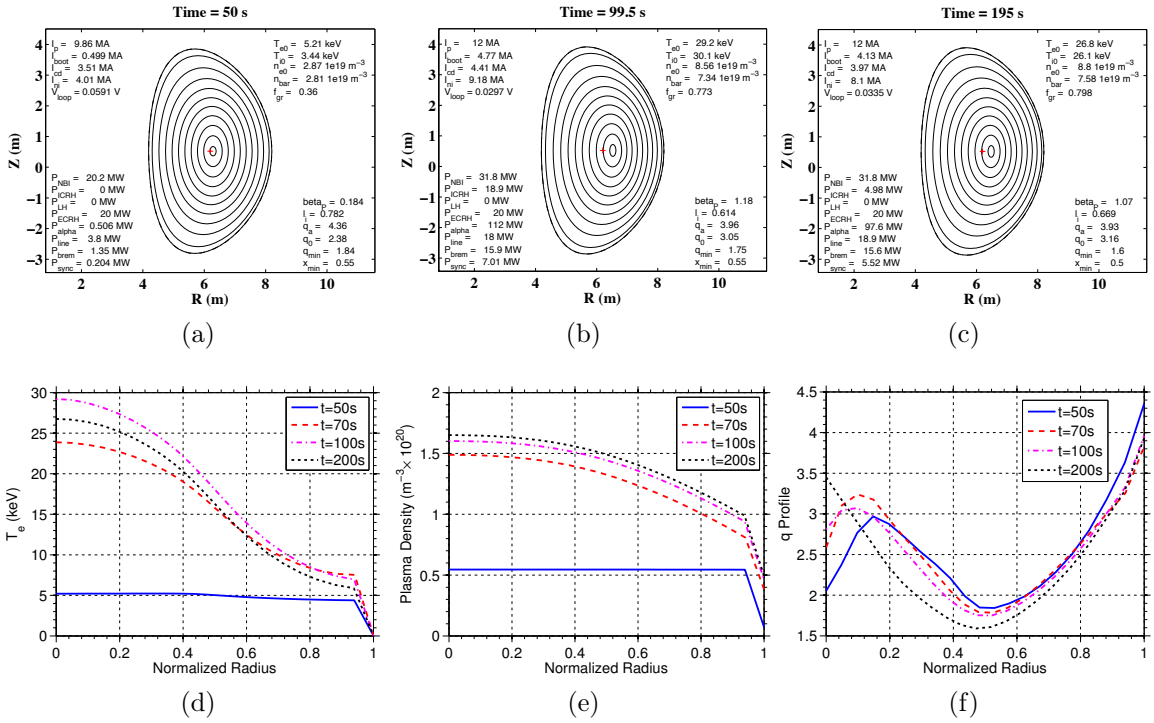

Figure 5.6: Evolution of the plasma cross-sectional shape (a-c) and parameter profiles (d-f) during Scenario 2.

In Figures 5.6a-c, the poloidal cross-section of the plasma is compared at various times during Scenario 2. Again, the shape remained fairly constant for most of the discharge. The spatial profiles of electron temperature T_e and plasma density n, depicted in Figures 5.6d and 5.6e at various times during the simulation, match closely with those of the previous state feedback simulation. The q profile evolution, shown in Figure 5.6f, is also quite similar to the previous scenario, though slight differences in the evolution near the plasma center can be noted, which are a result of differences in the transient response of the plasma temperature and density during the two simulations.

Figure 5.7 compares the output measurements during the METIS simulation to the values calculated from the estimated states predicted by the observer. Due to the integral action of the nonlinear proportional-integral observer, the observed outputs quickly converged to the measured values. In addition, Figures 5.7a and 5.7c show that the fusion heating and plasma temperature converged to the desired values specified in the cost function, (P_α^p and T^p) as a result of the online optimization scheme. The states of the system are compared with the estimated states in Figure 5.8. The estimated states converged to the actual values over time, and the output feedback scheme was able to drive the energy, density, and tritium fraction to their respective desired references. The optimization of the references E^r and n^r over time can be noted in Figures 5.8a and 5.8b. Finally, the feedback controlled actuator trajectories are shown in Figures 5.8e and 5.8f.

5.5 Conclusions

A simulation framework for studying burn control algorithms that combines the METIS integrated modeling code with a 0D density dynamics model and a customiz-

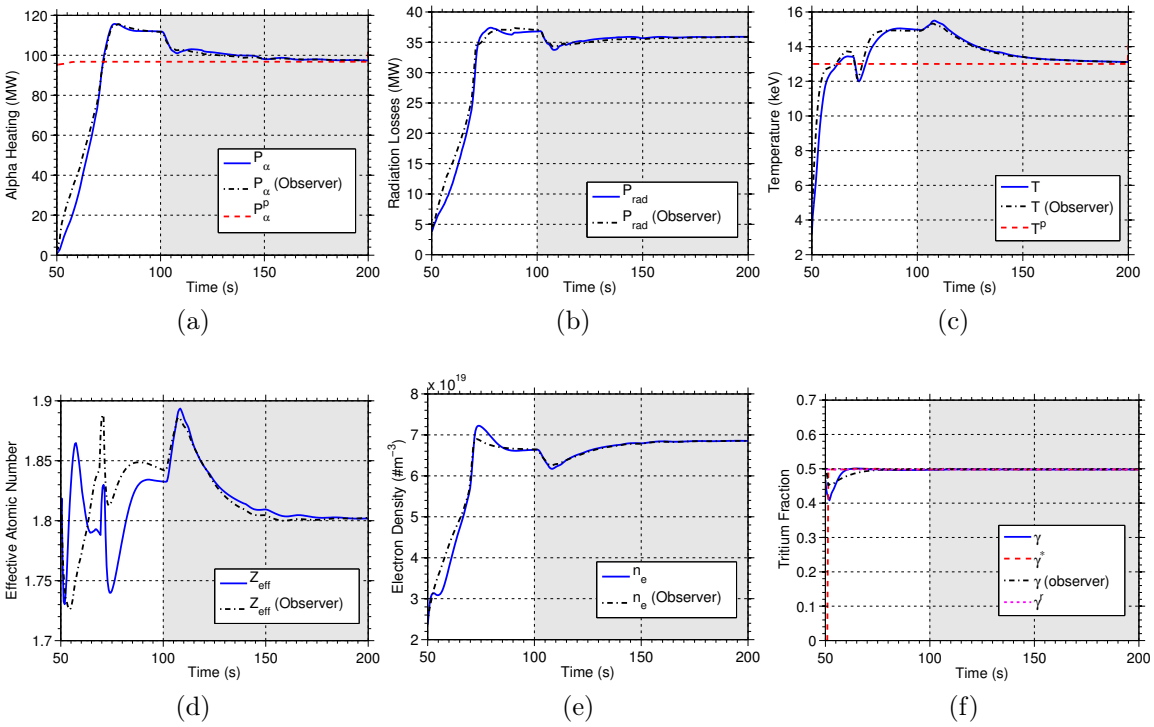

Figure 5.7: Comparison of measured outputs to the values calculated from the states of the observer during the online optimization METIS simulation using the uncertain model. The desired and controller requested tritium ratios, γ^r and γ^*, respectively, are also shown in (f).

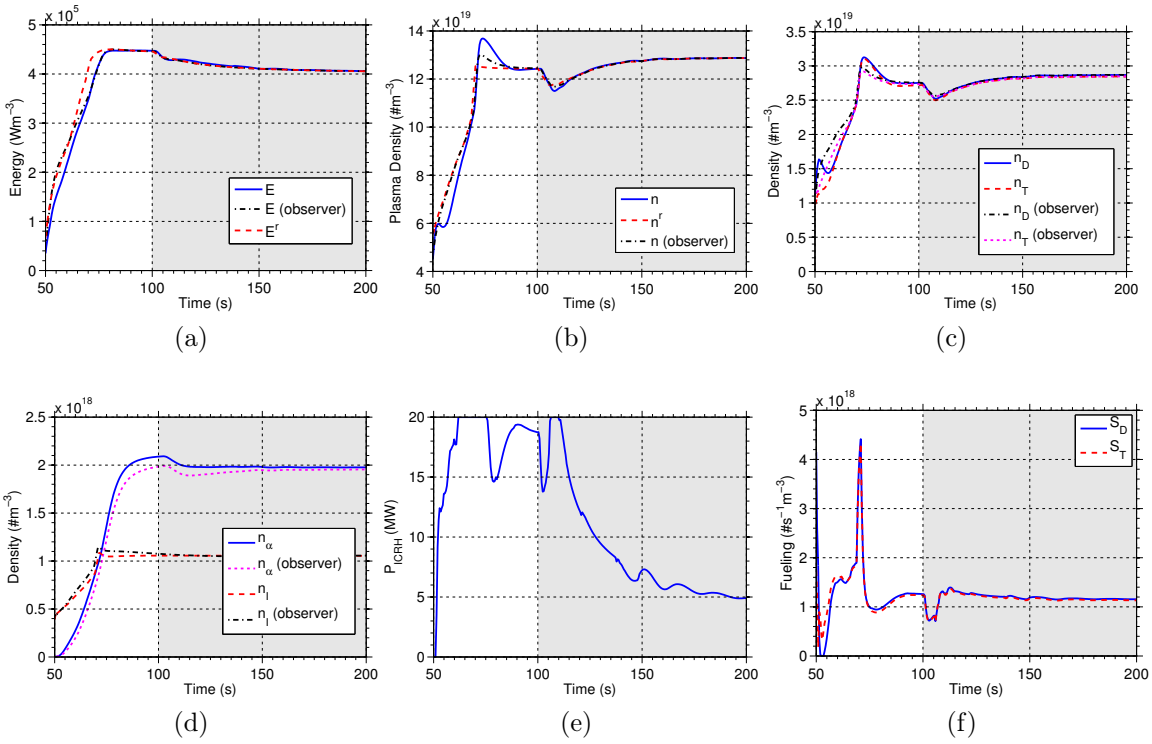

Figure 5.8: Comparison of states estimations to actual values (a,d) and actuator trajectories (e,f) during the METIS simulation using output feedback.

able controller block, has been implemented. The burn control schemes proposed in the previous chapters have been simulated in this framework to study their robustness to the increased complexity of the METIS model. The additional complexity of the METIS model could be exploited in the future to perform a more comprehensive test the designs, including analyzing performance during various experimental scenarios, and studying the effects of imperfect measurements, noise, and disturbances. Additionally, the additional complexity of the METIS code could enable study control strategies designed to simultaneously regulate the burn condition and kinetic profiles.

Chapter 6

Backstepping Control of Burning Plasma Density and Temperature Profiles

6.1 Introduction

In the previous several chapters, the problem of zero-dimensional burn condition control in ITER was studied in detail. This zero-dimensional approach to the problem only modulates the bulk heating and fueling in response to volume averaged densities and temperatures, and does not attempt to regulate the spatial distributions of these quantities. However, the shape of the temperature and density profiles not only directly affect the burn condition and particle/energy transport, but also affects the evolution of the current profile, which in turn plays an important role in achieving large fractions of non-inductively sustained current. The problem of profile control differs from the zero-dimensional burn control problem due to the spatially distributed, infinite-dimensional nature of the quantity being controlled. The system

is severely underactuated, as only a finite number of available actuators, either distributed throughout the spatial domain or located at the boundary, are available for control.

In this work, we apply the backstepping technique to the control of density and temperature profiles in burning plasmas. Backstepping provides a systematic method for designing control laws for PDE systems where actuation is applied at the boundary and must be propagated through spatial dynamics. The method achieves stability and performance improvement by using a feedback transformation to eliminate undesirable terms or to add missing terms, while leaving the system in a physically relevant and familiar form. This enables physical intuition to be used to shape the closed-loop response. The control gain is obtained by using a simple recursive numerical calculation, which avoids the need to solve high-dimensional Riccati equations. Furthermore, the approach can be used to handle time-varying model parameters and nonlinear terms, like those arising in the burning plasma system.

In this work, we have taken a discretize-then-design approach to designing the backstepping controller [69], rather than the design-then-discretize approach taken in [70]. This results in a simple recursive formula for an approximation to the infinite dimensional gain kernel that would be derived using the latter approach. The approximation, which holds for any finite spatial grid, can be improved through the use of a fine grid. However, it has been seen that a controller designed on a coarse grid (using a small number of measurements of the profile) can achieve satisfactory closed-loop response when tested in simulations (with a much finer grid used for simulating the PDE model) and experiments. We note that the discretize-then-design backstepping technique has been applied to open-loop unstable nonlinear chemical reactions in [71, 72] and has been applied to other tokamak control problems, specifically the problem of kinetic profile control, in [36, 37, 73]. In this work, the backstepping

technique is extended to include both boundary and distributed actuation, as well as online disturbance estimation, improving system response, disturbance rejection, and tracking performance.

The chapter is organized as follows. In Section 6.2 a one-dimensional burning plasma model is introduced. The control objective and controller design are outlined in Section 6.3 and Section 6.4, respectively. Simulation results showing successful stabilization of an unstable set of equilibrium profiles are contained in Section 6.5. Concluding remarks and a discussion of future work are given in Section 6.6.

6.2 One-Dimensional Burning Plasma Model

The one-dimensional burning plasma model must include the dynamics of the spatial profiles of the density of α-particles, the deuterium-tritium fuel, as well as the spatial profile of the energy in the system. The model used in this work is based on standard 1-D transport equations. To simplify presentation, we consider a constant diffusivity and a negligible pinch velocity, however, the control approach could be extended to account for these effects, as was done in [36]. The equations for particle densities and plasma energy are

$$\frac{\partial n_\alpha}{\partial t} = \frac{1}{r}\frac{\partial}{\partial r} r \left(D \frac{\partial n_\alpha}{\partial r} \right) + \left(\frac{n_{DT}}{2} \right)^2 \langle \sigma\nu \rangle, \tag{6.1}$$

$$\frac{\partial n_{DT}}{\partial t} = \frac{1}{r}\frac{\partial}{\partial r} r \left(D \frac{\partial n_{DT}}{\partial r} \right) - 2\left(\frac{n_{DT}}{2} \right)^2 \langle \sigma\nu \rangle + S_{DT}, \tag{6.2}$$

$$\frac{\partial E}{\partial t} = \frac{1}{r}\frac{\partial}{\partial r} r \left(D \frac{\partial E}{\partial r} \right) + Q_\alpha \left(\frac{n_{DT}}{2} \right)^2 \langle \sigma\nu \rangle - P_{rad} + P_{aux}, \tag{6.3}$$

where $\langle \sigma\nu \rangle$ is the DT reactivity, S_{DT} is the distributed DT fuel injection, and $Q_\alpha = 3.52$ MeV is the alpha particle energy. P_{aux} and P_{rad} represent the distributed auxiliary power and radiation losses, respectively. We consider the distributed actu-

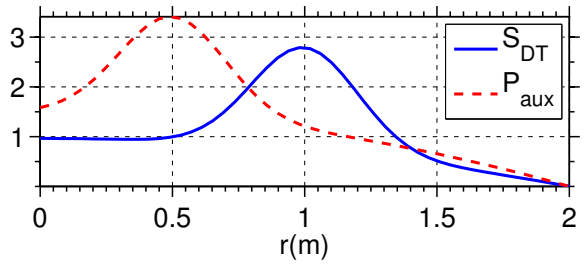

Figure 6.1: Distributed actuator deposition profiles used for simulations.

ators to be of the form

$$S_{DT} = u_{fuel}(t)\hat{S}_{DT}(r),$$
$$P_{aux} = u_{aux}(t)\hat{P}_{aux}(r),$$

i.e., they have fixed, spatial deposition profiles $\hat{S}_{DT}(r)$ and $\hat{P}_{aux}(r)$ and controllable magnitudes $u_{fuel}(t)$ and $u_{aux}(t)$. The deposition profiles used in this work are shown in Figure 6.1.

The DT reactivity $\langle\sigma\nu\rangle$ is a highly nonlinear, positive, and bounded function of the plasma temperature T and is calculated by

$$\langle\sigma\nu\rangle = exp\left(\frac{a_1}{T^r} + a_2 + a_3T + a_4T^2 + a_5T^3 + a_6T^4\right), \tag{6.4}$$

where the parameters a_i and r are taken from [43]. The plasma temperature is a function of the energy and total plasma density, i.e., $T = \frac{2}{3}\frac{E}{n}$, and the total plasma density is given by the sum of ion and electron densities, n_i and n_e

$$n_i = n_{DT} + n_\alpha, \tag{6.5}$$
$$n_e = n_{DT} + 2n_\alpha, \tag{6.6}$$
$$n = n_i + n_e = 2n_{DT} + 3n_\alpha, \tag{6.7}$$

The radiation loss P_{rad} considered in this work is given by

$$P_{rad} = P_{brem} = A_b Z_{eff} n_e^2 \sqrt{T}, \tag{6.8}$$

where $A_b = 5.5 \times 10^{-37}$ $\mathrm{Wm}^3/\sqrt{\mathrm{keV}}$ is the bremsstrahlung radiation coefficient, Z_{eff} is the effective atomic number, and n_e is the electron density. Note that the control design presented in this work could easily be extended to include other forms of radiation losses and this choice of model is only used for simplification of presentation. The effective atomic number is given by

$$Z_{eff} = \sum_i \frac{n_i Z_i^2}{n_e} = \frac{n_{DT} + 4n_\alpha}{n_e}. \tag{6.9}$$

The following boundary conditions are used:

$$\left.\frac{\partial n_\alpha}{\partial r}\right|_{r=0} = \left.\frac{\partial n_{DT}}{\partial r}\right|_{r=0} = \left.\frac{\partial E}{\partial r}\right|_{r=0} = 0, \tag{6.10}$$

$$n_\alpha(a) = u_\alpha(t), \tag{6.11}$$

$$n_{DT}(a) = u_{DT}(t), \tag{6.12}$$

$$E(a) = u_E(t), \tag{6.13}$$

where $u_\alpha(t)$, $u_{DT}(t)$, and $u_E(t)$ are considered actuators.

6.3 Control Objective

At equilibrium, the DT fuel, alpha particle, and energy densities are no longer changing with respect to time and the model simplifies to a set of ODEs with respect to

the space coordinate, i.e.,

$$0 = \frac{1}{r}\frac{\partial}{\partial r} r \left(D \frac{\partial \bar{n}_\alpha}{\partial r} \right) + \bar{S}_\alpha, \tag{6.14}$$

$$0 = \frac{1}{r}\frac{\partial}{\partial r} r \left(D \frac{\partial \bar{n}_{DT}}{\partial r} \right) - 2\bar{S}_\alpha + \bar{u}_{fuel} \hat{S}_{DT}, \tag{6.15}$$

$$0 = \frac{1}{r}\frac{\partial}{\partial r} r \left(D \frac{\partial \bar{E}}{\partial r} \right) + Q_\alpha \bar{S}_\alpha - \bar{P}_{rad} + \bar{u}_{aux} \hat{P}_{aux}, \tag{6.16}$$

where we have written the alpha particle generation as $S_\alpha = \left(\frac{n_{DT}}{2}\right)^2 \langle \sigma\nu \rangle$ and we use upper bar notation to represent the equilibrium value of a variable. The equilibrium profiles are determined by the equilibrium fueling, heating, and boundary conditions.

We consider perturbations in the profiles, i.e., $n_\alpha(r,t) = \bar{n}_\alpha(r) + \tilde{n}_\alpha(r,t)$, $n_{DT}(r,t) = \bar{n}_{DT}(r) + \tilde{n}_{DT}(r,t)$, $E(r,t) = \bar{E}(r) + \tilde{E}(r,t)$, $S_\alpha(r,t) = \bar{S}_\alpha(r) + \tilde{S}_\alpha(r,t)$, and $P_{rad}(r,t) = \bar{P}_{rad}(r) + \tilde{P}_{rad}(r,t)$, and the presence of distributed feedback ($\tilde{u}_{fuel}$, $\tilde{u}_{aux}$) and constant input disturbances (d_{DT}, d_{aux}), i.e.,

$$S_{DT}(r,t) = (\bar{u}_{fuel} + \tilde{u}_{fuel} + d_{fuel})\, \hat{S}_{DT}(r),$$

$$P_{aux}(r,t) = (\bar{u}_{aux} + \tilde{u}_{aux} + d_{aux})\, \hat{P}_{aux}(r).$$

We also consider boundary feedback ($\tilde{u}_\alpha$, $\tilde{u}_{DT}$, $\tilde{u}_E$) and constant boundary disturbances (d_α, d_{DT}, d_E). We first attempt to cancel the effect of the unknown disturbances by defining the feedback laws

$$\tilde{u}_\alpha = v_\alpha - \hat{d}_\alpha, \qquad \tilde{u}_{DT} = v_{DT} - \hat{d}_{DT}, \qquad \tilde{u}_E = v_E - \hat{d}_E,$$

$$\tilde{u}_{fuel} = v_{fuel} - \hat{d}_{fuel}, \qquad \tilde{u}_{aux} = v_{aux} - \hat{d}_{aux},$$

where v_α, v_{DT}, v_E, v_{fuel}, and v_{aux} are inputs to be defined later, and $\hat{d}_\alpha$, $\hat{d}_{DT}$, $\hat{d}_E$, $\hat{d}_{fuel}$, and $\hat{d}_{aux}$ are estimates of the disturbances, which will be obtained from update laws,

also to be defined later. We define the disturbance estimation errors $\tilde{d}_\alpha = d_\alpha - \hat{d}_\alpha$, $\tilde{d}_{DT} = d_{DT} - \hat{d}_{DT}$, $\tilde{d}_E = d_E - \hat{d}_E$, $\tilde{d}_{fuel} = d_{fuel} - \hat{d}_{fuel}$, and $\tilde{d}_{aux} = d_{aux} - \hat{d}_{aux}$. By substituting (6.14), (6.15), and (6.16) into (6.1), (6.2), and (6.3), and taking into account

$$\frac{1}{r}\frac{\partial}{\partial r}\left[rD\frac{\partial(\cdot)}{\partial r}\right] = \frac{\partial}{\partial r}\left[D\frac{\partial(\cdot)}{\partial r}\right] + \frac{1}{r}D\frac{\partial(\cdot)}{\partial r},$$

the dynamics of the deviation variables $\tilde{n}_\alpha(r,t)$, $\tilde{n}_{DT}(r,t)$, and $\tilde{E}(r,t)$ can be written as

$$\frac{\partial \tilde{n}_\alpha}{\partial t} = D\frac{\partial^2 \tilde{n}_\alpha}{\partial r^2} + \frac{1}{r}D\frac{\partial \tilde{n}_\alpha}{\partial r} + \tilde{S}_\alpha, \tag{6.17}$$

$$\frac{\partial \tilde{n}_{DT}}{\partial t} = D\frac{\partial^2 \tilde{n}_{DT}}{\partial r^2} + \frac{1}{r}D\frac{\partial \tilde{n}_{DT}}{\partial r} - 2\tilde{S}_\alpha + \left(v_{fuel} + \tilde{d}_{DT}\right)\hat{S}_{DT}, \tag{6.18}$$

$$\frac{\partial \tilde{E}}{\partial t} = D\frac{\partial^2 \tilde{E}}{\partial r^2} + \frac{1}{r}D\frac{\partial \tilde{E}}{\partial r} + Q_\alpha \tilde{S}_\alpha - \tilde{P}_{rad} + \left(v_{aux} + \tilde{d}_{aux}\right)\hat{P}_{aux}, \tag{6.19}$$

The boundary conditions are written as

$$\left.\frac{\partial \tilde{n}_\alpha}{\partial r}\right|_{r=0} = \left.\frac{\partial \tilde{n}_{DT}}{\partial r}\right|_{r=0} = \left.\frac{\partial \tilde{E}}{\partial r}\right|_{r=0} = 0, \tag{6.20}$$

$$\tilde{n}_\alpha(a) = v_\alpha(t) + \tilde{d}_\alpha, \tag{6.21}$$

$$\tilde{n}_{DT}(a) = v_{DT}(t) + \tilde{d}_{DT}, \tag{6.22}$$

$$\tilde{E}(a) = v_E(t) + \tilde{d}_E. \tag{6.23}$$

The objective of the controller is to force $\tilde{n}_\alpha(r,t)$, $\tilde{n}_{DT}(r,t)$ and $\tilde{E}(r,t)$ to zero using distributed actuators v_{fuel} and v_{aux}, and boundary actuators v_α, v_{DT}, and v_E, while accounting for the effect of disturbance estimation errors.

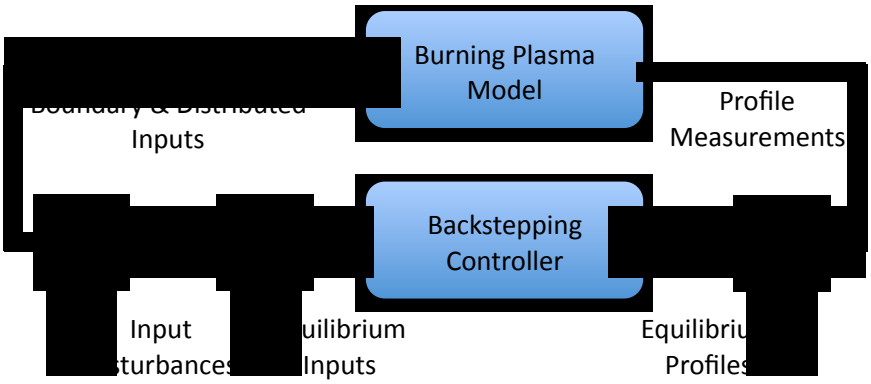

Figure 6.2: Block diagram of simulation process.

6.4 Controller Design

A backstepping technique, like the one used in the previous chapter, is used to transform the original system of equations into a particular target system. The target system is rendered asymptotically stable through the choice of boundary conditions, control laws for the distributed actuators, and update laws for the disturbance estimations.

By defining $h = \frac{1}{N}$, where N is an integer, and using the notation $x^i(t) = x(ih, t)$, $i = 0, 1, ..., N$, the discretized version of (6.17) - (6.19) can be written as

$$\dot{\tilde{n}}_\alpha^i = D\frac{\tilde{n}_\alpha^{i+1} - 2\tilde{n}_\alpha^i + \tilde{n}_\alpha^{i-1}}{h^2} + \frac{D}{ih}\frac{\tilde{n}_\alpha^{i+1} - \tilde{n}_\alpha^i}{h} + \tilde{S}_\alpha^i, \tag{6.24}$$

$$\begin{aligned}\dot{\tilde{n}}_{DT}^i =& D\frac{\tilde{n}_{DT}^{i+1} - 2\tilde{n}_{DT}^i + \tilde{n}_{DT}^{i-1}}{h^2} + \frac{D}{ih}\frac{\tilde{n}_{DT}^{i+1} - \tilde{n}_{DT}^i}{h} \\ & - 2\tilde{S}_\alpha^i + \left(v_{fuel} + \tilde{d}_{fuel}\right)\hat{S}_{DT}^i,\end{aligned} \tag{6.25}$$

$$\begin{aligned}\dot{\tilde{E}}^i =& D\frac{\tilde{E}^{i+1} - 2\tilde{E}^i + \tilde{E}^{i-1}}{h^2} + \frac{D}{ih}\frac{\tilde{E}^{i+1} - \tilde{E}^i}{h} \\ & + Q_\alpha \tilde{S}_\alpha^i - \tilde{P}_{rad}^i + \left(v_{aux} + \tilde{d}_{aux}\right)\hat{P}_{aux}^i,\end{aligned} \tag{6.26}$$

with the boundary conditions written as

$$\frac{\tilde{n}_\alpha^1 - \tilde{n}_\alpha^0}{h} = \frac{\tilde{n}_{DT}^1 - \tilde{n}_{DT}^0}{h} = \frac{\tilde{E}^1 - \tilde{E}^0}{h} = 0, \tag{6.27}$$

$$\tilde{n}_\alpha^N = v_\alpha(t) + \tilde{d}_\alpha, \tag{6.28}$$

$$\tilde{n}_{DT}^N = v_{DT}(t) + \tilde{d}_{DT}, \tag{6.29}$$

$$\tilde{E}^N = v_E(t) + \tilde{d}_E. \tag{6.30}$$

The following target system is considered

$$\begin{aligned}
\dot{\tilde{w}}^i =& D\frac{\tilde{w}^{i+1} - 2\tilde{w}^i + \tilde{w}^{i-1}}{h^2} + \frac{1}{ih}D\frac{\tilde{w}^{i+1} - \tilde{w}^i}{h} - C_w\tilde{w}^i \\
&+ \left(v_{fuel} + \tilde{d}_{fuel}\right)\Omega_{fuel}^i + \left(v_{aux} + \tilde{d}_{aux}\right)\Omega_{aux}^i, \qquad (6.31) \\
\dot{\tilde{m}}^i =& D\frac{\tilde{m}^{i+1} - 2\tilde{m}^i + \tilde{m}^{i-1}}{h^2} + \frac{1}{ih}D\frac{\tilde{m}^{i+1} - \tilde{m}^i}{h} - C_m\tilde{m}^i \\
&+ \left(v_{fuel} + \tilde{d}_{fuel}\right)B_{fuel}^i + \left(v_{aux} + \tilde{d}_{aux}\right)B_{aux}^i, \qquad (6.32) \\
\dot{\tilde{f}}^i =& D\frac{\tilde{f}^{i+1} - 2\tilde{f}^i + \tilde{f}^{i-1}}{h^2} + \frac{1}{ih}D\frac{\tilde{f}^{i+1} - \tilde{f}^i}{h} - C_f\tilde{f}^i \\
&+ \left(v_{fuel} + \tilde{d}_{fuel}\right)A_{fuel}^i + \left(v_{aux} + \tilde{d}_{aux}\right)A_{aux}^i, \qquad (6.33)
\end{aligned}$$

where $C_w, C_m, C_f > 0$ and

$$\begin{aligned}
\Omega_{fuel}^i &= -\sum_{k=1}^{i-1}\frac{\partial\omega^{i-1}}{\partial\tilde{n}_{DT}^k}\hat{S}_{DT}^k, & \Omega_{aux}^i &= -\sum_{k=1}^{i-1}\frac{\partial\omega^{i-1}}{\partial\tilde{E}^k}\hat{P}_{aux}^k, \\
B_{fuel}^i &= \hat{S}_{DT}^i - \sum_{k=1}^{i-1}\frac{\partial\beta^{i-1}}{\partial\tilde{n}_{DT}^k}\hat{S}_{DT}^k, & B_{aux}^i &= -\sum_{k=1}^{i-1}\frac{\partial\beta^{i-1}}{\partial\tilde{E}^k}\hat{P}_{aux}^k, \\
A_{fuel}^i &= -\sum_{k=1}^{i-1}\frac{\partial\alpha^{i-1}}{\partial\tilde{n}_{DT}^k}\hat{S}_{DT}^k, & A_{aux}^i &= \hat{P}_{aux}^i - \sum_{k=1}^{i-1}\frac{\partial\alpha^{i-1}}{\partial\tilde{E}^k}\hat{P}_{aux}^k.
\end{aligned}$$

We denote ω, β, and α as backstepping transformations of the form

$$\tilde{w}^i = \tilde{n}^i_\alpha - \omega^{i-1}(\tilde{E}^0, \ldots, \tilde{E}^{i-1}, \tilde{n}^0_{DT}, \ldots, \tilde{n}^{i-1}_{DT}, \tilde{n}^0_\alpha, \ldots, \tilde{n}^{i-1}_\alpha),$$
$$\tilde{m}^i = \tilde{n}^i_{DT} - \beta^{i-1}(\tilde{E}^0, \ldots, \tilde{E}^{i-1}, \tilde{n}^0_{DT}, \ldots, \tilde{n}^{i-1}_{DT}, \tilde{n}^0_\alpha, \ldots, \tilde{n}^{i-1}_\alpha),$$
$$\tilde{f}^i = \tilde{E}^i - \alpha^{i-1}(\tilde{E}^0, \ldots, \tilde{E}^{i-1}, \tilde{n}^0_{DT}, \ldots, \tilde{n}^{i-1}_{DT}, \tilde{n}^0_\alpha, \ldots, \tilde{n}^{i-1}_\alpha).$$

The boundary conditions of the target system are chosen as

$$\frac{\tilde{w}_1 - \tilde{w}_0}{h} = \frac{\tilde{m}^1 - \tilde{m}^0}{h} = \frac{\tilde{f}^1 - \tilde{f}^0}{h} = 0, \tag{6.34}$$
$$\tilde{w}^N = \tilde{d}_\alpha, \tag{6.35}$$
$$\tilde{m}^N = \tilde{d}_{DT}, \tag{6.36}$$
$$\tilde{f}^N = \tilde{d}_E. \tag{6.37}$$

The target system is chosen to maintain the parabolic character of the partial differential equation (to keep the highest order derivatives), remove the problematic nonlinear terms, and facilitate the combined use of distributed feedback and backstepping boundary feedback.

By subtracting (6.31) from (6.24), (6.32) from (6.25), and (6.33) from (6.26), the expressions $\dot{\omega}^{i-1} = \dot{\tilde{n}}^i_\alpha - \dot{\tilde{w}}^i$, $\dot{\beta}^{i-1} = \dot{\tilde{n}}^i_{DT} - \dot{\tilde{m}}^i$, and $\dot{\alpha}^{i-1} = \dot{\tilde{E}}^i - \dot{\tilde{f}}^i$ are obtained, which can be put in terms of $\omega^{k-1} = \tilde{n}^k_\alpha - \tilde{w}^k$, $\beta^{k-1} = \tilde{n}^k_{DT} - \tilde{m}^k$, and $\alpha^{k-1} = \tilde{E}^k - \tilde{f}^k$, for $k = i-1, i, i+1$ and rearranged to obtain

$$\begin{aligned}\omega^i = \frac{1}{D + D/i}\Bigg[&\left(2D + \frac{D}{i} + C_w h^2\right)\omega^{i-1} - D\omega^{i-2} \\ &- h^2 C_w \tilde{n}^i_\alpha + h^2 \dot{\omega}^{i-1} + h^2\left(v_{fuel} + \tilde{d}_{fuel}\right)\Omega^i_{fuel} \\ &+ h^2\left(v_{aux} + \tilde{d}_{aux}\right)\Omega^i_{aux} - h^2 \tilde{S}^i_\alpha\Bigg],\end{aligned} \tag{6.38}$$

$$\beta^i = \frac{1}{D + D/i}\left[\left(2D + \frac{D}{i} + C_m h^2\right)\beta^{i-1} - D\beta^{i-2}\right.$$
$$-h^2 C_m \tilde{n}^i_{DT} + h^2\dot{\beta}^{i-1} + h^2\left(v_{fuel} + \tilde{d}_{fuel}\right)B^i_{fuel} + 2h^2\tilde{S}^i_\alpha$$
$$\left. -h^2\left(v_{fuel} + \tilde{d}_{fuel}\right)\hat{S}^i_{DT} + h^2\left(v_{aux} + \tilde{d}_{aux}\right)B^i_{aux}\right], \tag{6.39}$$

$$\alpha^i = \frac{1}{D + D/i}\left[\left(2D + \frac{D}{i} + C_f h^2\right)\alpha^{i-1} - D\alpha^{i-2} - h^2 C_f \tilde{E}^i\right.$$
$$+h^2\dot{\alpha}^{i-1} - h^2 Q_\alpha \tilde{S}^i_\alpha + h^2\tilde{P}^i_{rad} - h^2\left(v_{aux} + \tilde{d}_{aux}\right)\hat{P}^i_{aux}$$
$$\left. +h^2\left(v_{fuel} + \tilde{d}_{fuel}\right)A^i_{fuel} + h^2\left(v_{aux} + \tilde{d}_{aux}\right)A^i_{aux}\right], \tag{6.40}$$

where $\omega^0 = \beta^0 = \alpha^0 = 0$ and $\dot{x}^{i-1}$ (for $x \in \{\omega, \beta, \alpha\}$) is given by

$$\dot{x}^{i-1} = \sum_{k=1}^{i-1}\frac{\partial x^{i-1}}{\partial \tilde{n}^k_{DT}}\dot{\tilde{n}}^k_{DT} + \sum_{k=1}^{i-1}\frac{\partial x^{i-1}}{\partial \tilde{E}^k}\dot{\tilde{E}}^k + \sum_{k=1}^{i-1}\frac{\partial x^{i-1}}{\partial \tilde{n}^k_\alpha}\dot{\tilde{n}}^k_\alpha. \tag{6.41}$$

Through its dependence on $\dot{\tilde{n}}_{DT}$, $\dot{\tilde{E}}$, and $\dot{\tilde{n}}_\alpha$, expression (6.41) depends on the to-be-designed control laws v_{fuel} and v_{aux}, which will not in general be spatially causal and would violate the strict-feedback structure required for backstepping. It also depends on the terms $\tilde{d}_{fuel}$ and $\tilde{d}_{aux}$, which are unknown. However, by our choice of target system, the terms involving Ω^i_{fuel}, Ω^i_{aux}, B^i_{fuel}, B^i_{aux}, A^i_{fuel}, and A^i_{aux} exactly remove the undesirable terms from the recursive expressions (6.38), (6.39), and (8.17) upon substitution, i.e.,

$$\omega^i = \frac{1}{D + D/i}\left[\left(2D + \frac{D}{i} + C_w h^2\right)\omega^{i-1} - D\omega^{i-2}\right.$$
$$\left. - h^2 C_w \tilde{n}^i_\alpha + h^2\dot{\omega}^{i-1}_{strict} - h^2\tilde{S}^i_\alpha\right],$$

$$\beta^i = \frac{1}{D + D/i}\left[\left(2D + \frac{D}{i} + C_m h^2\right)\beta^{i-1} - D\beta^{i-2} \right.$$
$$\left. -h^2 C_m \tilde{n}^i_{DT} + h^2 \dot{\beta}^{i-1}_{strict} + 2h^2 \tilde{S}^i_\alpha\right],$$

$$\alpha^i = \frac{1}{D + D/i}\left[\left(2D + \frac{D}{i} + C_f h^2\right)\alpha^{i-1} - D\alpha^{i-2} - h^2 C_f \tilde{E}^i \right.$$
$$\left. +h^2 \dot{\alpha}^{i-1}_{strict} - h^2 Q_\alpha \tilde{S}^i_\alpha + h^2 \tilde{P}^i_{rad}\right],$$

where the strict feedback terms $\dot{x}^{i-1}_{strict}$, (for $x \in \{\omega, \beta, \alpha\}$) are given by

$$\dot{x}^{i-1}_{strict} = \sum_{k=1}^{i-1} \frac{\partial x^{i-1}}{\partial \tilde{n}^k_{DT}}\left[D\frac{\tilde{n}^{k+1}_{DT} - 2\tilde{n}^k_{DT} + \tilde{n}^{k-1}_{DT}}{h^2} + \frac{D}{ih}\frac{\tilde{n}^{k+1}_{DT} - \tilde{n}^k_{DT}}{h}\right.$$
$$\left. -2\tilde{S}^k_\alpha\right] + \sum_{k=1}^{i-1} \frac{\partial x^{i-1}}{\partial \tilde{n}^k_\alpha}\dot{\tilde{n}}^k_\alpha + \sum_{k=1}^{i-1} \frac{\partial x^{i-1}}{\partial \tilde{E}^k}\left[Q_\alpha \tilde{S}^k_\alpha - \tilde{P}^k_{rad}\right.$$
$$\left. +D\frac{\tilde{E}^{k+1} - 2\tilde{E}^k + \tilde{E}^{k-1}}{h^2} + \frac{D}{ih}\frac{\tilde{E}^{k+1} - \tilde{E}^k}{h}\right]. \tag{6.42}$$

Next, subtracting (6.35) from (6.28), (6.36) from (6.29), and (6.37) from (6.30), the boundary control laws can be defined as

$$v_\alpha = \omega^{N-1}, \quad v_{DT} = \beta^{N-1}, \quad v_E = \alpha^{N-1}. \tag{6.43}$$

We design the control laws for the distributed actuators v_{fuel} and v_{aux}, as well as the update laws for the disturbance estimations by considering the control Lyapunov

function

$$V = \frac{1}{2}\sum_{i=1}^{N-1} Q_w^i \left(\tilde{w}^i\right)^2 + \frac{1}{2}\sum_{i=1}^{N-1} Q_m^i \left(\tilde{m}^i\right)^2 + \frac{1}{2}\sum_{i=1}^{N-1} Q_f^i \left(\tilde{f}^i\right)^2 + \frac{\tilde{d}_\alpha^2}{2k_\alpha} + \frac{\tilde{d}_{DT}^2}{2k_{DT}} + \frac{\tilde{d}_E^2}{2k_E} + \frac{\tilde{d}_{fuel}^2}{2k_{fuel}} + \frac{\tilde{d}_{aux}^2}{2k_{aux}},$$

where Q_w^i, Q_m^i, Q_f^i for $i \in [1, N-1]$ are positive definite weights, and k_α, k_{DT}, k_E, k_{fuel}, and k_{aux} are positive constants. We calculate its time derivative as

$$\dot{V} = \sum_{i=1}^{N-1} Q_w^i \tilde{w}^i \dot{\tilde{w}}^i + \sum_{i=1}^{N-1} Q_m^i \tilde{m}^i \dot{\tilde{m}}^i + \sum_{i=1}^{N-1} Q_f^i \tilde{f}^i \dot{\tilde{f}}^i + \frac{1}{k_\alpha}\tilde{d}_\alpha \dot{\tilde{d}}_\alpha + \frac{1}{k_{DT}}\tilde{d}_{DT}\dot{\tilde{d}}_{DT} + \frac{1}{k_E}\tilde{d}_E\dot{\tilde{d}}_E + \frac{1}{k_{fuel}}\tilde{d}_{fuel}\dot{\tilde{d}}_{fuel} + \frac{1}{k_{aux}}\tilde{d}_{aux}\dot{\tilde{d}}_{aux}.$$

Noting the dynamic equations (6.31), (6.32), and (6.33), and the boundary conditions (6.34), (6.35), (6.36), and (6.37), this can be written as

$$\begin{aligned}\dot{V} = &-W^T A_w W - M^T A_m M - F^T A_f F + v_{fuel}\Phi_{fuel} + v_{aux}\Phi_{aux} \\ &+ \tilde{d}_{fuel}\left[\Phi_{fuel} + \frac{\dot{\tilde{d}}_{fuel}}{k_{fuel}}\right] + \tilde{d}_{aux}\left[\Phi_{aux} + \frac{\dot{\tilde{d}}_{aux}}{k_{aux}}\right] \\ &+ \tilde{d}_\alpha\left[Q_w^{N-1}\frac{D}{h^2}\left(1 + \frac{1}{N-1}\right)\tilde{w}^{N-1} + \frac{\dot{\tilde{d}}_\alpha}{k_\alpha}\right] \\ &+ \tilde{d}_{DT}\left[Q_m^{N-1}\frac{D}{h^2}\left(1 + \frac{1}{N-1}\right)\tilde{m}^{N-1} + \frac{\dot{\tilde{d}}_{DT}}{k_{DT}}\right] \\ &+ \tilde{d}_E\left[Q_f^{N-1}\frac{D}{h^2}\left(1 + \frac{1}{N-1}\right)\tilde{f}^{N-1} + \frac{\dot{\tilde{d}}_E}{k_E}\right],\end{aligned} \tag{6.44}$$

where $W = [w^1, ..., w^{N-1}]^T$, $M = [m^1, ..., m^{N-1}]^T$, $F = [f^1, ..., f^{N-1}]^T$ are transformed

measurements. The elements of the matrix A_k (where $k \in \{w, m, f\}$) are given by

$$\begin{aligned} A_k^{i,i-1} &= -Q_k^i \frac{D}{h^2}, \quad A_k^{i,i} = Q_k^i \left[\frac{D}{h^2} \left(2 + \frac{1}{i} \right) + C_k \right], \\ A_k^{i,i+1} &= -Q_k^i \frac{D}{h^2} \left(1 + \frac{1}{i} \right), \end{aligned}$$

for $2, ..., i, ...N-2$, and by

$$\begin{aligned} A_k^{1,1} &= Q_k^1 \left(2\frac{D}{h^2} + C_k \right), \quad A_k^{1,2} = -2Q_k^1 \frac{D}{h^2}, \\ A_k^{N-1,N-1} &= Q_k^{N-1} \left[\frac{D}{h^2} \left(2 + \frac{1}{N-1} \right) + C_k \right], \\ A_k^{N-1,N-2} &= -Q_k^{N-1} \frac{D}{h^2}. \end{aligned}$$

Given positive diffusivity D, the matrix A_k is positive definite. The nonlinear functions Φ_{fuel} and Φ_{aux} are given by

$$\begin{aligned} \Phi_{fuel} &= \sum_{i=1}^{N-1} Q_w^i \tilde{w}^i \Omega_{fuel}^i + \sum_{i=1}^{N-1} Q_m^i \tilde{m}^i A_{fuel}^i + \sum_{i=1}^{N-1} Q_f^i \tilde{f}^i B_{fuel}^i, \\ \Phi_{aux} &= \sum_{i=1}^{N-1} Q_w^i \tilde{w}^i \Omega_{aux}^i + \sum_{i=1}^{N-1} Q_m^i \tilde{m}^i A_{aux}^i + \sum_{i=1}^{N-1} Q_f^i \tilde{f}^i B_{aux}^i. \end{aligned}$$

We take the control laws and update laws

$$v_{fuel} = -C_{fuel}\Phi_{fuel}, \quad v_{aux} = -C_{aux}\Phi_{aux}, \tag{6.45}$$

$$\dot{\hat{d}}_{fuel} = k_{fuel}\Phi_{fuel}, \quad \dot{\hat{d}}_{aux} = k_{aux}\Phi_{aux}, \tag{6.46}$$

$$\dot{\hat{d}}_{\alpha} = k_{\alpha} Q_w^{N-1} \frac{D}{h^2} \left(1 + \frac{1}{N-1} \right) \tilde{w}^{N-1}, \tag{6.47}$$

$$\dot{\hat{d}}_{DT} = k_{DT} Q_m^{N-1} \frac{D}{h^2} \left(1 + \frac{1}{N-1} \right) \tilde{m}^{N-1}, \tag{6.48}$$

$$\dot{\hat{d}}_{E} = k_{E} Q_f^{N-1} \frac{D}{h^2} \left(1 + \frac{1}{N-1} \right) \tilde{f}^{N-1}, \tag{6.49}$$

where $C_{fuel} \geq 0$ and $C_{aux} \geq 0$, which, assuming constant disturbances, reduces (8.28) to

$$\begin{aligned}\dot{V} =& - W^T A_w W - M^T A_m M - F^T A_f F - C_{fuel}\Phi_{fuel}^2 - C_{aux}\Phi_{aux}^2 \\ \leq& - W^T A_w W - M^T A_m M - F^T A_f F.\end{aligned}$$

Since A_w, A_m, and A_f are positive definite, we have that $\dot{V} \leq 0$. Since $V \geq 0$ and $\ddot{V}$ is bounded, the conditions of Barbalat's lemma are satisfied, and we have that $\dot{V} \to 0$. This implies that $\tilde{w}$, $\tilde{m}$, and $\tilde{f}$ are driven to zero, guaranteeing asymptotic stability of the target system, and, consequently, $\tilde{n}_\alpha$, $\tilde{n}_{DT}$, and $\tilde{E}$.

The control strategy is summarized in Figure 6.2. First, a desired set of equilibrium profiles is determined. These profiles are then used as references by the backstepping controller, which actuate the ion densities and energy at the plasma edge, as well as the magnitudes of the distributed heating and fueling actuators to achieve the desired profile shapes and spatial averages for the alpha particle, DT fuel, and energy density.

6.5 Simulation Results

In the following, the discretized burning plasma system was simulated using an implicit finite difference scheme with $N_{sim} = 50$, and the time step chosen to achieve suitable accuracy. The results shown are for an equilibrium described by $D_E = 0.4$, $D_{DT} = 0.2$, $D_\alpha = 0.13$, $\bar{u}_{aux} = 3.8 \times 10^4$, $\bar{u}_{fuel} = 1.6 \times 10^{19}$, $\bar{u}_\alpha = 9.5 \times 10^{17}$, $\bar{u}_{DT} = 5.3 \times 10^{19}$, and $\bar{u}_E = 2.0 \times 10^5$. Figure 6.3 shows that without feedback control, the chosen equilibrium of the simplified model is unstable. In this case, the initial perturbations in the shape and magnitude cause a thermal excursion and the system

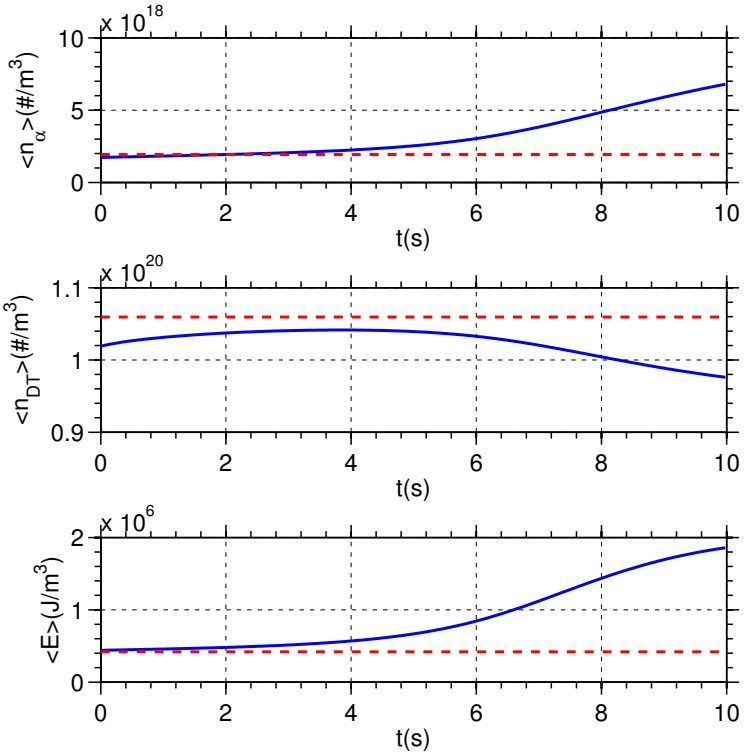

Figure 6.3: Spatial averages of the open-loop (uncontrolled) profiles. The desired equilibrium values are shown as red dotted lines. The solid blue lines show the simulated evolution of the system.

comes to rest at a higher temperature equilibrium. As a first test of the feedback controller, two closed loop simulations were run: one with boundary actuation only (i.e., $C_{fuel} = C_{aux} = 0$), and one with simultaneous boundary and distributed actuation ($Q_w^i = 10^{-36}$, $Q_m^i = 10^{-38}$, and $Q_f^i = 10^{-10}$ for $1, \ldots, i, \ldots N-1$, $C_{fuel} = 0.125 \times 10^{38}$, $C_{aux} = 0.1 \times 10^{10}$). Neither of these simulations included disturbances or disturbance estimation. In both cases, the controller was designed using $N_{control} = 3$, i.e., utilizing two measurement points inside the plasma core, and $C_w = C_m = C_f = 0.15$. Figure 6.4 shows the resulting profile evolutions. In both cases, the nonlinear controller was able to stabilize the desired equilibrium, however, the use of distributed actuation improved the response by adding more control authority in the interior of

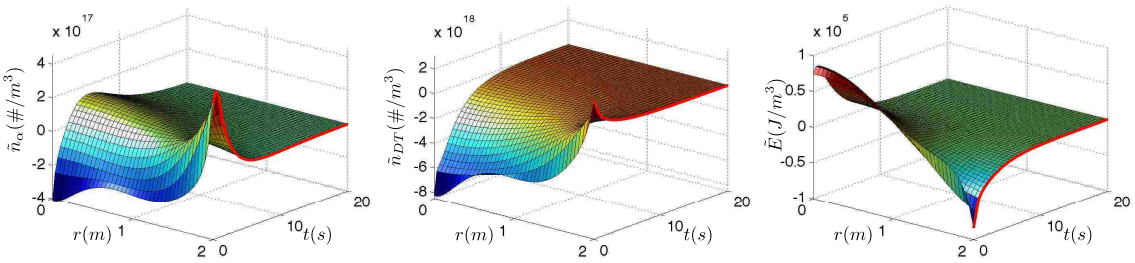

(a) Boundary feedback only.

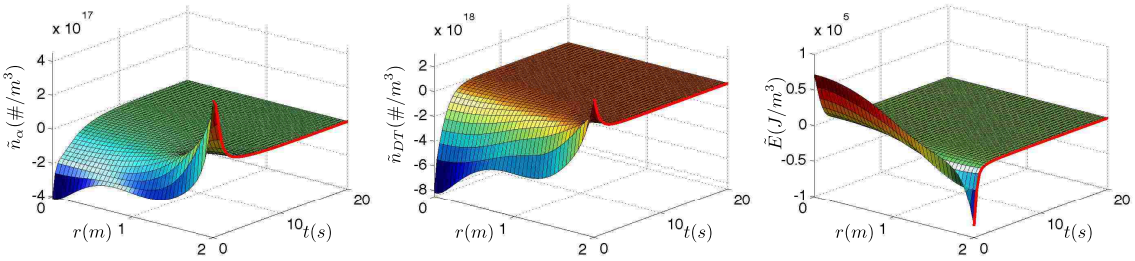

(b) Simultaneous boundary and distributed feedback.

Figure 6.4: Profile error evolution for a simulation with boundary feedback only (a) and one with simultaneous boundary and distributed feedback (b). Solid red lines indicate the boundary actuation.

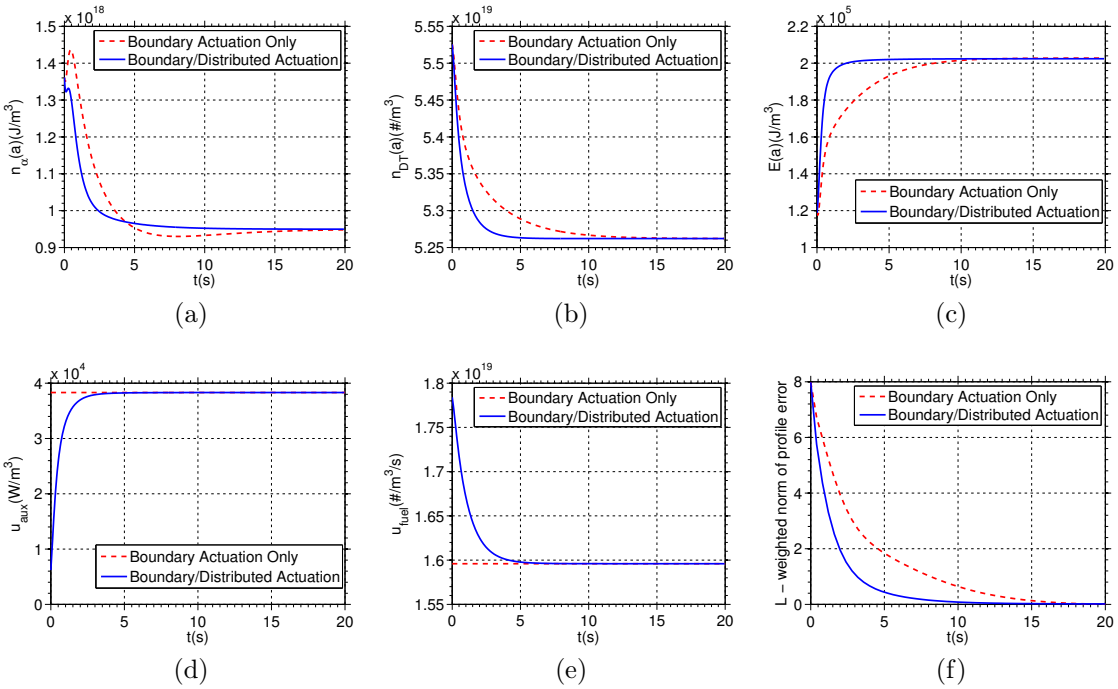

Figure 6.5: Boundary actuation (a-c), distributed actuation (d,e), and l_2 norm of profile error (f), comparing a simulation with boundary actuation only (red, dashed) to one employing simultaneous boundary and distributed actuation.

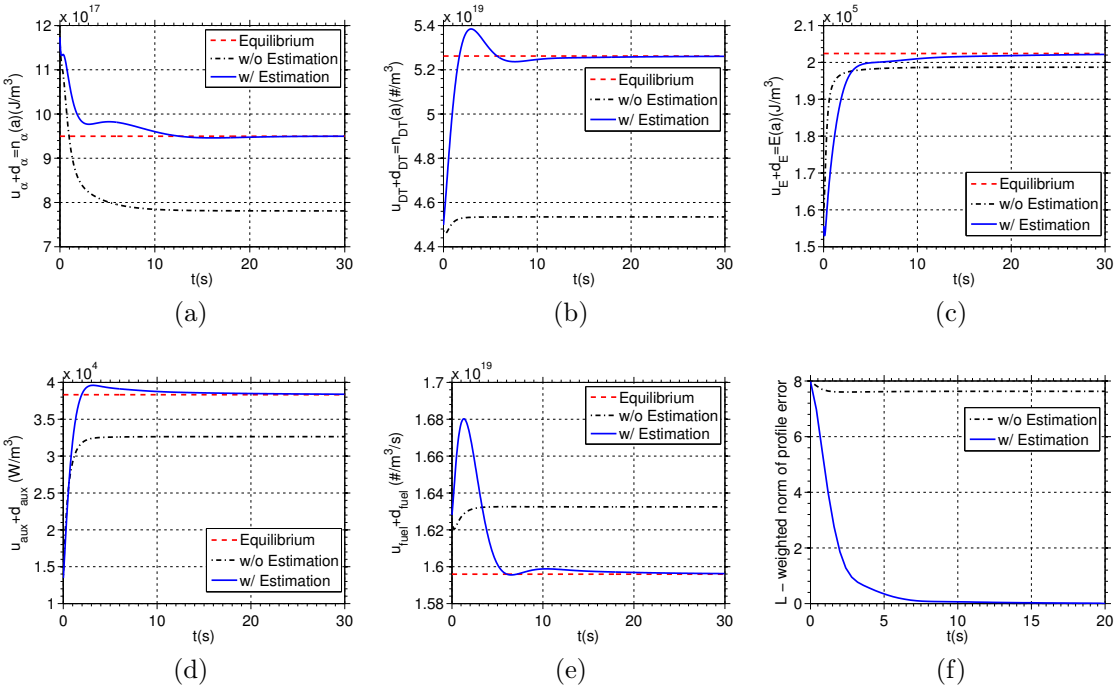

Figure 6.6: Realized (controlled input + input disturbance) boundary actuation (a-c) and distributed actuation (d,e), and the weighted norm of the profile error (f) during a simulation without disturbance estimation (black, dash-dot) and one with disturbance estimation (blue, solid). With disturbance estimation, the realized actuator values converge to the reference values for the desired equilibrium (red, dashed), and the profile error is driven to zero.

the plasma. Figures 6.5a-e compare the boundary and distributed actuation during the two simulations. By including distributed actuation, the amount of boundary actuation needed to stabilize the system was reduced. The weighted norm of the profile error

$$L = \sqrt{\sum_{i=1}^{N-1} \left[\left(10^{-5} \tilde{E}^i \right)^2 + (10^{-18} \tilde{n}_\alpha^i)^2 + (10^{-19} \tilde{n}_{DT}^i)^2 \right] h},$$

during both simulations is compared in Figure 6.5f, clearly showing that the profile error was driven to zero much more quickly when distributed actuation was added. To test disturbance rejection, a second set of simulations were run with input disturbances $d_\alpha = -0.2\bar{u}_\alpha$, $d_{DT} = -0.2\bar{u}_{DT}$, $d_E = 0.2\bar{u}_E$, $d_{fuel} = -0.2\bar{u}_{fuel}$, and $d_{aux} = 0.2\bar{u}_{aux}$. The first simulation was run without online disturbance estimation, while the estimation was active in the second simulation ($k_\alpha = 1.2 \times 10^{36}$, $k_{DT} = 1.5 \times 10^{38}$, $k_E = 1.2 \times 10^{10}$, $k_{fuel} = 0.03 \times 10^{10}$, and $k_{aux} = 0.06 \times 10^{38}$). Figures (6.6)a-e compare the realized (controlled actuation + input disturbance) values of $n_\alpha(a) = u_\alpha + d_\alpha$, $n_{DT}(a) = u_{DT} + d_{DT}$, $E(a) = u_E + d_E$, distributed heating $u_{aux} + d_{aux}$, and distributed fueling $u_{fuel} + d_{fuel}$, respectively, to the values associated with the desired equilibrium. Figure (6.6)f compares the weighted norm L for both cases. In these figures, the red-dashed line represents the equilibrium value, while the blue solid line and black dash-dot line represent the realized actuators during the simulations with and without disturbance estimation, respectively. In the first simulation, the system was stabilized by the feedback controller and the realized actuators converged to constant values, however, without estimation, a steady-state profile error developed, as made clear in Figure (6.6)f. Through online estimation of the disturbances in the second simulation, the controller was able to account for the disturbances and drive the profile error to zero. Indeed, the realized actuators

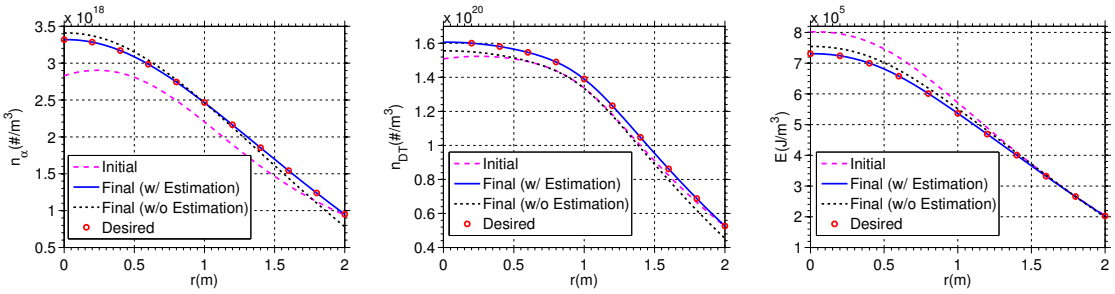

Figure 6.7: Initial (magenta, dashed), desired (red, circles), and final profiles, comparing the results a simulation with disturbance estimation (blue, solid) to one without (black, dotted). Note that the effect of input disturbances is removed at steady-state with the online estimation active.

converged to the reference values associated with the desired equilibrium. Figure 6.7 shows the initial and desired profiles, and compares the final profiles obtained in the two simulations. The steady-state profile error developed in the first simulation and the recovery of the desired profiles in the simulation with disturbance estimation are evident.

6.6 Conclusions

A non-linear feedback controller based on backstepping that achieves asymptotic stabilization of the equilibrium ion and energy density profiles in a cylindrical burning plasma has been designed. The controller uses actuation of the α-particle, energy, and DT ion density at the plasma's edge, as well as distributed heating and fueling to stabilize the respective profiles. The resulting controller holds for any finite discretization in space of the original PDE model and the simulation in this work shows that a controller using a very coarse discretization, successfully controls the density profiles. The feasibility of controlling kinetic profiles in a burning plasma using a combination of distributed and boundary feedback has been shown. However, more

study will be necessary to find physical methods for the modulation of the kinetic variables at the edge of the plasma, i.e. achieving the desired values of u_α, u_{DT}, and u_E. This will have to be done through modulation of the physical properties of the plasma scrape-off layer (SOL) such as gas puffing, gas pumping, or impurity injection. Moving forward, model improvements will be made by including models for the diffusivity and pinch velocity, as well as models of the SOL in order to apply more realistic boundary conditions to the system.

Because burning plasma experiments on ITER are still years away, it is not possible to experimentally test the proposed profile control approach at this time. However, the backstepping technique for PDE control design can be applied to the important issue of current profile control, which is a new and active area of research at many present-day tokamaks. In the following chapters, backstepping based control schemes are designed, implemented, and experimentally tested on the DIII-D tokamak.

Chapter 7

Backstepping Control of the Current Profile in L-mode Discharges

7.1 Introduction

Among the major challenges for future fusion reactors is to achieve scenarios in which a tokamak can operate with sufficiently long plasma discharges. It has been demonstrated that setting up a suitable spatial distribution of the toroidal plasma current can, in turn, enable certain advanced operating scenarios characterized by high fusion gain and non-inductive sustainment of plasma current that could lead to steady-state operation (see [33]). Typically, the spatial distribution of toroidal current is approximated as a one-dimensional radial profile by assuming axisymmetry in the toroidal coordinate and by averaging quantities over the poloidal magnetic flux surfaces, a set of nested surfaces of constant poloidal magnetic flux as shown in the cutaway view of the plasma inside the DIII-D tokamak in Figure 2. As part of the effort to identify and achieve suitable profiles for advanced operating scenarios, active control of the current profile or the safety factor profile, q, a related quantity defined as the number

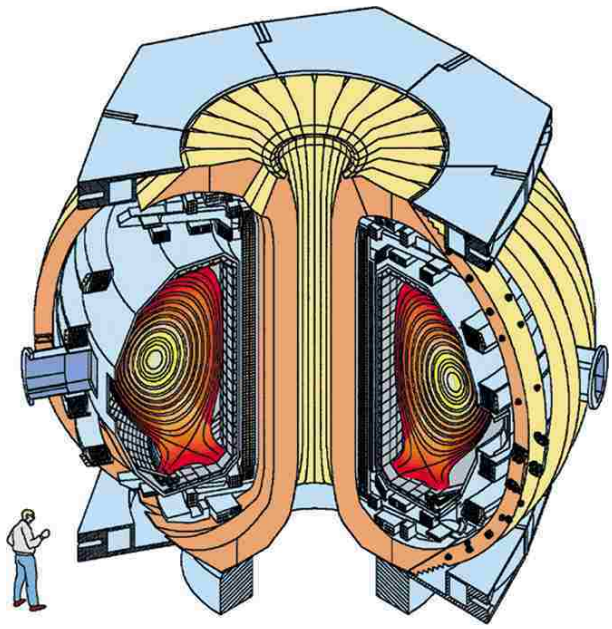

Figure 7.1: Illustration of the DIII-D tokamak. The toroidal field coils (cream colored) and poloidal field coils (light blue) produce the magnetic field that confines the plasma. The cross-section of the plasma within the machine is represented by a set of magnetic flux contours.(Source: General Atomics Fusion Education Outreach)

of times a magnetic field line goes around the machine toroidal for each time it goes around poloidally, has become an area of extensive research.

7.1.1 Prior Work

Most experiments in this area have thus far focused on the real-time feedback control of scalar parameters characterizing some aspect of the current profile. In [74], feedback control of $q(0,t)$, the safety factor at the magnetic axis of the plasma, or $q_{min}(t)$, the minimum value of the safety factor profile, was achieved by modifying either ECH (electron cyclotron heating) or NBI (neutral beam injection) on DIII-D. In [75], LHCD (lower hybrid current drive) was used to control the internal inductance parameter, $l_i(t)$, a measure of the current profile shape, on Tore Supra. Both experiments used simple non-model-based proportional control laws to modify single scalar parameters

describing some characteristic of the current profile. Non-model based approaches to real-time control of the current profile were also studied in [76, 77], and [78].

Though non-model-based techniques have had some success in manipulating single scalar outputs, like $l_i(t)$ or $q_{min}(t)$, it will be critical to control the shape of the entire current profile in order to achieve certain advanced tokamak operating scenarios. The strong nonlinear coupling between magnetic and kinetic profiles and the high dimensionality of this type of distributed control problem motivate the use of model-based techniques that can exploit knowledge of the dynamic response of the system to the available actuators within the controller design. Compared to non-model-based approaches, model-based designs can achieve high levels of performance without requiring significant amounts of experimental time for trial-and-error tuning. Work on dynamic modeling of the current profile evolution has focused on either generating models from experimental data or creating models motivated by a first-principles description of the system.

Data-driven models have recently been used to design controllers for simultaneous regulation of magnetic and kinetic plasma profiles around desired references during the flat-top phase of a plasma discharge at JET [79, 80, 81], JT-60U, and DIII-D [82, 83, 84]. In this approach, system identification techniques were used to develop linear dynamic models of the plasma profile response to various actuators based on data gathered during dedicated experiments. Because the resulting models are linear, they are only valid close to the reference scenario used for identification. As a result, controllers based on these models may perform poorly if the system states move far from their respective reference values. Additional dedicated system identification experiments must be carried out in order to apply this approach to new devices or to different operating scenarios.

By designing controllers using a first-principles description of the current pro-

file dynamics, the issues associated with identified models can be largely avoided. In practice, it is typically necessary to simplify or approximate parts of the first-principles description in order to facilitate control design, or to close the equations of model with empirical expressions. If these approximations are made carefully, the advantages of a first-principles based model based approach to control design can be largely retained while the complexity of the model and control design can be greatly reduced. To distinguish this simplified physics-based modeling approach from those based entirely on first-principles or linear-data-driven approaches based entirely on empirical data, we refer to the resulting simplified models as first-principles-driven, control-oriented models. Use of a first-principles-driven model allows a control design to incorporate the nonlinear coupling of plasma parameters, potentially enabling improved closed loop performance and allowing for operation over a wider range of conditions than control schemes based on linear data-driven models. Additionally, first-principles-driven controllers have the potential to be adapted to different scenarios or devices without significant changes to the structure of the control law and while avoiding the need for dedicated model identification experiments. Such models of the evolution of the plasma magnetic flux have recently been developed in [85, 86, 87]. In [88, 89], the model developed in [86] was used to calculate optimal feedforward actuator trajectories for achieving a desired safety factor profile, using extremum-seeking and nonlinear programming approaches, respectively. Some recent work on first-principles-driven feedback control designs have been presented in [90, 91, 92, 93, 94]. In these results, robust, optimal, and sliding mode based feedback controllers were developed and tested in simulations.

7.1.2 Results of This Work

In this chapter, a first-principles-driven model-based current profile control algorithm is designed for low-confinement mode discharges on DIII-D to be combined with feedforward actuator trajectories that can be calculated offline (as in [88, 89]) or based on previous experimental results. The model-based feedback control law enables the actuator trajectories to be adjusted in real-time in order to reproduce profile evolutions achieved in previous experiments or simulations despite perturbed initial conditions or other disturbances. The controller is designed to track a reference trajectory of the poloidal flux gradient profile θ, a quantity inversely related to the safety factor profile. Because the plasma current in the L-mode discharges studied in this work is primarily inductively driven, the most effective means of controlling the current profile is through the boundary condition, which can be actuated through modulation of the total plasma current. Boundary actuation will also be the primary actuator for controlling current profile formation during the ramp-up and early flattop phases of H-mode discharges, prior to the flattop phase, in which interior actuation through non-inductive current drive becomes more significant and adds more degrees of freedom for control. The design of a boundary feedback control law is therefore an important step towards the design of a comprehensive current profile control strategy for H-mode discharges. In this work, a boundary feedback control law is designed by discretizing partial differential equation (PDE) describing the evolution of θ in L-mode discharges on DIII-D in space using a finite difference method and applying a backstepping design to obtain a transformation from the original system into an asymptotically stable target system. The feedback term from the resulting control law is added to the feedforward input trajectories and, through a nonlinear transformation, references are obtained for the plasma current, non-inductive power, and line-averaged density. These references are then sent to existing dedicated controllers

for the individual physical quantities.

Numerical simulations show that improved performance is achieved through the use of the backstepping control scheme. However, because the resulting control law only uses proportional feedback, the controller's ability to reject disturbances is limited. To overcome this, we augment the backstepping control law with an adaptive law that effectively adds integral action to the closed loop system. The resulting control scheme takes the form of a proportional-integral controller coupled with nonlinear input transformation, with spatially-varying gains derived through the use of backstepping and tuned through choice of design parameters in the target system. Simulation results show that this approach can greatly improve the disturbance rejection capabilities of the closed loop system. As part of this work, a general framework for implementing real-time feedforward control of magnetic and kinetic plasma profiles was implemented in the DIII-D Plasma Control System (PCS). The framework was used to experimentally test the control design and demonstrate the feasibility of the proposed current profile control scheme. These results are part of the first experimental campaign to perform model-based feedback control of the current profile using the semi-empirical first-principles-driven modeling approach and represent the first experimental implementation of a backstepping boundary control law in a tokamak. Results of our other approaches to first-principles-driven model-based feedback control design for L-mode discharges that were tested during the same campaign can be found in [95, 96].

The chapter is organized as follows. In Section 7.2, a PDE model for the current profile evolution is introduced. The control objective is discussed in Section 7.3. In Section 7.4, a backstepping feedback control law is presented and the stability of the target system is shown. The addition of an adaptive law to improve upon disturbance rejection is also discussed. The real-time control algorithm and the simulation

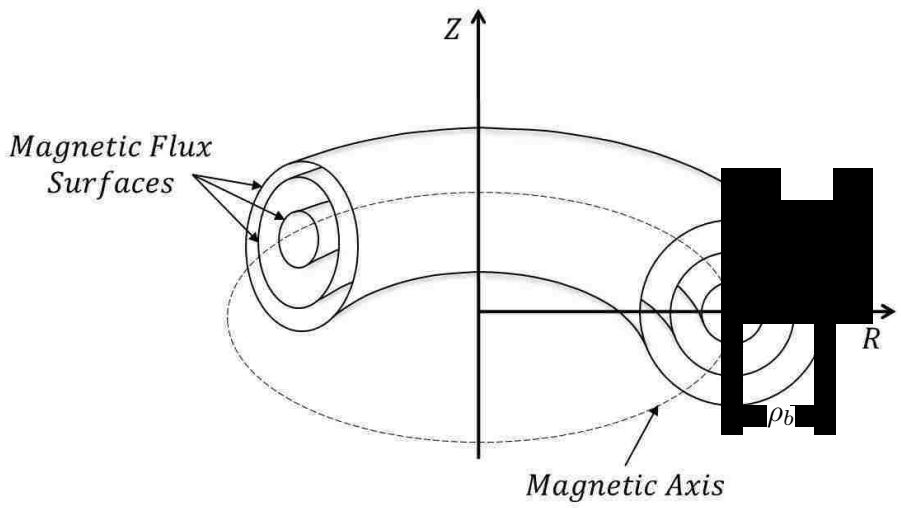

Figure 7.2: Illustration of the coordinates used in the current profile model.

framework are described in Section 7.5. The feedback control laws are studied in simulations and experimentally tested in Sections 7.6 and 7.7, respectively. Finally, conclusions and future work are stated in Section 7.8.

7.2 Current Profile Evolution Model

Figure 7.2 illustrates the coordinate system used in this work. We begin by taking ρ as a coordinate indexing the magnetic surfaces within a poloidal cross-section of the tokamak plasma. We choose the mean effective radius of the magnetic surface as the variable ρ, i.e., $\pi B_{\phi,0}\rho^2 = \Phi$, where Φ is the toroidal magnetic flux and $B_{\phi,0}$ is the reference magnetic field at the geometric major radius R_0 of the tokamak. By normalizing the quantity by ρ_b, the mean effective minor radius of the last closed magnetic surface, we obtain the coordinate $\hat{\rho} = \rho/\rho_b$. The safety factor, a quantity related to the toroidal current density, is given by $q(\rho, t) = -d\Phi/d\Psi(\rho, t)$, where Ψ is the poloidal magnetic flux. By noting the constant relationship between ρ and Φ,

i.e., $\pi B_{\phi,0}\rho^2 = \Phi$, and the definition of ρ_b, this can be written as

$$q\left(\hat{\rho},t\right) = -\frac{B_{\phi,0}\rho_b^2\hat{\rho}}{\partial\psi/\partial\hat{\rho}}, \tag{7.1}$$

where ψ is the poloidal stream function ($\Psi = 2\pi\psi$). Since the safety factor depends inversely on the spatial derivative of the poloidal flux, we define

$$\theta\left(\hat{\rho},t\right) = \frac{\partial\psi}{\partial\hat{\rho}}\left(\hat{\rho},t\right), \tag{7.2}$$

and take this quantity as the variable of interest to be controlled. This choice is motivated by the straightforward derivation of a PDE for the dynamics of $\theta\left(\hat{\rho},t\right)$, and is possible because any target for $q\left(\hat{\rho},t\right)$ can be uniquely related to a target for $\theta\left(\hat{\rho},t\right)$.

In order to obtain a PDE describing the evolution of $\theta\left(\hat{\rho},t\right)$, we start from the well known magnetic diffusion equation [97], which describes the poloidal magnetic flux evolution. This equation is given by

$$\frac{\partial\psi}{\partial t} = \frac{\eta(T_e)}{\mu_0\rho_b^2\hat{F}^2}\frac{1}{\hat{\rho}}\frac{\partial}{\partial\hat{\rho}}\left(\hat{\rho}\hat{F}\hat{G}\hat{H}\frac{\partial\psi}{\partial\hat{\rho}}\right) + R_0\hat{H}\eta(T_e)\frac{<\bar{j}_{NI}\cdot\bar{B}>}{B_{\phi,0}}, \tag{7.3}$$

where ψ represents the poloidal magnetic stream function, t is time, η is the plasma resistivity, which is dependent on the electron temperature, T_e, μ_0 is the vacuum permeability, $\bar{j}_{NI}$ is the non-inductive current density, $\bar{B}$ is the toroidal magnetic field, and $<>$ denotes the flux-surface average of a quantity. $\hat{F}$, $\hat{G}$, and $\hat{H}$ are spatially varying geometric factors of the reference magnetic equilibrium that are described in [86]. These factors vary in time as the plasma shape evolves (especially during the ramp-up phase), however, they are considered to be constant in this model. While the proposed control method could accommodate time-varying model parameters, initial

results indicate that it may not be necessary to include this increased complexity for the purposes of control design. The boundary conditions are given by

$$\left.\frac{\partial\psi}{\partial\hat{\rho}}\right|_{\hat{\rho}=0}=0, \qquad \left.\frac{\partial\psi}{\partial\hat{\rho}}\right|_{\hat{\rho}=1}=-\frac{\mu_0}{2\pi}\frac{R_0}{\hat{G}\Big|_{\hat{\rho}=1}\hat{H}\Big|_{\hat{\rho}=1}}I(t), \tag{7.4}$$

where $I(t)$ is the total plasma current.

Based on experimental observations of the ramp-up phase in low-confinement mode (L-mode) discharges in DIII-D, simplified scenario-oriented empirical models for the electron temperature, non-inductive current density, and plasma resistivity were identified [86]. The temperature and non-inductive current drive terms are considered to have fixed spatial profiles with time-varying magnitudes that scale with the values of physical actuators. The model for the electron temperature is given by

$$T_e\left(\hat{\rho},t\right)=k_{T_e}T_e^{profile}\left(\hat{\rho}\right)\frac{I(t)\sqrt{P_{tot}(t)}}{\bar{n}(t)}, \tag{7.5}$$

where k_{T_e} is a constant, $T_e^{profile}\left(\hat{\rho}\right)$ is a reference profile, $P_{tot}\left(t\right)$ is the total average NBI power and $\bar{n}(t)$ is the line averaged plasma density. This scaling law can be derived by considering an approximate steady-state energy balance, i.e., $\frac{E}{\tau_E}=P_{tot}$, where E is the plasma stored energy, and the energy confinement time τ_E is considered to be proportional to $IP_{tot}^{-0.5}$, as suggested in [98]. The steady-state solution is used because the energy time-scale is much shorter than the current diffusion time-scale. The model for the non-inductive toroidal current density is given by

$$\frac{<\bar{j}_{NI}\cdot\bar{B}>}{B_{\phi,0}}=k_{NI}j_{NI}^{profile}\left(\hat{\rho}\right)\frac{I(t)^{1/2}P_{tot}(t)^{5/4}}{\bar{n}(t)^{3/2}}, \tag{7.6}$$

where k_{NI} is a constant and $j_{NI}^{profile}\left(\hat{\rho}\right)$ is a reference profile for the non-inductive

current deposition. This scaling is derived by considering the neutral beam current drive to be proportional to $P_{tot}T^{0.5}n^{-1}$, which is a suitable approximation of the formula given in [99] for parameters in DIII-D, and substituting the temperature scaling (7.5). Since the plasma current is mainly driven by induction during L-mode discharges, the effect of the self-generated non-inductive bootstrap current is neglected in this model. The plasma resistivity $\eta\left(T_e\right)$ is given by

$$\eta\left(\hat{\rho},t\right)=\frac{k_{eff}Z_{eff}}{T_e^{3/2}\left(\hat{\rho},t\right)}, \tag{7.7}$$

where k_{eff} is a constant. The effective atomic number of the plasma, Z_{eff}, is considered to be constant in this model.

The models (7.5), (7.6), and (7.7) allow us to write the magnetic diffusion equation (7.3) as

$$\frac{\partial\psi}{\partial t}=f_1\left(\hat{\rho}\right)u_1(t)\frac{1}{\hat{\rho}}\frac{\partial}{\partial\hat{\rho}}\left(\hat{\rho}f_4\left(\hat{\rho}\right)\frac{\partial\psi}{\partial\hat{\rho}}\right)+f_2\left(\hat{\rho}\right)u_2(t), \tag{7.8}$$

with boundary conditions given by

$$\left.\frac{\partial\psi}{\partial\hat{\rho}}\right|_{\hat{\rho}=0}=0, \qquad \left.\frac{\partial\psi}{\partial\hat{\rho}}\right|_{\hat{\rho}=1}=-k_3u_3(t), \tag{7.9}$$

where

$$f_1\left(\hat{\rho}\right)=\frac{k_{eff}Z_{eff}}{k_{T_e}^{3/2}\mu_0\rho_b^2\hat{F}^2\left(\hat{\rho}\right)\left(T_e^{profile}\left(\hat{\rho}\right)\right)^{3/2}}, \tag{7.10}$$

$$f_2\left(\hat{\rho}\right)=\frac{k_{eff}Z_{eff}R_0k_{NI}\hat{H}\left(\hat{\rho}\right)j_{NI}^{profile}\left(\hat{\rho}\right)}{k_{T_e}^{3/2}\left(T_e^{profile}\left(\hat{\rho}\right)\right)^{3/2}}, \tag{7.11}$$

$$f_4\left(\hat{\rho}\right)\ =\hat{F}\left(\hat{\rho}\right)\hat{G}\left(\hat{\rho}\right)\hat{H}\left(\hat{\rho}\right), \qquad k_3=\frac{\mu_0}{2\pi}\frac{R_0}{\hat{G}\Big|_{\hat{\rho}=1}\hat{H}\Big|_{\hat{\rho}=1}}, \tag{7.12}$$

$$u_1(t)=\left(\frac{\bar{n}(t)}{I(t)\sqrt{P_{tot}(t)}}\right)^{3/2}, \qquad u_2(t)=\frac{\sqrt{P_{tot}(t)}}{I(t)}, \qquad u_3(t)=I(t). \tag{7.13}$$

Equation (7.8) admits diffusivity, interior, and boundary actuators u_1, u_2, and u_3, respectively, which each represent nonlinear combinations of the physical actuators, $I(t)$, $P_{tot}(t)$, and $\bar{n}(t)$. Note that the controller proposed in this work will generate waveforms for these physical actuators. These waveforms represent references to be sent to existing dedicated controllers for each of the respective quantities.

We expand (7.8) with the chain rule to obtain

$$\frac{\partial \psi}{\partial t} = f_1 u_1(t) \frac{1}{\hat{\rho}} \left(\hat{\rho} \frac{\partial \psi}{\partial \hat{\rho}} \frac{\partial f_4}{\partial \hat{\rho}} + f_4 \frac{\partial \psi}{\partial \hat{\rho}} + \hat{\rho} f_4 \frac{\partial^2 \psi}{\partial \hat{\rho}^2} \right) + f_2 u_2(t). \tag{7.14}$$

We then insert (7.2) into (7.14), resulting in

$$\frac{\partial \psi}{\partial t} = f_1 u_1 \frac{1}{\hat{\rho}} \left(\hat{\rho} \theta f_4' + f_4 \theta + \hat{\rho} f_4 \theta' \right) + f_2 u_2, \tag{7.15}$$

where $(\cdot)' = \partial / \partial \hat{\rho}$ and the dependencies on time and space have been dropped to simplify the representation. By differentiating (7.15) with respect to $\hat{\rho}$, the PDE governing the evolution of $\theta(\hat{\rho}, t)$ is found to be

$$\frac{\partial \theta}{\partial t} = h_0 u_1 \theta'' + h_1 u_1 \theta' + h_2 u_1 \theta + h_3 u_2, \tag{7.16}$$

with boundary conditions:

$$\theta \Big|_{\hat{\rho}=0} = 0 \quad \theta \Big|_{\hat{\rho}=1} = -k_3 u_3 \tag{7.17}$$

and where h_0, h_1, h_2, and h_3 are spatially varying functions given by

$$\begin{aligned} h_0 &= f_1 f_4, && (7.18)\\ h_1 &= f_1' f_4 + f_1 f_4 \frac{1}{\hat{\rho}} + 2 f_1 f_4', && (7.19)\\ h_2 &= f_1' f_4' + f_1' f_4 \frac{1}{\hat{\rho}} + f_1 f_4' \frac{1}{\hat{\rho}}, \\ &\quad -f_1 f_4 \frac{1}{\hat{\rho}^2} + f_1 f_4'', && (7.20)\\ h_3 &= f_2'. && (7.21) \end{aligned}$$

7.3 Control Objective

Let $u_{ff}(t) = \left[u_{1_{ff}}(t),\ u_{2_{ff}}(t),\ u_{3_{ff}}(t)\right]$ represent a set of feedforward control input trajectories and $\theta_{ff}(\hat{\rho}, t)$ be the associated poloidal flux gradient profile evolution for a nominal initial condition $\theta_{ff}(\hat{\rho}, 0)$. We note that the feedforward input and profile trajectories could be chosen based on the results of experimental testing or from offline optimization using the current profile evolution model, as was done in [88] and [89]. The nominal profile evolution satisfies

$$\frac{\partial \theta_{ff}}{\partial t} = u_{1_{ff}} \left(h_0 \theta_{ff}'' + h_1 \theta_{ff}' + h_2 \theta_{ff} \right) + h_3 u_{2_{ff}}, \tag{7.22}$$

$$\theta_{ff}\Big|_{\hat{\rho}=0} = 0, \qquad \theta_{ff}\Big|_{\hat{\rho}=1} = -k_3 u_{3_{ff}}. \tag{7.23}$$

Given errors in the initial conditions or other disturbances, the actual state will differ from the desired target, i.e. $\theta(\hat{\rho}, t) = \theta_{ff}(\hat{\rho}, t) + \tilde{\theta}(\hat{\rho}, t)$, where $\tilde{\theta}$ represents the error between the achieved and desired profile. Since the feedforward inputs are calculated offline, they cannot compensate for these deviations, so we consider the addition of

feedback control to actively regulate the poloidal flux gradient profile around the desired profile evolution. Because of the strong influence of the boundary actuator on the dynamics of the system, we will consider the design of a feedback law for the boundary control term u_3, i.e., we write $u_3 = u_{3_{ff}} + u_{3_{fb}}$. The incorporation of interior feedback control, which may enable improvements in closed-loop response, will be considered in future designs. The PDE (7.16) can then be written as

$$\begin{aligned}\frac{\partial\left(\theta_{ff}+\tilde{\theta}\right)}{\partial t} =& u_{1_{ff}}\left[h_0\left(\theta''_{ff}+\tilde{\theta}''\right)+h_1\left(\theta'_{ff}+\tilde{\theta}'\right)\right.\\ &\left.+h_2\left(\theta_{ff}+\tilde{\theta}\right)\right]+h_3 u_{2_{ff}},\end{aligned} \tag{7.24}$$

with the boundary conditions (7.17) becoming

$$\left(\theta_{ff}+\tilde{\theta}\right)\Big|_{\hat{\rho}=0}=0, \qquad \left(\theta_{ff}+\tilde{\theta}\right)\Big|_{\hat{\rho}=1}=-k_3\left(u_{3_{ff}}+u_{3_{fb}}\right). \tag{7.25}$$

Noting (7.22) and (7.23), these expressions can be reduced to

$$\frac{\partial\tilde{\theta}}{\partial t}=h_0 u_{1_{ff}}\tilde{\theta}''+h_1 u_{1_{ff}}\tilde{\theta}'+h_2 u_{1_{ff}}\tilde{\theta}, \tag{7.26}$$

with boundary conditions

$$\tilde{\theta}\Big|_{\hat{\rho}=0}=0, \qquad \tilde{\theta}\Big|_{\hat{\rho}=1}=-k_3 u_{3_{fb}}. \tag{7.27}$$

The control design objective is then to force $\tilde{\theta}$ to zero by augmenting the feedforward control trajectories with a boundary feedback term $u_{3_{fb}}$.

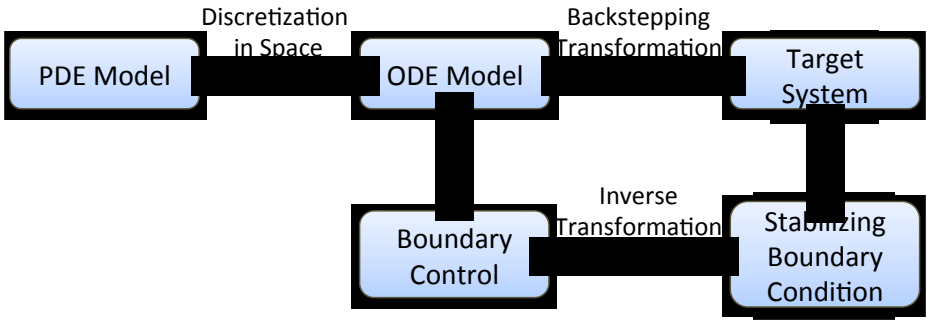

Figure 7.3: Backstepping control technique.

7.4 Backstepping Boundary Controller

A backstepping technique is used to transform a spatially discretized form of the original system of equations into an asymptotically stable target system. Then, by applying the inverse of the transformation to the boundary condition of the target system, a stabilizing boundary feedback law for the discretized model is found. The technique is illustrated in Figure 7.3.

7.4.1 Controller Design

By defining $h = \frac{1}{N}$, where N is an integer, and using the notation $x^i(t) = x(ih, t)$, the model (7.26) can be written as

$$\begin{aligned}\dot{\tilde{\theta}}^i =& h_0^i u_{1_{ff}} \frac{\tilde{\theta}^{i+1} - 2\tilde{\theta}^i + \tilde{\theta}^{i-1}}{h^2} + h_1^i u_{1_{ff}} \frac{\tilde{\theta}^{i+1} - \tilde{\theta}^{i-1}}{2h} \\ &+ h_2^i u_{1_{ff}} \tilde{\theta}^i, \end{aligned} \tag{7.28}$$

with boundary conditions (7.27) written

$$\begin{aligned}\tilde{\theta}^0 &= 0, \\ \tilde{\theta}^N &= -k_3 u_{3_{fb}}. \end{aligned} \tag{7.29}$$

We choose the following asymptotically stable target system:

$$\frac{\partial \tilde{w}}{\partial t} = h_0 u_{1_{ff}} \tilde{w}'' + h_1 u_{1_{ff}} \tilde{w}' + h_2 u_{1_{ff}} \tilde{w} - C_w(\hat{\rho}) u_{1_{ff}} \tilde{w}, \tag{7.30}$$

with boundary conditions

$$\tilde{w}\Big|_{\hat{\rho}=0} = 0, \qquad \tilde{w}\Big|_{\hat{\rho}=1} = 0. \tag{7.31}$$

The choice of target system is motivated by the need to maintain the parabolic character of the PDE (7.26) (to keep the highest order derivatives) while improving upon the performance of the system. The design parameter $C_w(\hat{\rho}) > 0$ is chosen based on a trade-off between desired levels of robustness and performance and the physical actuator limits and can be chosen to weight parts of the profile more than others. The target system (7.30) can be spatially discretized as

$$\begin{aligned} \dot{\tilde{w}}^i =& h_0^i u_{1_{ff}} \frac{\tilde{w}^{i+1} - 2\tilde{w}^i + \tilde{w}^{i-1}}{h^2} + h_1^i u_{1_{ff}} \frac{\tilde{w}^{i+1} - \tilde{w}^{i-1}}{2h} \\ &+ h_2^i u_{1_{ff}} \tilde{w}^i - C_w^i u_{1_{ff}} \tilde{w}^i, \end{aligned} \tag{7.32}$$

with boundary conditions (7.31) written as

$$\begin{aligned} \tilde{w}^0 &= 0, \\ \tilde{w}^N &= 0. \end{aligned} \tag{7.33}$$

Next, a backstepping transformation is sought in the form

$$\tilde{w}^i = \tilde{\theta}^i - \alpha^{i-1}\left(\tilde{\theta}^0, \ldots, \tilde{\theta}^{i-1}\right). \tag{7.34}$$

By subtracting (7.32) from (7.28), the expression $\dot{\alpha}^{i-1} = \dot{\tilde{\theta}}^i - \dot{\tilde{w}}^i$ is obtained in terms of $\alpha^{k-1} = \tilde{\theta}^k - \tilde{w}^k,\ k = i-1, i, i+1$, i.e.,

$$\begin{aligned}\dot{\alpha}^{i-1} =& h_0^i u_{1_{ff}} \frac{\alpha^i - 2\alpha^{i-1} + \alpha^{i-2}}{h^2} + h_1^i u_{1_{ff}} \frac{\alpha^i - \alpha^{i-2}}{2h} \\ &+ h_2^i u_{1_{ff}} \alpha^{i-1} + C_w^i u_{1_{ff}} \tilde{\theta}^i - C_w^i u_{1_{ff}} \alpha^{i-1},\end{aligned} \tag{7.35}$$

which can be solved for α^i to yield

$$\begin{aligned}\alpha^i =& -\left[\frac{1}{\frac{h_0^i}{h^2} + \frac{h_1^i}{2h}}\right]\left[\left(\frac{-2h_0^i}{h^2} + h_2^i - C_w^i\right)\alpha^{i-1}\right. \\ &\left. + \left(\frac{h_0^i}{h^2} - \frac{h_1^i}{2h}\right)\alpha^{i-2} - \frac{1}{u_{1_{ff}}}\dot{\alpha}^{i-1} + C_w^i \tilde{\theta}^i\right],\end{aligned} \tag{7.36}$$

where $\alpha^0 = 0$ and $\dot{\alpha}^{i-1}$ is calculated as

$$\dot{\alpha}^{i-1} = \sum_{k=1}^{i-1} \frac{\partial \alpha^{i-1}}{\partial \tilde{\theta}^k} \dot{\tilde{\theta}}^k, \tag{7.37}$$

Next, subtracting (7.33) from (7.29) and putting the resulting expression in terms of $\alpha^{k-1} = \tilde{\theta}^k - \tilde{w}^k,\ k = i-1, i, i+1$, the control law for $u_{3_{fb}}$ can be defined as

$$u_{3_{fb}} = -\frac{1}{k_3}\alpha^{N-1}. \tag{7.38}$$

For any choice of grid size N, the control law (7.38) will be a time-invariant linear combination of $N-1$ measurements from the interior of the plasma. The coefficients of this linear combination can be calculated ahead of time for a given set of model parameters $h_0,\ h_1$, and h_2, and are independent of the feedforward inputs and trajectories. To aid in the recursive calculation of the coefficients, we define $\Phi \in \mathbb{R}^{N-1 \times N}$ for which the elements of column $i+1$ represent the coefficients of the

$\tilde{\theta}$ measurements used to evaluate α^i, i.e.,

$$\alpha^i = \sum_{j=1}^{i} \Phi_{j,i+1} \tilde{\theta}^j, \tag{7.39}$$

for $1 \leq i \leq N-1$. The first column (associated with $i = 0$) is all zeros since $\alpha^0 = 0$. We note that we can then write

$$\dot{\alpha}^i = \sum_{j=1}^{i} \Phi_{j,i+1} \dot{\tilde{\theta}}^j. \tag{7.40}$$

We substitute (7.28) into this expression, yielding

$$\begin{aligned} \frac{\dot{\alpha}^i}{u_{1_{ff}}} = & \sum_{j=1}^{i} \Phi_{j,i+1} \left[h_0^j \frac{\tilde{\theta}^{j+1} - 2\tilde{\theta}^j + \tilde{\theta}^{j-1}}{h^2} \right. \\ & \left. + h_1^j \frac{\tilde{\theta}^{j+1} - \tilde{\theta}^{j-1}}{2h} + h_2^j \tilde{\theta}^j \right], \end{aligned}$$

for $1 \leq i \leq N-2$ (we do not need to evaluate at $N-1$ to calculate the control law). This term is also a time invariant linear combination of measurements, so we define a matrix $\Psi \in \mathbb{R}^{N-1 \times N}$ for which the elements of column $i+1$ represent the measurement coefficients needed to evaluate $\frac{\dot{\alpha}^i}{u_{1_{ff}}}$, i.e.,

$$\frac{\dot{\alpha}^i}{u_{1_{ff}}} = \sum_{j=1}^{i+1} \Psi_{j,i+1} \tilde{\theta}^j. \tag{7.41}$$

The first column of Ψ is all zeros since $\dot{\alpha}^0 = 0$. We can then write (7.36) as

$$\begin{aligned}\alpha^i = &\sum_{j=1}^{i} \Phi_{j,i}\tilde{\theta}^j = \\ &- \left[\frac{1}{\frac{h_0^i}{h^2} + \frac{h_1^i}{2h}}\right]\left[\left(\frac{-2h_0^i}{h^2} + h_2^i - C_w^i\right)\sum_{j=1}^{i-1}\Phi_{j,i-1}\tilde{\theta}^j \right. \\ &\left. + \left(\frac{h_0^i}{h^2} - \frac{h_1^i}{2h}\right)\sum_{j=1}^{i-2}\Phi_{j,i-2}\tilde{\theta}^j - \sum_{j=1}^{i}\Psi_{j,i}\tilde{\theta}^j + C_w^i\tilde{\theta}^i\right]. \end{aligned} \tag{7.42}$$

Starting with $\alpha^0 = 0$ and $\dot{\alpha}^0 = 0$, expressions (7.41) and (7.42) for $i = 1, \ldots, N$ can be used to recursively fill the columns of Φ and Ψ. The control law (7.38) can then be written in the explicit feedback form

$$u_{3_{fb}} = -\frac{1}{k_3}\sum_{j=1}^{N-1}\Phi_{j,N}\tilde{\theta}^j. \tag{7.43}$$

The control law (7.43) allows us to calculate $u_{3_{fb}}$, which is then added to $u_{3_{ff}}$. The new value of u_3 is subsequently used with the feedforward trajectories u_2 and u_1 in the nonlinear transformations

$$I_p = u_3, \tag{7.44}$$

$$P_{tot} = u_3^2 u_{2_{ff}}^2, \tag{7.45}$$

$$\bar{n} = u_{1_{ff}}^{2/3} u_3^2 u_{2_{ff}}, \tag{7.46}$$

to calculate the input requests I_p, P_{tot}, and $\bar{n}$. In experimental testing, these requests are then sent as references to the respective dedicated controllers on the DIII-D device.

7.4.2 Stability of the Target System

In order to facilitate the proof of stability of the chosen target system, we first write the discretized target system (7.32)-(7.33) as a matrix equation. By noting the boundary conditions (7.31), and defining $\mathbf{C_w}$ as a square diagonal matrix populated with the values of C_w^i for $1 \leq i \leq N-1$, the set of ODEs describing the target system can be expressed as

$$\dot{\beta}(t) = (M - \mathbf{C_w})\, \beta(t) u_{1_{ff}}(t), \tag{7.47}$$

where $\beta = \left[\tilde{w}^1, \ldots, \tilde{w}^{N-1}\right]^T \in \mathbb{R}^{N-2\times 1}$ is the value of $\tilde{w}^i$ at the interior nodes, and the elements of the system matrix $M \in \mathbb{R}^{N-1\times N-1}$ are defined as

$$M_{1,1} = h_2^1 - \frac{2h_0^1}{h^2}, \qquad M_{N-1,N-1} = h_2^{N-1} - \frac{2h_0^{N-1}}{h^2}, \tag{7.48}$$

$$M_{1,2} = \frac{h_0^1}{h^2} + \frac{h_1^1}{2h}, \qquad M_{N-1,N-2} = \frac{h_0^{N-1}}{h^2} - \frac{h_1^{N-1}}{2h}, \tag{7.49}$$

$$M_{i,i-1} = \frac{h_0^i}{h^2} - \frac{h_1^i}{2h}, \qquad M_{i,i} = h_2^i - \frac{2h_0^i}{h^2}, \tag{7.50}$$

$$M_{i,i-1} = \frac{h_0^i}{h^2} + \frac{h_1^i}{2h}, \qquad \text{for } 2 \leq i \leq (N-2)\,. \tag{7.51}$$

The remaining entries in the M matrix are all zero. Taking $V = \frac{1}{2}\beta^T \Gamma \beta$ as a Lyapunov functional, where Γ is a positive definite matrix. We can compute the time derivative as

$$\dot{V} = \beta^T \Gamma \dot{\beta} = \beta^T \Gamma \left(M - \mathbf{C_w}\right) u_{1_{ff}}(t) \beta. \tag{7.52}$$

Since $u_{1_{ff}}(t) > 0\ \forall t$ and Γ is positive definite, we have that $(M - \mathbf{C_w})$ must be negative definite to ensure that $\dot{V}$ is negative definite for $\beta \neq 0$. For the model parameters used in this work, which are representative of a particular DIII-D discharge, M is negative definite and, since $\mathbf{C_w} \geq 0$, we can be sure that the matrix $(M - \mathbf{C_w})$

is negative definite. As a result, the discretized target system is asymptotically stable. It can be seen from this analysis how the choice of $\mathbf{C_w}$ can adjust the speed of response of the system. A detailed study of the stability properties of the open loop current profile dynamics can be found in [100].

7.4.3 Adaptive Law for Disturbance Rejection

The feedback law (7.43) is designed to improve upon the speed of response and stability properties of the current profile in the event of perturbed initial conditions. In order to improve upon the disturbance rejection capabilities of the controller, we augment the backstepping control law with an adaptive law that estimates a potential input disturbance on u_3 and effectively adds integral action to the closed loop system. We consider the model (7.28) with the addition of a disturbance u_{3_d} at the boundary, such that the boundary conditions (7.29) become

$$\begin{aligned} \tilde{\theta}^0 &= 0 \\ \tilde{\theta}^N &= -k_3 \left(u_{3_{fb}} + u_{3_d} \right) \end{aligned} \tag{7.53}$$

We follow the same backstepping procedure as before to obtain the recursively calculated transformation (2.3). If the disturbance were a known quantity, we could find the control law for $u_{3_{fb}}$ by subtracting (7.33) from (7.53) and putting the result in terms of $\alpha^{k-1} = \tilde{\theta}^k - \tilde{w}^k$, $k = i-1,\ i,\ i+1$. This would result in

$$u_{3_{fb}} = -\frac{1}{k_3}\alpha^{N-1} - u_{3_d} = -\frac{1}{k_3}\sum_{j=1}^{N-1} \Phi_{j,N}\tilde{\theta}^j - u_{3_d}, \tag{7.54}$$

where the matrix Φ is found in the same way as shown in subsection 7.4-A. In practice, the disturbance is unknown and the controller must make use of an estimate $\hat{u}_{3_d}$, such

that the control law becomes

$$u_{3_{fb}} = -\frac{1}{k_3}\sum_{j=1}^{N-1}\Phi_{j,N}\tilde{\theta}^j - \hat{u}_{3_d}. \tag{7.55}$$

If we apply the transformation (2.3) and the control law (7.55), the disturbed system is transformed to

$$\begin{aligned}\dot{\hat{w}}^i &= u_{1_{ff}}\left(h_0^i\frac{\hat{w}^{i+1}-2\hat{w}^i+\hat{w}^{i-1}}{h^2}+h_1^i\frac{\hat{w}^{i+1}-\hat{w}^{i-1}}{2h}\right.\\ &\quad \left.+h_2^i\hat{w}^i - C_w^i\hat{w}^i\right), \end{aligned}\tag{7.56}$$

with boundary conditions

$$\hat{w}^0 = 0, \tag{7.57}$$

$$\begin{aligned}\hat{w}^N &= \tilde{\theta}^N - \hat{\alpha}^{N-1} = -k_3\left(u_{3_{fb}}+u_{3_d}\right)+k_3\left(u_{3_{fb}}+\hat{u}_{3_d}\right)\\ &= k_3\tilde{u}_{3_d}, \end{aligned}\tag{7.58}$$

where $\tilde{u}_{3_d} = \hat{u}_{3_d} - u_{3_d}$ is the error in the estimate of the input disturbance. We now look for an adaptive law for the estimate $\hat{u}_{3_d}$ that guarantees stability of the target system.

We can write the achieved target system as a matrix equation. By noting the boundary conditions (7.57) and (7.58), the set of ODEs describing the target system can then be expressed as

$$\dot{\beta}(t) = \left(M - \mathbf{C_w}\right)\beta(t)u_{1_{ff}}(t) + Zu_{1_{ff}}(t)\tilde{u}_{3_d}, \tag{7.59}$$

where β, M, and $\mathbf{C_w}$ are defined as before. The vector Z is all zeros except

$$Z_{N-1} = k_3 \left(\frac{h_0^{N-1}}{h^2} + \frac{h_1^{N-1}}{2h} \right). \tag{7.60}$$

We take

$$V = \frac{1}{2}\beta^T \Gamma \beta + \frac{C_3}{2}\tilde{u}_{3_d}^2 \tag{7.61}$$

as a Lyapunov functional, where Γ is a positive definite matrix and C_3 is a positive constant. We can then compute the time derivative as

$$\begin{aligned}
\dot{V} &= \beta^T \Gamma \dot{\beta} + C_3 \tilde{u}_{3_d} \dot{\tilde{u}}_{3_d} && (7.62)\\
&= \beta^T \Gamma \left(M - \mathbf{C_w}\right) u_{1_{ff}}(t)\beta + \beta^T \Gamma Z u_{1_{ff}}(t)\tilde{u}_{3_d} && (7.63)\\
&\quad + C_3 \tilde{u}_{3_d} \dot{\tilde{u}}_{3_d} && (7.64)\\
&= \beta^T \Gamma \left(M - \mathbf{C_w}\right) u_{1_{ff}}(t)\beta \\
&\quad + \left(\beta^T \Gamma Z u_{1_{ff}}(t) + C_3 \dot{\tilde{u}}_{3_d}\right) \tilde{u}_{3_d}. && (7.65)
\end{aligned}$$

If we assume a constant disturbance and take the adaptive law

$$\dot{\tilde{u}}_{3_d} = \dot{\hat{u}}_{3_d} - \dot{u}_{3_d} = \dot{\hat{u}}_{3_d} = -\frac{u_{1_{ff}}(t)}{C_3}\beta^T \Gamma Z, \tag{7.66}$$

we obtain

$$\dot{V} = \beta^T \Gamma \left(M - \mathbf{C_w}\right) u_{1_{ff}}(t)\beta. \tag{7.67}$$

As previously mentioned, M is negative definite for the model parameters used in this work and, since, $\mathbf{C_w} \geq 0$, we can be sure that the matrix $(M - \mathbf{C_w})$ is negative definite. Since $u_{1_{ff}}(t) > 0 \ \forall t$, Γ is positive definite, and (7.61) is a function of β

and $\tilde{u}_{3_d}$, $\dot{V}$ is negative semidefinite. Given that $\dot{u}_{ff}(t)$ is bounded, the conditions of Barbalat's lemma (see [51] p. 323) are satisfied and we can be sure that $\dot{V} \to 0$ as $t \to \infty$, and, as a result, $\beta \to 0$. It can be seen from this analysis how the choice of $\mathbf{C_w}$ can adjust the speed of response of the system and C_3 determines the speed of adaptation.

We note that the matrix Φ can be used to write the vector of target system states, β, in terms of the vector of measurements $\Theta = [\tilde{\theta}^1, \ldots, \tilde{\theta}^{N-1}]^T$, i.e.,

$$\beta = \Theta - \Phi\Theta = (I - \Phi)\Theta. \tag{7.68}$$

This allows us to write the adaptive law as

$$\dot{\hat{u}}_{3_d} \;=\; -\frac{u_{1_{ff}}(t)}{C_3} Z^T \Gamma^T \left(I - \Phi\right) \Theta. \tag{7.69}$$

The adaptive law (7.69) combined with the control law (7.43) allows for the calculation of the feedback term $u_{3_{fb}}$, which is then added to the feedforward term $u_{3_{ff}}$ to obtain u_3. The inputs u_1 and u_2 are again kept at their feedforward values. These signals are then used in the nonlinear transformations (7.44), (7.45), and (7.46) to obtain the requests for I_p, P_{tot}, and $\bar{n}$.

7.5 Controller Implementation in the DIII-D PCS

In this section, we present the real-time control algorithm implementation in the DIII-D Plasma Control System (PCS) along with the simulation framework used to test the controller and ensure the real-time algorithm was working correctly prior to experiments.

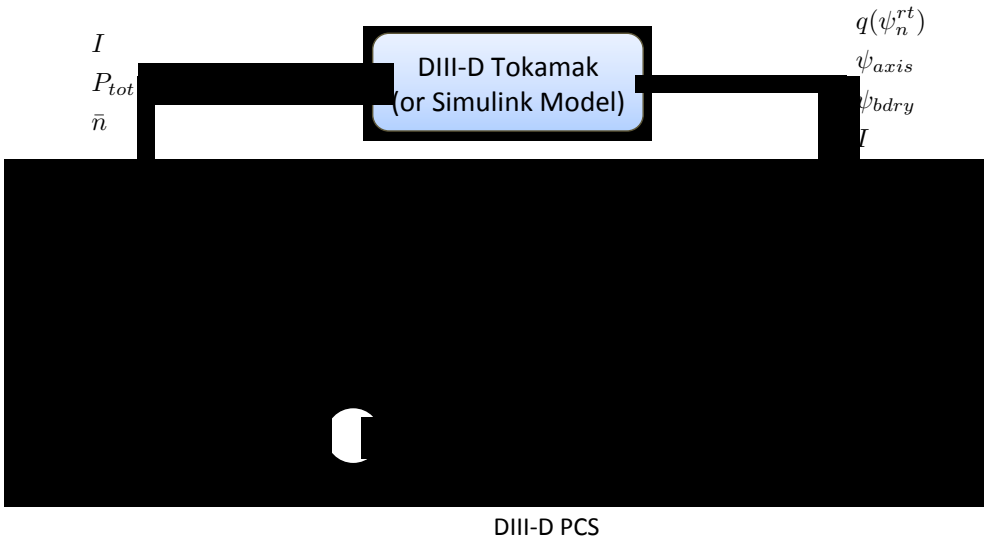

Figure 7.4: DIII-D PCS implementation of the magnetic profile control algorithm. Note that the PCS code can either be connected to the DIII-D tokamak or, through the simserver architecture, a Simulink model of the magnetic diffusion equation for simulation tests.

7.5.1 Real-Time Algorithm

The real-time feedforward+feedback algorithm we have implemented in the DIII-D PCS, depicted in Figure 7.4, is a general framework designed to enable testing of a variety of control laws, and can be used to control several different profiles and scalar quantities. Magnetic profiles that can be controlled include the safety factor, q, the rotational transform, $\iota = 1/q$, the poloidal magnetic flux, ψ, and the poloidal flux gradient, θ. Available kinetic profiles include the electron temperature, the ion temperature, and the toroidal rotation velocity. The framework can also be used to control scalar quantities, including normalized plasma beta β_N, the minimum q, or the internal inductance of the plasma, l_i. The rtEFIT code [101], a real-time magnetic equilibrium reconstruction code, and the real-time charge-exchange recombination (rtCER) code [102] were interfaced with the algorithm to provide measurements of magnetic and kinetic profiles on a grid of measurement points. Only the diagnostics

from rtEFIT were needed for feedback in testing the controller presented in this work. The real-time algorithm performs the necessary coordinate transformation to construct the variable of interest $\theta(\hat{\rho})$ from the data provided by rtEFIT (the plasma current $I(t)$, the poloidal stream function at the magnetic axis ψ_{axis} and the plasma boundary ψ_{bdry}, and the safety factor q at 64 evenly spaced points in the normalized flux spatial domain $\psi_n = (\psi - \psi_{axis}) / (\psi_{bdry} - \psi_{axis})$). The profile error $\tilde{\theta}$ is then generated by comparing the measurements to the target profile θ_{ff}. The feedback portion of the algorithm is a discrete time state-space system with a selectable sampling time. Based on the modulation rate of the MSE (motional Stark effect) beam used to obtain q profile measurements in real-time, a sampling time of 20ms was used in this work (the beam was on for 10 ms and off for 10 ms). Taking the estimate of the input disturbance $\hat{u}_{3_d}$ as a controller state, the control laws (7.43) and (7.69) were put into a state-space form and a discrete time approximation with the appropriate sample time was generated. Within the PCS, the discrete state space control law produces the output u_{fb}, which is added to the feedforward signal, u_{ff}, before being passed to the nonlinear transformations (7.44), (7.45), and (7.46). The resulting outputs $I(t)$, $P_{tot}(t)$, and $\bar{n}(t)$ are then sent to existing, empirically tuned single-input-single-output (SISO) control laws for the respective quantities. For example, a proportional-integral-derivative (PID) loop is used to regulate the plasma current to the desired waveform via actuation of the ohmic coil voltage and measurements taken using a Rogowski loop. A separate PID controller is used to regulate the density through gas injection. The beam power is regulated through pulse width modulation of the power supplies for each neutral beam injector. While the current and beam controllers are typically effective and respond to reference changes at a time scale much faster than the current diffusion time-scale, the density response can be slower, especially when being decreased. The experimental results presented

in Section 7.7 reflect this description (see Figure 7.12). While this dynamic could be accounted for in future controller designs, it is not directly accounted for in the present design. Nevertheless, simulations and preliminary experimental results show that the closed-loop system is robust to poor density control to some degree. We have also included in the PCS framework the possibility of introducing artificial disturbances for testing through the signal u_d, and to specify target trajectories through the signal θ_{ff}.

7.5.2 Simserver Architecture

Prior to experimental testing, the control scheme proposed in this work was evaluated through simulations using the simserver architecture, a simulation environment that allows the DIII-D PCS to exchange data with a Matlab/Simulink model that generates simulated diagnostics. This framework enables debugging of the real-time feedback code as well as assessment of the effectiveness of control designs prior to actual experiments [103]. After the simulation phase, the same PCS code used in the simserver simulations was used to control the actual device.

To test the control scheme proposed in this work, a Simulink model of the magnetic diffusion equation (7.3) was integrated into a simserver and the real-time implementation of the control algorithm was programmed into the PCS [104]. The Simulink model was constructed by discretizing the magnetic diffusion equation in space and was made to output the same set of measurements sent to the PCS by rtEFIT during experiments.

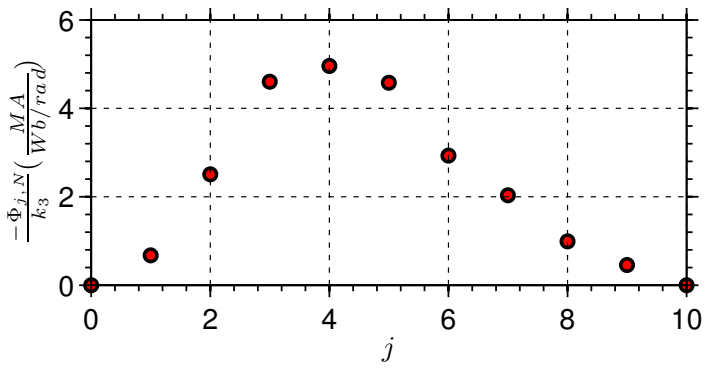

Figure 7.5: Coefficients of the linear combination of profile errors that generate the feedback control term $u_{3_{fb}}$.

7.6 Simulation Results

In this section, we present results of the simulation study used to test and tune the controller design and implementation prior to experimental testing. The simulations presented here demonstrate the ability of the controller to track a desired profile evolution despite disturbances and perturbed initial conditions.

7.6.1 Simulation of Static Controller

For the results presented in this subsection, as well as for the experimental results, we used the static, non-adaptive control law (7.43) designed with $C_w^i = 3.75 \times 10^{-16}$ for $1 \leq i \leq 5$ and $C_w^i = 7.5 \times 10^{-16}$ for $6 \leq i \leq N$ where $N = 10$ (note that the simulation model was discretized on a finer grid than that used for control). The elements of the vector $-\Phi_{j,N}/k_3$, which represent the coefficients of the linear combination of profile errors that generate the feedback control term $u_{3_{fb}}$, are shown in Figure 7.5.

As designed, the largest weight is placed on profile errors around $j = 4$, corresponding to $\hat{\rho} = 0.4$. In this simulation study, we tested the ability of the feedback controller to reject an artificially added input disturbance and to overcome errors in the initial condition of the profile. First, a particular set of feedforward inputs u_{ff}

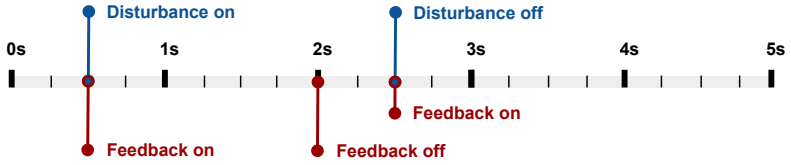

Figure 7.6: Timeline depicting when the artificial disturbance and the feedback controller are switched on and off during the closed loop simulation and the experimental shot 146454.

was used in a feedforward only simulation to generate a target poloidal flux gradient profile evolution θ_{ff}. The simulation was run again with the addition of an input disturbance of 0.1 MA (approximately 8%) to u_3 from $t = 0.5$s to $t = 2.5$s. The feedback controller was activated from $t = 0.5$s to $t = 2.0$s to test disturbance rejection and switched off from $t = 2.0$s to $t = 2.5$s to observe how the profile would drift away from the desired one under the influence of the uncontrolled input disturbance. Finally, at $t = 2.5$s, the controller was turned back on and the input disturbance was removed to see if the controller could recover the desired profile despite the profile error caused by the uncontrolled drift. The time intervals for which the system is disturbed and for which the feedback controller is turned on are summarized in Figure 7.6.

Time traces of q at several points along the profile are shown in Figure 7.7. The results of the closed loop simulation are compared with the reference generated in the feedforward simulation without the disturbance. A small error remained during the disturbance rejection phase of the simulation ($t = 0.5$s to $t = 2.0$s). This can be expected since there is no integral action in the static controller. The steady state error could be made smaller by increasing the gain of the controller (through the parameters C_w^i), however, this would increase the sensitivity of the closed loop system to measurement noise. Subsequent simulation results will show that this problem can be avoided by using the adaptive law (7.69). When the controller was turned off from

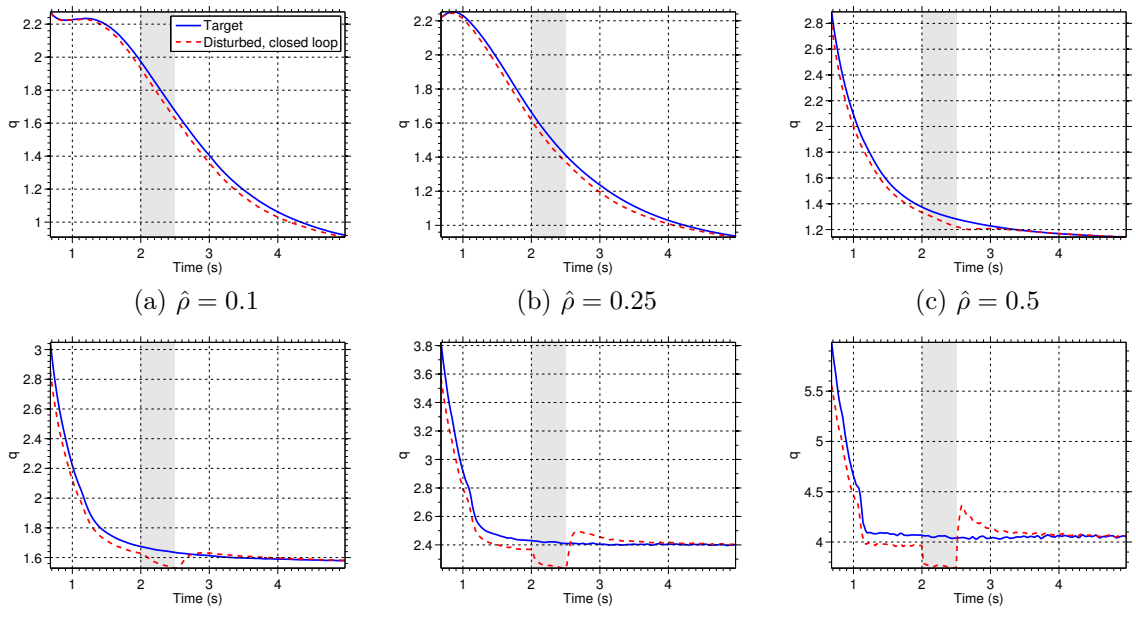

(a) $\hat{\rho} = 0.1$ (b) $\hat{\rho} = 0.25$ (c) $\hat{\rho} = 0.5$

(d) $\hat{\rho} = 0.65$ (e) $\hat{\rho} = 0.8$ (f) $\hat{\rho} = 0.95$

Figure 7.7: Time traces of q at various points comparing the nominal feedforward simulation (blue-solid) with the closed loop, disturbed simulation (red-dashed) using the static control law. Note the effect of turning off the controller between $t = 2.0$s and $t = 2.5$s (shaded regions on the plots).

$t = 2.0$s to $t = 2.5$s, the error caused by the boundary input disturbance (see Figure 7.7f) diffused in from the edge of the plasma over time, reaching at least as far as $\hat{\rho} = 0.5$ before $t = 2.5$s (see Figure 7.7c). At $t = 2.5$s, the disturbance was removed and the controller was turned back on. The controller increased the value of q at the boundary (see Figure 7.7f) and the effect of this increase diffused inward over time, causing the error initially present at $t = 2.5$s to be removed.

7.6.2 Simulation of Adaptive Controller

Here we present simulation results showing the improved disturbance rejection achieved with the addition of the adaptive law (7.69). The controller was designed, as in the previous case, using $C_w^i = 3.75 \times 10^{-16}$ for $1 \leq i \leq 5$ and $C_w^i = 7.5 \times 10^{-16}$ for

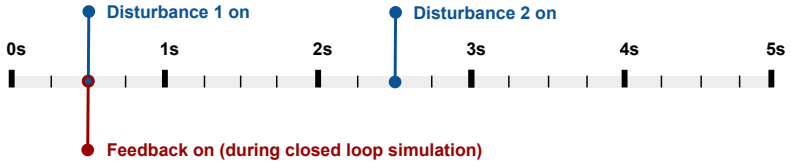

Figure 7.8: Timeline depicting when the artificial disturbance and the feedback controller are switched on and off during the closed loop simulation and the experimental shot 146454.

$6 \leq i \leq N$ and with $N = 10$. For the adaptive law, we chose $C_3 = 1.5 \times 10^{-15}$ and $\Gamma = I$, where I is the identity matrix. The feedforward inputs used during the study were the same as those used in the previous simulation and experiment. A disturbance in u_3 of -0.1 MA (approximately -8%) was applied from 0.5s$\leq t <$ 2.5s and a -0.2 MA disturbance (approximately -17%) was applied from 2.5s$\leq t \leq$ 5.0s. In addition, an unmatched disturbance of +10% in both u_1 and u_2 was applied throughout the discharge. A significant initial condition error was also imposed. Two simulation cases were run: (1) feedforward only, (2) feedforward+feedback using the adaptive law (7.69). The feedback controller was active throughout the second simulation. A timeline for the simulations is given in Figure 7.8.

In Figure 7.9, the q and θ profiles achieved in each of the simulation cases are compared with the target profiles at several times. The first three plots (Figures 8.3a-7.9c) show results during the first disturbance (+10% in u_1 and u_2, -0.1 MA in u_3), while Figures 8.3c-7.9f show results during the second disturbance (+10% in u_1 and u_2, -0.2 MA in u_3). The disturbances caused the open loop profiles to differ significantly from the target profiles. On the other hand, the adaptive backstepping controller was able to quickly reject the disturbances and match the target profile after a short time, as visible in Figures 7.9c and 7.9f. Even with the presence of unmatched disturbances, the controller was able to achieve excellent regulation of the

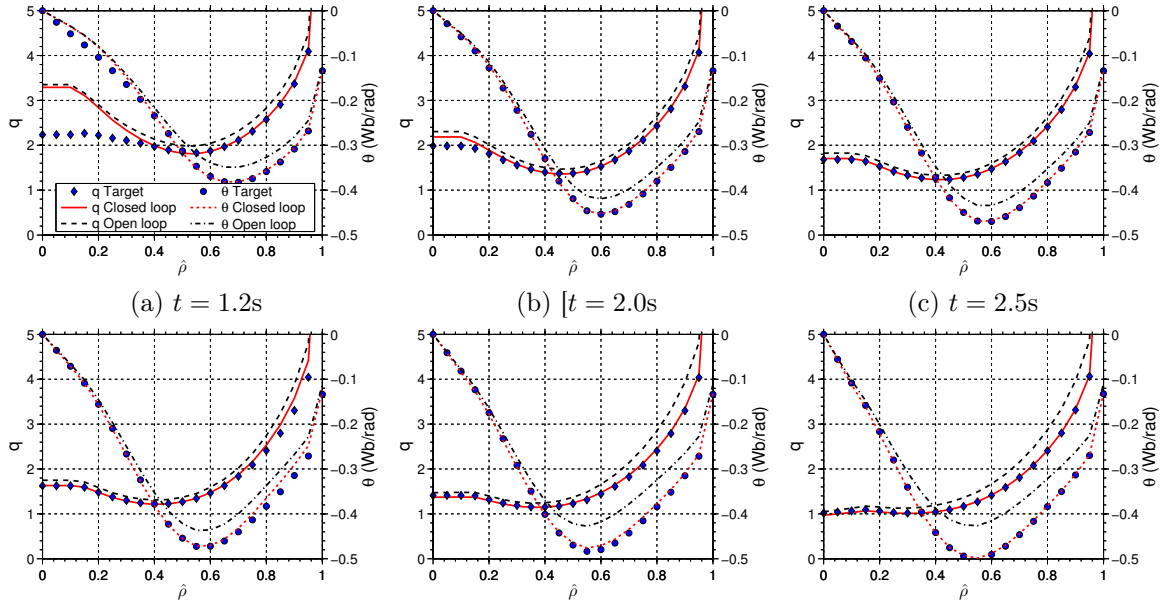

(a) $t = 1.2$s (b) [$t = 2.0$s (c) $t = 2.5$s

(d) $t = 2.6$s (e) $t = 3.0$s (f) $t = 4.0$s

Figure 7.9: Comparison of q and θ profiles at various times for the adaptive control simulation. The open loop, feedforward only profiles (q: black, dashed, θ: black, dash-dot) and closed loop profiles (q: red, solid, θ: red, dotted) are compared with the desired target (q: blue diamond markers, θ: blue circular markers).

desired target profile. It is expected that adding feedback control laws for the interior and diffusive actuators u_1 and u_2 could improve upon the results by adding extra degrees of freedom to the control scheme.

7.7 Experimental Testing

The goal of the experiment presented here was to verify that the feedback controller synthesized from a first principles based model of the poloidal flux profile evolution is able to drive the poloidal flux gradient profile in the DIII-D device to a desired target. While the feedback scheme could eventually be used to attempt to track an arbitrarily chosen target, we began by testing the controller using a target that is known to be achievable. We guaranteed the achievability of the target profile by

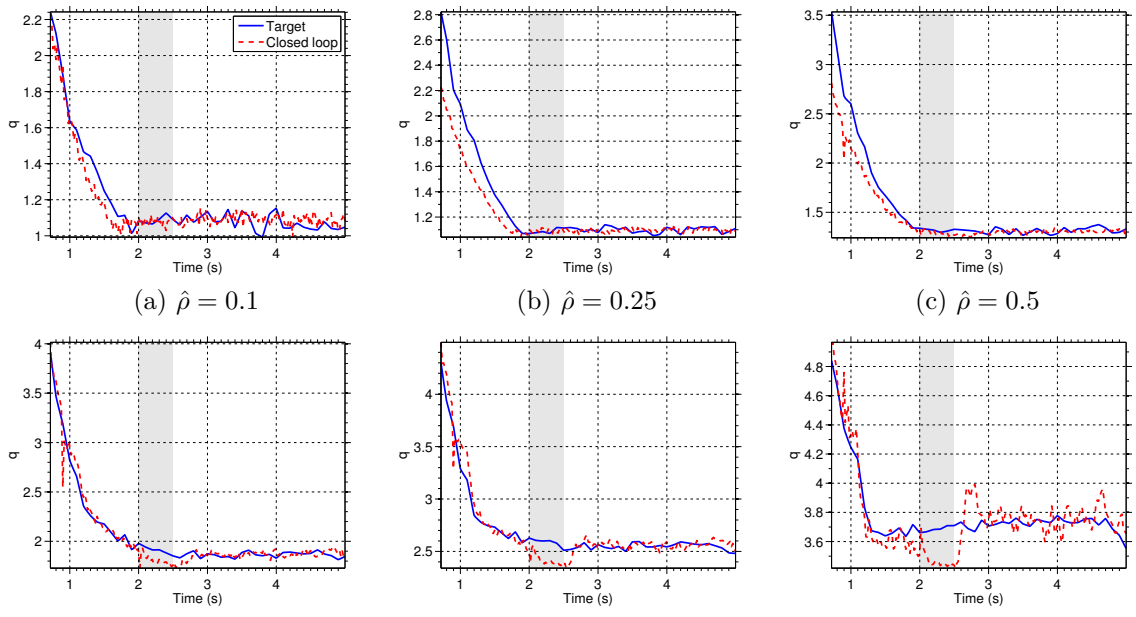

(a) $\hat{\rho} = 0.1$ (b) $\hat{\rho} = 0.25$ (c) $\hat{\rho} = 0.5$

(d) $\hat{\rho} = 0.65$ (e) $\hat{\rho} = 0.8$ (f) $\hat{\rho} = 0.95$

Figure 7.10: Time traces of q at various points comparing the experimental results for the reference shot 145477 (blue-solid) and the closed loop, disturbed shot 146454 (red-dashed). Note the effect of turning off the controller during the interval 2.0s$\leq t \leq$ 2.5s (shaded regions of plots).

generating it from the results of the open loop shot 145477 using the same feedforward inputs as those used in the simulation study. The reference scenario was a double-null plasma with a toroidal magnetic field of 1.85T, and flat-top values of I_p, $\bar{n}$, and β_N (a normalized figure of merit for plasma performance) of 1.2 MA, 2×10^{19} m$^-3$, and 0.8%, respectively. The resulting θ profile was then used as the target for the closed loop (feedforward+feedback) shot 146454. During shot 146454, we used the static control law (7.43) designed with $C_w^i = 3.75 \times 10^{-16}$ for $1 \leq i \leq 5$ and $C_w^i = 7.5 \times 10^{-16}$ for $6 \leq i \leq N$ where $N = 10$. Additionally, an input disturbance of 0.1 MA in the reference for u_3 was added from $t = 0.5$s to $t = 2.5$s. The feedback controller was turned on from $t = 0.5$s to $t = 2.0$s to test disturbance rejection and switched off from $t = 2.0$s to $t = 2.5$s to allow the θ profile to drift away from the desired one under the

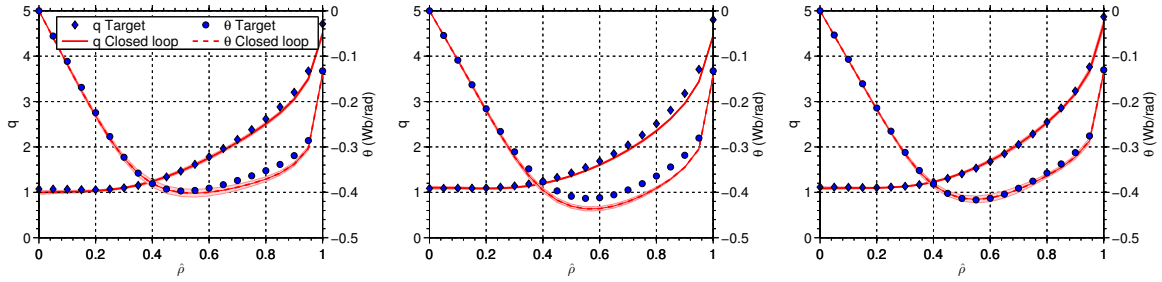

(a) $t = 1.98$s (feedback and disturbance on)

(b) $t = 2.5$s (feedback off, disturbance on)

(c) $t = 4.02$s (feedback on, disturbance off)

Figure 7.11: Comparison of experimentally achieved q and θ profiles at various times for reference shot 145477 (q: blue diamond markers, θ, blue circular markers) and the closed loop, disturbed shot 146454 (q: red-solid, θ: red-dashed). Partial disturbance rejection is seen in (a), the effect of the uncontrolled disturbance can be noted in (b), and the recovery of the target profile after the disturbance is removed and the controller is turned back on can be observed in (c). The red shaded regions represent the standard deviation of the measurements over a 0.25s window prior to the time shown.

influence of the input disturbance. Finally, at $t = 2.5$s the controller was turned back on and the input disturbance was removed to see if the controller could recover the desired profile despite the error caused by the drift. This is the same scenario that was used in the first simulation results.

Time traces of q at several points along the profile are given in Figure 7.10. The results of the closed loop shot 146454 are compared with the reference generated in the feedforward shot 145477. During the closed loop shot, there was an initial condition error, which can most clearly be seen in Figures 7.10b and 7.10c, in addition to the artificially applied input disturbance. Though the controller mostly rejected the disturbance during the first phase ($t = 0.5$s to $t = 2.0$s), a small amount of error remained at the end of the controlled interval (see Figure 7.10f). As was mentioned before, this offset is because the backstepping controller is static, that is, it contains only proportional feedback and no integral action. The offset could be reduced by increasing the gain of the controller, however, this would increase the sensitivity

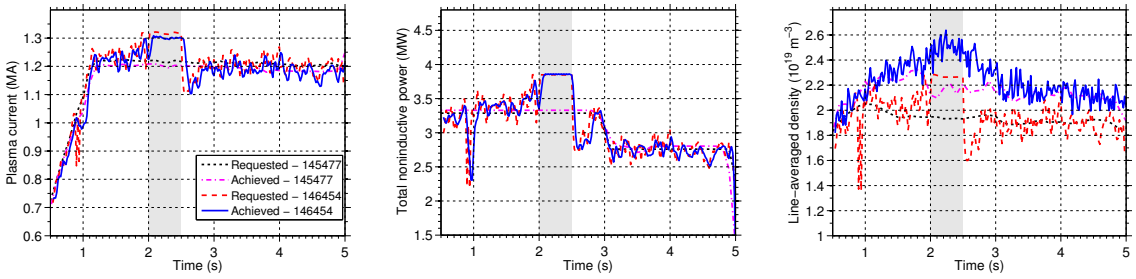

(a) Plasma current I_p (b) Total non-inductive current (c) Line-averaged density

Figure 7.12: Comparison of requested and achieved actuator values during the feed-forward shot 145477 and the closed loop, disturbed shot 146454. During the closed loop shot, the feedback control was turned off between $t = 2.0$s and $t = 2.5$s (shaded regions of plots).

to noise and may cause the controller to be too aggressive. The addition of the adaptive law (7.69), which will be tested in a future experimental campaign, should improve upon the disturbance rejection and tracking capabilities of this scheme, as was demonstrated in simulations. The error caused by the disturbance increased when the controller was turned off, and the error diffused in from the edge of the plasma throughout the brief uncontrolled drift phase ($t = 2.0$s to $t = 2.5$s), as can be seen in Figures 7.10c-7.10f. Finally, once the disturbance was removed and the controller was turned back on at $t = 2.5$s, the target values of q were quickly recovered.

In Figure 7.11, the q and θ profiles achieved in the closed loop, disturbed shot 146454 are compared with the desired reference profiles obtained from shot 145477 at several times. Figure 7.11a shows that the controller partially rejected the disturbance and achieved a profile close to the desired one shortly before it was turned off at $t = 2.0$s. Figure 7.11b shows the error resulting from the disturbance after the brief uncontrolled drift phase ($t = 2.0s$ to $t = 2.5s$), while the successful recovery of the desired profile after the controller was turned back on is clearly seen in Figure 7.11c. The red shaded regions, which represent the standard deviation of the measurements over a 0.25s window prior to the time shown, provide an indication of the measurement

noise.

Finally, the actuator requests and achieved values are compared in Figure 7.12. It should be noted that while the total plasma current and total power were tightly controlled and the requests were reproduced quite well, the request for line averaged density was often not achieved. This represented additional input disturbances aside from the intentional one added to the feedforward input references.

7.8 Conclusions

We have presented a scheme for controlling the current profile in L-mode discharges in DIII-D based on a dynamic model of the evolution of the poloidal magnetic flux profile. By employing a backstepping control design technique, a transformation was found from the spatially discretized system to an asymptotically stable target system, along with a boundary feedback control law. The resulting control law is designed to augment an arbitrary set of feedforward input trajectories. We have also presented an adaptive law to add integral action to the control scheme. Through a nonlinear transformation of the control inputs, the scheme provides stabilizing reference values for the total plasma current, non-inductive power, and plasma density. A simulation study shows the performance of the controller when initial conditions are perturbed and the input is biased. Preliminary experimental results are also presented, showing the controller to perform well despite the presence of additional disturbances caused by the physical actuators and noisy real-time measurements of the θ profile. Experimental testing of the adaptive scheme presented in this work will be carried out in future campaigns.

Chapter 8

Backstepping Control of the Current Profile in H-mode Discharges

8.1 Introduction

In the previous chapter, a first-principles-driven control-oriented model for the current profile evolution in L-mode discharges was used to design a backstepping boundary feedback control law. The proposed scheme was shown, through simulations and experimental results, to be capable of rejecting disturbances and regulating the current profile around a desired trajectory. The bootstrap current, a self-generated, non-inductive current source, was neglected in the model derivation, since L-mode discharges typically have a small fraction of bootstrap current. In this work, an extension of the model that includes the bootstrap current and is therefore suitable for H-mode discharges is used to develop a model-based controller for H-mode discharges (a detailed description of the model development can be found in [105]). Building upon the designs proposed in [106, 95], the PDE describing the current profile evolution is discretized in space using a finite difference method and a backstepping design

is applied to obtain a transformation from the original system into a particular target system. The target system is rendered asymptotically stable by control laws for the available distributed actuators, which complement the backstepping boundary control law. Numerical simulations show the ability of the scheme to track target profiles, and the disturbance rejection capability of the scheme is demonstrated in a preliminary experiment on DIII-D.

This chapter is organized as follows. In Section 8.2, a first-principles-driven model for the poloidal flux gradient profile evolution in H-mode discharges in DIII-D is introduced. The objectives of the proposed control scheme are given in Section 8.3, while the details of the design are presented in 8.4. In Section 8.5, the feedback controller performance is tested through simulations, and in Section 8.6, the controller is tested in a preliminary experiment in the DIII-D tokamak. Finally, concluding remarks are given in Section 8.7.

8.2 Current Profile Evolution Model

To obtain a PDE describing the evolution of θ in H-mode discharges, we again start from the well known magnetic diffusion equation [97],

$$\frac{\partial \psi}{\partial t} = \frac{\eta(T_e)}{\mu_0 \rho_b^2 \hat{F}^2} \frac{1}{\hat{\rho}} \frac{\partial}{\partial \hat{\rho}} \left(\hat{\rho} \hat{F} \hat{G} \hat{H} \frac{\partial \psi}{\partial \hat{\rho}} \right) + R_0 \hat{H} \eta(T_e) \frac{< \bar{j}_{NI} \cdot \bar{B} >}{B_{\phi,0}}, \tag{8.1}$$

which describes the poloidal magnetic flux evolution. The boundary conditions are again given by

$$\left. \frac{\partial \psi}{\partial \hat{\rho}} \right|_{\hat{\rho}=0} = 0, \qquad \left. \frac{\partial \psi}{\partial \hat{\rho}} \right|_{\hat{\rho}=1} = -\frac{\mu_0}{2\pi} \frac{R_0}{\hat{G}\Big|_{\hat{\rho}=1} \hat{H}\Big|_{\hat{\rho}=1}} I(t), \tag{8.2}$$

where $I(t)$ is the total plasma current.

In order to arrive at a control-oriented model of the current profile evolution, simplified empirical models of plasma parameters are used to capture the dominant physics describing how the available actuators affect the system. In developing these models, care was taken to ensure their applicability to high confinement mode (H-mode) discharges in DIII-D. The model for the electron density is given by

$$n_e\left(\hat{\rho},t\right) = n_e^{prof}(\hat{\rho})\bar{n}(t), \tag{8.3}$$

where $n_e^{prof}(\hat{\rho})$ is a reference electron density profile and $\bar{n}(t)$ is the line averaged density. The electron temperature is modeled as

$$T_e\left(\hat{\rho},t\right) = k_{T_e} T_e^{profile}\left(\hat{\rho}\right) \frac{I(t)\sqrt{P_{tot}(t)}}{\bar{n}(t)}, \tag{8.4}$$

where k_{T_e} is a constant, $T_e^{profile}\left(\hat{\rho}\right)$ is a reference profile, $P_{tot}\left(t\right)$ is the total average NBI and gyrotron heating power. The model for the non-inductive toroidal current density driven by each auxiliary source is given by

$$\frac{<\bar{j}_k \cdot \bar{B}>}{B_{\phi,0}} = k_k j_k^{profile}\left(\hat{\rho}\right) \frac{T_e\left(\hat{\rho},t\right) P_k(t)}{n_e(\hat{\rho},t)}, \tag{8.5}$$

where k_k is a constant and $j_k^{profile}\left(\hat{\rho}\right)$ is a reference profile for the non-inductive current deposition for the k-th auxiliary source. In this work, we consider the total gyrotron power ($k = 2$), the total on-axis beam power ($k = 3$), and the total off-axis beam power ($k = 4$) as available auxiliary sources. The bootstrap current, a self-generated non-inductive current source that arises due to gradients in the magnetic

field strength and plasma pressure, is modeled as [68]

$$\frac{<\bar{j}_{bs}\cdot\bar{B}>}{B_{\phi,0}} = \frac{k_{JkeV}R_0}{\hat{F}}\frac{1}{\theta}\left[2\mathcal{L}_{31}T_e\frac{\partial n_e}{\partial\hat{\rho}} + \left\{2\mathcal{L}_{31}+\mathcal{L}_{32}+\alpha\mathcal{L}_{34}\right\}n_e\frac{\partial T_e}{\partial\hat{\rho}}\right], \tag{8.6}$$

where $k_{JkeV} = 1.602\times10^{-16}J/keV$, and $\mathcal{L}_{31}(\hat{\rho})$, $\mathcal{L}_{32}(\hat{\rho})$, $\mathcal{L}_{34}(\hat{\rho})$, and $\alpha(\hat{\rho})$ depend on the particular magnetic equilibrium and on the particle collisionality of the plasma. The plasma resistivity, $\eta(T_e)$, is given by

$$\eta(\hat{\rho},t) = \frac{k_{eff}Z_{eff}}{T_e^{3/2}(\hat{\rho},t)}, \tag{8.7}$$

where k_{eff} and Z_{eff} are constants.

To obtain a PDE governing the evolution of $\theta(\hat{\rho},t)$, the empirical scaling models for the temperature, resistivity, and current drive are substituted in (8.1), the result is expanded with the chain rule and differentiated, yielding

$$\frac{\partial\theta}{\partial t} = \left(h_{1a}\frac{\partial^2\theta}{\partial\hat{\rho}^2}+h_{1b}\frac{\partial\theta}{\partial\hat{\rho}}+h_{1c}\theta\right)u_1(t)+\sum_{k=2}^{4}h_k u_k(t) + \left(\frac{1}{\theta}\frac{df_5}{d\hat{\rho}}+\frac{f_5}{\theta^2}\frac{\partial\theta}{\partial\hat{\rho}}\right)u_5(t), \tag{8.8}$$

$$\theta(0,t) = 0, \quad \theta(1,t) = -k_6u_6(t), \tag{8.9}$$

where h_{1a}, h_{1b}, and h_{1c} , h_k for $k=2,3,4$, f_5, and D_ψ are functions of $\hat{\rho}$, k_6 is a constant, and

$$u_1(t) = \left(\frac{\bar{n}}{I(t)\sqrt{P_{tot}(t)}}\right)^{3/2}, \quad u_k(t) = \frac{P_k}{\left(I_p\sqrt{P_{tot}}\right)^{1/2}\bar{n}^{1/2}},$$
$$u_5(t) = \frac{\bar{n}^{3/2}}{\left(I(t)\sqrt{P_{tot}}\right)^{1/2}}, \quad u_6(t) = I(t). \tag{8.10}$$

for $k = 2, 3, 4$. Equation (8.8) admits actuators $u = [u_1, \ldots, u_6]$, which each represent nonlinear combinations of the physical actuators, $I(t)$, $\bar{n}(t)$, and $P_k(t)$ for $k = 2, 3, 4$. The controller proposed in this work will generate waveforms for these physical actuators. These waveforms represent references to be sent to existing dedicated controllers for each of the respective quantities.

8.3 Control Objective

Let $u_{ff}(t) = \left[u_{1_{ff}}(t), \ldots, u_{6_{ff}}(t)\right]$ represent a set of feedforward control input trajectories and $\theta_{ff}(\hat{\rho}, t)$ be the associated poloidal flux gradient profile evolution for a nominal initial condition $\theta_{ff}(\hat{\rho}, 0)$. The nominal profile evolution satisfies

$$\begin{aligned}\frac{\partial \theta_{ff}}{\partial t} &= \left(h_{1a}\frac{\partial^2 \theta_{ff}}{\partial \hat{\rho}^2} + h_{1b}\frac{\partial \theta_{ff}}{\partial \hat{\rho}} + h_{1c}\theta_{ff}\right) u_{1_{ff}}(t) \\ &\quad + \sum_{k=2}^{4} h_k u_{k_{ff}}(t) + g\left(\theta_{ff}\right) u_{5_{ff}}(t), \\ \theta_{ff}(0,t) = 0, &\quad \theta_{ff}(1,t) = -k_6 u_{6_{ff}}(t),\end{aligned}$$

where $g\left(\theta\right) = \left(\frac{1}{\theta}\frac{df_5}{d\hat{\rho}} + \frac{f_5}{\theta^2}\frac{\partial \theta}{\partial \hat{\rho}}\right)$.

Given errors in the initial conditions or other disturbances, the actual state will differ from the desired target, i.e. $\theta(\hat{\rho}, t) = \theta_{ff}(\hat{\rho}, t) + \tilde{\theta}(\hat{\rho}, t)$, where $\tilde{\theta}$ represents the error between the achieved and nominal profile. We consider $u = u_{ff} + u_{fb} + d$ where the feedback control signals $u_{fb}(t) = \left[u_{1_{fb}}(t), \ldots, u_{6_{fb}}(t)\right]$ are generated by a to-be-designed control law and $d = [d_1, \ldots, d_6]$ represents a set of constant input

disturbances. The dynamics of the deviations can then be written as

$$\begin{aligned}\frac{\partial\tilde{\theta}}{\partial t} =& \left(h_{1a}\frac{\partial^2\tilde{\theta}}{\partial\hat{\rho}^2} + h_{1b}\frac{\partial\tilde{\theta}}{\partial\hat{\rho}} + h_{1c}\tilde{\theta}\right) u_{1_{ff}} + \tilde{g}u_{5_{ff}} \\ &+ \left(h_{1a}\frac{\partial^2\theta}{\partial\hat{\rho}^2} + h_{1b}\frac{\partial\theta}{\partial\hat{\rho}} + h_{1c}\theta\right)\left(u_{1_{fb}} + d_1\right) \\ &+ \sum_{k=2}^{4} h_k\left(u_{k_{fb}} + d_k\right) + g\left(u_{5_{fb}} + d_5\right), \end{aligned} \tag{8.11}$$

$$\tilde{\theta}(0,t) = 0, \quad \tilde{\theta}(1,t) = -k_6\left(u_{6_{fb}} + d_6\right) \tag{8.12}$$

where $\tilde{g} = g(\theta) - g(\theta_{ff})$.

We first attempt to cancel the effect of the unknown disturbances by defining the feedback laws $u_{k_{fb}} = v_k - \hat{d}_k$, for $k = 1, \ldots, 6$, where $\hat{d}_k$ is an estimate of the disturbances, and v_k is a to-be-designed control signal, resulting in

$$\begin{aligned}\frac{\partial\tilde{\theta}}{\partial t} =& \left(h_{1a}\frac{\partial^2\tilde{\theta}}{\partial\hat{\rho}^2} + h_{1b}\frac{\partial\tilde{\theta}}{\partial\hat{\rho}} + h_{1c}\tilde{\theta}\right) u_{1_{ff}} \\ &+ \left(h_{1a}\frac{\partial^2\theta}{\partial\hat{\rho}^2} + h_{1b}\frac{\partial\theta}{\partial\hat{\rho}} + h_{1c}\theta\right)\left(v_1 + \tilde{d}_1\right) \\ &+ \sum_{k=2}^{4} h_k\left(v_k + \tilde{d}_k\right) + g\left(v_5 + \tilde{d}_5\right) + \hat{g}u_{5_{ff}}\tilde{\theta}, \\ \tilde{\theta}(0,t) =& 0, \quad \tilde{\theta}(1,t) = -k_6\left(v_6 + \tilde{d}_6\right). \end{aligned}$$

where $\tilde{d}_k$ for $k = 1, \ldots, 6$ is the disturbance estimation error. Note that, while the proposed backstepping design can handle nonlinear terms, the term $\tilde{g}$ has been linearized in this case, i.e., we take $\tilde{g} \approx \hat{g}\tilde{\theta}$ where $\hat{g} = \left.\frac{\partial\tilde{g}}{\partial\theta}\right|_{\theta=\theta_{ff}}$, to simplify the design and implementation of the controller in the DIII-D plasma control system (PCS), which is currently set up to handle linear controller systems coupled with nonlinear transformations, but not general nonlinear control laws. The objective of the controller is

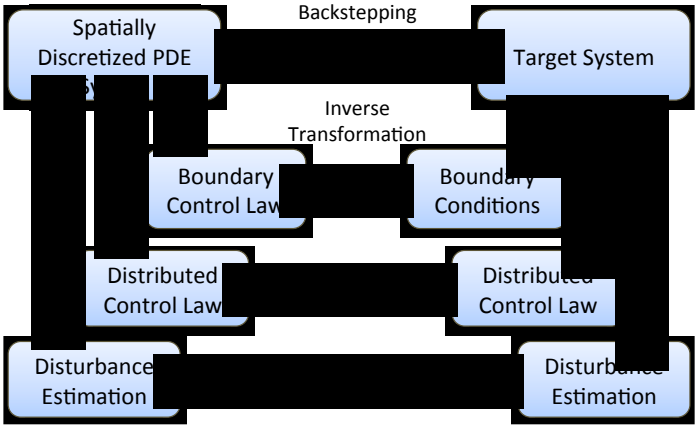

Figure 8.1: Schematic of the backstepping control design with boundary and distributed actuation augmented with disturbance estimation.

to force $\tilde{\theta}(\hat{\rho}, t)$ to zero using distributed actuators $v_k \ \forall k \in [1, 5]$, and the boundary actuator v_6, while accounting for the effect of disturbance estimation errors.

8.4 Controller Design

8.4.1 Backstepping Transformation

Figure 8.1 illustrates the control design approach. A backstepping technique is used to transform the original system into a particular target system. The target system is then rendered asymptotically stable through the choice of design parameters, boundary conditions, control laws for the distributed interior actuators, and update laws for the disturbance estimations. The combined boundary+interior control law is obtained using the inverse of the backstepping transformation.

By defining $h = \frac{1}{N}$, where N is an integer, and using the notation $x^i(t) = x(ih, t)$,

$i = 0, 1, ..., N$, we discretize the system as

$$\begin{aligned}\dot{\tilde{\theta}}^i = &\left(h_{1a}^i \frac{\tilde{\theta}^{i+1} - 2\tilde{\theta}^i + \tilde{\theta}^{i-1}}{h^2} + h_{1b}^i \frac{\tilde{\theta}^{i+1} - \tilde{\theta}^{i-1}}{2h} \right. \\ &\left. + h_{1c}^i \tilde{\theta}^i \right) u_{1_{ff}} + \left(h_{1a}^i \frac{\theta^{i+1} - 2\theta^i + \theta^{i-1}}{h^2} \right. \\ &\left. + h_{1b}^i \frac{\theta^{i+1} - \theta^{i-1}}{2h} + h_{1c}^i \theta^i \right) \left(v_1 + \tilde{d}_1 \right) \\ &+ \sum_{k=2}^{4} h_k^i \left(v_k + \tilde{d}_k \right) + g^i \left(v_5 + \tilde{d}_5 \right) + \hat{g}^i u_{5_{ff}} \tilde{\theta}^i, \end{aligned} \tag{8.13}$$

with the boundary conditions written as

$$\tilde{\theta}^0 = 0, \quad \tilde{\theta}^N = -k_6 \left(v_6 + \tilde{d}_6 \right). \tag{8.14}$$

The following target system is considered:

$$\begin{aligned}\dot{\tilde{w}}^i = &\left(h_{1a}^i \frac{\tilde{w}^{i+1} - 2\tilde{w}^i + \tilde{w}^{i-1}}{h^2} + h_{1b}^i \frac{\tilde{w}^{i+1} - \tilde{w}^{i-1}}{2h} \right. \\ &\left. + h_{1c}^i \tilde{w}^i - C_1 \tilde{w}^i \right) u_{1_{ff}} + \hat{g}^i u_{5_{ff}} \tilde{w}^i + J^i \left(v_1 + \tilde{d}_1 \right) \\ &+ \sum_{k=2}^{4} H_k^i \left(v_k + \tilde{d}_k \right) + G^i \left(v_5 + \tilde{d}_5 \right), \end{aligned} \tag{8.15}$$

with the boundary conditions chosen to be

$$\tilde{w}^0 = 0, \quad \tilde{w}^N = -k_6 \tilde{d}_6, \tag{8.16}$$

and where

$$
\begin{aligned}
J^i =& \left(h_{1a}^i \frac{\theta^{i+1} - 2\theta^i + \theta^{i-1}}{h^2} + h_{1b}^i \frac{\theta^{i+1} - \theta^{i-1}}{2h} + h_{1c}^i \theta^i \right) \\
& - \sum_{j=1}^{i-1} \frac{\partial \alpha^{i-1}}{\partial \tilde{\theta}^j} \left(h_{1a}^j \frac{\theta^{j+1} - 2\theta^j + \theta^{j-1}}{h^2} \right. \\
& \left. + h_{1b}^j \frac{\theta^{j+1} - \theta^{j-1}}{2h} + h_{1c}^j \theta^j \right), \\
H_k^i =& h_k^i - \sum_{j=1}^{i-1} \frac{\partial \alpha^{i-1}}{\partial \tilde{\theta}^j} h_k^j, \ \forall k \in \{2, 3, 4\} \\
G^i =& g^i - \sum_{j=1}^{i-1} \frac{\partial \alpha^{i-1}}{\partial \tilde{\theta}^j} g^j.
\end{aligned}
$$

The term α is a to-be-found backstepping transformation in the form

$$
\tilde{w}^i = \tilde{\theta}^i - \alpha^{i-1} \left(\tilde{\theta}^0, \ldots, \tilde{\theta}^{i-1} \right).
$$

By subtracting (8.15) from (8.13), the expression $\dot{\alpha}^{i-1} = \dot{\tilde{\theta}}^i - \dot{\tilde{w}}^i$ is obtained in terms of $\alpha^{k-1} = \tilde{\theta}^k - \tilde{w}^k, \ k = i-1, i, i+1$, i.e.,

$$
\begin{aligned}
\dot{\alpha}^{i-1} =& \left(h_{1a}^i \frac{\alpha^i - 2\alpha^{i-1} + \alpha^{i-2}}{h^2} + h_{1b}^i \frac{\alpha^i - \alpha^{i-2}}{2h} \right. \\
& \left. + h_{1c}^i \alpha^{i-1} + C_1 \tilde{w}^i \right) u_{1_{ff}} + \left(h_{1a}^i \frac{\theta^{i+1} - 2\theta^i + \theta^{i-1}}{h^2} \right. \\
& \left. + h_{1b}^i \frac{\theta^{i+1} - \theta^{i-1}}{2h} + h_{1c}^i \theta^i - J^i \right) \left(v_1 + \tilde{d}_1 \right) \\
& + \sum_{k=2}^{4} \left(h_k^i - H_k^i \right) \left(v_k + \tilde{d}_k \right) + \left(g^i - G^i \right) \left(v_5 + \tilde{d}_5 \right) \\
& + u_{5_{ff}} \hat{g}^i \alpha^{i-1},
\end{aligned}
$$

which can be solved for α^i to yield

$$\begin{aligned}\alpha^i =&\frac{1}{u_{1_{ff}}}\left(\frac{h^i_{1a}}{h^2}+\frac{h^i_{1b}}{2h}\right)^{-1}\Bigg[-\Bigg(h^i_{1a}\frac{-2\alpha^{i-1}+\alpha^{i-2}}{h^2}\\ &-h^i_{1b}\frac{\alpha^{i-2}}{2h}+h^i_{1c}\alpha^{i-1}+C_1\tilde{w}^i\Bigg)u_{1_{ff}}+\dot{\alpha}^{i-1}\\ &-\Bigg(h^i_{1a}\frac{\theta^{i+1}-2\theta^i+\theta^{i-1}}{h^2}+h^i_{1b}\frac{\theta^{i+1}-\theta^{i-1}}{2h}\\ &-h^i_{1c}\theta^i-J^i\Bigg)\left(v_1+\tilde{d}_1\right)-\left(g^i-G^i\right)\left(v_5+\tilde{d}_5\right)\\ &-\sum_{k=2}^{4}\left(h^i_k-H^i_k\right)\left(v_k+\tilde{d}_k\right)-u_{5_{ff}}\hat{g}^i\alpha^{i-1}\Bigg],\end{aligned} \tag{8.17}$$

where $\alpha^0=0$ and $\dot{\alpha}^{i-1}$ is calculated as

$$\dot{\alpha}^{i-1}=\sum_{k=1}^{i-1}\left(\frac{\partial\alpha^{i-1}}{\partial\tilde{\theta}^k}\dot{\tilde{\theta}}^k+\frac{\partial\alpha^{i-1}}{\partial\theta^k_{ff}}\dot{\theta}^k_{ff}\right)+\sum_{j=1}^{6}\frac{\partial\alpha^{i-1}}{\partial u_{j_{ff}}}\dot{u}_{j_{ff}}. \tag{8.18}$$

Through its dependence on $\dot{\tilde{\theta}}$, expression (7.37) depends on the to-be-designed distributed control laws which will not in general be spatially causal and would violate the strict-feedback structure required for backstepping. It also depends on the disturbance terms, which are unknown. However, by our choice of target system, the terms involving J^i, H^i_k, and G^i exactly remove the undesirable terms from the recursive expression (8.17), upon substitution, i.e.,

$$\begin{aligned}\alpha^i =&\left(\frac{h^i_{1a}}{h^2}+\frac{h^i_{1b}}{2h}\right)^{-1}\Bigg[-\Bigg(h^i_{1a}\frac{-2\alpha^{i-1}+\alpha^{i-2}}{h^2}\\ &-h^i_{1b}\frac{\alpha^{i-2}}{2h}+h^i_{1c}\alpha^{i-1}+C_1\tilde{\theta}^i-C_1\alpha^{i-1}\Bigg)\\ &-\frac{u_{5_{ff}}}{u_{1_{ff}}}\hat{g}^i\alpha^{i-1}+\frac{\dot{\alpha}^{i-1}_{strict}}{u_{1_{ff}}}\Bigg],\end{aligned} \tag{8.19}$$

where

$$\dot{\alpha}^{i-1}_{strict} = \sum_{k=1}^{i-1} \frac{\partial \alpha^{i-1}}{\partial \tilde{\theta}^k} \left[\left(h^i_{1a} \frac{\tilde{\theta}^{k+1} - 2\tilde{\theta}^k + \tilde{\theta}^{k-1}}{h^2} + h^k_{1c} \tilde{\theta}^k + h^k_{1b} \frac{\tilde{\theta}^{k+1} - \tilde{\theta}^{k-1}}{2h} \right) u_{1_{ff}} + \hat{g}^k u_{5_{ff}} \tilde{\theta}^k \right] + \sum_{j=1}^{6} \frac{\partial \alpha^{i-1}}{\partial u_{j_{ff}}} \dot{u}_{j_{ff}} + \sum_{k=1}^{i-1} \frac{\partial \alpha^{i-1}}{\partial \theta^k_{ff}} \dot{\theta}^k_{ff}. \tag{8.20}$$

Next, subtracting (8.16) from (8.14) and putting the resulting expression in terms of $\alpha^{k-1} = \tilde{\theta}^k - \tilde{w}^k,\ k = i-1, i, i+1$, the control law for v_6 can be defined as

$$v_6 = -\frac{1}{k_6} \alpha^{N-1}. \tag{8.21}$$

8.4.2 Stability of Target System

We design the control laws for the distributed actuators, as well as the update laws for the disturbance estimations to stabilize the target system. We consider the control Lyapunov function

$$V = \frac{1}{2} \sum_{i=1}^{N-1} Q^i_w \left(\tilde{w}^i \right)^2 + \frac{1}{2} \sum_{k=1}^{6} \frac{\tilde{d}^2_k}{K_k},$$

where Q_w^i, for $i \in [1, N-1]$ are positive definite weights, and K_k are positive constants. We calculate its time derivative as

$$\begin{aligned}
\dot{V} &= \sum_{i=1}^{N-1} Q_w^i \tilde{w}^i \dot{\tilde{w}}^i + \sum_{k=1}^{6} \frac{\tilde{d}_k \dot{\tilde{d}}_k}{K_k} \\
&\leq - W^T A_W W u_{1_{ff}} + \sum_{k=1}^{5} v_k \Theta_k + \sum_{k=1}^{5} \tilde{d}_k \left[\Theta_k + \frac{\dot{\tilde{d}}_k}{K_k} \right] \\
&\quad + \tilde{d}_6 \left[-k_{17} Q_w^{N-1} \tilde{w}^{N-1} \left[\frac{h_{1a}^{N-1}}{h^2} + \frac{h_{1b}^{N-1}}{h} \right] u_{1_{ff}} + \frac{\dot{\tilde{d}}_6}{K_6} \right],
\end{aligned} \tag{8.22}$$

where

$$\begin{aligned}
A_W^{1,1} &= - \left\{ \left[-\frac{2h_{1a}^1}{h^2} + h_{1c}^1 - C_1 \right] u_{1_{ff}} + u_{5_{ff}} \hat{g}^1 \right\}, \\
A_W^{1,2} &= - \left[\frac{h_{1a}^1}{h^2} - \frac{h_{1b}^1}{h} \right] u_{1_{ff}},
\end{aligned}$$

$$\begin{aligned}
A_W^{i,i-1} &= - \left[\frac{h_{1a}^i}{h^2} + \frac{h_{1b}^i}{h} \right] u_{1_{ff}}, \\
A_W^{i,i} &= - \left\{ \left[-\frac{2h_{1a}^i}{h^2} + h_{1c}^i - C_1 \right] u_{1_{ff}} + u_{5_{ff}} \hat{g}^i \right\}, \\
A_W^{i,i+1} &= - \left[\frac{h_{1a}^i}{h^2} - \frac{h_{1b}^i}{h} \right] u_{1_{ff}},
\end{aligned}$$

$$\begin{aligned}
A_W^{N-1,N-2} &= - \left[\frac{h_{1a}^{N-1}}{h^2} + \frac{h_{1b}^{N-1}}{h} \right] u_{1_{ff}}, \\
A_W^{N-1,N-1} &= - \left\{ \left[-\frac{2h_{1a}^{N-1}}{h^2} + h_{1c}^{N-1} - C_1 \right] u_{1_{ff}} + u_{5_{ff}} \hat{g}^{N-1} \right\},
\end{aligned}$$

are the elements of the positive definite matrix A_W, and

$$\Theta_1 = \sum_{i=1}^{N-1} Q_w^i \tilde{w}^i J^i,$$
$$\Theta_k = \sum_{i=1}^{N-1} Q_w^i \tilde{w}^i H_{k,}^i \ \forall k \in \{2,3,4\}$$
$$\Theta_5 = \sum_{i=1}^{N-1} Q_w^i \tilde{w}^i G^i,$$

are nonlinear, time-varying functions of the error measurements. We take the control laws and update laws

$$v_1 = -T_1\Theta_1, \tag{8.23}$$
$$v_k = -T_k\Theta_k, \ \forall k \in \{2,3,4\} \tag{8.24}$$
$$v_5 = -T_5\Theta_5, \tag{8.25}$$
$$\dot{\hat{d}}_k = K_k\Theta_k, \tag{8.26}$$
$$\dot{\hat{d}}_6 = -K_6 Q_w^{N-1}\tilde{w}^{N-1}\left[\frac{h_{1a}^{N-1}}{h^2} + \frac{h_{1b}^{N-1}}{h}\right] u_{1_{ff}}, \tag{8.27}$$

where $T_k \geq 0 \ \forall k \in \{1,2,3,4,5\}$ are design constants. Assuming constant disturbances, this reduces (8.22) to

$$\dot{V} \leq -W^T A_W W - \sum_{k=1}^{5} T_k\Theta_k^2. \tag{8.28}$$

Since A_W is positive definite, we have that $\dot{V} \leq 0$. Since $V \geq 0$ and $\ddot{V}$ is bounded, the conditions of Barbalat's lemma are satisfied, and we have that $\dot{V} \to 0$. This implies that $\tilde{w}$ is driven to zero, guaranteeing asymptotic stability of the target system, and, consequently, $\tilde{\theta}$. Note that the nonlinear control laws are linearized around the feedforward trajectories for implementation in the PCS.

8.4.3 Physical Actuator Requests

The nonlinear transformations (8.10), must be inverted to obtain references for the physical actuators from the combined feedforward+feedback output of the controller. However, because the output of the controller is $u \in \mathbb{R}^{6\times 1}$, whereas there are only five physical actuators available, there is not, in general, a solution to the inverse transformation. To overcome this, an additional actuator is required that provides heating without driving current, allowing for P_{tot} to be independently modulated. On DIII-D, this type of actuation could be achieved with a combination of co- and counter-current beam injection that drives very little current, however, counter-current beams were not used during the present experimental campaign. Instead, a weighted least squares fit was used to find the the individual beam and gyrotron powers that would best match the outputs of the controller.

The inverse nonlinear transformations between the controlled inputs (u_k for $k = 1, \ldots, 6$) and the physical actuators on DIII-D are

$$\begin{aligned} I_p = u_6,\ P_{ec} = \frac{u_2 u_5}{u_1^{2/3}},\ P_{nbi,on} = \frac{u_3 u_5}{u_1^{2/3}},\ P_{nbi,off} = \frac{u_4 u_5}{u_1^{2/3}}, \\ P_{tot} = \left(\frac{u_5}{u_1 u_6}\right)^2,\ u_n = \frac{u_5}{u_1^{1/3}}. \end{aligned} \tag{8.29}$$

We consider a linear least squares problem of the form

$$\hat{\beta}_{LS} = \arg\min_{\beta} \left(y_{LS} - X_{LS}\beta_{LS}\right)^T Q_{LS} \left(y_{LS} - X_{LS}\beta_{LS}\right),$$

where

$$y_{LS} = \begin{bmatrix} \frac{u_2 u_5}{u_1^{2/3}} \\ \frac{u_3 u_5}{u_1^{2/3}} \\ \frac{u_4 u_5}{u_1^{2/3}} \\ \left(\frac{u_5}{u_1 u_6}\right)^2 \end{bmatrix}, \quad \beta_{LS} = \begin{bmatrix} P_{ec} \\ P_{nbi_{on}} \\ P_{nbi_{off}} \end{bmatrix}, \quad X_{LS} = \begin{bmatrix} 1 & 0 & 0 \\ 0 & 1 & 0 \\ 0 & 0 & 1 \\ 1 & 1 & 1 \end{bmatrix},$$

and Q_{LS} is a diagonal weighting matrix included to weight the importance of each element of the residual. This results in the solution

$$\hat{\beta}_{LS} = \left[(X'_{LS})^T X'_{LS} \right]^{-1} (X')^T y'_{LS}, \tag{8.30}$$

where

$$X'_{LS} = q_{LS} X_{LS}, \quad y'_{LS} = q_{LS} y,$$

and $q_{LS}^{i,i} = \sqrt{Q_{LS}^{i,i}}$. The references in the vector $\hat{\beta}_{LS}$ can then be sent to the appropriate physical actuators on DIII-D.

8.5 Simulation Results

In this section, we present results of the simulation study used to test and tune the controller design and implementation prior to experimental testing.

8.5.1 Disturbance Rejection

In this simulation, one disturbance ($d_1 = d_4 = -0.065$, $d_6 = 0.1$) was applied from 0.5s to 3.0s, and a different disturbance ($d_3 = d_4 = -0.1$, $d_5 = -0.25$, $d_6 = 0.1$) was applied from 3.0s to the end of the simulation. The feedback controller was turned on throughout the simulation. The time-varying controller matrices were updated

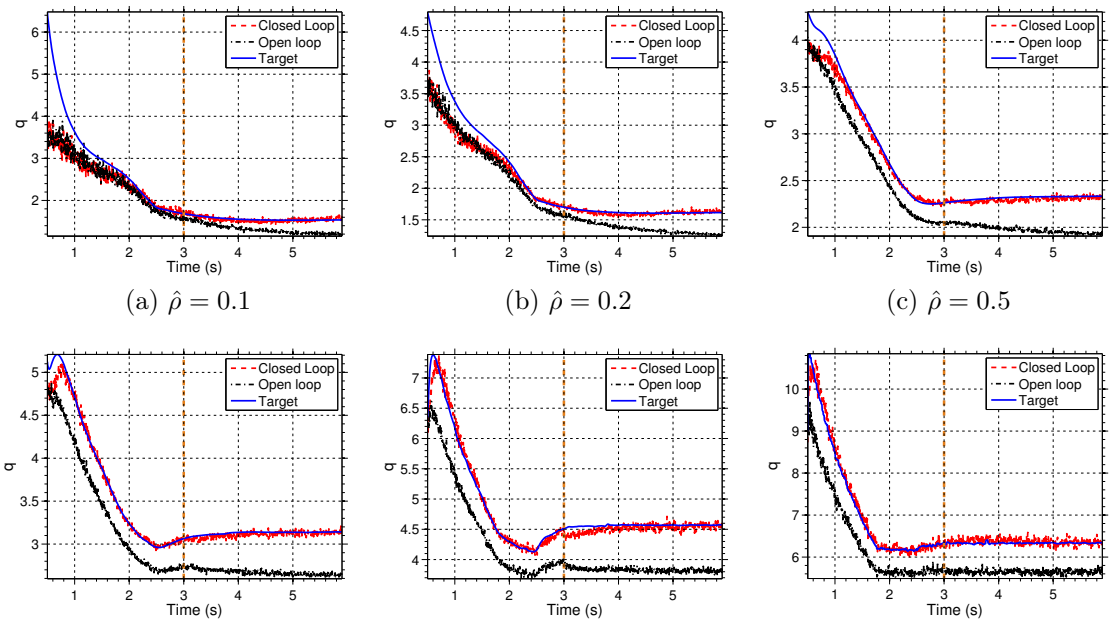

(a) $\hat{\rho} = 0.1$ (b) $\hat{\rho} = 0.2$ (c) $\hat{\rho} = 0.5$

(d) $\hat{\rho} = 0.65$ (e) $\hat{\rho} = 0.8$ (f) $\hat{\rho} = 0.95$

Figure 8.2: Time traces of q at various points during the disturbance rejection scenario, comparing the nominal feedforward simulation (blue, solid) with the closed loop, disturbed simulation (red, dashed) and the open loop, disturbed simulation (black, dash-dot).

every 500ms between 0.5s and 3.0s. An artificial noise signal was also added to the measurements of θ. Time traces of q at various points are shown in Figure 8.2. The controller was able to quickly reject the initial condition errors in the outer part of the domain (Figure 8.2d, 8.2e, and 8.2f), while the interior part of the domain took longer (around 2-3s) to achieve the desired target, due to the slower dynamics in the interior region (Figure 8.2a, 8.2b, and 8.2c). Despite the change in the disturbance at $t = 3.0$s, the controller was able to keep the profile very close to the desired target throughout the remainder of the simulation. Figure 8.3 shows the q and θ profiles at several times, showing that the closed loop response is improved from the open loop case, most noticeably in Figure 8.3d. Figure 8.4 shows the actuator trajectories during the simulation. The plasma current (Figure 8.4a), which represents

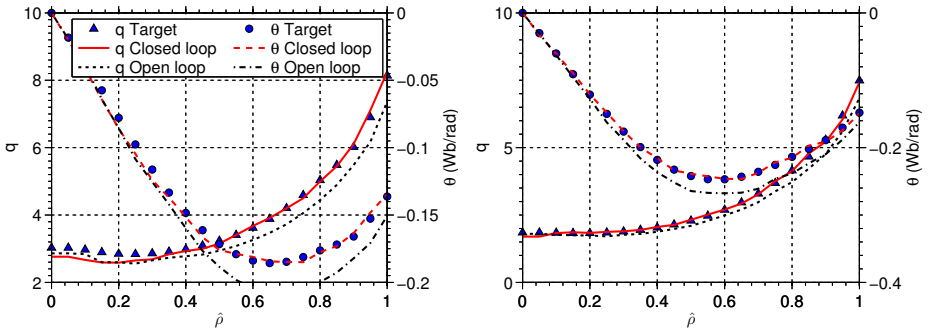

(a) $t = 1.5$s (b) $t = 2.49$s

(c) $t = 3.5$s (d) $t = 5.5$s

Figure 8.3: Comparison of q and θ profiles at various times for the disturbance rejection scenario. The closed loop profiles (q: red solid, θ: red dashed) and open loop profiles (q: black dotted, θ: black dash-dot) are compared with the desired targets (q: blue, triangular markers, θ: blue, circular markers).

the boundary actuator, was modified significantly by the backstepping controller. It can be noted that the controller increased the off-axis beam power while decreasing the on-axis power during the first disturbance. In response to the second disturbance, the EC (electron-cyclotron) power and off-axis beam power were increased until they reached saturation (around $t = 4$s and $t = 5$s, respectively), as seen in Figures 8.4c and 8.4e. As the controller determined additional power was still necessary to maintain the desired profile, the on-axis beam power (Figure 8.4d) was increased around $t = 5$s. The diagnostic power, shown in Figure 8.4f, is a portion of the on-axis beam power that is required to be held constant for current profile measurements in experiments. It was therefore held constant throughout the simulation to better

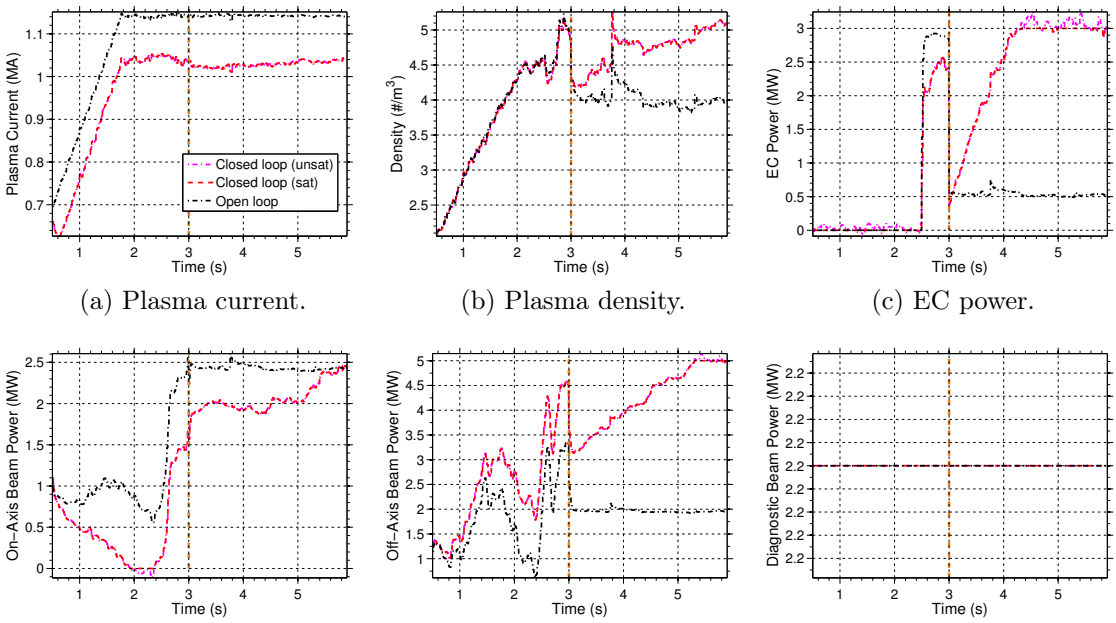

(a) Plasma current. (b) Plasma density. (c) EC power.

(d) On-axis beam power. (e) Off-axis beam power. (f) Diagnostic Beam Power.

Figure 8.4: Plots of plasma current, density, EC power, on-axis beam power, off-axis beam power, and diagnostic beam power during the disturbance rejection scenario comparing the unsaturated requests during the closed loop simulation (magneta, dash-dot), the saturated values (red, dashed) from the feedback controller, and the open loop values (black, dash-dot). Shaded regions indicated time intervals during which the feedback controller was turned off.

recreate the conditions of experiments.

8.5.2 Profile Reference Tracking

To test the target tracking capability of the control scheme, two input trajectories Feedforward 1 and Feedforward 2 were used to generate two distinct target current profile evolutions Target 1 and Target 2. During the closed loop simulation, Feedforward 1 was provided to the controller throughout the simulation. The initial conditions were perturbed, and the controller target was changed from 1 to 2 at 2.5s. The feedback controller was turned on throughout the simulation. The time-varying controller matrices were again updated every 500ms between 0.5s and 3.0s. An ar-

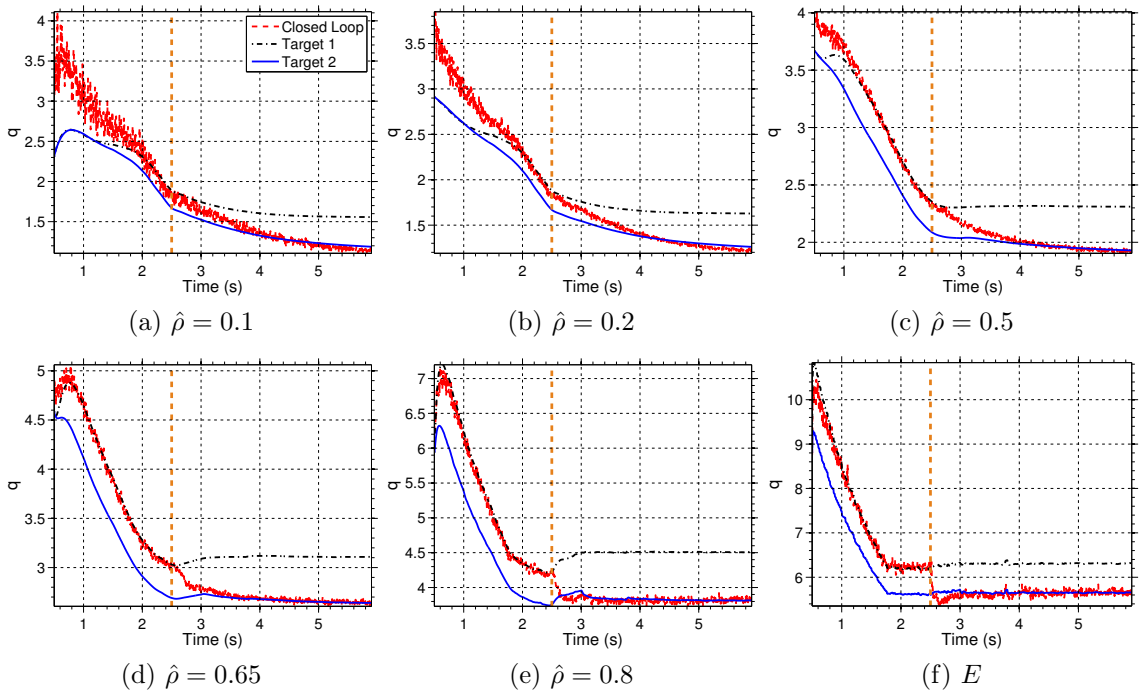

(a) $\hat{\rho} = 0.1$ (b) $\hat{\rho} = 0.2$ (c) $\hat{\rho} = 0.5$

(d) $\hat{\rho} = 0.65$ (e) $\hat{\rho} = 0.8$ (f) E

Figure 8.5: Time traces of q at various points during the target tracking scenario, comparing Targets 1 and 2 (black, dash-dot and blue, solid, respectively) with the closed loop simulation (red-dashed). The controller targets were switched at 2.5s (indicated by the vertical orange dashed line).

tificial noise signal was also added to the measurements of θ. Time traces of q at various points are shown in Figure 8.5, showing that the controller was able to reject the initial condition errors (most noticeable in Figures 8.5a and 8.5b) and to achieve Target 1 prior to 2.5s. After the target was switched, as indicated by the vertical orange dashed line, the controller was able to move the profile to Target 2 by around 4.0s. Figure 8.6 shows the q and θ profiles at several times. Figures 8.6a and 8.6b clearly show the controller achieved Target 1 by $t = 2.5$s, while Figures 8.6c and 8.6d show progress toward and achievement of Target 2. Figure 8.7 shows the actuator trajectories during the simulation. While the actuators remained fairly close to the feedforward values during the first part of the discharge, since they only needed to be modified to account for initial condition errors, increased feedback actuation can be

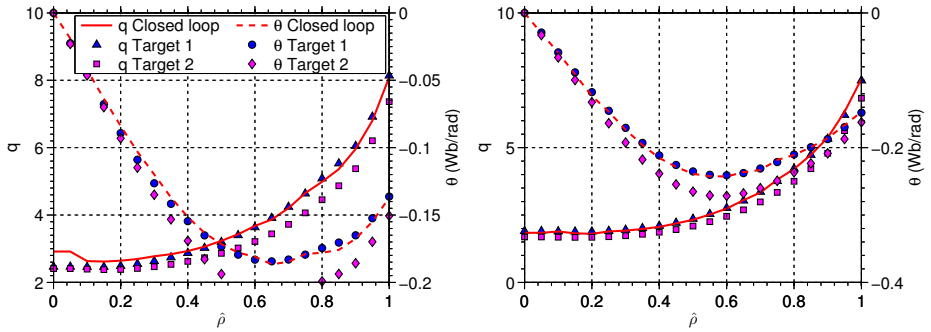

(a) $t = 1.5$s (b) $t = 2.49$s

(c) $t = 3.5$s (d) $t = 5.5$s

Figure 8.6: Comparison of q and θ profiles at various times for the profile tracking scenario. The closed loop profiles (q: red solid, θ: red dashed) are compared with Target 1 (q: blue, circular markers, θ: blue, triangular markers) and Target 2 (q: magenta, square markers, θ: magenta, diamond markers).

noted in the second phase (after $t = 2.5$s). The plasma current was increased, while the density was reduced (Figures 8.7a and 8.7b, respectively). The EC power and off-axis beam power (Figures 8.7c and 8.7e) are essentially turned off to achieve Target 2, while the on-axis power (Figure 8.7d) remains close to the feedforward value. The diagnostic beam power was again kept constant in the simulation, as shown in Figure 8.7f.

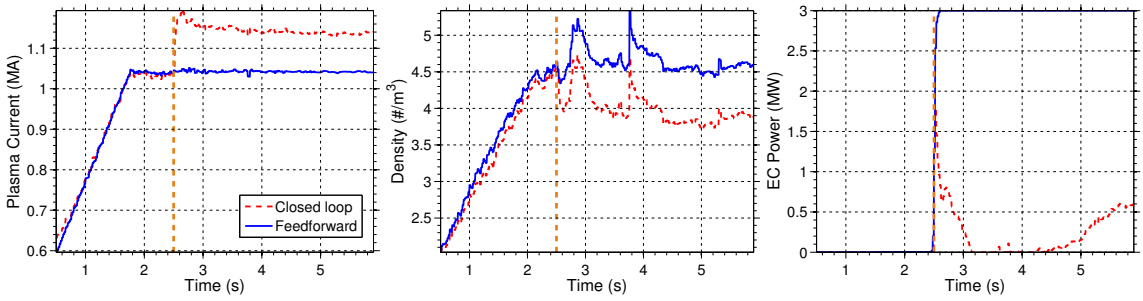

(a) Plasma current. (b) Plasma density. (c) EC power.

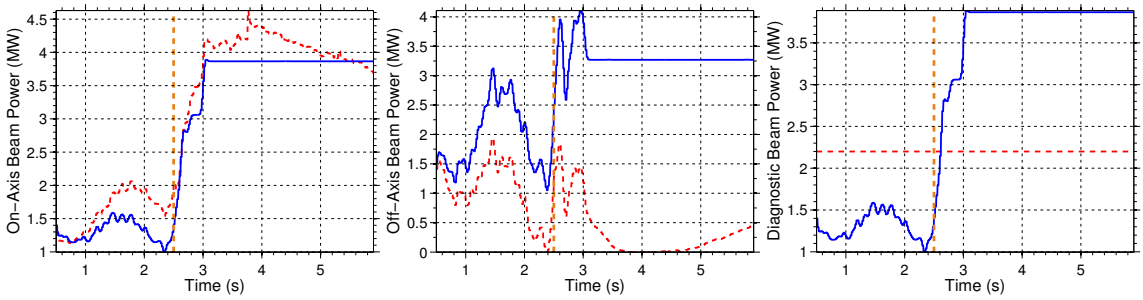

(d) On-axis beam power. (e) Off-axis beam power. (f) Diagnostic Beam Power.

Figure 8.7: Plots of plasma current, density, EC power, on-axis beam power, off-axis beam power, and diagnostic beam power during the first target tracking scenario comparing the feedforward values (blue solid) and the closed loop values (red dashed).

8.6 Experimental Results

In this section, we present preliminary experimental results showing the controller's performance on the DIII-D device. A target profile was generated based on the results of an open loop reference shot #150320. Again, no balanced beam was available during this closed loop experiment, removing a degree of freedom. In addition, two of the beams were needed for current profile diagnostics and were therefore unavailable for feedback. Furthermore, the gyrotrons, which were turned on at 2.5s in the reference shot, were unavailable during the closed loop shot. This reduced the available current drive and heating, and contributed to increased MHD instabilities. The increased MHD activity during the shot caused the shot to be terminated early at 3.7s. Additional artificial disturbances were also introduced in the feedforward beam

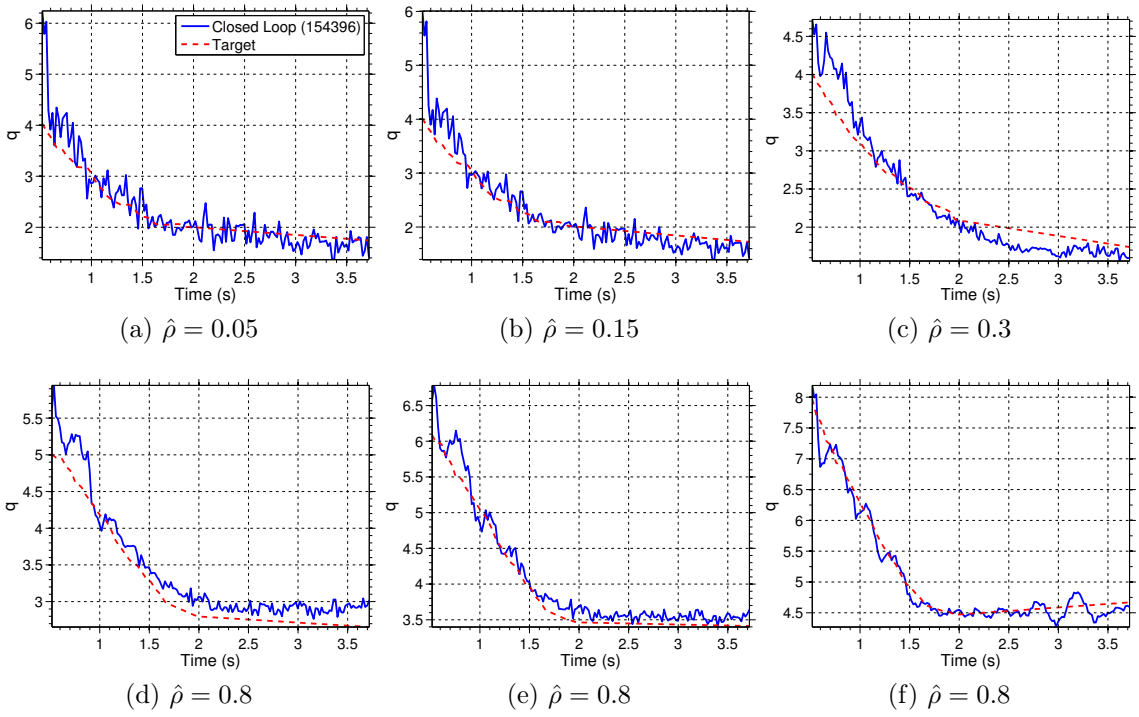

(a) $\hat{\rho} = 0.05$ (b) $\hat{\rho} = 0.15$ (c) $\hat{\rho} = 0.3$

(d) $\hat{\rho} = 0.8$ (e) $\hat{\rho} = 0.8$ (f) $\hat{\rho} = 0.8$

Figure 8.8: Time traces of q at various points, comparing the closed loop (blue, solid) with the target (red-dashed) during shot #154398.

power trajectories. Time traces of q at various locations are presented in Figure (8.8), showing that, despite the disturbances, the controller was able to achieve fairly good tracking of the desired target throughout the discharge. Figure (8.9) shows the q profile at various times, along with a shaded region representing the standard deviation of the measurements over a window of 0.25s prior to the displayed time. Figure (8.10) compares the achieved, requested (output of the controller), and feedforward actuator trajectories, showing the modification of the input trajectories by the controller. In response to the disturbances, the density was reduced. Because the lack of EC power reduced the amount of off-axis current drive, the controller responded by increasing the off-axis beam power (until it hit saturation) and decreasing the on-axis beam power. The plasma current began to oscillate around the desired reference, apparently because the controller was amplifying the measurement noise, which was much

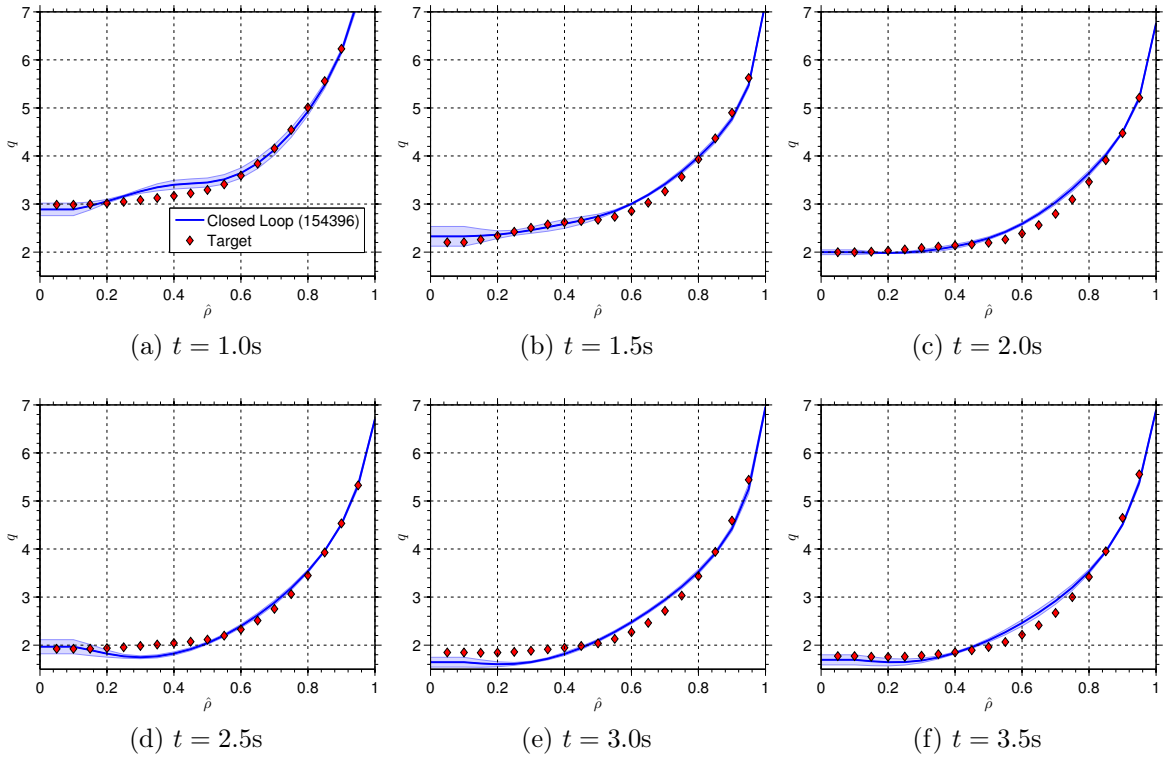

(a) $t = 1.0$s (b) $t = 1.5$s (c) $t = 2.0$s

(d) $t = 2.5$s (e) $t = 3.0$s (f) $t = 3.5$s

Figure 8.9: Comparison of q profiles at various times during shot #154398. The closed loop profiles (blue solid) are compared with the target (red, diamond markers). The shaded regions represent the standard deviation of the measurements over a window of 0.25s prior to the time shown.

larger in this experiment than expected. This will be addressed in future experiments by reducing the gain K_6.

8.7 Conclusions

We have presented simulation and preliminary experimental results showing the performance of a backstepping boundary+interior current profile controller based on first-principles-driven model of H-mode DIII-D discharges. By employing a backstepping control design technique, a transformation was found from the spatially discretized system to a particular target system. The target system was rendered asymptotically

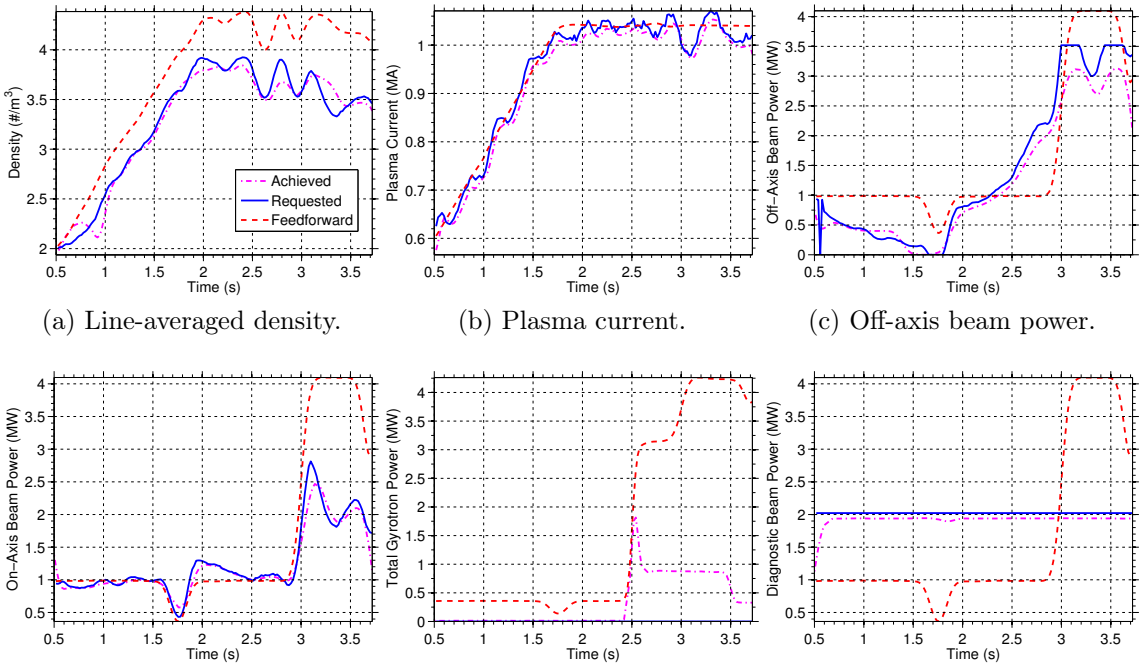

(a) Line-averaged density. (b) Plasma current. (c) Off-axis beam power.

(d) On-axis beam power. (e) Gyrotron power. (f) Diagnostic beam power.

Figure 8.10: Plots of density, plasma current, on-axis beam power, and off-axis beam power during shot #154398 comparing the feedforward values (red dashed) and the closed loop values (blue solid). Values actually achieved by the physical actuators are also shown (magenta dash-dot).

stable via the design of distributed feedback control laws and disturbance estimation update laws. The resulting feedback controller is designed to augment an arbitrary set of feedforward input trajectories. Through a nonlinear transformation of the control inputs, the scheme provides stabilizing reference values for the total plasma current, total EC power, on-axis NBI power, off-axis NBI power, and plasma density. A simulation study showed the performance of the controller during tracking and disturbance rejection scenarios. Promising preliminary experimental results demonstrated the ability of the scheme to track a desired profile evolution despite significant disturbances. Further experimental testing, using EC power and an implementation of the full nonlinear controller, will be done in the future to better assess the performance of the control scheme in a variety of scenarios, including disturbance rejection,

and target tracking.

Chapter 9

Conclusions and Future Work

This dissertation has focused on developing and studying nonlinear burn condition and kinetic profile control strategies in tokamak fusion plasmas. In this final chapter, we summarize the results of the work and briefly describe some areas that merit future research.

9.1 Contributions

The contributions of this dissertation are:

1. Nonlinear model-based zero-dimensional burn control combining available actuation. The effect of the tritium ratio on the fusion heating power is exploited to modulate plasma heating and control the temperature through isotopic fuel tailoring. For scenarios in which the combined modulation of auxiliary power and isotopic mix cannot achieve stability and performance requirements, impurity injection is used as a back-up actuator. The controller synthesis is based on the full nonlinear model, allowing the controller to deal with a larger set of perturbations in initial conditions than linear model based controllers. The

controller handles both thermal excursions and quenches and depends parametrically on the equilibrium point, allowing it to be used to drive the system from one equilibrium point to another.

2. Nonlinear adaptive burn control with online operating point optimization. While many of the model parameters necessary for implementation of the proposed nonlinear control scheme are either measured or can be calculated based on first-principles equations or scaling laws, some parameters will be, in practice, uncertain or unknown. A nonlinear adaptive control scheme is proposed to ensure that the burn condition reference is asymptotically stable despite model uncertainty. In addition, an online optimization scheme is used which alters the controller references in real-time to optimize a given figure of merit for reactor performance.

3. Nonlinear output feedback based burn control. Due to the extreme conditions in fusion reactors the diagnostic systems needed to provide the state measurement necessary for implementation of the proposed control designs may not all be available. To overcome this obstacle, an observer is used to estimate the required states based on the available measurements. Due to the nonlinearity of the burning plasma dynamics and, in general, the measured output map, a nonlinear observer is proposed. The observer is augmented with an integral term, resulting in a nonlinear proportional-integral observer, which guarantees convergence of the predicted and measured outputs, despite model uncertainty. The output feedback control design is coupled with adaptive parameter estimation and operating point optimization to ensure desired reactor performance is achieved.

4. Simulation framework for testing burn control strategies in METIS. The fast

integrated modeling code METIS is coupled with a volume averaged model of particle dynamics and a general feedback control block in Simulink, enabling the simulation of various burn control strategies. With this tool burn control strategies can be simulated in a wide-range of operating conditions and scenarios, and their effect on other plasma parameters can be assessed.

5. Backstepping density and temperature profile control in burning plasmas. The novel design is an extension of the backstepping technique for PDE systems that allows for simultaneous boundary+interior feedback control design and incorporates adaptive disturbance estimation to improve system response. The resulting nonlinear controller is demonstrated in simulations to be able to stabilize a set of unstable equilibrium profiles, even in the presence of input disturbances.

6. Backstepping current profile control in L- and H-mode discharges in DIII-D. A set of nonlinear profile control strategies were developed, based on a first-principles-driven model of the current profile dynamics. The approaches were successfully demonstrated in simulations, as well as in experiments on DIII-D as part of the first ever campaign to experimentally test first-principles-driven model-based current profile control laws.

9.2 Future Work

While the simulation framework for testing burn control designs in METIS is a significant step towards the development of controllers for ITER, a comprehensive study of controllers under the complete range of expected operating conditions (including potential fault scenarios, like the loss of certain diagnostics or actuators) should be carried out. As much as possible, burn control designs should be tested experimentally in existing devices. Although present-day tokamaks cannot actually achieve

burning plasma conditions, through careful experimental design, the dynamics of burning plasmas can be mimicked to some degree.

Though the feasibility of controlling kinetic profiles in a burning plasma using a combination of distributed and boundary feedback was shown in Chapter 6, more study will be necessary to find physical methods for the modulation of the kinetic variables at the edge of the plasma, i.e. achieving the desired values of u_α, u_{DT}, and u_E. This will have to be done through modulation of the physical properties of the plasma scrape-off layer (SOL) such as gas puffing, gas pumping, or impurity injection. Moving forward, model improvements will be made by including models for the diffusivity and pinch velocity, as well as models of the SOL in order to apply more realistic boundary conditions to the system.

The current profile control strategy developed in Chapters 7 and 8 will be tested through additional experiments and extended to other tokamaks, including NSTX at Princeton Plasma Physics Laboratory. Because of the coupling of the dynamics of the current, density, and temperature profiles, as well as the fact that they share many of the same actuators, the problem of integrating current profile control and burn control strategies must also be explored.

Bibliography

[1] A. Pironti and M. Walker, "Fusion, tokamaks, and plasma control: an introduction and tutorial," *IEEE Control Systems Magazine*, vol. 25, no. 5, pp. 30–43, 2005.

[2] A. Pironti and M. Walker, "Control of tokamak plasmas," *IEEE Control Systems Magazine*, vol. 25, no. 5, pp. 24–29, 2005.

[3] J. Wesson, *Tokamaks*. Oxford: Clarendon Press, 3rd ed., 2004.

[4] J. Mandrekas and W. M. Stacey, "Evaluation of Different Burn Control Methods for the International Thermonuclear Experimental Reactor," *Proceedings of the 13th IEEE Symposium on Fusion Engineering*, vol. 1, pp. 404–407, 1989.

[5] S. Haney, L. J. Perkins, J. Mandrekas, and W. M. Stacey, "Active Control of Burn Conditions for the International Thermonuclear Experimental Reactor," *Fusion Technology*, vol. 18, no. 4, pp. 606–17, 1990.

[6] D. Anderson, T. Elevant, H. Hamen, M. Lisak, and H. Persson, "Studies of Fusion Burn Control," *Fusion Technology*, vol. 23, no. 1, pp. 5–41, 1993.

[7] L. Bromberg, J. L. Fisher, and D. R. Cohn, "Active Burn Control of Nearly Ignited Plasmas," *Nuclear Fusion*, vol. 20, p. 203, 1980.

[8] E. Chaniotakis, J. Freidberg, and D. Cohn, "CIT burn control using auxiliary power modulation," in *Proc. 13th IEEE/NPSS Symp. Fusion Engineering*, pp. 400–403, Institue of Electrical and Electronics Engineers/Nuclear and Plasma Sciences Society, 1990.

[9] S. Haney and L. Perkins, "Operating point selection and burn stability control for the International Thermonuclear Experimental Reactor," in *Proc. 13th IEEE/NPSS Symp. Fusion Engineering*, pp. 396–399, Institue of Electrical and Electronics Engineers/Nuclear and Plasma Sciences Society, 1990.

[10] D. Ashby and M. H. Hughes, "Dynamic burn control of a tokamak reactor by fuel injection," *Nuclear Fusion*, vol. 20, pp. 451–457, 1980.

[11] W. Hui and G. H. Miley, "Burn control by refueling," *Bull. Am. Phys. Soc*, vol. 37, no. 6, p. 1399, 1992.

[12] B. A. Bamieh, W. Hui, and G. H. Miley, "Robust Burn Control of a Fusion Reactor by Modulation of the Refueling Rate," *Fusion Technology*, vol. 25, no. 3, p. 318, 1994.

[13] W. Hui, K. Fischbach, B. A. Bamieh, and G. H. Miley, "Effectiveness and constraints of using the refueling system to control fusion reactor burn," in *15th IEEE/NPSS Symp. Fusion Engineering*, vol. 2, pp. 562–564, Institue of Electrical and Electronics Engineers/Nuclear and Plasma Sciences Society, 1994.

[14] D. Plummer, "Fusion Reactor Control," in *Proc. 16th IEEE/NPSS Symp. Fusion Engineering*, vol. 2, pp. 1186–1189, Institue of Electrical and Electronics Engineers/Nuclear and Plasma Sciences Society, 1995.

[15] O. Mitarai, A. Sagara, R. Sakamoto, N. Ohyabu, A. Komori, and O. Motojima, "High-Density, Low Temperature Ignited Operations in FFHR," *Plasma and Fusion Research*, vol. 5, pp. S1001–S1001, 2010.

[16] A. Sestero, "Proposed scenario for burn control in tokamak reactors," *Nucl. Technology/Fusion*, vol. 4, p. 437, 1983.

[17] O. Mitarai and K. Muraoka, "A proposed set of diagnostics for core ignition burn control in a tokamak reactor," *Nuclear Fusion*, vol. 39, pp. 725–745, June 1999.

[18] G. Sager, G. Miley, and I. Maya, "Optimal control theory applied to fusion plasma thermal stabilization," *Fusion Technology*, vol. 8, p. 1795, 1985.

[19] O. Mitarai, "Fuel Ratio and Fueling Control for Safe Ignited Operation in ITER class Tokamak Reactors," in *Advances in Plasma Physics Research, Vol. 2*, p. 37, Nova Science Publishers, 2002.

[20] O. Mitarai, A. Sagara, R. Sakamoto, N. Ohyabu, A. Komori, and O. Motojima, "The low temperature and high density ignition in the FFHR helical reactor by pellet injections," no. 1.

[21] M. A. Firestone and C. E. Kessel, "Plasma Kinetic Control in a Tokamak," *Plasma Physics*, vol. 19, no. I, 1991.

[22] G. Miley and V. Varadarajan, "On self-tuning control of tokamak thermokinetics," *Fusion Technology*, vol. 22, p. 425, 1992.

[23] V. Fuchs, M. M. Shoucri, G. Thibaudeau, L. Harten, and A. Bers, "High-Q Thermally Stable Operation of a Tokamak Reactor," *IEEE Transactions on Plasma Science*, vol. PS-11, no. 1, pp. 4–18, 1983.

[24] V. M. Leonov, Y. V. Mitrishkin, and V. E. Zhogolev, "Simulation of burning ITER plasma in multi-variable kinetic control system," in *32nd EPS Conference on Plasma Physics*, vol. 29, pp. 2–5, 2005.

[25] E. Schuster and M. Krstic, "Burn Control in Fusion Reactors Via Nonlinear Stabilization Techniques," *Fusion Science and Technology*, vol. 43, 2003.

[26] J. Vitela, "Burn conditions stabilization with artificial neural networks of subignited thermonuclear reactors with scaling law uncertainties," *Plasma Physics and Controlled Fusion*, vol. 43, pp. 99–119, 2001.

[27] J. Vitela, "Stabilization of burn conditions in a thermonuclear reactor using artificial neural networks," 1998.

[28] K. D. Zastrow, J. M. Adams, Y. F. Baranov, P. Belo, L. Bertalot, and A. Others, "Tritium transport experiments on the JET tokamak," *Plasma Physics and Controlled Fusion*, vol. 46, pp. B255–B265, Dec. 2004.

[29] M. J. Gouge, W. A. Houlberg, S. E. Attenberger, and S. L. Milora, "Fuel Source Isotopic Tailoring and Its Impact on ITER Design, Operation and Safety," *Fusion Technology*, pp. 1–18, 1995.

[30] L. Baylor, P. Parks, T. Jernigan, J. Caughman, S. Combs, C. Foust, W. A. Houlberg, S. Maruyama, and D. Rasmussen, "Pellet fuelling and control of burning plasmas in ITER," *Nuclear Fusion*, vol. 47, pp. 443–448, 2007.

[31] K. Asai, N. Naoi, T. Iguchi, K. Watanabe, J. Kawarabayashi, and T. Nishitani, "Neutron Spectrometer for DD / DT Burning Ratio Measurement in Fusion Experimental Reactor," *Journal of Nuclear Science and Technology*, vol. 43, no. 4, p. 320, 2006.

[32] K. Okada, K. Kondo, N. Kubota, K. Ochiai, S. Sato, T. Nishitani, C. Konno, a. Okamoto, S. Kitajima, and M. Sasao, "Development of a Time of Flight Spectrometer for nd/nt Fuel Ratio Measurement in Burning Plasma," *Plasma and Fusion Research*, vol. 2, pp. S1083–S1083, 2007.

[33] M. Murakami, M. R. Wade, C. M. Greenfield, *et al.*, "Progress toward fully noninductive, high beta conditions in DIII-D," *Physics of Plasmas*, vol. 13, no. 5, p. 056106, 2006.

[34] M. A. Firestone, J. W. Morrow-Jones, and T. K. Mau, "Comprehensive Feedback Control of a Tokamak Fusion Reactor," *Fusion Technology*, vol. 32, pp. 390–403, 1997.

[35] M. A. Firestone, J. W. Morrow-Jones, and T. K. Mau, "Developing Integrated Tokamak Dynamics Models for Next Generation Machine Control," *Fusion Technology*, vol. 32, pp. 526–544, 1997.

[36] E. Schuster and M. Krstić, "Control of a non-linear PDE system arising from non-burning tokamak plasma transport dynamics," *International Journal of Control*, vol. 76, pp. 1116–1124, Jan. 2003.

[37] D. Boyer and E. Schuster, "Simultaneous control of effective atomic number and electron density in non-burning tokamak plasmas," in *Proceedings of the 2010 American Control Conference (ACC)*, pp. 1985–1990, IEEE, 2010.

[38] D. K. Owens, H. Adler, P. Alling, C. Ancher, H. Anderson, , *et al.*, "Plasma-surface Interactions in TFTR DT experiments," *Journal of Nuclear Materials*, vol. 220-222, pp. 62–72, 1995.

[39] Y. Hirooka, S. Masuzaki, H. Suzuki, T. Kenmotsu, and T. Kawamura, "Modeling of wall recycling effects on the global particle balance in magnetic fusion devices," *Journal of Nuclear Materials*, vol. 290-293, pp. 423–427, 2001.

[40] G. Maddison, A. Turner, S. J. Fielding, and S. You, "Global modelling of tank gas density and effects on plasma density control in MAST," *Plasma Physics and Controlled Fusion*, vol. 48, pp. 71–107, 2006.

[41] J. Ehrenberg, "Wall effects on particle recycling in tokamaks," in *Physical processes of the interaction of fusion plasmas with solids*, p. 35, Academic Press, 1996.

[42] P. Andrew, D. Brennan, J. Coad, J. Ehrenberg, M. Gadeberg, A. Gibson, M. Groth, J. How, O. N. Jarvis, H. Jensen, D. L. Hillis, J. Hogan, R. Lasser, F. Marcus, R. Monk, P. Morgan, J. Orchard, A. Peacock, R. Pearce, M. Pick, A. Rossi, B. Schunke, M. Stamp, and M. von Hellermann, "Tritium recycling and retention in JET," *Journal of Nuclear Materials*, vol. 266-269, pp. 153–159, 1999.

[43] L. Hively, "Special Topic Convenient Computational Forms For Maxwellian Reactivities," *Nuclear Fusion*, vol. 17, no. 4, p. 873, 1977.

[44] W. M. Stacey, *Fusion: An Introduction to the Physics and Technology of Magnetic Confinement Fusion*. Weinheim: Wiley-VCH, 2nd ed., 2010.

[45] "Summary of the ITER final design report," tech. rep., International Atomic Energy Agency, Vienna, 2001.

[46] N. Uckan, "Confinement capability of ITER-EDA design," *15th IEEE/NPSS Symposium. Fusion Engineering*, pp. 183–186, 1994.

[47] P. Ioannou and B. Fidan, *Adaptive Control Tutorial*. Philadelphia: Society for Industrial and Applied Mathematics, 2006.

[48] M. Krstić, I. Kanellakopoulos, and P. Kokotović, *Nonlinear and Adaptive Control Design*. New York: John Wiley & Sons, Inc., 1995.

[49] V. Adetola and M. Guay, "Adaptive output feedback extremum seeking receding horizon control of linear systems," *Journal of Process Control*, vol. 16, pp. 521–533, June 2006.

[50] M. Guay and T. Zhang, "Adaptive extremum seeking control of nonlinear dynamic systems with parametric uncertainties," *Automatica*, vol. 39, no. 7, 2003.

[51] H. Khalil and J. Grizzle, *Nonlinear systems*. Englewood Cliffs, NJ: Prentice Hall, 2nd ed., 1996.

[52] E. Dozal-Mejorada, P. Thakker, and B. Ydstie, "Supervised adaptive predictive control using dual models," in *8th International IFAC Symposium on Dynamics and Control of Process Systems*, vol. 3, (Cancun, Mexico), pp. 109–114, 2007.

[53] V. Adetola and M. Guay, "Excitation Signal Design for Parameter Convergence in Adaptive Control of Linearizable Systems," *Proceedings of the 45th IEEE Conference on Decision and Control*, pp. 447–452, 2006.

[54] E. A. Misawa, J. K. Hedrick, and E. K. Filter, "Nonlinear Observers - A State-of- the-Art Survey," *Journal of Dynamic Systems, Measurement, and Control*, vol. 111, no. 3, pp. 344–352, 1989.

[55] A. Johansson and A. Medvedev, "An observer for systems with nonlinear output map," *Automatica*, vol. 39, pp. 909–918, May 2003.

[56] A. Krener and W. Respondek, "Nonlinear Observers With Linearizable Error Dynamics," *SIAM Journal on Control and Optimization*, vol. 23, no. 2, 1985.

[57] S. Linder and B. Shafai, "Rejecting Disturbances to Flexible Structures using PI Kalman Filters," in *Proceedings of the 1997 IEEE International Conference on Control Applications*, (Hartford, CT), pp. 475–477, 1997.

[58] S. Beale and B. Shafai, "Robust Control System Design with the Proportional Integral Observer," *International Journal of Control*, vol. 50, no. 1, pp. 554–557, 1989.

[59] R. Orjuela, B. Marx, J. Ragot, and D. Maquin, "Proportional-Integral observer design for nonlinear uncertain systems modelled by a multiple model approach," *2008 47th IEEE Conference on Decision and Control*, pp. 3577–3582, 2008.

[60] J. Jung, K. Huh, and T. Shim, "Dissipative Proportional Integral Observer for a Class of Uncertain Nonlinear Systems," in *2007 American Control Conference*, (New York City, NY), pp. 269–274, IEEE, July 2007.

[61] J. Snipes, D. Beltran, T. Casper, Y. Gribov, a. Isayama, J. Lister, S. Simrock, G. Vayakis, a. Winter, Y. Yang, and L. Zabeo, "Actuator and diagnostic requirements of the ITER Plasma Control System," *Fusion Engineering and Design*, vol. 87, pp. 1900–1906, Dec. 2012.

[62] PTRANSP: Predictive Integrated Modeling Code `http://w3.pppl.gov/transp`.

[63] J. Artaud, V. Basiuk, F. Imbeaux, M. Schneider, J. Garcia, *et al.*, "The CRONOS Suite of Codes for Integrated Tokamak Modelling," *Nuclear Fusion*, vol. 50, p. 043001, Apr. 2010.

[64] H. J. de Blank, "Plasma Equilibrium in Tokamaks," *Fusion Science and Technology*, vol. 49, pp. 111–117, 2006.

[65] D. E. Post, R. V. Jensen, C. B. Tarter, W. H. Grasberger, and W. A. Lokke, "Steady-state radiative cooling rates for low-density, high-temperature plasmas," *Atomic Data and Nuclear Data Tables*, vol. 20, pp. 397–439, 1977.

[66] G. B. Rybicki and A. P. Lightman, *Radiative Processes in Astrophysics*. New York: Wiley-Interscience, 1979.

[67] F. Albajar, M. Bornatici, and F. Engelmann, "Electron cyclotron radiative transfer in fusion plasmas," *Nuclear Fusion*, vol. 42, no. 6, p. 670, 2002.

[68] O. Sauter, C. Angioni, and Y. R. Lin-Liu, "Neoclassical conductivity and bootstrap current formulas for general axisymmetric equilibria and arbitrary collisionality regime," *Physics of Plasmas*, vol. 6, no. 7, p. 2834, 1999.

[69] D. Boskovic, A. Balogh, and M. Krstic, "Backstepping in infinite dimension for a class of parabolic distributed parameter systems," *Mathematics of Control, Signals, and Systems*, vol. 16, no. 1, pp. 44–75, 2003.

[70] M. Krstic and A. Smyshlyaev, *Boundary Control of PDEs*. Society for Industrial and Applied Mathematics, 2008.

[71] D. Boskovic and M. Krstic, "Backstepping control of chemical tubular reactors," *Computers & Chemical Engineering*, vol. 26, pp. 1077–1085, Aug. 2002.

[72] D. Boskovic and M. Krstic, "Stabilization of a Solid Propellant Rocket Instability by State Feedback," *International Journal of Robust and Nonlinear Control*, vol. 13, pp. 483–495, Apr. 2003.

[73] M. D. Boyer and E. Schuster, "Backstepping control of density and energy profiles in a burning tokamak plasma," in *Proceedings of the 50th IEEE Conference on Decision and Control (CDC)*, IEEE, 2011.

[74] J. Ferron, P. Gohil, C. Greenfield, *et al.*, "Feedback control of the safety factor profile evolution during formation of an advanced tokamak discharge," *Nuclear Fusion*, vol. 46, pp. L13–L17, Oct. 2006.

[75] T. Wijnands, D. V. Houtte, G. Martin, X. Litaudon, and P. Froissard, "Feedback control of the current profile on Tore Supra," *Nuclear Fusion*, vol. 37, pp. 777–791, June 1997.

[76] O. Barana, D. Mazon, L. Laborde, and F. Turco, "Feedback control of the lower hybrid power deposition profile on Tore Supra," *Plasma Physics and Controlled Fusion*, vol. 49, pp. 947–967, July 2007.

[77] T. Suzuki, "Recent RF experiments and application of RF waves to real-time control of safety factor profile in JT-60U," in *AIP Conference Proceedings*, vol. 787, pp. 279–286, Aip, 2005.

[78] T. Suzuki, S. Ide, T. Oikawa, T. Fujita, M. Ishikawa, M. Seki, G. Matsunaga, T. Hatae, O. Naito, K. Hamamatsu, M. Sueoka, H. Hosoyama, and M. Nakazato, "Off-axis current drive and real-time control of current profile in JT-60U," *Nuclear Fusion*, vol. 48, p. 045002, Apr. 2008.

[79] D. Moreau, F. Crisanti, X. Litaudon, *et al.*, "Real-time control of the q -profile in JET for steady state advanced tokamak operation," *Nuclear Fusion*, vol. 43, pp. 870–882, Sept. 2003.

[80] D. Moreau, D. Mazon, M. Ariola, , *et al.*, "A two-time-scale dynamic-model approach for magnetic and kinetic profile control in advanced tokamak scenarios on JET," *Nuclear Fusion*, vol. 48, p. 106001, Oct. 2008.

[81] L. Laborde, D. Mazon, D. Moreau, *et al.*, "A model-based technique for integrated real-time profile control in the JET tokamak," *Plasma Physics and Controlled Fusion*, vol. 47, pp. 155–183, Jan. 2005.

[82] D. Moreau, D. Mazon, M. Walker, J. Ferron, K. Burrell, S. Flanagan, P. Gohil, R. Groebner, a.W. Hyatt, R. La Haye, J. Lohr, F. Turco, E. Schuster, Y. Ou, C. Xu, Y. Takase, Y. Sakamoto, S. Ide, and T. Suzuki, "Plasma models for real-time control of advanced tokamak scenarios," *Nuclear Fusion*, vol. 51, p. 063009, June 2011.

[83] W. Shi, W. Wehner, J. Barton, M. Boyer, *et al.*, "Multivariable robust control of the plasma rotational transform profile for advanced tokamak scenarios in DIII-D," in *Proceedings of the 2012 American Control Conference*, 2012.

[84] W. Wehner, W. Shi, E. Schuster, D. Moreau, M. L. Walker, J. R. Ferron, T. C. Luce, D. A. Humphreys, B. G. Penaflor, and R. D. Johnson, "Optimal feedback control of the poloidal magnetic flux profile in the DIII-D tokamak based on identified plasma response models," in *Proceedings of the 2012 American Control Conference*, 2012.

[85] F. Felici, O. Sauter, S. Coda, B. Duval, T. Goodman, J.-M. Moret, and J. Paley, "Real-time physics-model-based simulation of the current density profile in tokamak plasmas," *Nuclear Fusion*, vol. 51, p. 083052, 2011.

[86] Y. Ou, T. Luce, E. Schuster, *et al.*, "Towards model-based current profile control at DIII-D," *Fusion Engineering and Design*, vol. 82, pp. 1153–1160, Oct. 2007.

[87] E. Witrant, E. Joffrin, S. Bremond, *et al.*, "A control-oriented model of the current profile in tokamak plasma," *Plasma Physics and Controlled Fusion*, vol. 49, pp. 1075–1105, July 2007.

[88] Y. Ou, C. Xu, E. Schuster, *et al.*, "Design and simulation of extremum-seeking open-loop optimal control of current profile in the DIII-D tokamak," *Plasma Physics and Controlled Fusion*, vol. 50, p. 115001, Nov. 2008.

[89] C. Xu, Y. Ou, J. Dalessio, *et al.*, "Ramp-up-phase current-profile control of tokamak plasmas via nonlinear programming," *IEEE Transactions on Plasma Science*, vol. 38, pp. 163–173, Feb. 2010.

[90] S. Kim and J. Lister, "Feedback control of the safety factor profile evolution during formation of an advanced tokamak discharge," *Nuclear Fusion*, vol. 52, p. 074002, 2012.

[91] Y. Ou, C. Xu, E. Schuster, *et al.*, "Optimal tracking control of current profile in tokamaks," *IEEE Transactions on Control Systems Technology*, vol. 19, pp. 432–441, Mar. 2011.

[92] O. Gaye, E. Moulay, S. Bremond, L. Autrique, R. Nouailletas, and Y. Orlov, "Sliding mode stabilization of the current profile in tokamak plasmas," in *Proceedings of the 50th IEEE Conference on Decision and Control and European Control Conference (CDC-ECC)*, pp. 2638–2643, 2011.

[93] Y. Ou, C. Xu, and E. Schuster, "Robust control design for the poloidal magnetic flux profile evolution in the presence of model uncertainties," *IEEE Transactions on Plasma Science*, vol. 38, p. 375, 2010.

[94] F. Argomedo, E. Witrant, C. Prieur, D. Georges, and S. Bremond, "Model-based control of the magnetic flux profile in a tokamak plasma," in *Proceedings*

of the 49th IEEE Conference on Decision and Control (CDC), pp. 6926–6931, 2010.

[95] M. D. Boyer, J. Barton, E. Schuster, T. C. Luce, *et al.*, "First-principles-driven model-based current profile control for the DIII-D tokamak via LQI optimal control," *Plasma Physics and Controlled Fusion*, vol. 55, p. 105007, Oct. 2013.

[96] J. Barton, M. Boyer, W. Shi, E. Schuster, T. Luce, J. Ferron, M. Walker, D. Humphreys, B. Penaflor, and R. Johnson, "Toroidal current profile control during low confinement mode plasma discharges in DIII-D via first-principles-driven model-based robust control synthesis," *Nuclear Fusion*, vol. 52, p. 123018, 2012.

[97] F. L. Hinton and R. D. Hazeltine, "Theory of plasma transport in toroidal confinement," *Reviews of Modern Physics*, vol. 48, p. 239, 1976.

[98] R. Goldston, "Energy confinement scaling in Tokamaks: some implications of recent experiments with Ohmic and strong auxiliary heating," *Plasma Physics and Controlled Fusion*, vol. 30, no. 8, pp. 87–103, 1990.

[99] P. Politzer and G. Porter, "Power threshold for neutral beam current drive," *Nuclear Fusion*, vol. 30, no. 8, p. 1605, 1990.

[100] F. Argomedo, E. Witrant, and C. Prieur, "Input-to-state stability of a time-varying nonhomogeneous diffusive equation subject to boundary disturbances," in *Proceedings of the 2012 American Control Conference*, 2012.

[101] J. Ferron, M. Walker, L. Lao, H. John, D. Humphreys, and J. Leuer, "Real time equilibrium reconstruction for tokamak discharge control," *Nuclear Fusion*, vol. 38, p. 1055, 1998.

[102] D. Piglowski, J. Ferron, P. Gohil, R. Johnson, and B. Penaflor, "Enhancements in the second generation DIII-D digital plasma control system," *Fusion Engineering and Design*, vol. 82, no. 5-14, p. 1058, 2007.

[103] M. Walker, J. R. Ferron, S. H. Hahn, D. A. Humphreys, Y. In, R. D. Johnson, J. S. Kim, R. J. La Haye, J. A. Leuer, and B. G. Penaflor, "Advances in integrated plasma control on DIII-D," *Fusion Engineering and Design*, vol. 82, no. 5-14, pp. 1051–1057, 2007.

[104] J. Barton, Y. Ou, C. Xu, E. Schuster, and M. Walker, "Simserver simulation of a model-based current profile controller in the DIII-D plasma control system," *Fusion Engineering and Design*, vol. 86, no. 6-8, p. 1116, 2011.

[105] J. Barton, W. Shi, and E. Schuster, "Physics-Based Control-Oriented Modeling of the Safety Factor Profile Dynamics in High Performance Tokamak Plasmas," in *Proceedings of the 52nd IEEE Conference on Decision and Control (CDC)*, IEEE, 2013.

[106] M. D. Boyer, J. Barton, E. Schuster, T. C. Luce, J. R. Ferron, M. L. Walker, D. A. Humphreys, B. G. Penaflor, and R. D. Johnson, "Backstepping control of the plasma current profile in the DIII-D tokamak," in *Proceedings of the 2012 American Control Conference*, 2012.

Appendix A

Particle Recycling Model Derivation

The following particle recycling model derivation is based on a similar model derived in [41]. The particle balance for deuterium and tritium ions can then be written as

$$\frac{dn_D}{dt} = -\frac{n_D}{\tau_D} + f_{eff} S_D^R + S_D^{inj}, \tag{A.1}$$

$$\frac{dn_T}{dt} = -\frac{n_T}{\tau_T} + f_{eff} S_T^R + S_T^{inj}, \tag{A.2}$$

where S_D^R and S_T^R represent the total recycling fluxes from the plasma facing components that reaches the plasma edge. The recycled flux satisfies

$$S_D^R = f_{ref}\frac{n_D}{\tau_D} + \left(1-\gamma^{PFC}\right) S^{PFC} + f_{ref}\left(1-f_{eff}\right) S_D^R, \tag{A.3}$$

$$S_T^R = f_{ref}\frac{n_T}{\tau_T} + \gamma^{PFC} S^{PFC} + f_{ref}\left(1-f_{eff}\right) S_T^R, \tag{A.4}$$

where γ^{PFC} is the tritium fraction of the particle flux from the plasma facing components, S^{PFC}. The third term in each expression represents the recycled flux that is screened by the plasma due to imperfect core fueling efficiency and subsequently reflected by the surface. To avoid the need for a self-consistent model of wall implan-

tation, diffusion, and re-emmission to obtain the desorbed flux S^{PFC}, we simplify the model by considering a recycling coefficient defined as the ratio of total recycling flux to the total flux to the surface, i.e.

$$R^{eff} = \frac{S_D^R + S_T^R}{S_D^S + S_T^S} = \frac{S^R}{S^S}. \tag{A.5}$$

Note that the recycling coefficient includes the effect of wall pumping and active pumping. In order to incorporate the recycling coefficient into the model, we must write an expression for the flux to the surface

$$\begin{aligned} S_D^S &= \frac{n_D}{\tau_D} + (1 - f_{eff}) \left(1 - \gamma^{PFC}\right) S^{PFC} + f_{ref} (1 - f_{eff}) S_D^S, & \text{(A.6)} \\ S_T^S &= \frac{n_T}{\tau_T} + (1 - f_{eff}) \gamma^{PFC} S^{PFC} + f_{ref} (1 - f_{eff}) S_T^S, & \text{(A.7)} \end{aligned}$$

where the third term represents the surface flux that is reflected and subsequently returned to the surface due to imperfect fueling efficiency. Since the recycling coefficient compares total hydrogen fluxes, not individual isotopes, we sum corresponding equations to obtain

$$\begin{aligned} S^R &= f_{ref} \left(\frac{n_D}{\tau_D} + \frac{n_T}{\tau_T} \right) + S^{PFC} + f_{ref} (1 - f_{eff}) S^R, & \text{(A.8)} \\ S^S &= \frac{n_D}{\tau_D} + \frac{n_T}{\tau_T} + (1 - f_{eff}) S^{PFC} + f_{ref} (1 - f_{eff}) S^S. & \text{(A.9)} \end{aligned}$$

Using these expressions, we can solve to obtain

$$\begin{aligned} S^{PFC} &= S^R \left[1 - f_{ref} (1 - f_{eff})\right] - f_{ref} \left(\frac{n_D}{\tau_D} + \frac{n_T}{\tau_T} \right), & \text{(A.10)} \\ S^S &= \left(\frac{n_D}{\tau_D} + \frac{n_T}{\tau_T} \right) + (1 - f_{eff}) S^R. \end{aligned}$$

From the definition of the recycling coefficient, we have that $S^S = S^R/R^{eff}$. Substituting this definition and rearranging, we can obtain

$$S^R = \frac{R^{eff}}{1 - R^{eff}\left(1 - f_{eff}\right)} \left(\frac{n_D}{\tau_D} + \frac{n_T}{\tau_T}\right). \tag{A.11}$$

Substituting into (A.10) yields

$$S^{PFC} = \left[\frac{\left(1 - f_{ref}\left(1 - f_{eff}\right)\right) R^{eff}}{1 - R^{eff}\left(1 - f_{eff}\right)} - f_{ref}\right] \left(\frac{n_D}{\tau_D} + \frac{n_T}{\tau_T}\right). \tag{A.12}$$

Solving (A.3) and (A.4) for S_D^R and S_T^R, respectively, and substituting (A.12) results in

$$\begin{aligned} S_D^R &= \frac{1}{1 - f_{ref}\left(1 - f_{eff}\right)} \left\{ f_{ref} \frac{n_D}{\tau_D} \right. \\ &\quad \left. + \left(1 - \gamma^{PFC}\right) \left[\frac{\left(1 - f_{ref}\left(1 - f_{eff}\right)\right) R^{eff}}{1 - R^{eff}\left(1 - f_{eff}\right)} - r\right] \left(\frac{n_D}{\tau_D} + \frac{n_T}{\tau_T}\right) \right\}, \end{aligned} \tag{A.13}$$

$$\begin{aligned} S_T^R &= \frac{1}{1 - f_{ref}\left(1 - f_{eff}\right)} \left\{ f_{ref} \frac{n_T}{\tau_T} \right. \\ &\quad \left. + \gamma^{PFC} \left[\frac{\left(1 - f_{ref}\left(1 - f_{eff}\right)\right) R^{eff}}{1 - R^{eff}\left(1 - f_{eff}\right)} - f_{ref}\right] \left(\frac{n_D}{\tau_D} + \frac{n_T}{\tau_T}\right) \right\}. \end{aligned} \tag{A.14}$$

Appendix B

Lyapunov Stability Basics

In this appendix we review the basics of Lyapunov stability theory, which is crucial to the stability proof in this paper. Consider a nonlinear dynamic system of the form

$$\dot{x} = f(x, u), \tag{B.1}$$

where x (state variable) and u (control input) are vector valued functions of time. We seek a feedback control law of the form

$$u = k(x), \tag{B.2}$$

to achieve a desired property, for example, stability of a certain equilibrium point. A point $x = x_e$ is an equilibrium of the system when

$$f\left(x_e, k\left(x_e\right)\right) = 0.$$

With a shift of the system's origin, i.e, $\tilde{x} = x - x_e$ the equilibrium can be made to occur at $\tilde{x} = 0$. An equilibrium $\tilde{x} = 0$ of (B.1) and (B.2) is globally asymptotically

stable if there exists a continuously differentiable function $V(\tilde{x})$ such that

$$V(x) > 0 \text{ for all } x \neq 0 \text{ and } V(0) = 0,$$

$$V(x) \to \infty \text{ as } |x| \to \infty,$$

$$\dot{V} = \frac{dV}{d\tilde{x}} f(x, k(x)) < 0 \text{ for all } \tilde{x} \neq 0.$$

For example, if we can find a quadratic Lyapunov function $V = \tilde{x}^T P \tilde{x}$ with $\dot{V} = -\tilde{x}^T Q \tilde{x}$, P, $Q > 0$, all of the conditions are satisfied and the equilibrium x_e is asymptotically stable.

The problem of finding a Lyapunov function $V(x)$, even for a system known to be stable, can be very difficult in general. It is often even more difficult when we have to find $V(x)$ and the feedback law $k(x)$ at the same time.

We note that for linear systems, other stability tests exist, for example, Routh-Hurwitz. However, for nonlinear systems such as the one considered in this work, some form of Lyapunov analysis is the only tool available. See [51] for a complete approach to the Lyapunov stability theory.

Curriculum Vitae

Education

Lehigh University, Bethlehem, Pennsylvania
Ph.D., Mechanical Engineering. GPA: 3.95
December 2013

York College of Pennsylvania, York, Pennsylvania
B.S., Mechanical Engineering. Mathematics minor, *Summa Cum Laude*. GPA: 3.94
August 2009

Skills & Expertise

- ◇ *Control Systems*: Model-based control design · Optimization · Real-time software implementation
- ◇ *Engineering*: Complex system modeling and simulation · Machine design and computer aided drafting · Manufacturing and part fabrication
- ◇ *Software*: Matlab · Simulink · Solidworks · AutoCAD · ANSYS · Word · PowerPoint · Excel · LaTeX 2_ε
- ◇ *Programming and platforms*: C/C++ · HTML · Windows · Macintosh · Unix

Research Experience

Lehigh University, Bethlehem, Pennsylvania
Research Assistant **August 2010 – December 2013**

- ◇ Created innovative control algorithms for stabilization and real-time optimization of the power produced by nuclear fusion reactors, applying multivariable, adaptive nonlinear techniques, and testing designs using Matlab/Simulink simulations of particle and energy transport. Designs enable operation at economically attractive conditions that would otherwise be unstable.

CEA Cadarache, Saint-Paul-lès-Durance, France
Visiting Researcher **Spring 2012**

- ◇ Tested approaches to stabilizing density and temperature in fusion plasmas using a predictive modeling code (implemented in Matlab/Simulink), and created new modules to extend the existing simulation capabilities. Demonstrated robustness of designs to the complex physics captured by the predictive code.

General Atomics, San Diego, California
Visiting Researcher **Summer 2010 & 2011**

- ◇ Designed and experimentally tested feedback control algorithms for the DIII-D nuclear fusion reactor, demonstrating solutions that could facilitate more efficient and longer duration operation. Tested controllers based on first-principles models as well as data-driven models. Implemented a flexible framework for real-time control that has already been utilized for several experimental campaigns.

Teaching Experience

Lehigh University, Bethlehem, Pennsylvania
Instructor **Fall 2013**

- ◇ Developed and facilitated a group project course (ENG-005) for over 100 engineering freshman in which students designed and tested miniature wind turbines.
- ◇ Lectured and guided 30 students through tutorial sessions in a numerical methods course (ME-196) covering Excel and Matlab.

Teaching Assistant **Fall 2011, Fall 2012**

◇ Assisted students during office hours and graded homework for undergraduate courses in aerodynamics (50 students), control systems (50 students), and nuclear fusion (15 students). Delivered lectures on nuclear fusion reactor confinement techniques and nonlinear control design.

Graduate STEM Fellow in K-12 Education **Fall 2009, Spring 2010**

◇ Developed and taught an engineering curriculum for middle school (8 classes of 20-30 students each week) including lessons on the design process, alternative energy, and computer aided drafting. Encouraged students to pursue careers in science, and provided lesson plans to teachers for subsequent school years.

Engineering Experience

Graham Packaging Corporation, York, Pennsylvania
Project Development Engineering Co-op **Fall 2008**

◇ Designed plant layouts (using AutoCAD), and analyzed process systems (chillers, air handling units, etc.) for bottle production lines. Evaluated existing lines and identified potential additions and modifications in plants across the country to make more efficient use of capital equipment and space.

Komax Systems York, York, Pennsylvania
Process Engineering Co-op **Spring 2008**

◇ Experimentally identified the root cause of errors in solar panel manufacturing robots, and investigated methods for improving the soldering process. Results contributed to designs that kept product within tolerances while reducing solar cell breakage during manufacturing.

BenCo Technology, LLC, Honey Brook, Pennsylvania
Mechanical Engineer/Drafter **June 2004 - January 2008**

◇ Modeled and designed hundreds of custom parts/assemblies for a sheet metal laser cutting company, using SolidWorks and AutoCAD to generate flat patterns, as well as detailed drawings for forming/welding/ assembly. Led projects from customer consultation and design through pricing and production. Ensured final products met cost/performance expectations.

York College of PA Formula SAE, York, Pennsylvania
Vehicle Suspension Designer **June 2008 - June 2009**

◇ Teamed with 15 student engineers to design and build a Formula-style race car. Led the design/fabrication of the suspension (using SolidWorks for design and COSMOSWorks to perform FEA analysis), improving upon previous designs to achieve better handling/performance and reduced weight.

Honors and Awards

Lehigh University

◇ Rossin Doctoral Fellow, 2012
◇ RCEAS Fellowship, 2011

Institute of Electrical and Electronics Engineers

◇ Best Presentation in Session, 2012 American Controls Conference
◇ Finalist, Best Student Paper Award, 2012 American Controls Conference

National Science Foundation

◇ Graduate Research Fellowship Program Honorable Mention, 2010

◇ Graduate Research Fellowship Program Honorable Mention, 2011

York College of Pennsylvania

◇ Trustee (full-tuition) Scholarship, 2005-2009

Memberships & Certifications

Pennsylvania State Registration Board for Professional Engineers

◇ Engineer in Training, License Number: ET018342

Institute of Electrical and Electronics Engineers

◇ Control Systems Society · Technical Committee on Power Generation

Journal Articles

M. D. Boyer, E. Schuster, "Adaptive Nonlinear Control and Optimization of the Burn Condition in ITER", in preparation.

M. D. Boyer, E. Schuster, "Control of Density and Temperature Profiles in Burning Fusion Plasmas via Backstepping Boundary and Interior Control", in preparation.

M. D. Boyer and E. Schuster, "Nonlinear Burn Condition Control for ITER via Isotopic Fuel Tailoring," in preparation.

W. Shi, W. Wehner, J. E. Barton, **Mark D. Boyer**, E. Schuster, et al. "System Identification and Robust Control of the Plasma Rotational Transform Profile and Normalized Beta Dynamics for Advanced Tokamak Scenarios in DIII-D," submitted to *Nuclear Fusion*.

M. D. Boyer, J. Barton, E. Schuster, M. L. Walker, T. C. Luce, et al., "Backstepping Control of the Toroidal Plasma Current Profile in the DIII-D Tokamak," accepted for publication in *IEEE Transactions on Control Systems Technology*, 2013.

M. D. Boyer, J. Barton, E. Schuster, T. C. Luce, J. R. Ferron, et al., "First-Principles-Driven Model-Based Current Profile Control for the DIII-D Tokamak via LQI Optimal Control," *Plasma Physics and Controlled Fusion*, 2013.

D. Moreau, M. L. Walker, J. R. Ferron, F. Liu, E. Schuster, J. E. Barton, **M. D. Boyer**, et al., "Integrated magnetic and kinetic control of advanced tokamak plasmas on DIII-D based on data-driven models," *Nuclear Fusion*, 2013.

J. E. Barton, **Mark D. Boyer**, W. Shi, E. Schuster, T. C. Luce, et al., "Toroidal Current Profile Control During Low Confinement Mode Plasma Discharges in DIII-D via First-Principles-Driven Model-Based Robust Control Synthesis," *Nuclear Fusion*, 2012.

Refereed Conference Proceedings

M. D. Boyer, J. Barton, W. Shi, W. Wehner, E. Schuster, J. Ferron, et al. "Simultaneous Boundary and Distributed Feedback Control of the Current Profile and Stored Energy in H-mode Discharges on DIII-D", submitted to the *19th World Congress of the International Federation of Automatic Control*, Cape Town, South Africa, August 24-29, 2014.

M. D. Boyer, E. Schuster, "Nonlinear Burn Control in Tokamak Fusion Reactors via Output Feedback", submitted to the *19th World Congress of the International Federation of Automatic Control*, Cape Town, South Africa, August 24-29, 2014.

J. Barton, **Mark D. Boyer**, W.Shi, W. Wehner, E. Schuster, et al., "Experimental and Simulation Testing of Physics-model-based Safety Factor Profile and Internal Energy Feedback Controllers in DIII-D Advanced Tokamak Scenarios", submitted to the *19th World Congress of the International Federation of Automatic Control*, Cape Town, South Africa, August 24-29, 2014.

M. D. Boyer, E. Schuster, "Burn Control in Fusion Reactors Using Simultaneous Boundary and Distributed Actuation", accepted, *52nd IEEE Conference on Decision and Control*, Florence, Italy, December 10-13, 2013.

W. Shi, J. Barton, W. Wehner, **M. D. Boyer**, et al., "First-principles-driven Control of the Rotational Transform Profile in High Performance Discharges in the DIII-D Tokamak," accepted, *52nd IEEE Conference on Decision and Control*, Florence, Italy, December 10-13, 2013.

M. D. Boyer and E. Schuster, "Nonlinear Control and Optimization of the Burn Condition in Tokamak Nuclear Fusion Reactors," *2013 American Controls Conference*.

W. Shi, W. Wehner, J. Barton, **M. D. Boyer**, E. Schuster, et al., "PTRANSP Simulation and Experimental Test of a Robust Current Profile and β_N Controller for Off-Axis Current-Drive Scenarios in the DIII-D Tokamak," *2013 American Controls Conference*.

M. D. Boyer, J. Barton, E. Schuster, and M. L. Walker, "Current Profile Tracking for the DIII-D Tokamak via LQI Optimal Control," *51st IEEE Conference on Decision and Control*, Maui, HI, USA, Dec. 2012.

W. Shi, W. Wehner, J. Barton, **M. D. Boyer**, E. Schuster, et al., "A Two-time-scale Model-based Combined Magnetic and Kinetic Control System for Advanced Tokamak Scenarios on DIII-D," *51st IEEE Conference on Decision and Control*, Maui, HI, USA, Dec. 10-13, 2012.

M. D. Boyer, J. Barton, E. Schuster, and M. L. Walker, "Backstepping Control of the Plasma Current Profile in the DIII-D Tokamak," *2012 American Control Conference*, Montréal, Canada, June 27-29, 2012.

M. D. Boyer and E. Schuster, "Adaptive Nonlinear Burn Control in Tokamak Fusion Reactors," *2012 American Control Conference*, Montréal, Canada, June 27-29, 2012.

J. E. Barton, **M. D. Boyer**, W. Shi, E. Schuster and M. L. Walker, "Robust Control of the Current Profile Evolution During the Ramp-up and Early Flat-top Phases of the Plasma Discharge in the DIII-D Tokamak," *2012 American Control Conference*, Montréal, Canada, June 27-29, 2012.

W. Shi, W. Wehner, J. E. Barton, **M. D. Boyer**, E. Schuster and M. L. Walker, "Multivariable Robust Control of the Plasma Rotational Transform Profile for Advanced Tokamak Scenarios in DIII-D," *2012 American Control Conference*, Montréal, Canada, June 27-29, 2012.

M. D. Boyer and E. Schuster, "Backstepping Control of Density and Energy Profiles in a Burning Tokamak Plasma", *50th IEEE Conference on Decision and Control*, Orlando, FL, USA, Dec. 12-15, 2011.

M. D. Boyer and E. Schuster, "Zero-dimensional Nonlinear Burn Control Using Isotopic Fuel Tailoring For Thermal Excursions", *IEEE Multiconference on Systems and Control*, Denver, CO, USA, Sept. 28-30, 2011.

M. D. Boyer and E. Schuster, "Simultaneous Control of Effective Atomic Number and Electron Density in Non-Burning Tokamak Plasmas", *2010 American Control Conference*, Baltimore, MD, USA, June 30-July 2, 2010.

Conference Proceedings

J. E. Barton, **M. D. Boyer**, W. Shi, W. Wehner, E. Schuster, et al., "First-Principles Model-based Closed-loop Control of the Current Profile Dynamic Evolution on DIII-D," *24th IAEA Fusion Energy Conference*, San Diego, CA, USA, Oct. 8-13, 2012.

D. Moreau, E. Schuster, M. Walker, J. R. Ferron, D. Humphreys, J. E. Barton, **M. D. Boyer**, et al., "Integrated Magnetic and Kinetic Control of Advanced Tokamak Scenarios Based on Data-Driven Models," *24th IAEA Fusion Energy Conference*, San Diego, CA, USA, Oct. 8-13, 2012.

Presentations

M. D. Boyer, E. Schuster, "Nonlinear Control and Real-time Optimization of the Burn Condition in ITER", 18th Workshop on MHD Stability Control, Santa Fe, New Mexico, November 18-20, 2013.

M. D. Boyer, E. Schuster, "Nonlinear Burn Control and Operating Point Optimization in ITER", 55th Division of Plasma Physics Annual Meeting of the American Physical Society, Denver, Colorado, November 11-15, 2013.

M. D. Boyer, E. Schuster, S. Bremond, R. Nouailletas, J. Artaud, "Analysis of Fusion Burn Control Approaches Using METIS", 54th Division of Plasma Physics Annual Meeting of the American Physical Society, Providence, Rhode Island, October 29-November 2, 2012.

M. D. Boyer "Burn Condition Control in ITER," Seminar, CEA Cadarache, Saint-Paul-lès-Durance, France, June 16, 2012.

M. D. Boyer, E. Schuster, "Burn Control in Fusion Reactors via Isotopic Fueling", 53rd Division of Plasma Physics Annual Meeting of the American Physical Society, Salt Lake City, Utah, November 14-18, 2011.

M. D. Boyer, E. Schuster,"Backstepping Control of the Current Profile in the DIII-D Tokamak", 53rd Division of Plasma Physics Annual Meeting of the American Physical Society, Salt Lake City, Utah, November 14-18, 2011.

M. D. Boyer and E. Schuster, "Nonlinear Burn Condition Control in Tokamak Fusion Reactors", National Control Engineering Students Workshop, College Park, Maryland, April 28-30, 2011.

M. D. Boyer and E. Schuster, "Burn Control in Nuclear Fusion Reactors", 2011 Academic Symposium, Lehigh University, Bethlehem, Pennsylvania, March 29, 2011.

M. D. Boyer, E. Schuster,"One-Dimensional Burn Control in Fusion Reactors", 52nd Division of Plasma Physics Annual Meeting of the American Physical Society, Chicago, Illinois, November 8-12, 2010.

M. D. Boyer, E. Schuster, "One-Dimensional Simulation of a Zero-Dimensional Nonlinear Burn Stability Controller", 4th ITER International Summer School, University of Texas, Austin, Texas, May 21-June 4, 2010.

M. D. Boyer, P. Boyle, E. Schuster, G. Bateman, A. Kritz, "Simultaneous Control of Electron Density and Effective Atomic Number in Non-burning Tokamak Plasmas," 51st Division of Plasma Physics Annual Meeting of the American Physical Society, Atlanta, Georgia, November 2-6, 2009.